



Correlating Structure and Photophysics in Metal Halide Perovskite Crystals

Liang, Mingli

Publication date:
2021

Document Version
Publisher's PDF, also known as Version of record

[Link back to DTU Orbit](#)

Citation (APA):
Liang, M. (2021). *Correlating Structure and Photophysics in Metal Halide Perovskite Crystals*. Technical University of Denmark.

General rights

Copyright and moral rights for the publications made accessible in the public portal are retained by the authors and/or other copyright owners and it is a condition of accessing publications that users recognise and abide by the legal requirements associated with these rights.

- Users may download and print one copy of any publication from the public portal for the purpose of private study or research.
- You may not further distribute the material or use it for any profit-making activity or commercial gain
- You may freely distribute the URL identifying the publication in the public portal

If you believe that this document breaches copyright please contact us providing details, and we will remove access to the work immediately and investigate your claim.

Correlating Structure and Photophysics in Metal Halide Perovskite Crystals

Mingli Liang

Ph.D. Thesis

Department of Chemistry

Technical University of Denmark

January 2021

Correlating Structure and Photophysics in Metal Halide Perovskite Crystals

Ph.D. Thesis

January 15th, 2021

Mingli Liang

milia@kemi.dtu.dk

Main supervisor

Kaibo Zheng

Co-supervisors

Qijin Chi

Jens Øllgaard Duus

Department of Chemistry

Technical University of Denmark

II

Abstract

As a new type of semiconductor material, metal halide perovskite (MHP) has shown great application potential in many fields, such as solar cells, light-emitting diodes (LEDs), photodetectors, X-ray detectors, and lasing devices. In particular, since Miyasaka et al. first employed three-dimensional (3D) MAPbI₃ in photovoltaics (PVs) in 2009, the certified power conversion efficiencies (PCEs) of the perovskite PV devices have been improved from 3.8% to 25.2% today. This is mainly due to their advantageous physical properties, such as high light absorption coefficient, slow charge carrier recombination rate, and high carrier mobility. However, 3D MHPs are very sensitive to moisture and temperature, *etc.*, which hindered their commercialization. In this case, more and more researchers set their sights on more stable low-dimensional MHPs, such as 2D layered, 1D linear, and 0D punctuated MHPs.

This thesis is devoted to the design, synthesis, and structure refinement of novel 3D, 2D, and 0D MHP crystals. More importantly, the detailed structure-related photo-physical properties, including electronic band structures, photo-induced excited-state dynamics, the formation of free excitons and self-trapped excitons (STEs), charge carrier trapping and recombination *etc.*, were studied using a variety of spectroscopic methods. The findings from those studies can provide an essential reference for future materials engineering and device application.

Chapter 3 (**Paper I**) reports the spontaneous growth of MAPbBr₃/N-rGO hybrid structures using a facile solution method and their applications for photodetectors. In MAPbBr₃/N-rGO hybrid structures, **3D MHP** were homogeneously wrapped by N-rGO sheets through strong hydrogen bonding, which facilitates the charge carrier transport across the perovskite crystals. The obtained device exhibits excellent optoelectronic performance: the responsivity (R) to be 3.6×10^4 A/W, external quantum efficiency (EQE) exceeding 105 %, and detectivity up to 10^{12} Jones. In Chapter 4 (**Paper II**), we demonstrated the synthesis of the two **2D MHPs** single crystals, (n-BA)₂(MA)₂Pb₃I₁₀ and (n-BA)₂(EA)₂Pb₃I₁₀. Detailed structural analysis shows that the larger lattice distortions of (n-BA)₂(EA)₂Pb₃I₁₀ with the increase in the Pb-I bond length leads to the widening of the bandgap by mainly lowering the position of valence band maximum (VBM) compare with (n-BA)₂(MA)₂Pb₃I₁₀. Besides, we observed charge carrier trapping and trap filling in

both crystals. Based on the trapping dynamics modeling, we confirmed ultra-long-lived trap states in both crystals with the trap densities of $\sim 2.18 \times 10^{16} \text{ cm}^{-3}$ and $\sim 3.76 \times 10^{16} \text{ cm}^{-3}$, respectively. In Chapter 5 (**Paper III**), we revealed the tight dependence of STE formation and their recombination dynamics in **2D MHPs** on the local structures by studying PL emission dynamics at different surface facets of $(\text{iso-BA})_2(\text{MA})\text{Pb}_2\text{Br}_7$, $(\text{n-BA})_2(\text{MA})\text{Pb}_2\text{Br}_7$ and $(\text{n-PA})_2(\text{MA})\text{Pb}_2\text{Br}_7$ single crystals. At the in-plane facet parallel to the 2D inorganic layers (IF), the STEs are less likely to be formed, whereas free excitons (FEs) dominate due to the weak electron-phonon coupling in a more symmetric lattice. At the edge facet perpendicular to the 2D inorganic layers (PF), large distortion of the lead halide octahedra due to the accumulation of the strain along the 2D layers enhance the electron-phonon coupling, and therefore facilitate the formation of STEs. It also leads to different intensity-dependent PL dynamics at two facets. Finally, in chapter 6 (**Paper IV**), we introduced a novel structure of **0D MHP**, Cs_3BiBr_6 . The photodetector, based on its micron crystals (MCs), shows good responsivity ($\sim 25 \text{ mA W}^{-1}$ at a light density of 4 mW cm^{-2}) and detectivity ($0.8 \times 10^9 \text{ Jones}$), which demonstrates its potential in the application of optoelectronic devices.

Abstract – Danish

Som en ny type halvleder materiale har metalhalogen perovskit (MHP) vist et stort anvendelsespotentiale inden for mange områder, såsom solceller, lysemitterende dioder (LED), fotodetektorer, røntgendetektorer, og lasing enheder. Især er den certificerede effektkonverteringseffektivitet (PCE) af perovskit PV-enheder blevet forbedret siden Miyasaka et al. første gang anvendte tredimensionel (3D) MAPbI₃ i solceller (PVs) i 2009 fra 3,8 % til 25,2 % i dag. Dette skyldes hovedsagelig deres fordelagtige fysiske egenskaber, såsom høj lysabsorptionskoefficient, langsom rekombinationshastighed for ladebærer og høj bærer mobilitet. Imidlertid er 3D MHPs meget følsomme over for fugt og temperatur, m.m., hvilket har hindret deres kommercialisering. Derfor har flere og flere forskere flyttet deres fokus til mere stabile lav-dimensionelle MHPs, såsom 2D lagdelte, 1D lineære, og 0D punktuerede MHPs.

Denne afhandling er fokuseret på design, syntese og strukturraffinering af nye 3D, 2D og 0D MHP krystaller. Ydermere er de detaljerede struktur-relaterede fotofysiske egenskaber, herunder elektroniske båndstrukturer, dynamik af fotoinducerede anslåede tilstande, dannelse af frie excitoner og selvfangede excitoner (STEs), ladebærer indfangning og rekombination osv., blevet undersøgt ved hjælp af en række spektroskopiske metoder. Resultaterne af disse undersøgelser kan være en vigtig reference for fremtidige materialeudvikling og anvendelse.

I kapitel 3 (**Artikel I**) viser vi den spontane vækst i MAPbBr₃/N-rGO-hybridstrukturer ved hjælp af en let væskebaseret metode og deres anvendelse i fotodetektorer. I MAPbBr₃/N-rGO hybridstrukturen blev 3D MHP homogent pakket ind af N-rGO-lag gennem stærke hydrogenbindinger, hvilket øger ladebærertransporten henover perovskitkrystallerne. Den fremstillede enhed udviser fremragende optoelektronisk ydeevne: responsiviteten (R) på $3,6 \times 10^4$ A/W, ekstern kvanteeffektivitet (EQE) på over 105 % og detektivitet op til 10^{12} Jones. I kapitel 4 (**Artikel II**) demonstrerede vi syntesen af de to 2D MHP'er enkeltkrystaller (n-BA)₂(MA)₂Pb₃I₁₀ og (n-BA)₂(EA)₂Pb₃I₁₀. En detaljeret strukturel analyse viser, at de større gitterfordrejninger på (n-BA)₂(EA)₂Pb₃I₁₀, især stigningen i Pb-I-bindingslængden, udvider båndgapet ved hovedsagelig at sænke valensbåndets position (VBM) sammenlignet med (n-BA)₂(MA)₂Pb₃I₁₀. Derudover observerede vi ladebærerindfangst og bærerfældeudfyldning i begge krystaller. Baseret

på dynamik modellering af bærerindfangst, bekræftede vi en ultra-lang levetid af fældetilstande i begge forbindelser med fældetætheder på hhv. $\sim 2,18 \times 10^{16} \text{ cm}^{-3}$ og $\sim 3,76 \times 10^{16} \text{ cm}^{-3}$. I kapitel 5 (**Artikel III**) afslørede vi STE-formationens tætte afhængighed og deres rekombinationsdynamik i 2D MHPs på de lokale strukturer ved at studere PL-emissionsdynamik ved forskellige overfladekrystalfacetter af $(\text{iso-BA})_2(\text{MA})\text{Pb}_2\text{Br}_7$, $(\text{n-BA})_2(\text{MA})\text{Pb}_2\text{Br}_7$ og $(\text{n-PA})_2(\text{MA})\text{Pb}_2\text{Br}_7$ enkelte krystaller. På facetten parallel med de 2D-uorganiske lag (IF) er der mindre sandsynlighed for, at STEs kan dannes, mens frie excitoner (FES) dominerer på grund af den svage elektron-phonon kobling i et mere symmetrisk gitter. På kantfacetten vinkelret på de 2D uorganiske lag (PF) er der stor forvrængning af blyhalid oktaedrene på grund af af ophobning af forstrækning langs 2D lagene forbedre elektron-phonon koblingen og derfor letter dannelsen af STEs. Dette fører også til forskellige intensitetsafhængige PL-dynamikker ved de to krystalfacetter. Til sidst introduceres i kapitel 6 (**Artikel IV**) en ny struktur af 0D MHP, Cs_3BiBr_6 . En fotodetektoren baseret på dens mikrokrytaller udviser god responsivitet ($\sim 25 \text{ mA W}^{-1}$ ved en lystæthed på 4 mW cm^{-2}) og detektivitet ($0,8 \times 10^9 \text{ Jones}$), som understreger dens potentiale for anvendelse i optoelektroniske apparater.

Acknowledgements

I would like to give my sincerest thanks to all the people who have helped me during my Ph.D. career, and the completion of this thesis cannot be separated from their supports.

First and foremost, I would like to thank my main-supervisor Assoc. Prof. Kaibo Zheng, for giving me the most professional guidance to help me successfully complete my Ph.D. thesis. In my mind, you are also one of my best friends. You are very kind, patient, and optimistic, which makes my Ph.D. journey relaxed and happy. We (you, me and other group members) experienced many interesting things together, such as participating in 'beam times' in Germany, Sweden etc., hiking, team BBQ, and so on. I really enjoy these experiences, and they will become valuable assets in my life.

I would also like to thank my co-supervisors, Assoc. Prof. Qijin Chi and Prof. Jens Øllgaard Duus. As the main-supervisor in the first year of my Ph.D. career, Qijin not only give me the opportunity to pursue a Ph. D. degree at DTU Chemistry, but also guided me to complete my study plan. To Jens, you are so friendly, and helped me to integrate into the big family of DTU Chemistry faster and helped me a lot in daily life.

Prof. Sophie E. Canton and Tönu Pullerits, you helped me a lot in my Ph.D project. In particular, you gave me a lot of valuable comments when I was writing academic papers. Thank you very much for your professional knowledge, which makes my work more perfect and meaningful. Prof. Ivano E. Castelli, you and your student, Zhenyun Lan, have helped me a lot in theoretical calculations for my papers. Thank you very much for your efforts.

I am grateful to the whole our group members, both in Denmark and Sweden. Dr. Yingying Tang, you taught me a lot of experimental skills. We have done a lot of excellent work together. Weihua Lin, you helped me measure a lot of photophysical properties, many thanks for your contributions. Jie Meng, thank you for helping me measure TEM. It also includes Qinying Pan, Sol Laura Gutierrez Alvarez, Qian Zhao, Mohamed Abdellah, Yang Liu and Meng Dan. I really enjoy the group meetings, discussions, team activities with all of you.

Besides, thanks to many friends, Qi Shi, Xianshao Zou, Huili Cao, Christian Engelbrekt, Xiaomei Yan, Jun Li, Wei Huang, Jing Tang, Fei Shen, Fangyuan Diao, Zhiyong Zheng,

Xinxin Xiao. Thank you very much for your support in my work and daily life, which have brought me a colourful and interesting three-year Ph.D. career.

I would also like to thank many people at DTU Chemistry, Kenny Ståhl, David Frej Nielsen, Johanne Marie Nielsen, Marie Koefoed, Mette Hansen, and Jette Berg Nestén for their great help to me during these three years.

Last but not least, thanks to my parents, girlfriend and sister. My love Sasa Wang, you not only gave me a lot of help in my work, but also comforted me in my soul. The support and understanding from them allow me to focus more on my work and study.

December 2020, Kgs. Lyngby

Mingli Liang

List of publications

This thesis is based on the following papers, which are referred to in the text by Roman numerals.

I. Photodetector Based on Spontaneously Grown Strongly Coupled MAPbBr₃/N-rGO Hybrids Showing Enhanced Performance

Yingying Tang*, Mingli Liang*, MinWei Zhang, Alireza Honarfar, Xianshao Zou, Mohamed Abdellah, Tönu Pullerits, Kaibo Zheng, and Qijin Chi

ACS Appl. Mater. Interfaces 2020, 12, 858–867. (Co-first author)

II. Electronic Structure and Trap-States of Two-Dimensional Ruddlesden-Popper Perovskites with Relaxed Goldschmidt Tolerance Factor

Mingli Liang, Weihua Lin, Zhenyun Lan, Jie Meng, Qian Zhao, Xianshao Zou, Ivano E. Castelli, Tönu Pullerits, Sophie E. Canton, and Kaibo Zheng

ACS Appl. Electron. Mater. 2020, 2, 1402–1412.

III. Free excitons versus self-trapped excitons at different facets of Ruddlesden Poppers two-dimensional lead halide perovskite single crystals

Mingli Liang, Weihua Lin, Xianshao Zou, Qian Zhao, Zhenyun Lan, Tönu Pullerits, Sophie E. Canton, and Kaibo Zheng

Manuscript

IV. Lead-free double halide perovskite Cs₃BiBr₆ with well-defined crystal structure and high thermal stability for optoelectronics

Yingying Tang, Mingli Liang, Bingdong Chang, Hongyu Sun, Kaibo Zheng, Tönu Pullerits and Qijin Chi

J. Mater. Chem. C 2019, 7, 3369–3374.

My contribution to the papers

I. I designed the study and conducted the experiments together with Yingying, did the analysis related to PXRD, XPS and NMR parts, and wrote these parts of the manuscript.

II. I designed the experiments, synthesized the samples, and performed the spectroscopy experiments together with Weihua. Then, I analyzed the data and wrote the manuscript with help from Kaibo and Sophie.

III. I designed the experiments, synthesized the samples, and performed the spectroscopy experiments with Weihua and Xianshao. Then, I analyzed the data and wrote the manuscript with help from Kaibo.

IV. I assisted Yingying in the PXRD and electrochemical measurements, prepared the corresponding figures, and helped finalize the manuscript.

Other publications not included in the thesis.

I contributed to these papers, which are outside the scope of this thesis.

V. Modulating Charge-Carrier Dynamics in Mn-Doped All-Inorganic Halide Perovskite Quantum Dots through the Doping-Induced Deep Trap States

Jie Meng, Zhenyun Lan, Mohamed Abdellah, Bin Yang, Susanne Mossin, **Mingli Liang**, Maria Naumova, Qi Shi, Sol Laura Gutierrez Alvarez, Yang Liu, Weihua Lin, Ivano E. Castelli, Sophie E. Canton, Tõnu Pullerits, and Kaibo Zheng

J. Phys. Chem. Lett. 2020, 11, 9, 3705–3711.

VI. Photostability and Photodegradation Processes in Colloidal CsPbI₃ Perovskite Quantum Dots

Rui An, Fengying Zhang, Xianshao Zou, Yingying Tang, **Mingli Liang**, Ihor Oshchapovskyy, Yuchen Liu, Alireza Honarfar, Yunqian Zhong, Chuanshuai Li, Huifang Geng, Junsheng Chen, Sophie E. Canton, Tõnu Pullerits, and Kaibo Zheng

ACS Appl. Mater. Interfaces 2018, 10, 45, 39222–39227.

Abbreviations

MHP: Metal halide perovskite

HOIP: Hybrid organic-inorganic perovskite

PV: Photovoltaic

LED: Light-emitting diode

PCE: Power conversion efficiency

EQE: External quantum efficiency

PLQY: High photoluminescence quantum yield

LDR: Linear dynamic range

STE: Self-trapped Excitons

MA: Methylammonium

FA: Formamidinium

EA: Ethylammonium

iso-BA: iso-butylamine

n-BA (or BA): n-butylamine

n-PA: n-pentylamine

N-rGO: Nitrogen-doped reduced graphene oxide

PL: Photoluminescence

TRPL: Time-resolved photoluminescence

TRIR: Time-Resolved Infrared Spectroscopy

TCSPC: Time correlated single photon counting

FWHM: Full width at half maximums

XRD: X-ray diffraction

SCXRD: Single-crystal X-ray diffraction

SC: Single crystal

VBM: Valence Band Maximum

CBM: Conduction band minimum

LES: Low energy edge state

XPS: X-ray photoelectron spectroscopy

SEM: Scanning electron microscopy

AFM: Atomic force microscopy

Contents

Abstract	III
Abstract – Danish.....	V
Acknowledgements.....	VII
List of publications.....	IX
My contribution to the papers	X
Abbreviations.....	XI
Chapter 1 Introduction	14
1.1 The history of perovskite materials.....	14
1.2 The structure of metal halide perovskites	15
1.2.1 The structure of 3D MHPs.....	16
1.2.2 The structure of 2D layered MHPs.....	18
1.2.3 The structure of 1D and 0D MHPs.....	19
1.3 Typical Photophysics in MHPs	21
1.3.1 Charge carrier Dynamics in MHPs.....	21
1.3.2 Excitons and Self-trapped Excitons in MHPs.....	22
1.3.3 Electron-phonon coupling strength calculation	26
1.3.4 Trapping and trap filling dynamics.....	28
Chapter 2 Methodology.....	31
2.1 Synthesis of MHP crystals.....	31
2.1.1 Synthesis of Organic Amine Halides.....	31
2.1.2 Growth of large single crystals	32
2.1.3 Synthesis of pure MAPbBr ₃ (microcrystals) and hybrid MAPbBr ₃ /N-rGO composite microcrystals	33
2.2 Structural Characterization	34
2.2.1 Single crystal crystallography	34
2.2.2 Spectroscopic techniques.....	36
2.2.3 Microscopic techniques.....	39
Chapter 3 Spontaneously Grown Strongly Coupled 3D MAPbBr ₃ /N-rGO Hybrids and their Photodetector application	42
3.1 Morphological and structural characterization of MAPbBr ₃ /N-rGO Hybrids	42
3.2 The performance of photodetector device based on MAPbBr ₃ /N-rGO hybrids.....	44

3.3 Interfacial Structure and Photophysics in MAPbBr ₃ /N-rGO hybrids.	45
Chapter 4 Electronic Structure and Trap States of 2D RP Perovskites.....	48
4.1 Relaxed Tolerance Factor and Intraoctahedral Distortions in the 2D RPPs	48
4.2 Impact of the Intraoctahedral Distortions on the Electronic Structures	50
4.3 Impact of the Intraoctahedral Distortions on the Trap-Mediated Charge Recombination.....	51
Chapter 5 Free excitons versus self-trapped excitons at different facets of 2D RP Perovskite single crystals	53
5.1 Structural difference between the in-plane facet and prearticular facet in 2D perovskite single crystals.....	53
5.2 Formation of the STE vs. FE (free excitons) in three SCs at different facets	54
5.3 Emission Dynamics of STE vs. FE in three SCs at different facets	56
Chapter 6 Lead-free 0D halide perovskite Cs ₃ BiBr ₆ with high thermal stability for optoelectronics.....	59
6.1 The structure of the newly developed lead-free perovskite, Cs ₃ BiBr ₆	59
6.2 The photodetector application of Cs ₃ BiBr ₆	60
Conclusions.....	62
References	64
Publications.....	73

Chapter 1

Introduction

In this chapter, we provide a brief introduction to the development of perovskite materials. Then, the structures of metal halide perovskites (MHPs) are classified into three categories (3D, 2D, 0D) for description. In the last part, we introduced some typical photophysics that dominates the device application of those materials involved in this thesis, including emissive state dynamics, exciton and self-trap exciton formation, electron-phonon coupling, and trap filling/accumulation, *etc.*

1.1 The history of perovskite materials

Calcium titanate (CaTiO_3) was the first discovered perovskite material in a piece of chloride-rich skarn at Ural Mount of Russia by Gustav Rose in 1839.¹ Afterward, it was named after Russian mineralogist L. A. Perovski (1792-1856) as Perovskite.¹ However, it was not until 1902 that the detailed structural analysis of perovskites was implemented.² Early investigations on perovskites mostly focused on titanate-based oxide compounds (BaTiO_3) encompassing their optical and ferroelectrical properties, which paves the way for new technologies in high-response piezoelectrics, memory storage devices, and colossal magneto resistors.³ The initial study of metal halide perovskites (MHPs) originated from 1893, where inorganic CsPbX_3 ($X = \text{Cl}, \text{Br}, \text{I}$) were firstly synthesized by a solution-processed method. The structures of state-of-the-art hybrid organic-inorganic perovskites (HOIPs), MAPbX_3 and FAPbX_3 , however, were first reported in 1978.^{4, 5}

Although the MHPs have already been widely studied for the applications in transistors and light-emitting diodes (LEDs) in 1990s, they were considered to be at the forefront of materials science since 2009.⁶⁻⁹ MAPbI_3 was first applied to photovoltaics (PVs), where it was used as a light absorption layer in a liquid dye-sensitized solar cells.⁹ Over the past decade, MHPs have been extensively developed in many fields such as

optoelectronics, LEDs, lasers, and photodetectors. The certified power conversion efficiencies (PCEs) of the perovskite-based PV devices have been improved from 3.8% in 2009 to 25.2% at the moment (Fig. 1.1).¹⁰⁻¹³

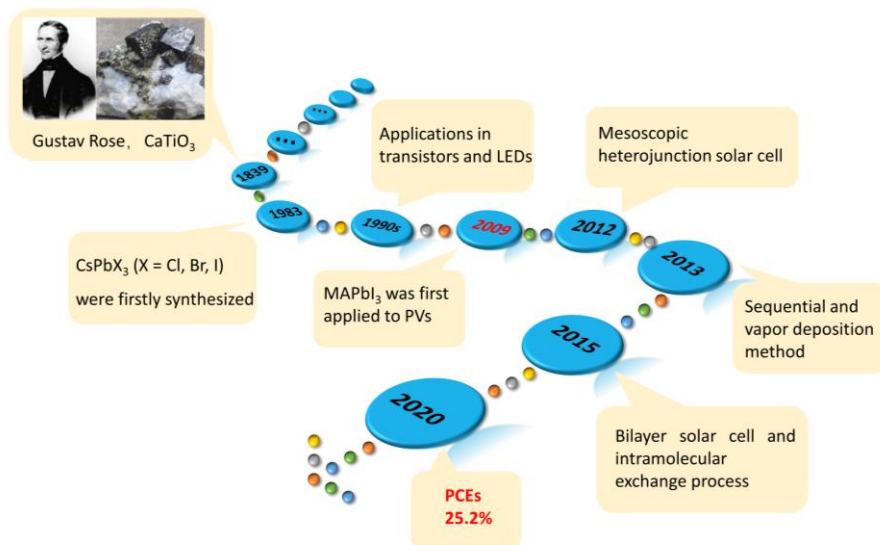


Fig. 1.1. Milestones in the development of perovskite materials.

1.2 The structure of metal halide perovskites

The term perovskite is usually referred to as any compound with a crystal structure similar to the CaTiO_3 , with a chemical formula ABX_3 (where A and B are two cations, X is an anion).^{14,15} The idealized cubic phase ($Pm\bar{3}m$) of it is rarely observed as its structural lattice is usually distorted into a lower symmetric space group. Therefore, orthorhombic ($Amm2$) and tetragonal ($P4mm$) non-cubic structures are the most common phases.¹⁶⁻¹⁸

Generally speaking, the perovskite structure of MHPs refers to a 3D structure. In their typical chemical formula ABX_3 , A is a monovalent cation like MA^+ , FA^+ , Cs^+ ; B is a divalent metal cation like Pb^{2+} or Sn^{2+} ; and X refers to a halide ion like Cl⁻, Br⁻, I⁻.^{19, 20} For instance, Fig. 1.2a shows the structure of a benchmark 3D MHP CsPbBr_3 , where numerous PbBr_6 octahedra connected to form a lattice by corner-shared links. Besides conventional 3D structures, many low-dimensional metal halide compounds are also classified as MHPs, in which the metal halide octahedra form layers (2D) (Fig. 1.2b),

chains (1D) (Fig. 1.2c), or isolated dots (0D) (Fig. 1.2d).²¹⁻²⁵ In the following part, we will introduce their fine structure based on some representative examples.

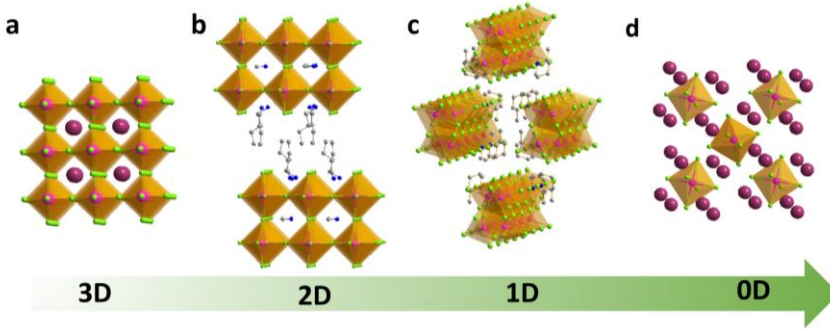


Fig. 1.2. Scheme of the crystal structures of some typical perovskites in different dimensionalities: 3D CsPbBr₃ (a), 2D (n-BA)₂(MA)Pb₂Br₇ (n-BA = n-butylamine) (b), 1D (2-MP)PbI₃ (2-MP = 2-methylpiperidine) (c), and 0D Cs₄PbBr₆ (d).

1.2.1 The structure of 3D MHPs

In the case of 3D MHPs (ABX₃), the size of A-cation is crucial in determining whether a close-packed perovskite structure can be formed, where it must fit the void space formed by four adjacent corner-sharing BX₆ octahedra. People usually use the Goldschmidt tolerance factor (τ) to estimate the stability of 3D MHPs and guide the selection of the appropriate-sized cations.^{14-15,20, 26, 27} τ is a geometrical parameter related to the ionic radii of the elemental constituents, defined as follows:

$$\tau = \frac{r_A + r_X}{\sqrt{2}(r_B + r_X)} \quad (1.1)$$

where r_A , r_B , and r_X are the effective radii of the A-cations, B-cations and the halogen ions, respectively. Here, B-cations stand for lead (Pb²⁺) or tin (Sn²⁺) cations. In principle, the stable 3D perovskite structure requires the τ ranges from 0.8 to 1.0 (Fig. 1.3).^{14-15,27} This is the reason why only a limited number of small A-cations, such as caesium (Cs⁺), rubidium (Rb⁺), methylammonium (MA⁺), or formamidinium (FA⁺) cations can be used to construct stable MHP lattice. For example, the τ -value of stable MAPbI₃ is 0.911 with the effective radius of MA⁺ to be 217 pm. In contrast, the effective radius of ethylammonium (EA⁺) (274 pm) is too large to form a stable 3D perovskite phase.²⁸ Therefore, EAPbI₃ with

a τ -value of 1.031 are stabilized in an orthorhombic space group $Pna2_1$ with open 1D structure at RT.²⁹

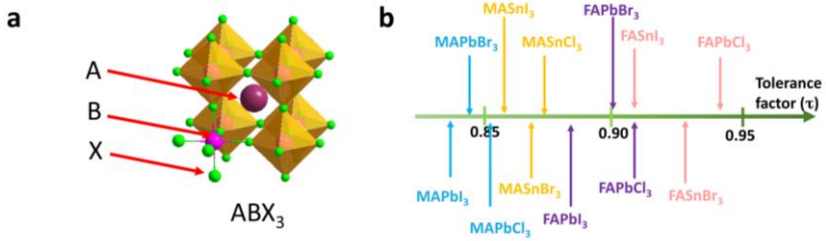


Fig. 1.3. The unit cell of ABX₃ with octahedral structure (a); the tolerance factor of different crystal structures (b).

In 3D MHPs, BX₆ octahedra are corner-shared among each other forming 3D lattices with the A-cations situated in the [BX₃]⁻ cages. Generally speaking, their 3D lattice will be distorted with changes in temperature or pressure. Moreover, when the distortions are significant, they will experience a phase transition. For example, MAPbI₃ exhibits two major phase transition processes with the temperature changes: the cubic phase ($Pm-3m$) transits into the tetragonal phase ($I4/mcm$) at around 330 K, and further changes into the orthorhombic phase ($Pnma$) at around 160 K (Fig. 1.4).³⁰ Meanwhile, such phase transition processes can also be triggered by external pressure. According to the previous reports, MAPbI₃ is stable in the tetragonal phase ($I4/mcm$) in the pressure ranging from 0 to 0.35 GPa, and possesses a cubic phase ($Im-3$) in the pressure range 0.35 to 2.5 GPa. When the pressure is higher than 2.5 Ga, the Pb-I bond length, Pb-I-Pb angles will undergo a substantial change despite the same cubic phase ($Im-3$).^{31, 32} Such phase transition processes in 3D MHPs are expected to affect their optical and electrical properties drastically.

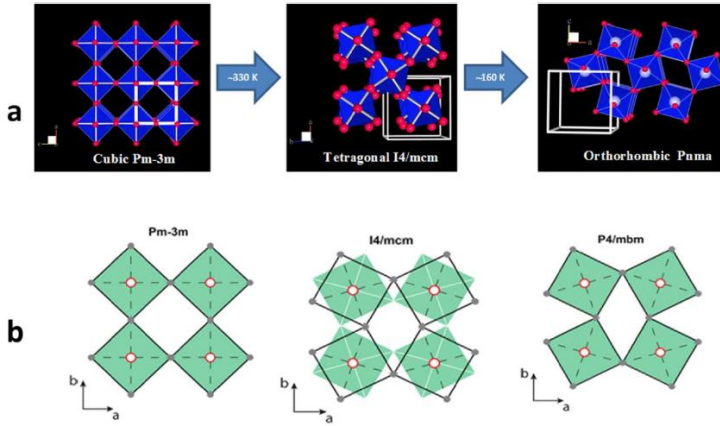


Fig. 1.4. Crystal structures of MAPbI₃ at different temperatures (a); the relative rotations of neighboring layers of PbI₆ octahedral along the *c*-axis (b); Figures were taken from Reference [30] with permission.

1.2.2 The structure of 2D layered MHPs

Unlike 3D MHPs, 2D layered MHPs are exempted from the restriction of τ with a more flexible structure.²⁰ Therefore, 2D MHPs exhibit a large diversity. According to the crystallographic layer slicing direction cutting along a specific (*hkl*) plane of the parent 3D structure, they can be classified into three categories: the (100) oriented, the (110) oriented, and the (111) oriented structures.³³ 2D MHPs in the first two cases have a chemical formula of A'₂A_{*n*-1}B_{*n*}X_{3*n*+1} or A'A_{*n*-1}B_{*n*}X_{3*n*+1} (A' is a monovalent or divalent long-chain amine action, A is a monovalent cation, B is a divalent metal cation, and X is a halide ion).^{22,33-35} These involve (BA)₂(MA)_{*n*-1}Pb_{*n*}I_{3*n*+1} (*n* = 1, 2, 3, 4; BA = butylammonium)³⁶, (PEA)₂(MA)_{*n*-1}Pb_{*n*}I_{3*n*+1} (*n* = 1, 2, 3, 4; PEA = phenylthylammonium)³⁷, and (3AMP)(MA)_{*n*-1}Pb_{*n*}I_{3*n*+1} (*n* = 1, 2, 3, 4; 3AMP = 3-(aminomethyl)piperidinium)²² *etc.* The chemical formula of (111) oriented 2D MHPs is A'_{*n*+1}B_{*n*}X_{3*n*+3}, where B-cation's valence is trivalent or mixed-valence averaging trivalent.³³ Typical example of that includes MA₃Bi₂X₉ (X = Cl, Br, I).³⁸ Among these three types of 2D MHPs, (100) oriented 2D MHPs are the most common and well-reported with a wide variety of spacing cations.

Those (100) oriented 2D MHPs can be further divided into two types depending on the species of the organic spacer layers: Ruddlesden-Popper (RP) phases and Dion-Jacobson (DJ) phases.²² RP perovskites consist of two interdigitated monovalent spacing cations per unit cell. In contrast, DJ perovskites are composed of only one divalent interlayer spacing cation layer per formula unit (Fig. 1.5). The BX_6 octahedra in both RP and DJ MHPs are all linked by a corner-shared pattern where semiconductor quantum wells (QWs) and spacing cations alternately appear stacked into their structure. The electronic structures of 2D MHPs can be customized by precisely controlling the number of octahedra layers in the QWs (i.e., layer thickness n) using facile synthetic methods.

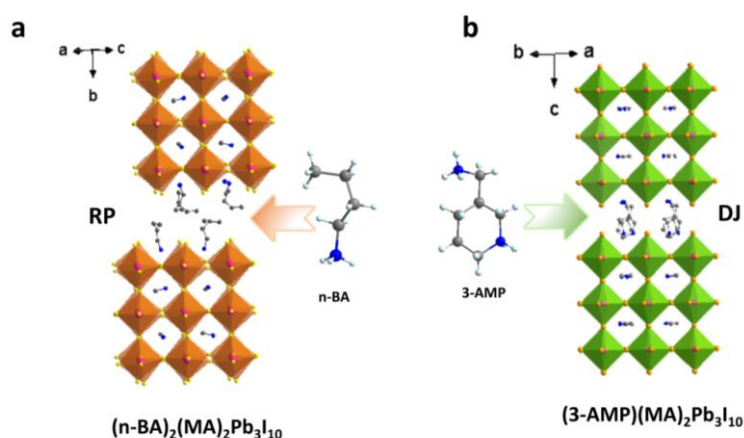


Fig. 1.5. Structural comparison between the crystal structures of RP phases, DJ phase perovskites with $n = 3$: $(n\text{-BA})_2(\text{MA})_2\text{Pb}_3\text{I}_{10}$ (a); $(3\text{-AMP})(\text{MA})_2\text{Pb}_3\text{I}_{10}$ [(3-AMP= 3-(aminomethyl)piperidinium)] (b).

1.2.3 The structure of 1D and 0D MHPs

In low-dimensional 1D MHPs, their chemical formulas vary with the connection configurations and the organic cations utilized. The metal halide octahedra (MX_6) in 1D MHPs can be connected to form a linear or zigzag chain by the following three configurations: corner-sharing, edge-sharing, or face-sharing.²⁵ The other extra inorganic or organic cations would occupy the void space, which can also be considered to surround

the MX_6 chains. However, in the 0D MHPs individual MX_6 octahedra are entirely isolated by the cations. They are like seeds, distributed in watermelon, and the whole watermelon can be considered the bulk crystals. When these seeds exist alone, 0D MHPs have a chemical formula of A_4MX_6 , where A is a monovalent organic cation, and M is a divalent metal cation, like the typical compound Cs_4PbBr_6 .³⁹ However, this formula does not apply when the seeds are clusters, like $\text{Cs}_3\text{Bi}_2\text{I}_9$.⁴⁰ Unlike 3D and 2D MHPs that have been extensively investigated, 1D and 0D MHPs are still mostly underexplored until recent years. In the following, we will introduce the structure of some emerging examples.

$(\text{EA})_2\text{PbBr}_4$ (EA = ethylammonium) is structured in *Imma* space group and features a 1D linear chain structure.⁴¹⁻⁴³ PbBr_6 octahedra are linked together by corner-sharing of one Br atom to form a chain, and EA cations are arranged among 1D chains as the blocks (Fig. 1.6a). $(\text{EA})_2\text{BiBr}_5$ (EA = ethylamine) can also crystallize in *Pna21* space group but with a 1D alone zigzag chain structure.^{42, 44} In $(\text{EA})_2\text{BiBr}_5$, BiBr_6 octahedra are connected by corner-sharing mode along the c-direction, forming a zigzag chain separated by EA cations (Fig. 1.6b).

Cs_4PbX_6 are perhaps the most well-known 0D MHPs. In Cs_4PbX_6 , PbX_6 octahedra are isolated in Cs_4PbBr_6 (*R-3c*), while Cs^+ ions are filled between them (Fig. 1.6c).³⁹ However, in the structure of $\text{Cs}_3\text{Bi}_2\text{I}_9$ ⁴⁵ and $\text{MA}_3\text{Bi}_2\text{I}_9$ ⁴⁶ 0D MHPs, the isolated units are indeed in the form of dimers. Fig. 1.6d shows the 0D structure of $\text{Cs}_3\text{Bi}_2\text{I}_9$ (*P63/mmc*), where the BiI_6 octahedra formed an isolated $\text{Bi}_2\text{I}_9^{3-}$ dimer.

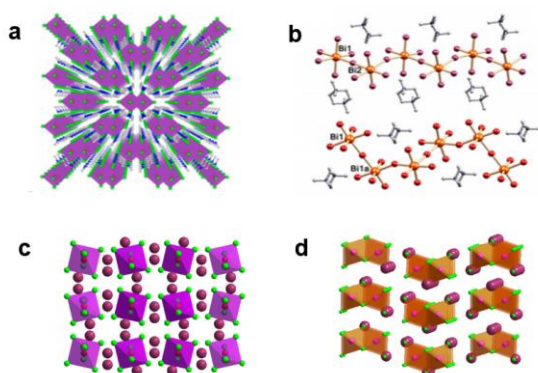


Fig. 1.6. Structure of 1D perovskites $(EA)_2PbBr_4$ (a) and $(EA)_2BiBr_5$ (b) (these two figures were taken from Reference [43] and [44] with permission); and the structure of 0D perovskites Cs_4PbBr_6 (c) and $Cs_3Bi_2I_9$ (d).

1.3 Typical Photophysics in MHPs

1.3.1 Charge carrier Dynamics in MHPs.

MHPs as the prime candidates for commercialization, their equipment-centric development has improved rapidly over the past ten years. The corresponding fundamental studies using optical spectroscopy techniques have been pivotal in uncovering crucial insights into their light-harvesting, charge generation, recombination, and transport mechanisms.⁴⁷ These techniques include femtosecond transient absorption spectroscopy (fs-TAS), time-resolved photoluminescence spectroscopy (TRPL), transient terahertz absorption spectroscopy (TRTS) *etc.* In the following, we take MAPbI₃ as an example to briefly introduce the photophysical processes that may occur inside the MHP materials.

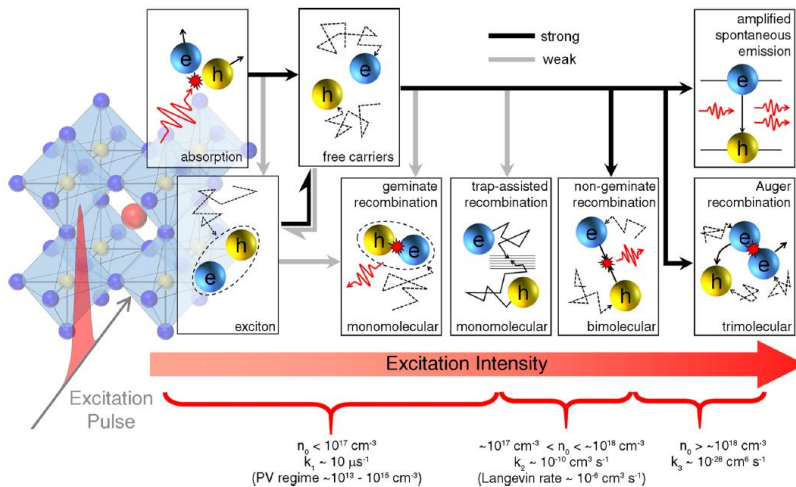


Fig. 1.7. Various photophysical processes and recombination rates in MAPbI₃ over a range of photoexcited carrier densities n_0 ; the figure was taken from Reference [47] with permission

As shown in Fig. 1.7, under photoexcitation, the excitons in MAPbI₃ will be spontaneously dissociated into free charges due to its extremely low exciton binding energy.⁴⁸ When the excited carrier density is low ($n_0 < 10^{17} \text{ cm}^{-3}$), monomolecular processes dominate, such as the geminate recombination of minor undissociated excitons and trap-assisted recombination of free carriers. Their first order recombination coefficients k_1 are about $10 \mu\text{s}^{-1}$.⁴⁹ At higher photoexcited carrier densities ($n_0 > 10^{17} \text{ cm}^{-3}$), multiparticle processes like nongeminate recombination (bimolecular) and Auger processes (trimolecular) become more probable. Among them, when $n \approx 10^{17}\text{-}10^{18} \text{ cm}^{-3}$, non-geminate recombination processes dominate.⁵⁰ On the other hand, the bimolecular recombination constants ($10^{-10} \text{ cm}^3 \text{ s}^{-1}$) are almost four orders lower than the Langevin rates determined by assuming free electron-hole annihilation.^{49,51} However, Auger recombination mainly occurs when $n > 10^{18} \text{ cm}^{-3}$ with Auger rates $k_3 \approx 10^{-28} \text{ cm}^6 \text{ s}^{-1}$.^{49,52} Besides, some other photophysical processes may also influence the excited state dynamics of the MHPs, such as band-filling effects,^{53,54} bandgap renormalization,⁵⁵ hot phonon bottleneck effect⁵⁶ *etc.*

1.3.2 Excitons and Self-trapped Excitons in MHPs.

1.3.2.1-Excitons in MHPs

In a semiconductor, when the photon energy it absorbs is higher or equal to the bandgap energy (E_g), it will cause the formation of electrically neutral quasiparticles, which are called excitons.^{57,58} In principle, exciton related absorption or emission energy at a position below the E_g , due to the extra attractive Coulomb interaction within the electron-hole pair. Excitons have two types: Frenkel excitons and Wannier-Mott excitons.^{59,60} In the former case, the electrons and holes are bound tightly within a single unit cell. On the other hand, weaker Wannier-Mott excitons are free to move in a bulk crystal. The excitons

present in MHPs generally belong to Wannier-Mott excitons often described in the hydrogen model. The energy of the n th excitonic level can be given by:⁵⁹

$$E_n = E_g - \frac{E_b}{n^2} \quad (1.2)$$

where E_g is bandgap energy, E_b can be treated as an effective Rydberg for the excitons. On the other hand, E_b determines the thermal dissociation Wannier excitons into free charge carriers. The thermal dynamics equilibrium between the Wannier-Mott excitons and dissociated charge carriers in the bulk semiconductors can be modeled by the similar ion-electron balance in a hot plasma using a Saha-Langmuir expression:

$$\frac{x^2}{1-x} = \frac{1}{n} \left(\frac{2\pi m k_B T}{h^2} \right)^{1.5} e^{\frac{-E_b}{k_B T}} \quad (1.3)$$

where E_b is exciton binding energy, m is the exciton effective mass, T is the temperature and n is the excitation concentration.⁶¹ Due to the general low E_b in 3D MHPs, the above Saha-Langmuir model indicates only minimal parts of the photo-generated species are Wannier excitons while the majority is the spontaneously dissociated free carriers.

In order to determine the E_b of MHPs, many experiment methods have been carried out, including absorption method, temperature-depend PL method, ultrafast THz method etc.⁶²⁻⁶⁵ However, the results obtained according to different methods vary greatly. Among them, the absorption method is the most straightforward. Nevertheless, in this Ph.D. project, we used the temperature-depend PL method to determine the E_b of our MHP crystals. In the following, we will briefly introduce these two methods.

Absorption method. For a direct bandgap semiconductor, the absorption spectrum is described by the Eliot Equation:⁶²

$$\alpha = [A\Theta(\hbar\omega - E_g) \cdot D_{cv}(\hbar\omega)] \cdot \frac{\pi x \exp(\pi x)}{\sinh(\pi x)} + A \cdot E_b \sum_{n=1}^{\infty} \frac{4\pi}{n^3} \delta(\hbar\omega - E_g + \frac{E_b}{n^2}) \quad (1.4)$$

where A is a transition matrix element related constant, $\hbar\omega$ refers to the photon energy, δ represents a delta function, D_{cv} is the joint density of VB and CB states, Θ is the Heaviside (step) function, $x = \sqrt{E_b(\hbar\omega - E_g)}$. Ignoring the broadening of the transition, the eq. 1.2 can be represented, as shown in Fig. 1.8a. The E_b (it corresponding to R^*) can be determined by the energy separation between ground state (S1) and band edge absorption. Fig. 1.8b is an experiment absorption spectrum for MPbI₃ films at 30 K, we can see the exciton peak in this picture.⁶⁶ However, E_b obtains a large error bar in this method because the exciton peaks gradually widen as the temperature rises. For intense, the E_b

obtained by the MAPbI₃ is very dispersed: 5-29 meV at room temperature; 15-34 meV at low temperature.^{53,67-72} Therefore, this is not a perfect method for precise quantification of the E_b .

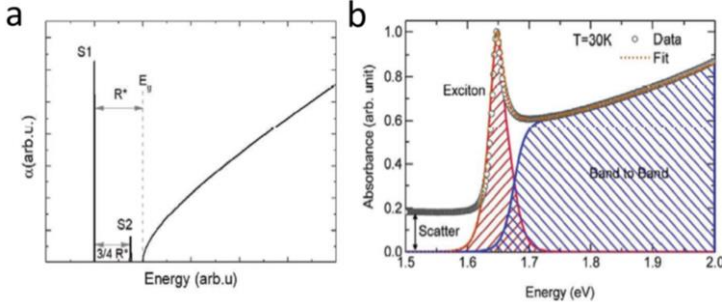


Fig.1.8. Idealized absorption spectra of semiconductors with excitonic effects according to Equation (3) (a). Example of the fitting of the absorption spectra of MAPbI₃ at 30 K using Elliott's formula with the excitonic and band-to-band contribution (b). The figure was taken from Reference [66] with permission

Temperature-depend PL method. This method is based on monitoring the quenching of the integrated PL intensity under various temperatures. The temperature-dependent PL intensity can be expressed using the following Arrhenius formula:^{63,64,73-75}

$$I(T) = \frac{I_0}{1 + A e^{(-E_b/k_B T)}} \quad (1.4)$$

where I_0 is the PL intensity at low temperature, and k_B is the Boltzmann constant. However, such a method has an essential premise: the rate of nonradiative recombination is related solely to the thermally activated exciton dissociation (in actual measurement, this assumption is an inaccurate simplification). Shuangyong *et al.* obtained the E_b of MAPbI₃ about 19 meV using this method (Fig. 1.9).⁶³ This means in conventional 3D MHPs, the major photogenerated species should be the free carrier dissociated from the excitons, where the charge carrier dynamics described in the last section dominate the excited state dynamics.

The E_b values in my works for low-dimensional MHPs also come from this method. In **Paper II**, the calculated E_b of (n-BA)₂(MA)₂Pb₃I₁₀ and (n-BA)₂(EA)₂Pb₃I₁₀ are ~65.8 and ~46.4 meV, respectively. In **paper III**, we studied the E_b at the bulk facet (IF) of our

large-sized 2D MHP crystals to be ~ 59.1 meV for $(\text{iso-BA})_2(\text{MA})\text{Pb}_2\text{Br}_7$; ~ 93.2 meV for $(\text{n-BA})_2(\text{MA})\text{Pb}_2\text{Br}_7$; and ~ 88.4 meV for $(\text{n-PA})_2(\text{MA})\text{Pb}_2\text{Br}_7$, respectively. It indicates the E_b in 2D MHPs is much larger than that in conventional 3D MHPs, which should increase the population of photogenerated excitons under equilibrium conditions.

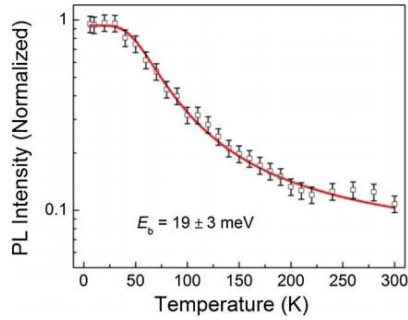


Fig. 1.9 Temperature-dependent integrated PL intensity of the MAPbI_3 film under excitation of a 532 nm continuous-wave laser beam. The solid line is the best fit based on the Arrhenius equation. The figure was taken from Reference [63] with permission.

2.3.2.2- Self-trapped Excitons (STEs) in MHPs

STEs widely exist in halide crystals, organic molecular crystals, and condensed rare gases, with their energy smaller than the free exciton energy (Fig. 1.10a).⁷⁶⁻⁷⁸ Under a strong electron-phonon interaction, the excited carriers will induce elastic deformation in the surrounding crystal lattice. To delay the lattice distortion, once electrons and holes are photogenerated, they will quickly self-trap from a mobile state to a more stable self-trapping state.^{79,80} And self-trapping energy (E_{st}) is defined as the energy loss of exciton in this process (Fig. 1.10b). In general, the structure of 2D MHPs is more flexible, allowing larger distortions, which favor the STEs formation. STE emissions usually correspond to broad Stokes/shifted (i.e., red-shifted) peaks with some peaks spanning the entire visible light region. Therefore, STEs in 2D MHPs have been extensively studied as potential properties to achieve white LEDs.⁸¹⁻⁸³

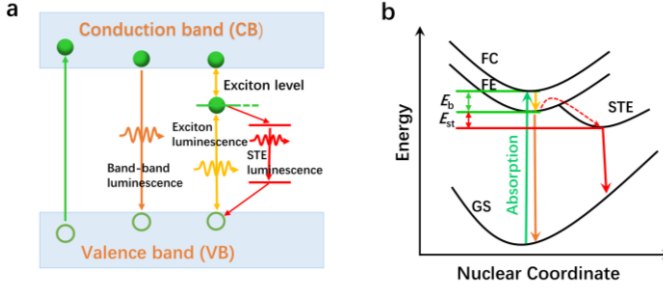


Fig.1.10. (a) Schematic of various intrinsic photoluminescence phenomena, including band-to-band luminescence, exciton luminescence, STE luminescence, and cross luminescence. (b) Schematic of the energy level structure of STE (GS, ground state; FE, free exciton state; FC, free carrier state; E_g , bandgap energy; E_{st} , self-trapping energy).

1.3.3 Electron-phonon coupling strength calculation

As the formation of STE is associated with the deformation of local lattice, it is largely determined by the electron-phonon coupling. In other words, the STE formation only occurs with a strongly electron-phonon coupling. In addition to that, the interaction of charge carriers with lattice vibrations (phonons) has been considered as a vital factor to rationalize the charge-carrier recombination mechanisms.^{84,85} The electron-phonon interactions determine the charge-carrier mobilities up-limit, excluding the extrinsic scattering of impurities or interfaces.⁸⁶ Furthermore, the hot carrier cooling process after excitation with high energy photons above the bandgap is also dominated by electron-phonon interaction. Moreover, the electron-phonon coupling also accounts for the homogeneous emission line broadening in hybrid lead iodide perovskite at RT.⁸⁷

Temperature-dependent PL emission broadening analysis is a frequently used method to study electron-phonon coupling mechanisms in semiconductors. The electron-phonon coupling strength can be extracted from FWHM analysis of temperature-dependent PL using the following model:⁸⁸⁻⁹⁰

$$\begin{aligned}\Gamma(T) &= \Gamma_0 + \Gamma_{ac} + \Gamma_{LO} + \Gamma_{imp} \\ &= \Gamma_0 + \gamma_{ac}T + \gamma_{LO}N_{LO}(T) + \gamma_{imp}e^{-E_b/k_B T}\end{aligned}\quad (1.6)$$

here, Γ_0 refers to temperature-independent inhomogeneous broadening contribution due to disorder and imperfections related scattering. Γ_{ac} and Γ_{LO} are homogeneous broadening

terms from acoustic and Fröhlich scattering, corresponding to the coupling strengths of γ_{ac} and γ_{LO} , respectively. $N_{LO}(T) = 1/(e^{E_{LO}/k_B T} - 1)$, where the E_{LO} is an energy representative of the frequency for the weakly dispersive LO phonon branch, and k_B is Boltzmann constant. Γ_{imp} is inhomogeneous broadening due to the ionized impurities. The temperature-dependent PL FWHMs of four typical hybrid lead halide perovskites fitted by eq. 1.6 are shown in Fig. 1.11a.⁸⁸ In addition, the modeling of each component of eq. 1.6 were given in the inset of Fig. 1.11a. When the temperature is higher than 100K, the FWHM evolutions share the same trend, where Γ_0 and Γ_{LO} provide the main contributions and Γ_{imp} can be neglected. Based on a recent analysis of the temperature dependence of charge-carrier mobility, Γ_{imp} can be regarded as approximately equal to 0 in perovskite materials.⁸⁹ Hence, we model the linewidth broadening of the compounds using equation (1.7) at high temperatures:

$$\Gamma(T) = \Gamma_0 + \gamma_{LO} N_{LO}(T) \quad (1.7)$$

At the lower temperatures ($T < 50$ K), the gradient of the FWHM versus temperature approaches zero for the FAPbI₃ and FAPbBr₃ (Fig. 1.11a and b), which suggests the acoustic phonon contribution is negligible ($\gamma_{ac} \approx 0$). However, in MAPbI₃ and MAPbBr₃, the acoustic phonon contribution is non-zero, leading to an additional broadening of the emission at the low-temperature phase. In this thesis, we studied the temperature-dependent PL of newly developed 2D MHP crystals. The PL FWHM evolution with the temperature of our samples is similar to those of FAPbI₃ and FAPbBr₃ (**Paper III**). Therefore we can use eq. 1.7 to analyze and calculate their electron-phonon coupling strength.

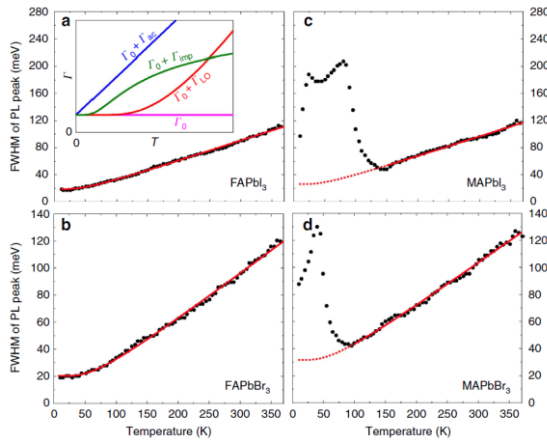


Fig. 1.11. Temperature dependence of PL spectra linewidth. FWHM of the steady-state PL spectra as a function of temperature for FAPbI₃ (a), FAPbBr₃ (b), MAPbI₃, (c), and MAPbBr₃ (d) thin films plotted as black dots. The solid red lines are fits of eq. 1.7. Figures were taken from Reference [88] with permission

1.3.4 Trapping and trap filling dynamics

1.3.4.1-*Trapping and Trap filling/accumulation of charge carriers*

In MHP materials, most of the intrinsic structural deficiencies such as vacancy and interstitials would only generate states within the band or shallow in the bandgap according to the theoretical calculation, which renders conventional 3D MHPs enhanced trap tolerance.⁸⁹ This is the reason for long diffusion length and low recombination rates in 3D MHPs materials. In addition to this, another important observation is the pronounced trapping filling or trap accumulation. Such a phenomenon was first discovered in the process of measuring the TRPL kinetics for bulk samples. With the increment of excitation fluences, the PL lifetimes gradually increase (Fig. 1.12a). This phenomenon is well-interpreted by trap filling or trap accumulation in most of the perovskite materials.⁹⁰⁻⁹² It occurs when the depopulation time of traps is longer than the time interval between the repetitive laser pulses so that part of the traps is still filled when the new excitation pulse comes. Fig. 1.12b shows a schematic describing the process of trap filling/accumulation.⁹³ If the sample is excited at low fluence, the density of photogenerated charges is much lower than the density of free holes due to the trapping of the electrons. The additional photogenerated charge does not noticeably change the concentration of holes, so the recombination of electrons and holes is almost monomolecular. However, at high fluences, when most of the traps become occupied due to sufficient photo-excited electrons, the recombination of additional photoexcited electrons and holes from the next pulse become bimolecular.⁹³

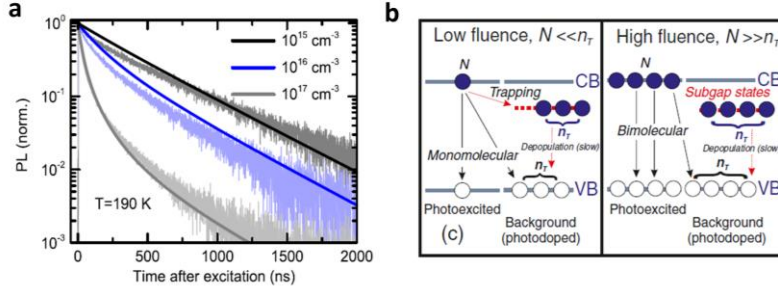


Fig. 1.12, PL decays detected at 780 nm from perovskite samples at 190 K (a), following pulsed excitation (510 nm, 300-kHz repetition rate). Solid lines fit the model; Schematic to illustrate recombination mechanisms for the low- and high-fluence regimes (b). Figures were taken from Reference [93] with permission.

1.3.4.2- Modelling the trapping and trap filling

The above-mentioned trap filling drastically influence the charge carrier dynamics after excitation. However, the consequent fluence dependent PL kinetics offers us an opportunity to calculate the trap densities by modeling trap filling/accumulation processes.⁹³⁻⁹⁵ When photodoping (i.e., accumulated trap filling) is present, the equilibrium between the trapping and trap filling can be generalized using the following equation expressing the concentrations of electrons (n_e), holes (n_h), and excitons (n_x) corresponding to the overall untrapped photo-generated species density N :

$$n_h = -\frac{(A \cdot n_T)}{2} + \frac{1}{2}\sqrt{(A+N_T)^2 + 4AN} \quad (1.8)$$

$$n_e = n_h \cdot n_T \quad (1.9)$$

where $A = v_x(v_h v_e) \exp[-E_b/(k_B T)]$ and $v_i = \lambda_i^{-3}$, λ_i is the thermal wavelength of the species i . n_T is concentration of filled traps and N_T is the concentration of total traps.

Here we assume that n_T varies little and is only dependent on the average concentration of electrons $\overline{n_e(t)} = \frac{1}{t_0} \int_0^{t_0} n_e(t) dt$ during the PL recording time t_0 among the repetition pulses.

Then we can get the following rate equations:

$$\frac{dn_T}{dt} = R_{pop}(N_T - n_T)\overline{n_e(t)} - R_{dep}(N_T^2 + n_T\overline{n_e(t)}) = 0 \quad (1.10)$$

where R_{pop} and R_{dep} are the recombination rates of trap population and depopulation, respectively. Taking equations (1.8) and (1.9) we can obtain the average concentration of electrons as:

$$\overline{n_e(t)} = \frac{1}{t_0} \int_0^{t_0} n_e(t) \approx K(A + n_T), K = \frac{1}{\gamma_0 t_0} \ln \left[1 + \frac{AN(0)}{N_T(A + N_T)} \right] \quad (1.11)$$

where $N(0)$ can be simplified as initial excitation density N_c . γ_0 is the total rate of electronic decay not involving traps. Substitution of equation (1.11) into (1.10) gives:

$$n_T = -\frac{1}{2}\alpha + \frac{1}{2}\sqrt{\alpha^2 + 4\beta N_T} \quad (1.12)$$

$$\alpha = \frac{[A + R(A - N_T)]}{\left(1 + \frac{1}{K} + R\right)} \quad (1.13)$$

$$\beta = \frac{RA}{\left(1 + \frac{1}{K} + R\right)} \quad (1.14)$$

$$K = \frac{1}{\gamma_0 t_0} \ln \left[1 + \frac{AN_c}{N_T(A + N_T)} \right], R = R_{pop}/R_{dep} \quad (1.15)$$

here R represents the ratio between the population and depopulation rates of the traps; γ_0 is the total electronic decay rate, excluding traps; t_0 is the time interval between the laser pulses. Combining the equation 1.12-1.15, the trap densities and R values in the samples can be globally fitted from a series PL kinetics at various excitation intensities.

Chapter 2

Methodology

This chapter is an overview of the experimental methods for this Ph.D. project, including the materials synthesis, characterization, and spectroscopic measurement. A detailed method of large-size single crystal growth of low-dimensional MHPs will be described in this chapter. Besides, the basic principles of some crucial structural characterization and spectroscopy techniques are introduced, such as single-crystal X-ray Diffraction (SCXRD), X-ray photoelectron spectroscopy (XPS), time-correlated single-photon counting (TCSPC), transient absorption spectroscopy (TA), etc.

2.1 Synthesis of MHP crystals

2.1.1 Synthesis of Organic Amine Halides

Preparation of organic Amine Halides is an indispensable preliminary step for the growth of MHP crystals. This thesis presents three short-chain organic amine halides (MABr, MAI, and EAI) and four long-chain organic amine halides (iso-BABr, n-BABr, n-PABr, and n-BAI) were synthesized.

2.1.1.1-Short-chain organic amine halides

The precursors of them were first synthesized by the reaction of concentrated hydro halogen acid (i.e., HI, 57 % in water; HBr, 47 % in water) with methylamine or ethylamine solution. The synthesis methods of MABr, MAI, and EAI are the same. Taking MABr as an example, first, HBr (25 ml, HBr, 47 % in water) was put into methylamine (20 mL, 33% in absolute ethanol). Absolute ethanol (50 mL) was then added to such mixture with stirring in an ice-water bath under N₂ atmosphere for 2 h. The solvent of the obtained solution was rotary evaporated at 40 °C. A white precipitate of MABr crystals was

obtained after washing the residuals with diethyl ether three times. It was dissolved again in ethanol and recrystallized from diethyl ether. In the end, such purified MABr crystals were vacuum dried at RT for two days. Commercial MABr, MAI has also been tested for crystal synthesis with the identical outcome to the synthesized precursors.

2.1.1.2-Long-chain organic amine halides

The long-chain amine halides were manufactured by adding an equal stoichiometric ratio iso-BA, n-BA, and n-PA to dilute aqueous HBr or HI (25% in mixed ethanol/water) under vigorous stirring in an ice-water bath. The white products of them were obtained by rotary evaporation at 60 °C. After that, a large number of white crystals of long-chain amine halides (iso-BABr, n-BABr, n-PABr, and n-BAI) were obtained by washing three times with ethanol and vacuum drying for 24h.

2.1.2 Growth of large single crystals

2.1.2.1-(n-BA)₂(MA)₂Pb₃I₁₀ and (n-BA)₂(EA)₂Pb₃I₁₀

We synthesized the above two single crystals by a well-known temperature gradient growth method using PbI₂, n-BAI, and MAI/EAI dissolved in 5 ml hydroiodic acid. This detailed ingredient is: 1.5 mmol PbI₂, 3.0 mmol EAI, and 2.0 mmol n-BAI for (n-BA)₂(EA)₂Pb₃I₁₀; 1.5 mmol PbI₂, 2.5 mmol MAI, and 2.0 mmol n-BAI for (n-BA)₂(MA)₂Pb₃I₁₀. The mixtures were added into glass vials (20 ml) with additional 0.25 ml hypophosphorous acid to avoid the oxidation of the hydroiodic acid. Then, the glass vials were sealed, and the solution was stirred to produce red precipitates. The obtained clear solutions after reaction for minutes at 80 °C is used as an initial precursor. Bulk single crystals were finally grown from it via gradient cooling with a typical cooling rate of 0.5 °C per day starting from 55 °C (Fig. 2.1).

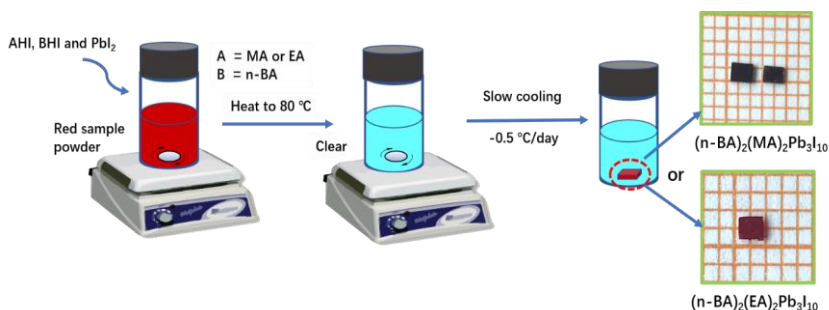


Fig. 2.1. A schematic diagram of the single crystal growth and the resulting two single 2D MHP crystals.

2.1.2.2-*(iso-BA)*₂(MA)Pb₂Br₇, *(n-BA)*₂(MA)Pb₂Br₇ and *(n-PA)*₂(MA)Pb₂Br₇

The synthetic methods of these three single crystals are the same as above. The ratio of raw materials is: PbBr₂ (2.5 mmol), MABr (1.5 mmol), *iso*-BABr/ *n*-BABr/ *n*-PABr (3.0 mmol), 5 ml HBr (47 % in water). Finally, the single crystals were grown from the precursor at a cooling rate of 0.5 °C per day starting from 50 °C.

2.1.3 Synthesis of pure MAPbBr₃ (microcrystals) and hybrid MAPbBr₃/N-rGO composite microcrystals

2.1.3.1- Synthesis of N-rGO

We first mixed 1:1 molar ratio of lysine and graphene oxide into an autoclave. 6h hydrothermal treatment was then conducted at 160 °C in an oven. After cooling to RT, the as-obtained products were washed by Milli-Q water three times. The resultant N-rGO was finally freeze-dried under a vacuum and ball-grounded.

2.1.3.2- Synthesis of MAPbBr₃ and MAPbBr₃/N-rGO hybrid

The synthesis protocol of hybrid MAPbBr₃/N-rGO materials is illustrated in Fig.2.2. MABr was initially mixed with 3 mg/mL N-rGO in 2 mL γ -butyrolactone followed five minute ultrasonication and five minute thermal treatment at 60 °C, sequentially. PbBr₂ was then injected to the above solution and react under stirring for another 10 minutes at 60 °C. Consequently, MAPbBr₃/N-rGO was obtained. To prepare the pure MAPbBr₃ microcrystals, the method is the same but not adding N-rGO.

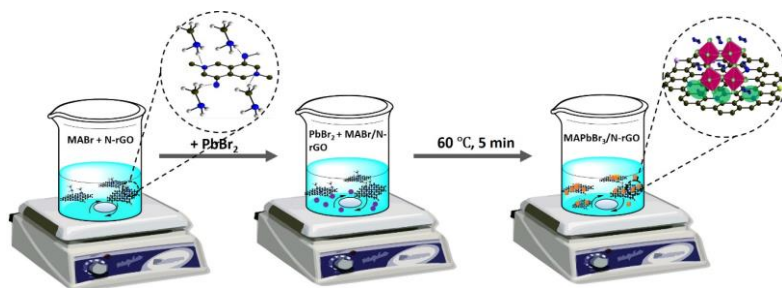


Fig. 2.2. Schematic illustration of the in-situ synthesis of MAPbBr₃/N-rGO.

2.2 Structural Characterization

2.2.1 Single crystal crystallography

2.2.1.1-Single-crystal X-ray Diffraction (SCXRD)

It is a non-destructive analytical technique, where an object crystal is bombarded with an X-ray beam from many different angles, and the resulting diffraction patterns are collected and analyzed. By aggregating the diffraction patterns and converting them via Fourier transform to an electron density map, we could obtain extensive crystallographic information, including unit cell dimensions, bond-lengths, bond-angles, and relative orientations of the materials. Finally, the fine structure of the crystal can be resolved by single-crystal refinement.⁹⁶⁻⁹⁹

SCXRD is based on constructive interference of monochromatic X-rays and a crystal. These X-rays beam must fall on the parallel planes of atoms in a crystal. When this satisfies Bragg's Law (eq. 2.1), the interaction of the incident X-rays with the crystal

produces constructive interference (Fig. 2.3).^{98,99} By changing the geometry of the incident beams, the orientation of the centered crystal, and the detector, a complete picture of the reciprocal lattice should be attained.

$$N\lambda = 2d \sin\theta \quad (2.1)$$

where n is an integer, λ is the wavelength of light, d is the distance between parallel planes in the crystal lattice, and θ is the angle of incidence between the X-ray beam and the diffracting planes.

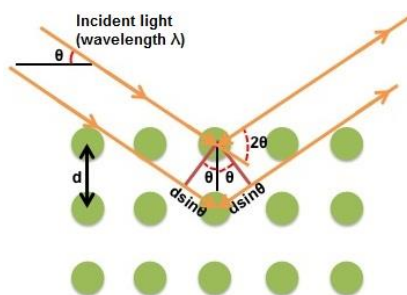


Fig. 2.3. Schematics of the requirements for Bragg's law. Modified from Wide Angle X-ray Diffraction Studies of Liquid Crystals.

In this thesis, the crystallographic data collections for all the crystals were performed using a SuperNova Dual Wavelength CCD diffractometer (Agilent Technologies) with a graphite-monochromatic Mo-K α radiation ($\lambda = 0.71073 \text{ \AA}$) at RT. Furthermore, the data sets were corrected for Lorentz and polarization factors as well as for absorption by the Multi-scan method.¹⁰⁰ We solved all the crystalline structures by direct methods and refined them by full-matrix least-squares fitting on F^2 using SHELX-97.¹⁰¹ All of the non-hydrogen atom positions were refined with anisotropic thermal parameters. These crystallographic data were also checked for possible missing symmetry with the program PLATON, to ensure that no higher symmetry was discovered.¹⁰² Fig. 2.4 is the picture of the single-crystal diffractometer we used together with an obtained diffraction pattern.

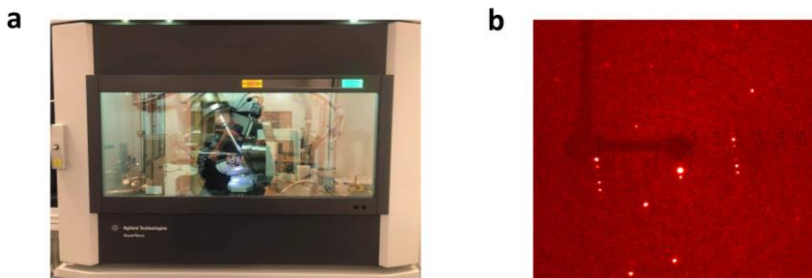


Fig. 2.4. The picture of SuperNova Dual Wavelength CCD diffractometer (a); and an X-ray diffraction from our sample.

2.2.2 Spectroscopic techniques

2.2.2.1-Ultraviolet-visible (UV-vis) absorption spectroscopy

It is one of the most fundamental steady-state optical measurements, where light absorption by solution, solids, and gaseous samples are recorded from the ultraviolet to the full visible spectral regions. UV-vis absorption spectroscopy mainly monitors the relationship of light intensity I with a given photon frequency ν before and after passing through the sample, when the light beam passes through the sample, which conforms to the Beer-Lambert law:¹⁰³

$$A(\nu) = -\log\left(\frac{I}{I_0}\right) = \varepsilon(\nu)lc \quad (2.2)$$

where A refers to the absorbance, I_0 is the intensity of the incident light at a given wavelength, I is the transmitted intensity, l is the path length through the sample, and c refers to the concentration of the targeting species. In my project, the obtained absorption spectra can be further converted into a $Tauc$ plot to determine the optical band edge. Since all our MHPs belong to the direct bandgap compounds, $Tauc$ plot is expressed as follows:¹⁰⁴

$$(ah\nu)^2 = C(h\nu - E_g) \quad (2.3)$$

where $h\nu$ is the energy of the light, E_g is bandgap, a is the absorption coefficient, C is proportionality constant. In this Ph.D. project, all UV-vis absorption spectra were

measured with a UV-Vis-NIR absorption spectrophotometer from PerkinElmer (Lambda 1050) at room temperature.

2.2.2.2-Steady-state photoluminescence spectroscopy (PL)

It is also a fundamental technique to characterize the emission of our MHP samples. PL is the emission of light by a matter after absorbing photons, as it decays from an excited state. The steady-state PL spectra in this thesis were acquired on a spectrometer (Avantes AvaSpec-2048) under a specific excitation wavelength.

2.2.2.3-Time-correlated single photon counting (TCSPC)

It is a method to measure the time-resolved photoluminescence dynamics with picosecond time-resolution and extremely high detectivity. The history of TCSPC can be traced back to the late 1960s, and it originates from the measurement of excited nuclear states. The early classic TCSPC is limited to recording the waveform of periodic light signals due to the low intensity and low repetition rate of the light sources. After more than half a century of development, the current TCSPC systems became bigger, faster, more flexible, and multidimensionality. They can not only record the relationship between photon distribution and fluorescence decay time, but also versus a spatial coordinate or the wavelength of the photons.¹⁰⁵

The TCSPC technique is based on the repetitive, precisely timed registration of single photons of the fluorescence signal.^{106,107} Fig 2.5 is a schematic showing how the histogram of photons is formed over multiple cycles.¹⁰⁸ In this process, the fluorescence of the sample is excited by the laser pulses with a high repetition rate. The time difference between excitation and emission is measured by electronics that act as a stopwatch. It should be noted that in addition to photons, there will be many empty cycles (as shown after the second laser pulse in Fig. 2.5a), both photons and empty cycles are entirely random and can only be described by probability (according to the laws of quantum physics). By counting many events, a histogram consisting of a range of “time bins” is built up (Fig. 2.5b). The width of the “time bins” typically corresponds to the resolution of the stopwatch

(some picoseconds). Furthermore, the delay time information is obtained by converting time to a voltage ramp.¹⁰⁸

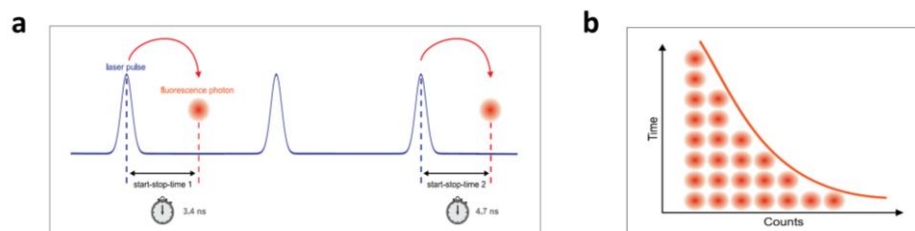


Fig. 2.5. Measurement of start-stop times in time-resolved fluorescence measurement with TCSPC (a); Histogram of start-stop times in time-resolved fluorescence measurement with TCSPC (b). Figures were taken from Reference [108] with permission.

The time resolution of a TCSPC set-up can be characterized by its Instrumental Response Function (IRF). Typically, the time resolution is limited by the response limit of the detector to detect a photon, and the time uncertainty of different photodetectors can range from 25-400 ps.¹⁰⁸ IRF is also broadened by other factors, such as the excitation pulse, the jitter given by the electronic components, *etc.* In this Ph.D. project, we used a pulsed diode laser triggered externally at 2.5 MHz (TCSPC device of PicoQuant). In **Paper II**, a 438 nm laser with a pulse duration of 40 ps was used to excite our samples. Simultaneously, we selected a long-pass filter from 450 nm to pick up only the band-edge emission. In **Paper III**, the excitation laser wavelength is 375 nm with a 400nm long-pass filter placed in front of the detector.

2.2.2.4-X-ray photoelectron spectroscopy (XPS)

XPS is a quantitative, surface-sensitive spectroscopic technique based on the photoelectric effect. It is often used to measure elemental compositions, empirical formula, chemical state, the overall electronic structure, and density of the electronic states at the sample surface.^{109,110} Fig.2.6 displays the working principle of this technique, which mainly involves X-ray absorption and photoelectron emission.¹¹¹ After an excited atom absorbs X-rays, it will produce photoelectrons with the binding energies lower than the X-ray photon energy. Then, photoelectrons can escape to the vacuum and be captured by

the detector with a specific kinetic energy. In XPS, the binding energy of each emitted electrons can be determined by using Ernest Rutherford's equation:¹⁰⁹

$$E_{\text{binding}} = E_{\text{photon}} - (E_{\text{kinetic}} + \Phi) \quad (2.4)$$

where E_{binding} refers to the binding energy of the photoelectron, E_{photon} is the X-ray photon energy, E_{kinetic} is the electron kinetic energy, Φ is the work function.

The E_{binding} profile of detected photoelectrons constitutes the XPS spectra where each excited atom (element) can generate a set of characteristic XPS peaks, which can be assigned to the various electron configuration in the atoms, e.g., 1s, 2s, 2p, 3s, etc. Moreover, the number of photoelectrons detected in each XPS peak is also directly related to the quantity of this element on the sample surface. This is the basis for XPS to be able to perform element quantification.

In this thesis, XPS was used to analyze the elemental compositions and valence of compounds. All the measurements are based on ThermoScientific XPS instrument with X-ray photon energy of 1486 eV (Al K α X-ray source).

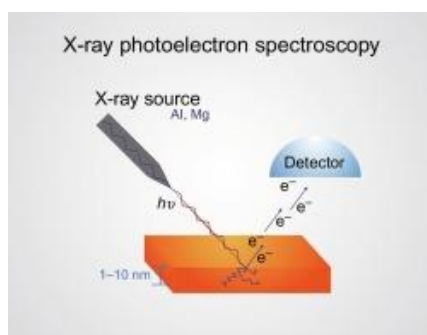


Fig.2.6. Schematics of the working principle of XPS measurement [111].

2.2.3 Microscopic techniques

2.2.3.1-Scanning electron microscopy (SEM)

SEM is a commonly used electron microscope that can visualize target objects by scanning the surface with focused electron beam. **Fig.2.7** demonstrates the basic principle of the SEM instrument.^{112,113} An electron beam is thermionically produced from an electron gun,

and is induced to the condenser lenses and focused to a spot. The beam will afterward travel within pairs of scanning coils, which deflect the beam in two directions (i.e. the x and y direction). Therefore it can scan the sample surface in a raster fashion, which generally requires the objective lens to focus the electron beam again. When the electron beam hits the sample surface, three types of signals are generated: backscattering electrons, secondary electrons, and X-rays. They are collected by different detectors, and converted into the amplified electrical signal to produce images. Among them, characteristic X-ray is the base for energy-dispersive X-ray spectroscopy (EDX) and can provide the spatial mapping of the elemental composition. In this thesis, all the SEM and EDX pictures are taken with a Quanta FEG 200 ESEM instrument.

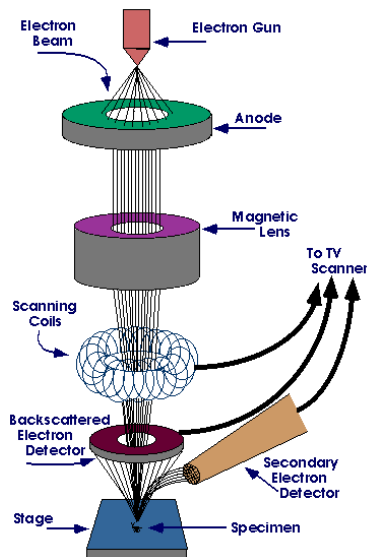


Fig. 2.7. Schematics of the structure and principle of SEM [112].

2.2.3.2-Atomic force microscopy (AFM)

AFM is a type of scanning probe microscopy with a nanometer-level resolution. The information is gathered by "feeling" or "touching" the morphological contract at the surface with a mechanical probe. It works by using a tip (the radius of curvature is several nanometers) at the mechanical cantilever to "feeling" or "touching" the sample surface to collect information.¹¹⁴ Fig. 2.8 is a brief schematic illustrating the AFM working principle.¹¹⁵ A sharp tip at the free end of a flexible cantilever would contact with the

sample surface. A laser beam is reflected from the top surface of the cantilever to the position-sensitive photodiode detector. The characteristics of the sample surface cause the cantilever to bend to different angles. As a result, the position of the laser beam changes compared with the original positioning when the scanning is conducted. The profile of the laser beam deviation can be transformed into the morphologic information of the sample surface. In this thesis, we mainly used AFM technique (Agilent Technologies 5500) to measure the thickness and morphology of 2D MHP films (**Paper II**) and N-rGO (**Paper III**).

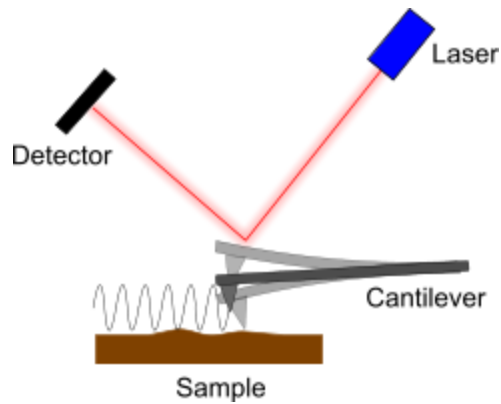


Fig. 2.8. Working principles of AFM setup [115].

Chapter 3

Spontaneously Grown Strongly Coupled 3D MAPbBr₃/N-rGO Hybrids and their Photodetector application

MHPs have emerged as promising candidates for photodetectors. However, instability and poor photoconductivity have limited their future commercialization.⁹⁻¹³ In this chapter (**Paper I**), we report the spontaneous growth of 3D perovskite/N-rGO hybrid crystal using a facile solution method and apply them to the photodetectors. In the hybrid structures, 3D perovskite microcrystals were homogeneously wrapped by N-rGO sheets through strong hydrogen bonding. The strongly coupled N-rGOs facilitate the charge carrier transport across the perovskite crystals but also distort the surface lattice of the perovskite, creating a potential barrier for charge transfer. We optimize the addition of N-rGO in the hybrid structures to balance the interfacial structural distortion and the inter-crystal conductivity. A high-performance photodetection up to 3×10^4 A/W, external quantum efficiency (EQE) exceeding 105 %, and detectivity up to 10^{12} Jones were achieved in the optimal device.

3.1 Morphological and structural characterization of MAPbBr₃/N-rGO Hybrids

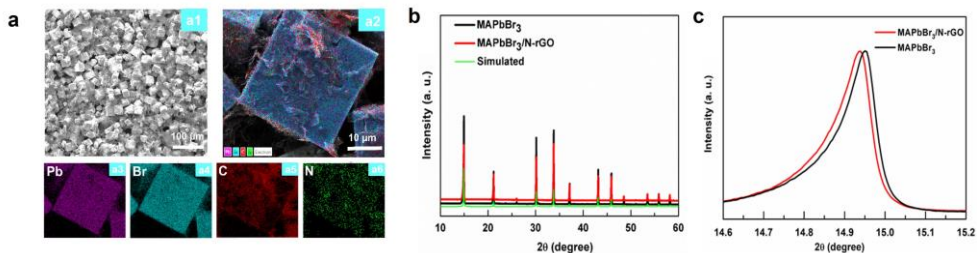


Fig.3.1. SEM characterization of MAPbBr₃/N-rGO hybrid (a); XRD patterns of MAPbBr₃ and MAPbBr₃/N-rGO (b), and magnified XRD spectra (c).

Fig. 3.1a is the SEM characterization of as-synthesized hybrid MAPbBr₃/N-rGO. We can clearly see that the morphology of the sample is relatively uniform (Fig. 3.1 a1), and N-rGOs evenly cover the 3D MAPbBr₃ micro-crystal (MC) surface (Fig. 3.1 a2). The elemental composition mapped by energy-dispersive EDX of Pb, Br, C, N (Fig. 3.1 a3-a6) show that Pb, Br elements over the MCs; and C, N elements reside both at the surface of the MAPbBr₃ and the interspaces among the crystals, which demonstrate the interconnection among MAPbBr₃ MCs via N-rGOs. To further characterize the influence of N-rGO addition on the perovskites' formation, we compare the crystal structures between MAPbBr₃ with and without N-rGO using XRD (Fig. 3.1b). The MAPbBr₃ of them all crystallize in the typical perovskite phase (space group *Pm-3m*). From the magnified XRD spectra (Fig. 3.1c), we could observe the main diffraction peak of MAPbBr₃ corresponding to (001) crystalline plane shifts from 14.951° towards the smaller diffraction angle of 14.937° after coating with N-rGO, indicating a lattice expansion.

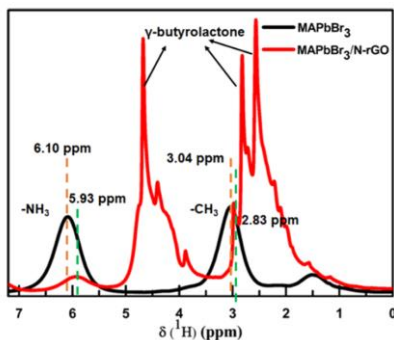


Fig.3.2. ¹H solid-state NMR spectra at room temperature.

Furthermore, solid-state ^1H NMR was also performed to verify the interaction between the N-rGO and perovskite, as shown in Fig.3.2. From it, we could find out the difference between $\text{MAPbBr}_3/\text{N-rGO}$ and MAPbBr_3 . According to the literature, the peaks at 6.10 and 3.04 ppm can be attributed to NH_3 and CH_3 in pure MAPbBr_3 , respectively.¹¹⁶ However, in $\text{MAPbBr}_3/\text{N-rGO}$, those peaks appeared to have shifted to the low field at 5.93 and 2.83 ppm, which indicates the shortening of the hydrogen bonding as well as the stronger hydrogen bonding interaction in the $\text{MAPbBr}_3/\text{N-rGO}$.¹¹⁷ This is direct evidence for the interfacial conjugation between N-rGO and perovskite via strong hydrogen bonding.

3.2 The performance of the photodetector device based on $\text{MAPbBr}_3/\text{N-rGO}$ hybrids.

The photodetector was fabricated by casting $\text{MAPbBr}_3/\text{N-rGO}$ hybrids onto two neighboring ITO electrodes with distance to 40 μm as illustrated in Fig. 3.3a. The perovskite microcrystals are tightly wrapped by N-rGO as evidence in Fig. 3.3b. In order to optimize the device performance, we varied the mass ratios between perovskite and N-rGO and in the hybrids (8 : 0, 8 : 0.25, 8 : 0.5, 8 : 1, 8 : 1.5, 8 : 2 denoted as MAPbBr_3 , $\text{PNrGO}_{0.25}$, $\text{PNrGO}_{0.5}$, PNrGO_1 , $\text{PNrGO}_{1.5}$, and PNrGO_2 , respectively). Finally, the test results show that $\text{PNrGO}_{1.5}$ has the largest photocurrent and superior photodetection characteristics. By analyzing the $\text{PNrGO}_{1.5}$ results, we found that the photocurrent clearly increases with the increment of the power density. Moreover, from the light-intensity-dependent photocurrent in Fig. 3.3c, we can extract the linear dynamic range (LDR) to be 94.4 dB and the responsivity (R) to be 3.6×10^4 A/W. The detectivity (D) and external quantum efficiency (EQE), electrons/incident photons of the device, can reach as high as 0.98×10^{12} Jones and $\sim 0.9 \times 105$ %, respectively (Fig. 3.3d).¹¹⁸⁻¹²⁰

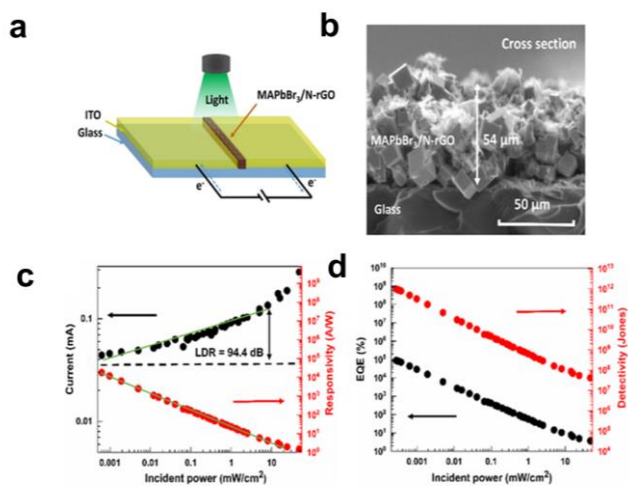


Fig.3.3. Schematic illustration of the photodetector device with the gap between two ITO plates to be 40 μm (a); cross-sectional SEM image of the photodetector (b); photocurrent and responsivity versus incident power under 4V bias (c); EQE and detectivity versus incident power under bias of 4V (d).

3.3 Interfacial Structure and Photophysics in MAPbBr₃/N-rGO hybrids.

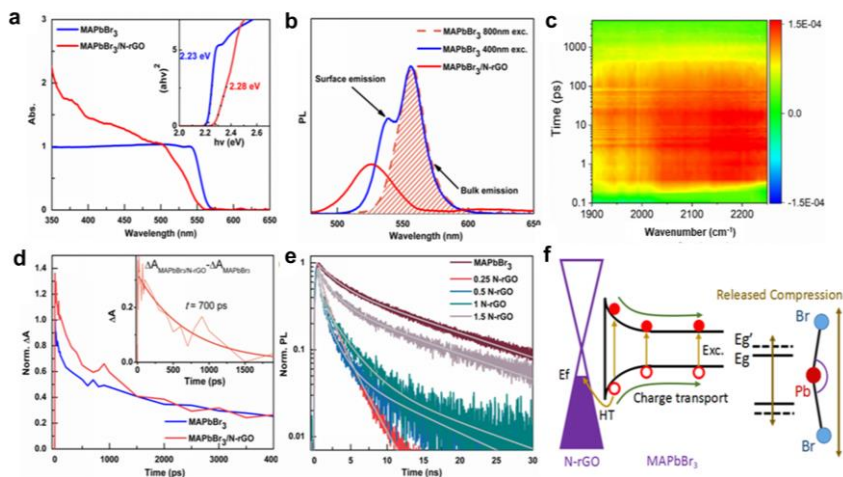


Fig. 3.4. Steady-state absorption spectrum, inset Tauc plot representing the bandgap of MAPbBr₃ and MAPbBr₃/N-rGO, respectively (a); steady-state PL spectra for MAPbBr₃ and MAPbBr₃/N-rGO excited at 400 nm and 800 nm, respectively (b); time-resolved infrared absorption spectra after 400 nm excitation for MAPbBr₃ crystals (c); normalized bleaching kinetics of MAPbBr₃ and MAPbBr₃/N-rGO probed at 400 nm excitation; the inset shows the differential curves of bleaching kinetics between MAPbBr₃/N-rGO and MAPbBr₃ (d); transient PL kinetics excited at 400 nm (e); schematic view of the mechanism for the charge transport in MAPbBr₃/N-rGO (f).

The absorption band edge of MAPbBr₃/N-rGO sample exhibits a pronounced blue-shift of ~ 20 nm (0.05 eV) compared with neat MAPbBr₃ (Fig. 3.4a), which can be attributed to structure distortion of perovskite due to N-rGO coverage. The intrinsic octahedral tilting induced by the cation-related hydrogen bonding in perovskites would be suppressed by graphene coverage, which results in a wider bandgap according to both theoretical calculations and experimental observation, as shown in Fig. 3.4f.¹²¹ The band edge emission of MAPbBr₃/N-rGO samples is also blue-shifted accordingly, as shown in Fig. 3.4b. The doublet PL emission band of the neat MAPbBr₃ crystals features the coexistence of the surface-emission (blue side) as well as bulk emission (red side) with different optical transition energy.¹²²

The primary condition of photocurrent generation in perovskite/N-rGO composites should be the transportation of photo-generated charge carriers from perovskite to N-rGO

by either charge transfer or energy transfer. In order to distinguish these two processes, we used TRIR to probe the excited state dynamics. Fig. 3.4c shows the time evolution of TRIR spectra after 400 nm excitation of MAPbBr₃ crystals. The broad featureless positive signal is a fingerprint of photo-generated free carriers in the lead halide perovskites representing the intraband absorption transition of excited charges carriers.¹²³ The decay of such absorption bands refers to the radiative/nonradiative recombination of the excited charges carriers, as shown in Fig. 3.4d. After attached to N-rGO, the spectral feature in TRIR keeps the same but with faster decay rate indicating an extra excited-state depopulation pathway in the MAPbBr₃. This demonstrates that there should be charge transfer (probably hole transfer according to the band alignment) instead of energy transfer from perovskites to N-rGO after photoexcitation. We fit the hole transfer time from the differential decay signal between MAPbBr₃ and MAPbBr₃/N-rGO samples to be 700 ps (inset of Fig. 3.4d). In addition, the PL quenching observed in the time-resolved photoluminescence (TRPL) measurement confirms the interfacial charge transfer dynamics, as shown in Fig. 3.4e. We noticed the hole transfer times (fastest components) first decrease and then increase with the increment of the N-rGO ratio. This means the hole injection (HT) from MAPbBr₃ to N-rGO is firstly enhanced with the addition of N-rGO up to 0.5 ratio and then diminished when more N-rGO is introduced. The initial enhancement of the HT can be easily understood as the increased coverage of N-rGO on the perovskite surface. However, the more interplay between N-rGO and perovskite, the more lattice compression is released leading to the wider bandgap on the surface. A surface barrier would then be created inhibiting the HT as illustrated in Fig. 3.4f, which explained the observation in TRPL.

Chapter 4

Electronic Structure and Trap States of 2D RP Perovskites

In general, the formation of 3D APbX_3 perovskites is governed by the Goldschmidt tolerance factor (τ), τ needs to fall into the range from 0.8 to 1.0 for the stable cubic or distorted 3D perovskite structures to be formed.^{14,15,26,27} However, it has been recently realized that the τ range restriction can be relaxed in 2D RPPs, which allows larger A-cations, such as ethyl-ammonium (EA) and guanidinium (GA), to fill into the inorganic $[\text{PbI}_3]^-$ cages.²⁰ Inserting larger A-cation will further distort the inorganic lattice. In this chapter (**Paper II**), we systematically study the effect of the lattice distortions by large A-cation integration on the electronic structure and photo-physical properties of two 2D RP perovskites (RPPs), $(\text{n-BA})_2(\text{MA})_2\text{Pb}_3\text{I}_{10}$ (BMAPI) and $(\text{n-BA})_2(\text{EA})_2\text{Pb}_3\text{I}_{10}$ (BEAPI). It can provide a robust reference for future materials engineering and device application of 2D perovskite materials.

4.1 Relaxed Tolerance Factor and Intraoctahedral Distortions in the 2D RPPs

The 3D APbX_3 perovskites are stable only when their τ -value falls between 0.8 and 1.0. For instance, EAPbI_3 tends to crystallize in an orthorhombic space group $Pna2_1$ (no.33) at room temperature and cannot form a traditional continuous 3D perovskite lattice. This is due to the larger effective radius of EA ($r_{\text{EA}} = 274$ pm), which leads to a τ -value of 1.031.^{28,29} However, BEAPI can exist at room temperature. This indicates that the conventional τ -value threshold can be relaxed if the target compound is expected to adopt a 2D structure rather than a 3D structure. In a 2D RP perovskite structure, the organic spacing cations act as “buffers” to the compression imposed on the rigid inorganic layers.

The intensive strain accumulation is directly reflected by the increasing distortion of the PbI_6 octahedron that forms the inorganic layers (Fig. 4.1a). To get detailed insight into the lattice distortion, the PbI_6 octahedral structures in BMAPI and BEAPI were systematically compared by analyzing the crystallography data of the single crystals. Fig. 4.1 b-f are the five calculated structural parameters, including bond distance parameter ($\langle D \rangle$), distance distortion parameter (ζ), tilting distortion parameter (Δ), torsional distortion parameter (Θ), and angle distortion parameter (Σ), using the following equations:^{124,125}

$$\langle D \rangle = (\sum_{i=1}^6 d_i) / 6 \quad (3.1)$$

$$\zeta = \sum_{i=1}^6 |d_i - \langle D \rangle| \quad (3.2)$$

$$\Delta = \sum_{i=1}^6 \left(\frac{d_i - \langle D \rangle}{\langle D \rangle} \right)^2 \quad (3.3)$$

$$\Theta = \sum_{i=1}^{24} |60 - \theta_i| \quad (3.4)$$

$$\Sigma = \sum_{i=1}^{12} |90 - \varphi_i| \quad (3.5)$$

where d_i are the individual Pb–I bond distances in the PbI_6 octahedron. θ_i are the angles of the 24 unique projections of the I–Pb–I angles to the triangular faces of the PbI_6 octahedron along its pseudo-3-fold axis. φ_i are the 12 cis-angles of I–Pb–I around the Pb atom. By comparing these parameters, we find both an increase in PbI_6 octahedral distortions and an increase in compression for organic layers in BEAPI, which account for the stable accommodation of larger EA cations in the $[\text{PbI}_3]^-$ cages.

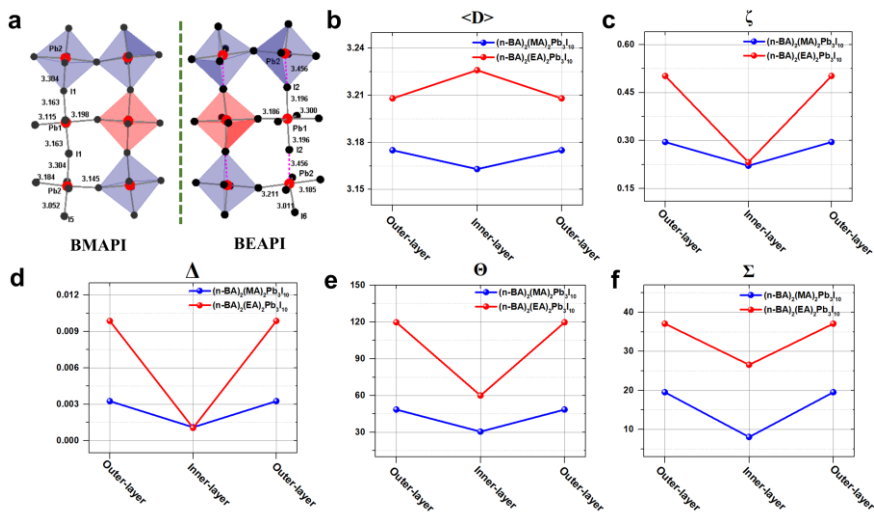


Fig. 4.1. Inorganic lattice and the PbI₆ octahedral distortions in BMAPI and BEAPI (a); the magnitude of distortion parameters: bond distance parameter ($\langle D \rangle$) (b), distance distortion parameter (ζ) (c), tilting distortion parameter (Δ) (d), torsional distortion parameter (Θ) (e), and angle distortion parameter (Σ) (f).

4.2 Impact of the Intraoctahedral Distortions on the Electronic Structures

In the XPS spectra shown in Fig. 4.2a, we can clearly observe that the red-shift of Pb 4f core levels in BMAPI compared with that of BEAPI by 0.2 eV. It means the electronic density at the Pb center is higher in BMAPI than in BEAPI, owing to the more pronounced delocalization of the outer charges caused by a shorter Pb–I distance. On the other hand, the XPS spectra of the I 3d core level are identical in two compounds (Fig. 4.2b), indicating similar chemical environments around the I atoms. A possible reason could be the contribution of N–H \cdots I hydrogen bonding between N and I that could balance the charge reorganization within the Pb–I covalent bond. The electronic structures of two crystals are illustrated in Fig. 4.2c-d. According to the structural analysis, the Pb–I bond distance ($\langle D \rangle$ parameter) of BMAPI is shorter than that of BEAPI. This reflects a stronger

interaction, hence a larger degree of charge delocalization over the I-5p and Pb-6s orbitals. As a result, the energy difference between the bonding orbitals (σ) and anti-bonding orbitals (σ^*) increases. Therefore, the VBM position of BMAPI is higher compared to the VBM position of BEAPI. In contrast, unlike the hybridization mode between I-5p and Pb-6s orbitals, I-5p and Pb-6p orbitals are hybridized into bonding orbitals (π) and anti-bonding orbitals (π^*), with the CBM being less affected by Pb-I bond distance. Hence, the CBM positions of them are almost identical.

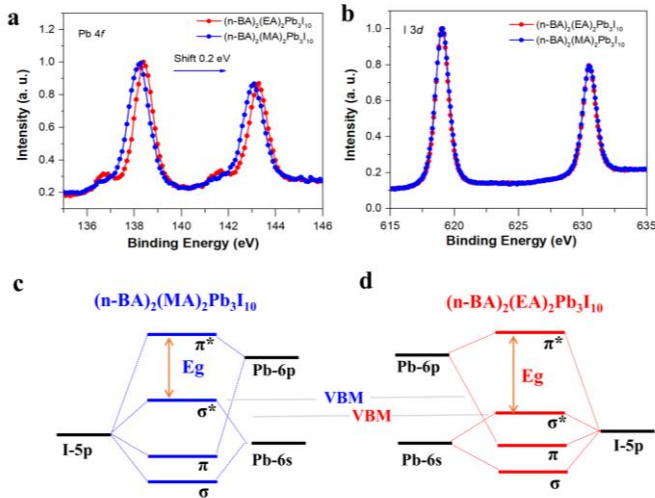


Fig. 4.2. XPS core emission of (a) Pb 4f doublet and (b) I 3d doublet; and the lone-pair model with stereochemical activity of the s2 electrons in the (c) BMAPI and (d) BEAPI.

4.3 Impact of the Intraoctahedral Distortions on the Trap-Mediated Charge Recombination.

Fig. 4.3a and b show the PL kinetic of BMAPI and BEAPI crystals. We can observe a prolongation of the PL lifetime with the increase of excitation intensity for both compounds. This behavior is a well-known fingerprint of trap filling/accumulation seen in other perovskite materials.^{92,93} It occurs when the depopulation time of traps is longer than the time interval between the laser pulses so that part of the traps is still filled when the new excitation pulse comes. Furthermore, we can fit their trap densities as well as

the trap lifetimes according to trap filling model (Fig. 4,3 c).^{93,95} The summary of the trap-mediated charge recombination dynamics are given in Fig.4.3d. We confirmed two kinds of traps (trap 1 and trap 2) in the 2D perovskite crystals. Table 4.1 summarize the fitted trap densities of them. Compared with trap 1, the densities of trap 2 are small and can be neglected. Therefore, the trap-mediated recombination is dominated by the trap 1 under low excitation density. The density of trap 1 in BEAPI is 1.7 times higher than that in BAMPI. We believe such a difference in trap density can be attributed to the more considerable degree of intraoctahedral lattice distortions in BEAPI with larger EA cations filling into the crystal lattice.

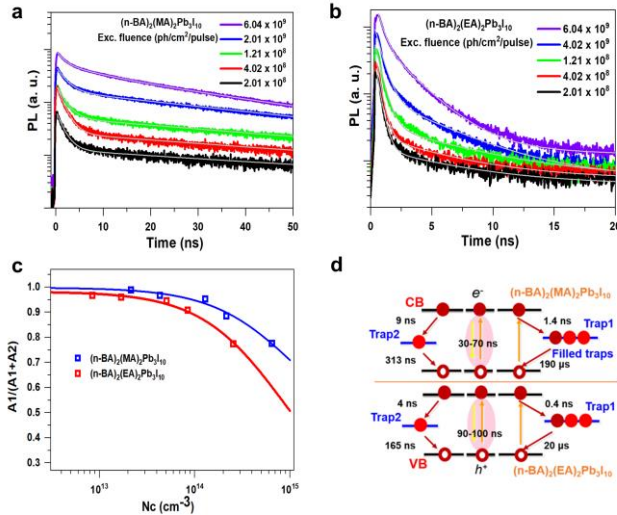


Fig. 4.3. PL decay kinetics with different excitation fluence for BAMPI (a) and BEAPI (d); dependence of the amplitude ratios $A_1/(A_1 + A_2)$ in the multi-exponential fitting of the decays on the initial charge densities N_c for two compounds. (f) Illustration of the trap-mediated charge recombination in the two compounds.

Table 4.1. Trap densities obtained from the fitting shown in Fig. 4.3c.

Crystals	N_{T1} (10^{15} cm ⁻³)	N_{T2} (10^{15} cm ⁻³)
BAMPI	21.8	0.11
BAEPI	37.6	0.59

Chapter 5

Free excitons versus self-trapped excitons at different facets of 2D RP Perovskite single crystals

Sub-band gap band photoluminescence has been widely observed in RP 2D lead halide perovskites (LHPs). However, the occurrence of such band emission varies among different 2D structures. Whether the formation of self-trapped excitons (STEs) or in-gap defect states account for such band emission is still under debate.¹²⁶⁻¹²⁹ In the chapter 5 (**Paper III**), three target centimeter-scaled single crystals (SCs) with various spacing cations, (iso-BA)₂(MA)Pb₂Br₇ (iso-BAPB), (n-BA)₂(MA)Pb₂Br₇ (n-BAPB) and (n-PA)₂(MA)Pb₂Br₇ (n-PAPB) were synthesized by temperature gradient method. We studied photoluminescence features at different facets of those crystals. Our results show that self-trapped excitons do induce sub-bandgap emission but depend highly on the local structures of the single crystals. At the in-plane facet parallel to the 2D inorganic layers (IF), the STEs are less likely to be formed, whereas free excitons dominate due to the weak electron-phonon coupling in a more symmetric lattice. In the edge facet perpendicular to the 2D inorganic layers (PF), large distortion of the lead halide octahedra due to the accumulation of the strain along the 2D layers enhance the electron-phonon coupling, and therefore the formation of STEs is favorable. The distinction of dominant photo-excited species also reflects in different behaviors at two facets in temperature-dependent steady-state PL as well as excitation intensity-dependent PL dynamics.

5.1 Structural difference between the in-plane facet and prearticular facet in 2D perovskite single crystals.

According to the theoretic calculation, the prearticular facets (PF) in 2D RP perovskites are mainly induced by the relaxation of the interface strain along the 2D inorganic layer nucleating the surface reorganization while such strain along the direction vertical to the 2D layer would be released by the spacing cations.²⁴ As demonstrated by an example structure of $(A')_2(A)_{n-1}Pb_nX_{3n+1}$ ($n=2$) (Fig. 5.1), the (002), (110), and (111) PFs correspond to the small crystal facets in the macroscopic crystal (Fig. 5.1a and b). The lattice strain along the direction vertical to the (200) IF facet can be released into the organic spacing cations every two periodic layers (Fig. 5.1c). Therefore, no big structural difference should occur between the surface and the bulk volume area. We can then consider the surface IF facet as bulk state. On the other hand, lattice strain would continuously accumulate along the (002), (110), and (111) directions and release at the PFs. Thus, the surface lattice structure along them should be different from the inner bulk area. (Fig. 5.1c).^{130,131}

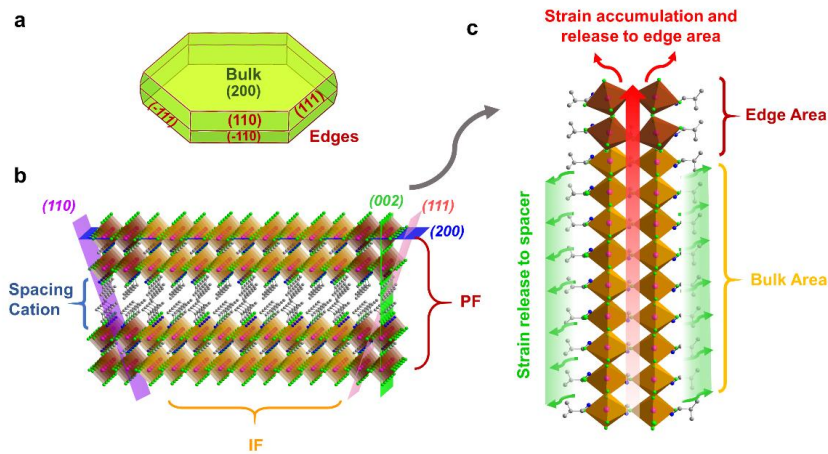


Fig. 5.1. A macroscopic simulation of crystal morphology of a 2D RP perovskite (a), schematics show the definition of bulk and edge states (b) and the directions of strain accumulation release (c).

5.2 Formation of the STE vs. FE (free excitons) in three SCs at different facets

Steady-state PL shows that the emission at PFs of three SCs drastically red-shift compared to that at IFs (as shown in the schematic of Fig. 5.2a). In addition, we conducted

the temperature-dependent PL at PF and IF of three crystals over temperatures from 100 to 280 K for three samples (Fig. 5.2b-g). Unlike the other two crystals where the PL intensity at two facets decrease with temperature due to the thermalization of the excitons into free charges (Fig. 5.2b,c,e,f), the dual emission peaks in n-PAPB occur all over the temperature region at the PF with high-energy PL becoming more dominant at low temperature (Fig. 5.2g). This phenomenon is against the traditional exciton trapping mechanism where the trap state emission and intrinsic band-edge exciton emission are competing and modulated by the thermal dependent equilibrium between the trapping and detrapping of the excited carriers. We believe the low-energy emission at the PFs should be attributed to STE as the STE (or polaron state) in perovskite is formed by the electron-LO phonon coupling via the Fröhlich interaction, which is dominant at RT but diminished with decreased temperature. Furthermore, the line-shape of PL spectra in n-BAPB and iso-BAPB indicates more pronounced/stabilized STE in those samples.

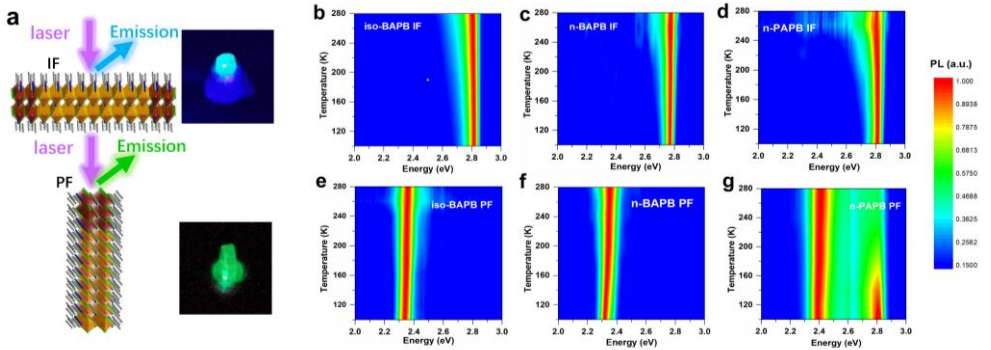


Fig. 5.2. Schematics of PL measurements (a); temperature-dependent PL spectral colour plots of bulk (b-d) and edge states (e-g) of the three SCs.

In order to verify our assumption, we characterize the electron-phonon coupling strength from the FWHMs of temperature-dependent PL spectra using method introduced in section 1.3.3 (Fig. 5.3).⁸⁸ Extracted from the results, the coupling strength γ_{LO} of PFs are significantly larger than those of IFs in three samples except for n-PAPB. The stronger electron-phonon coupling at the PFs supports STE formation at the edge area in our 2D perovskite SCs. On the other hand, the relatively weaker coupling of electrons with lattice deformation at the PFs of n-PAPB can explain the less stabilized STE.

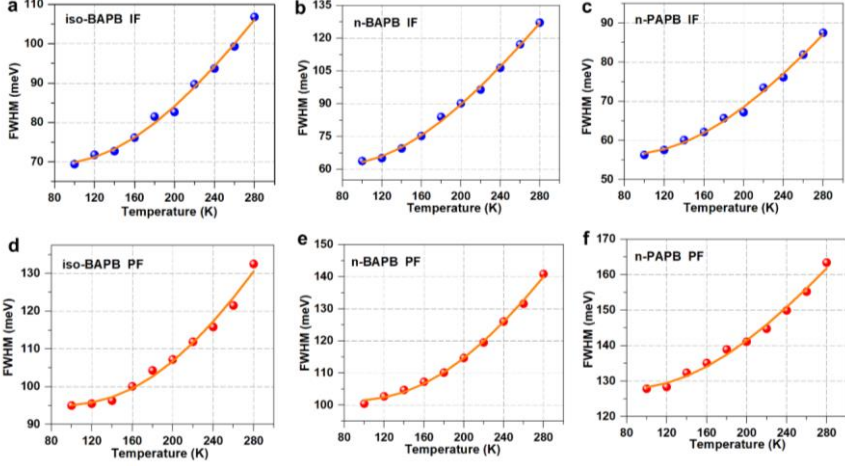


Fig. 5.3. FWHM of the temperature-dependent PL for the PF and IF of the three SCs, and the solid orange lines are fits of equation 1.7.

Table 5.1. Extracted linewidth parameters.

IFs	Γ_0 (meV)	γ_{LO} (meV)	E_{LO} (meV)
iso-BAPB	69.1	251.5	49.5
n-BAPB	61.3	359.9	45.1
n-PAPB	56.1	218.3	50.3
PFs	Γ_0 (meV)	γ_{LO} (meV)	E_{LO} (meV)
iso-BAPB	94.8	452.5	63.1
n-BAPB	101.1	434.1	60.3
n-PAPB	127.5	233.4	49.6

5.3 Emission Dynamics of STE vs. FE in three SCs at different facets

Fig. 5.4a-f depicts the excitation intensity-dependent PL kinetics at IFs and PFs of all three SCs. The PL lifetimes of the IFs increase with the excitation intensity as illustrated

in Fig. 5.4a and b. This behavior has been explained by trap filling/accumulation (as shown in the schematic Fig. 5.4g). We can obtain the trap density of IFs of iso-BAPB and n-BAPB to be $4.7 \times 10^{16} \text{ cm}^{-3}$ and $2.9 \times 10^{16} \text{ cm}^{-3}$, respectively, by globally fitting the intensity-dependent PL kinetics using a dynamic trap-filling model.⁸¹ The unique intensity-dependent PL kinetics at PFs (Fig. 5.4d-f) can be well interpreted by the STE model ((as shown in the schematic Fig. 5.4h). Unlike in 3D perovskite or at IF of 2D perovskite where the electron-phonon coupling would generate mainly large polaron, a larger degree of lattice distortion at the PF of 2D perovskites tends to form STEs where the motion of them occurs through site-to-site hopping.^{132,133} At low excitation density, it's difficult for the STEs at the PFs to diffuse to the trap state and undergoes a trapping process. Therefore the dominant excited state depopulation pathway is the STE radiative recombination as shown in Fig. 5.4h. The increasing excitation intensity would increase the STE density at the PFs, enhancing the diffusivity of the STE hopping. Such polaron concentration dependence has been observed in OPV materials interpreted by the change of spatial confinement.^{134,135} In our samples, the improved motion of the STE at the PFs increases the possibility of fast trapping by the defect states, and thereby the PL lifetime is shortened as illustrated in Fig. 5.4i.

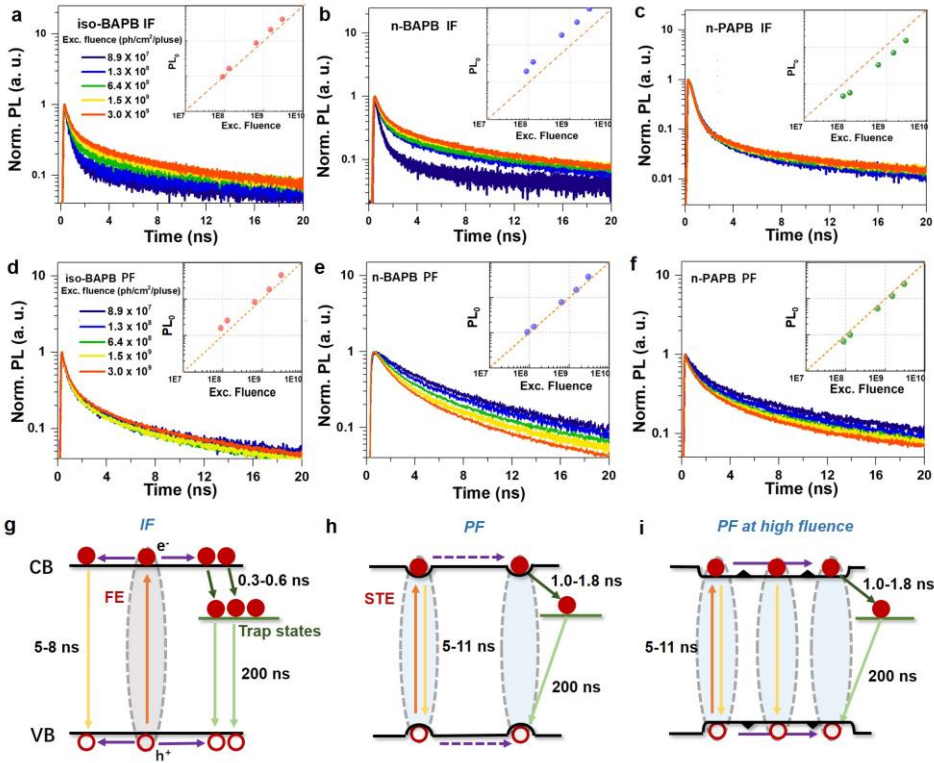


Fig. 5.4. PL decay kinetics with different excitation fluence for the IFs (a-c) and PFs (d-f) of these three SCs, inserts: PL intensities change with fluence intensity; Illustrations of the charge recombination processes in these three SCs (g-i).

Chapter 6

Lead-free 0D halide perovskite Cs_3BiBr_6 with high thermal stability for optoelectronics

The state-of-the-art Pb-containing perovskites are containing poisonous heavy metal elements and could lead to serious environmental issues.^{9-13,136,137} Therefore, there is a strong desire to replace toxic Pb with a benign element such as Sn, Ge, Bi, etc., without drastically degrading their optoelectronic performance.¹³⁸⁻¹⁴⁰ In this chapter (**Paper IV**), we developed a novel lead-free Cs_3BiBr_6 single-crystal. It exhibits a high thermal stable 0D perovskite structure. Furthermore, a photodetector based on this perovskite was fabricated. It enriches the structural family of lead-free perovskites and holds the potential for optoelectronic applications.

6.1 The structure of the newly developed lead-free perovskite, Cs_3BiBr_6 .

Single crystal X-ray analysis discovered that Cs_3BiBr_6 crystallizes in the orthorhombic system of space group $Pbcm$ (No, 57) with $a = 8.689(2) \text{ \AA}$, $b = 13.628(1) \text{ \AA}$, and $c = 27.694(9) \text{ \AA}$. There are two Bi atoms, three Cs atoms, and seven Br atoms in an asymmetric unit. As shown in Fig. 6.1a and 1b, each Bi atom is coordinated by six Br atoms, forming distorted BiBr_6 octahedra. Cs_3BiBr_6 can be regarded as a typical 0D halide perovskite structure with the unconnected BiBr_6 octahedral spots, and Cs^+ cations filled up the remaining spaces (Fig. 6.1c). In addition, Cs_3BiBr_6 showed good thermal stability. It can be observed that Cs_3BiBr_6 is stable with increasing temperature up to 425 °C. For typical 3D MAPbBr_3 , the loss in the weight of the sample starts from 285 °C (Fig. 6.1d).

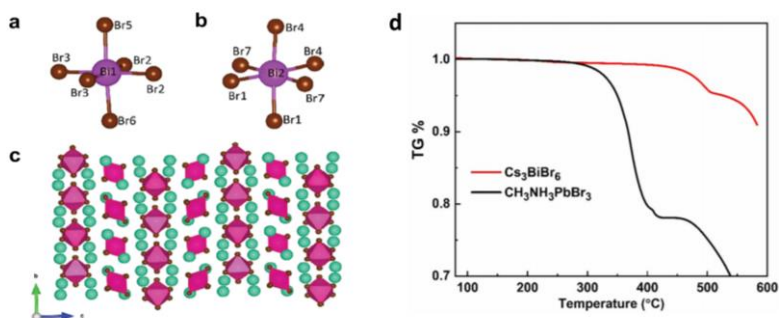


Fig. 6.1. View of structural characteristics for Cs_3BiBr_6 . Bromide coordination environment for Bi1 (a) and Bi2 (b); 0D structure view on the bc -plane (c). TGA curves of Cs_3BiBr_6 and MAPbBr₃.

6.2 The photodetector application of Cs_3BiBr_6 .

In order to demonstrate the optoelectronic property of Cs_3BiBr_6 , a photodetector was fabricated on ITO electrodes, as illustrated in Fig. 6.2a. Fig. 6.2b shows the I - V characteristics in the dark and under light illumination at different light densities. Apparently, the photocurrent increases with the increase of the light density and voltage. Under a 6 V bias, an ultralow dark current of 0.3 nA was obtained. Fig. 6.2c shows the dynamic current-time (i - t) curves for the Cs_3BiBr_6 based photodetectors under repeated switching of 400 nm monochromatic illumination with a light density of 25 mW cm^{-2} . Upon illumination, the photocurrent increases to 70 nA cm^{-2} by increasing the voltage up to 8 V. Fig. 6.2d shows the responsivity and detectivity of the photodetector versus voltage. At the voltage of 6 V, the responsivity (R) of this material can reach $\sim 25 \text{ mA W}^{-1}$ at a light density of 4 mW cm^{-2} . The detectivity (D^*) was calculated to be around 0.8×10^9 Jones, which demonstrates the potential of this material for its application in optoelectronic devices.

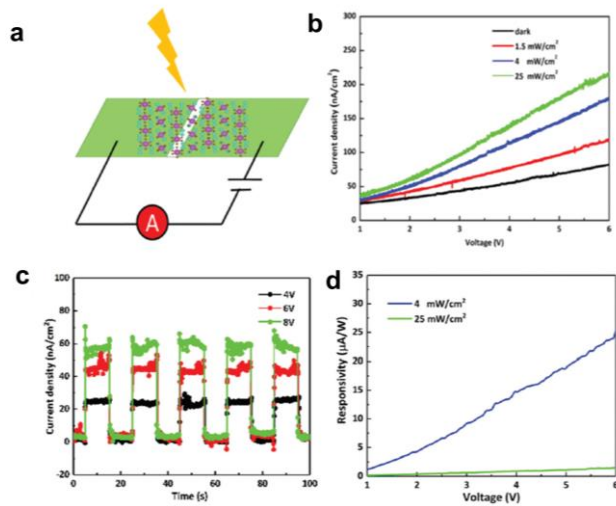


Fig. 6.2. Schematic view of the photodetector based on Cs_3BiBr_6 MCs (a). I–V characteristics at different power densities (b). Photocurrent responses under various bias voltages with fixed light density of 25 mW cm^{-2} (c). Comparison of the responsivity at two different light densities (d).

Conclusions

In this thesis, we developed the MHP crystals with molecular dimensionality from 3D, 2D to 0D, analyzed their structures and investigated their photophysical properties. We tried to correlate those intrinsic features with their structural characteristics. In addition, we achieved some prototype photodetector devices based on those MHP materials with enhanced performance after structural engineering. Our results revealed the entirely different critical structural factors that dominate the optical features of the MHPs with various dimensionality.

Generally speaking, in **3D** perovskite crystals, the charge transport is dominated by the motion of free carriers due to small exciton binding energy. Moreover, the low recombination rate and high trap tolerance level render an almost non-restricted charge transport with a long diffusion length. Hence the only bottleneck for the charge transport is the condition of grain boundary or crystal surface. Therefore, in **Paper I**, we put N-rGO to modulate the interfacial photophysics of typical 3D MAPbBr₃ crystals. We synthesized MAPbBr₃/N-rGO hybrids by an in-situ method. In the hybrids, MAPbBr₃ crystals were homogeneously wrapped by N-rGO sheets through strong hydrogen bonding, which facilitates the charge carrier transport across the perovskite crystals and protects the MAPbBr₃ from being quickly damaged by moisture. The photodetector based on this hybrid exhibits significantly enhanced stability under light illumination in ambient conditions, and the optimized device exhibited a high responsivity of 3×10^4 A/W, EQE of 10^5 % and detectivity up to 10^{12} Jones.

In **2D** perovskite crystals, excitons instead of the free carriers dominate the photogenerated species due to the larger exciton binding energy. In addition, the softer lattice structures lead to much strong electron-phonon coupling accounting for the lattice deformation. Therefore, the photophysics is strongly modulated by the local structure. In **Paper II and III**, we developed some novel 2D RP perovskites single crystals with various A cations and L spacing cations and investigated the relationship between their structures and photophysical behaviors. By studying (n-BA)₂(MA)₂Pb₃I₁₀ and (n-BA)₂(EA)₂Pb₃I₁₀, **paper II** shows that the latter with large-size A cations and relaxed τ exhibit the increased inorganic layer distortions and compression on long organic spacing

cation bilayers. Such structural change broadened its bandgap structure by lowering the position of the VBM, which is due to the prolongation of Pb-I bond, leading to a smaller degree of charge delocalization over the I-5p and Pb-6s orbitals. From their TRPL studies, we revealed ultra-long-lived trap states in both two compounds with the trap densities of $\sim 2.18 \times 10^{16} \text{ cm}^{-3}$ and $\sim 3.76 \times 10^{16} \text{ cm}^{-3}$ for $(\text{n-BA})_2(\text{MA})_2\text{Pb}_3\text{I}_{10}$ and $(\text{n-BA})_2(\text{EA})_2\text{Pb}_3\text{I}_{10}$, respectively. In paper **III**, we investigated the local structure and photophysics at different surface facets of 2D MHP crystals with three spacing cations, $(\text{iso-BA})_2(\text{MA})\text{Pb}_2\text{Br}_7$, $(\text{n-BA})_2(\text{MA})\text{Pb}_2\text{Br}_7$, and $(\text{n-PA})_2(\text{MA})\text{Pb}_2\text{Br}_7$. The research reveals that the large PL redshift at their perpendicular facets was attributed to the STE emission. From TRPL kinetics studies of the in-plane (IF) and perpendicular facets (PF) of these crystals, we found that the FE can move freely at the IF and get trapped by the intrinsic defect states, leading to the fast PL quenching. The STEs at PF are more localized due to the lattice deformation and therefore are more exempted from the defect states.

Finally, in the **0D** perovskite crystals the individual or clusters of the octahedra are stabilized by cations and not flexible anymore. Therefore, their structure and optical properties are much more stable. In **Paper IV**, we first reported a 0D lead-free perovskite structure Cs_3BiBr_6 . A photodetector based on this perovskite was fabricated, exhibiting a good detectivity of 0.8×10^9 Jones under 400 nm light illumination. Besides, the crystals display high thermodynamic stability.

References

1. A. R. Chakhmouradian and P. M. Woodward, *Physics and Chemistry of Minerals*, 2014, **41**, 387-391.
2. H. L. Bowman and Pfitschthal, *Tyrol. Mineral. Mag.*, 1908, **15**, 156–176.
3. A. von Hippel, R. G. Breckenridge, F. G. Chesley, L. Tisza, *Ind. Engin. Chem.*, 1946, **38**, 1097–1109.
4. H. L. Wells, *Zeitschrift für Anorg. Chemie.*, 1893, **3**, 195–210.
5. M. V. Kovalenko, L. Protesescu, M. I. Bodnarchuk, *Science*, 2017, **358**, 745–750.
6. D. B. Mitzi, C. A. Feild, W. T. A. Harrison and A. M. Guloy, *Nature*, 1994, **369**, 467–469.
7. D. B. Mitzi, S. Wang, C. A. Feild, C. A. Chess and A. M. Guloy, *Science*, 1995, **267**, 1473.
8. C. R. Kagan, D. B. Mitzi and C. D. Dimitrakopoulos, *Science*, 1999, **286**, 945.
9. A. Kojima, K. Teshima, Y. Shirai, T. Miyasaka, *J. Am. Chem. Soc.*, 2009, **131**, 6050–6051.
10. H. Tsai, W. Nie, J. C. Blancon, C. C. Stoumpos, R. Asadpour, B. Harutyunyan, A. J. Neukirch, R. Verduzco, J. J. Crochet, S. Tretiak, L. Pedesseau, J. Even, M. A. Alam, G. Gupta, J. Lou, P. M. Ajayan, M. J. Bedzyk and M. G. Kanatzidis, *Nature*, 2016, **536**, 312-316.
11. X. Gong, O. Voznyy, A. Jain, W. Liu, R. Sabatini, Z. Piontkowski, G. Walters, G. Bappi, S. Nokhrin, O. Bushuyev, M. Yuan, R. Comin, D. McCamant, S. O. Kelley and E. H. Sargent, *Nat Mater*, 2018, **17**, 550-556.
12. M. A. Green, A. Ho-Baillie and H. J. Snaith, *Nat. Photonics*, 2014, **8**, 506–514.
13. (NREL), T. N. C. for P. (NCPV) at the N. R. E. L. Best Research-Cell Efficiency available from: http://www.nrel.gov/pv/assets/images/efficiency_chart.jpg.
14. B. Charles, J. Dillon, O. J. Weber, M. S. Islam and M. T. Weller, *J. Mater. Chem. A*, 2017, **5**, 22495–22499.
15. Z. Li, M. Yang, J.-S. Park, S.-H. Wei, J. J. Berry and K. Zhu, *Chem. Mater.*, 2016, **28**, 284–292.
16. K. Shen, J. Hu, Z. Liang, J. Hu, H. Sun, Z. Jiang and F. Song, *Crystals*, 2018, **8**.
17. H. F. Kay and P. C. Bailey, *Acta Crystallogr.*, 1957, **10**, 219-226.

-
18. S. Sasaki, C. T. Prewitt, J. D. Bass and W. A. Schulze, *Acta Crystallogr., Sect. C: Struct. Chem.*, 1987, **43**, 1668-1674.
 19. S. Gholipour, A. M. Ali, J. P. Correa-Baena, S. H. Turren-Cruz, F. Tajabadi, W. Tress, N. Taghavinia, M. Gratzel, A. Abate, F. De Angelis, C. A. Gaggioli, E. Mosconi, A. Hagfeldt and M. Saliba, *Adv Mater*, 2017, **29**.
 20. Y. Fu, M. P. Hautzinger, Z. Luo, F. Wang, D. Pan, M. M. Aristov, I. A. Guzei, A. Pan, X. Zhu and S. Jin, *ACS Cent Sci*, 2019, **5**, 1377-1386.
 21. Y. Chen, Y. Sun, J. Peng, J. Tang, K. Zheng and Z. Liang, *Advanced Materials*, 2018, **30**.
 22. L. Mao, W. Ke, L. Pedesseau, Y. Wu, C. Katan, J. Even, M. R. Wasielewski, C. C. Stoumpos and M. G. Kanatzidis, *J. Am. Chem. Soc.*, 2018, **140**, 3775-3783.
 23. Y. Liang, Y. Zang, X. Huang, C. Tian, X. Wang and T. Cui, *J. Phys. Chem. C*, 2020, **124**, 8984-8991.
 24. B. Traore, L. Pedesseau, L. Assam, X. Che, J. C. Blancon, H. Tsai, W. Nie, C. C. Stoumpos, M. G. Kanatzidis, S. Tretiak, A. D. Mohite, J. Even, M. Kepenekian and C. Katan, *ACS Nano*, 2018, **12**, 3321-3332.
 25. H. Lin, C. Zhou, Y. Tian, T. Siegrist, B. Ma, *ACS Energy Lett.* 2018, **3**, 54-62
 26. L. Q. Xie, L. Chen, Z. A. Nan, H. X. Lin, T. Wang, D. P. Zhan, J. W. Yan, B. W. Mao and Z. Q. Tian, *J. Am. Chem. Soc.*, 2017, **139**, 3320-3323.
 27. M. Becker, T. Klüner and M. Wark, *Dalt. Trans.*, 2017, **46**, 3500-3509.
 28. S. Han, P. Wang, J. Zhang, X. Liu, Z. Sun, X. Huang, L. Li, C. Ji, W. Zhang, B. Teng, W. Hu, M. Hong, J. Luo, *Laser Photonics Rev.* 2018, 1800060
 29. P. Gao, A. R. Bin Mohd Yusoff and M. K. Nazeeruddin, *Nat. Commun.*, 2018, **9**, 5028.
 30. P. S. Whitfield, N. Herron, W. E. Guise, K. Page, Y. Q. Cheng, I. Milas and M. K. Crawford, *Sci. Rep.* 2016, **6**, 35685.
 31. M. Li, T. Liu, Y. Wang, W. Yang and X. Lü, *Matter and Radiation at Extremes*, 2020, **5**.
 32. M. Szafranski and A. Katrusiak, *J. Phys. Chem. Lett.*, 2016, **7**, 3458-3466.
 33. L. Mao, C. C. Stoumpos and M. G. Kanatzidis, *J. Am. Chem. Soc.*, 2019, **141**, 1171-1190.

-
34. X. Li, W. Ke, B. Traore, P. Guo, I. Hadar, M. Kepenekian, J. Even, C. Katan, C. C. Stoumpos, R. D. Schaller and M. G. Kanatzidis, *J. Am. Chem. Soc.*, 2019, **141**, 12880-12890.
35. Y. H. Chang, J. C. Lin, Y. C. Chen, T. R. Kuo and D. Y. Wang, *Nanoscale Res. Lett.*, 2018, **13**, 247.
36. C. C. Stoumpos, D. H. Cao, D. J. Clark, J. Young, J. M. Rondinelli, J. I. Jang, J. T. Hupp and M. G. Kanatzidis, *Chem. Mater.*, 2016, **28**, 2852-2867.
37. J. M. Urban, G. Chehade, M. Dyksik, M. Menahem, A. Surrente, G. Trippe-Allard, D. K. Maude, D. Garrot, O. Yaffe, E. Deleporte, P. Plochocka and M. Baranowski, *J. Phys. Chem. Lett.*, 2020, **11**, 5830-5835.
38. M. Y. Leng, Z. W. Chen, Y. Yang, Z. Li, K. Zeng, K. H. Li, G. D. Niu, Y. S. He, Q. C. Zhou and J. Tang, *Angew. Chem. Int. Ed.*, 2016, **55**, 15012–15016.
39. F. Palazon, C. Urso, L. De Trizio, Q. Akkerman, S. Marras, F. Locardi, I. Nelli, M. Ferretti, M. Prato and L. Manna, *ACS Energy Lett.*, 2017, **2**, 2445-2448.
40. B.-W. Park, B. Philippe, X. L. Zhang, H. Rensmo, G. Boschloo and E. M. J. Johansson, *Adv. Mater.*, 2015, **27**, 6806-6813.
41. Y. Kim, C. Bae, H. S. Jung and H. Shin, *APL Materials*, 2019, **7**.
42. C. Zhou, H. Lin, S. Lee, M. Chaaban and B. Ma, *Materials Research Letters*, 2018, **6**, 552-569.
43. Z. Yuan, C. Zhou, Y. Tian, Y. Shu, J. Messier, J. C. Wang, L. J. van de Burgt, K. Kountouriotis, Y. Xin, E. Holt, K. Schanze, R. Clark, T. Siegrist and B. Ma, *Nat. Commun.*, 2017, **8**, 14051.
44. R. Jakubas, A. Ga Gor, M. J. Winiarski, M. Ptak, A. Piecha-Bisiorek and A. Cizman, *Inorg. Chem.*, 2020, **59**, 3417-3427.
45. Z. Qi, X. Fu, T. Yang, D. Li, P. Fan, H. Li, F. Jiang, L. Li, Z. Luo, X. Zhuang and A. Pan, *Nano Research*, 2019, **12**, 1894-1899.
46. C. Ran, Z. Wu, J. Xi, F. Yuan, H. Dong, T. Lei, X. He and X. Hou, *J. Phys. Chem. Lett.*, 2017, **8**, 394-400.
47. T. C. Sum, N. Mathews, G. Xing, S. S. Lim, W. K. Chong, D. Giovanni and H. A. Dewi, *Acc. Chem. Res.*, 2016, **49**, 294-302.
48. C. X. Sheng, C. Zhang, Y. X. Zhai, K. Mielczarek, W.W. Wang, W. L. Ma, A. Zakhidov, Z. V. Vardeny, *Phys. Rev. Lett.* 2015, **114**, 116601.

-
49. C. Wehrenfennig, G. E. Eperon, M. B. Johnston, H. J. Snaith, L. M. Herz, *Adv. Mater.* 2014, **26**, 1584–1589.
50. G. Xing, N. Mathews, S. S. Lim, N. Yantara, X. Liu, D. Sabba, M. Graetzl, S. Mhaisalkar, T. C. Sum, *Nat. Mater.* 2014, **13**, 476–480.
51. T. J. Savenije, C. S. Ponseca, L. Kunneman, M. Abdellah, K. B. Zheng, Y. X. Tian, Q. S. Zhu, S. E. Canton, I. G. Scheblykin, T. Pullerits, A. Yartsev, *J. Phys. Chem. Lett.*, 2014, **5**, 2189–2194.
52. V. I. Klimov, A. A. Mikhailovsky, D. W. McBranch, C. A. Leatherdale, M. G. Bawendi, *Science*, 2000, **287**, 1011–1013.
53. M. Saba, M. Cadelano, D. Marongiu, F. P. Chen, V. Sarritzu, N. Sestu, C. Figus, M. Aresti, R. Piras, A. G. Lehmann, C. Cannas, A. Musinu, F. Quochi, A. Mura, G. Bongiovanni, *Nat. Commun.*, 2014, **5**, 5049.
54. J. S. Manser, P. V. Kamat, *Nat. Photonics*, 2014, **8**, 737–743.
55. M. B. Price, J. Butkus, T. C. Jellicoe, A. Sadhanala, A. Briane, J. E. Halpert, K. Broch, J. M. Hodgkiss, R. H. Friend, F. Deschler, *Nat. Commun.* 2015, **6**, 8420.
56. G. C. Xing, N. Mathews, S. Y. Sun, S. S. Lim, Y. M. Lam, M. Gratzel, S. Mhaisalkar, T. C. Sum, *Science*, 2013, **342**, 344–347.
57. M. Baranowski and P. Plochocka, *Adv. Energy Mater.*, 2020, **10**.
58. A. M. Soufiani, F. Huang, P. Reece, R. Sheng, A. Ho-Baillie and M. A. Green, *Appl. Phys. Lett.*, 2015, **107**.
59. J. C. Blancon, A. V. Stier, H. Tsai, W. Nie, C. C. Stoumpos, B. Traore, L. Pedesseau, M. Kepenekian, F. Katsutani, G. T. Noe, J. Kono, S. Tretiak, S. A. Crooker, C. Katan, M. G. Kanatzidis, J. J. Crochet, J. Even, A. D. Mohite, *Nat. Commun.* 2018, **9**, 2254.
60. P. Y. Yu, C. Manuel, *Springer, New Delhi* 2007.
- 61 V. D’Innocenzo, G. Grancini, M. J. P. Alcocer, A. R. S. Kandada, S. D. Stranks, M. M. Lee, G. Lanzani, H. J. Snaith and A. Petrozza, *Nat. Commun.*, 2014, **5**, 3586.
62. R. Elliott, *Phys. Rev.* 1957, **108**, 1384.

-
63. S. Sun, T. Salim, N. Mathews, M. Duchamp, C. Boothroyd, G. Xing, T. C. Sum, Y. M. Lam, *Energy Environ. Sci.* 2014, **7**, 399.
64. K. Wu, A. Bera, C. Ma, Y. Du, Y. Yang, L. Li, T. Wu, *Phys. Chem. Chem. Phys.* 2014, **16**, 22476.
65. D. A. Valverde-Chávez, C. S. Ponseca, C. C. Stoumpos, A. Yartsev, M. G. Kanatzidis, V. Sundström, D. G. Cooke, *Energy Environ. Sci.*, 2015, **8**, 3700.
66. S. Singh, C. Li, F. Panzer, K. L. Narasimhan, A. Graeser, T. P. Gujar, A. Köhler, M. Thelakkat, S. Huettner, D. Kabra, *J. Phys. Chem. Lett.*, 2016, **7**, 3014.
67. J. Even, L. Pedesseau, C. Katan, *J. Phys. Chem. C*, 2014, **118**, 11566.
68. Y. Yang, Y. Yan, M. Yang, S. Choi, K. Zhu, J. M. Luther, M. C. Beard, *Nat. Commun.*, **2015**, **6**, 1.
69. Y. Yang, D. P. Ostrowski, R. M. France, K. Zhu, J. Van De Lagemaat, J. M. Luther, M. C. Beard, *Nat. Photonics*, 2016, **10**, 53.
70. Y. Yamada, T. Nakamura, M. Endo, A. Wakamiya, Y. Kanemitsu, *IEEE J. Photovoltaics*, 2015, **5**, 401.
71. F. Ruf, M. F. Aygüler, N. Giesbrecht, B. Rendenbach, A. Magin, P. Docampo, H. Kalt, M. Hetterich, *APL Mater.*, 2019, **7**, 031113.
72. A. M. Soufiani, F. Huang, P. Reece, R. Sheng, A. Ho-Baillie, M. A. Green, *Appl. Phys. Lett.*, 2015, **107**, 231902
73. T. J. Savenije, C. S. Ponseca Jr., L. Kunneman, M. Abdellah, K. Zheng, Y. Tian, Q. Zhu, S. E. Canton, I. G. Scheblykin, T. Pullerits, A. Yartsev, V. Sundstrom, *J. Phys. Chem. Lett.*, 2014, **5**, 2189.
74. K. Zheng, Q. Zhu, M. Abdellah, M. E. Messing, W. Zhang, A. Generalov, Y. Niu, L. Ribaud, S. E. Canton, T. Pullerits, *J. Phys. Chem. Lett.*, 2015, **6**, 2969.
75. W. Zhang, M. Saliba, S. D. Stranks, Y. Sun, X. Shi, U. Wiesner, H. J. Snaith, *Nano Lett.*, 2013, **13**, 4505.
76. S. Li, J. Luo, J. Liu and J. Tang, *J. Phys. Chem. Lett.*, 2019, **10**, 1999-2007.

-
77. R. T. Williams, K. S. Song, W. L. Faust, C. H. Leung, *Phys. Rev. B: Condens. Matter Mater. Phys.*, 1986, **33**, 7232–7240.
78. W. B. Fowler, M. J. Marrone, M. N. Kabler, *Phys. Rev. B*, 1973, **8**, 5909–5919.
79. R. T. Williams, K. S. Song, W. L. Faust, C. H. Leung, *Rev. B: Condens. Matter Mater. Phys.*, 1986, **33**, 7232–7240.
80. M. D. Smith and H. I. Karunadasa, *Acc. Chem. Res.*, 2018, **51**, 619–627.
81. J. Li, H. Wang and D. Li, *Front. Optoelectronics*, 2020, **13**, 225–234.
82. X. Wu, M. T. Trinh, D. Niesner, H. Zhu, Z. Norman, J. S. Owen, O. Yaffe, B. J. Kudisch, X. Y. Zhu, *J. Am. Chem. Soc.*, 2015, **137**, 2089–2096.
83. R. T. Williams, K. S. Song, *J. Phys. Chem. Soli.*, 1990, **51**, 679–716.
84. M. B. Johnston, L. M. Herz, *Acc. Chem. Res.* 2016, **49**, 146–154.
85. X.-Y. Zhu, V. J. Podzorov, *Phys. Chem. Lett.* 2015, **6**, 4758–4761.
86. P. Y. Yu, M. Cardona, *Fundamentals of Semiconductors, Graduate Texts in Physics* (Springer-Verlag) 2010.
87. Y. Yang, D. P. Ostrowski, R. M. France, K. Zhu, J. van de Lagemaat, J. M. Luther, M. C. Beard, *Nature Photon.* 2015, **10**, 53–59.
88. A. D. Wright, C. Verdi, R. L. Milot, G. E. Eperon, M. A. Perez-Osorio, H. J. Snaith, F. Giustino, M. B. Johnston and L. M. Herz, *Nat. Commun.*, 2016, **7**, 11755.
89. H. Jin, E. Debroye, M. Keshavarz, I. G. Scheblykin, M. B. J. Roeflaers, J. Hofkens and J. A. Steele, *Mater. Hor.*, 2020, **7**, 397–410.
90. S. Rudin, T. L. Reinecke, and B. Segall, *Phys. Rev. B*, 1990, **42**, 11218–11231.
91. J. Lee, E. S. Koteles and M. O. Vassell, *Phys. Rev. B*, 1986, **33**, 5512–5516
92. K. Zheng, K. Židek, M. Abdellah, M. E. Messing, M. J. Al-Marri and T. Pullerits, *J. Phys. Chem. C*, 2016, **120**, 3077–3084.
93. S. D. Stranks, V. M. Burlakov, T. Leijtens, J. M. Ball, A. Goriely and H. J. Snaith, *Physical Review Applied*, 2014, **2**.

-
94. V. D'Innocenzo, G. Grancini, M. J. Alcocer, A. R. Kandada, S. D. Stranks, M. M. Lee, G. Lanzani, H. J. Snaith, and A. Petrozza, *Nat. Commun.*, 2014, **5**, 3586.
95. J. Szczytko, L. Kappei, J. Berney, F. Morier-Genoud, M. T. Portella-Oberli, and B. Deveaud, *Phys. Rev. Lett.*, 2004, **93**, 137401.
96. L. Merrill and W. A. Bassett, *Review of Scientific Instruments*, 1974, **45**, 290-294.
97. R. M. Suter, D. Hennessy, C. Xiao and U. Lienert, *Review of Scientific Instruments*, 2006, **77**.
98. I. C. Noyan and J. B. Cohen, *Springer-Verlag, New York Inc.*, 1987.
99. M. E. Fitzpatrick, A.T. Fry, P. Holdway, F. A. Kandil, J. Shackleton, and L. Suominen, *Measurement Good Practice Guide*, 2005, **2**, 52.
100. R. H. Blessing, *Acta Crystallogr. Sect. A*, 1995, **51**, 33–38.
101. G. M. Sheldrick, *Acta Crystallographica Section A: Foundations of Crystallography*. International Union of Crystallography January 1, 2008, 112–122.
102. A. L. Spek, *J. Appl. Crystallogr.* 2003, **36**, 7-13.
103. D. F. Swinehart, *J. Chem. Educ.*, 1962, **39**, 333.
104. P. R. Jubu, F. K. Yam, V. M. Igba and K. P. Beh, *J. Solid State Chem.*, 2020, **290**.
105. L. M. Hirvonen and K. Suhling, *Measurement Science and Technology*, 2017, **28**.
106. J. R. Lakowicz, "Principles of Fluorescence Spectroscopy", 3rd Edition, Springer Science Business Media, New York, 2006.
107. D. V. O. Connor, D. Phillips, Academic Press, London, 1984.
108. M. Wahl, Rudower Chaussee 29, 12489 Berlin, Germany, 2017.
109. M. P. Seah and W. A. Dench, *Surface and interface analysis*, 1979, **1**, 1.
110. P. Andrew and M. A. Peter, *Sherwood Anal. Chem.* 1982, **54**, 13-19.
111. L. H. Yahia, L. K. Mireles, In *Characterization of Ploymeric Biomaterials*, 2017, 83-97.
112. Schematic for scanning electron microscopy column, 2003, <http://www-archive.mse.iastate.edu/microscopy/path2.html>

-
113. F.-Y. Zhu, Q.-Q. Wang, X.-S. Zhang, W. Hu, X. Zhao, H.-X. Zhang, *Nanotechnology*, 2014, **25**, 185705.
114. R. W. Carpick, *Chem. Rev.* 1997, **97**, 1163-1194.
115. Y. Fu, X. Jiang, X. Li, B. Traore, I. Spanopoulos, C. Katan, J. Even, M. G. Kanatzidis and E. Harel, *J. Am. Chem. Soc.*, 2020, **142**, 4008-4021.
116. <https://pubchem.ncbi.nlm.nih.gov/compound/gamma-Butyrolactone#section=1D-NMRSpectra>.
117. M. Petrova, R. Muhamadejev, B. Vigante, G. Duburs, E. Liepinsh, *R. Soc. Open Sci.* 2018, **5**, 180088.
118. J. X. Ding, S. J. Du, Z. Y. Zuo, Y. Zhao, H. Z. Cui, X. Y. Zhan, *J. Phys. Chem. C*, 2017, **121**, 4917-4923.
119. C. X. Bao, Z. L. Chen, Y. J. Fang, H. T. Wei, Y. H. Deng, X. Xiao, L. L. Li, J. S. Huang, *Adv. Mater.*, 2017, **29**, 1703209.
120. Y. S. Wang, Y. P. Zhang, Y. Lu, W. D. Xu, H. R. Mu, C. Y. Chen, H. Qiao, J. C. Song, S. J. Li, B. Q. Sun, Y. -B. Cheng, Q. L. Bao, *Adv. Optical Mater.*, 2015, **3**, 1389-1396.
121. L. P. Kong, G. Liu, J. Gong, Q. Y. Hu, R. D. Schaller, P. Dera, D. Z. Zhang, Z. X. Liu, W. G. Yang, K. Zhu, Y. Z. Tang, C. Y. Wang, S. H. Wei, T. Xu, *PNAS*, 2016, **113**, 8910-8915.
122. B. Yang, F. Y. Zhang, J. S. Chen, S. Q. Yang, X. S. Xia, T. Pullerits, W. Q. Deng, K. L. Han, *Adv. Mater.*, 2017, **29**, 1703758.
123. Y. Y. Tang, X. Y. Cao, A. Honarfar, M. Abdellah, C. Y. Chen, J. Avila, M. C. Asensio, L. Hammarström, J. Sa, S. E. Canton, K. B. Zheng, T. Pullerits, Q. J. Chi, *ACS Appl. Mater. Interfaces*, 2018, **10**, 29574-29582.
124. M. W. Lufaso and P. M. Woodward, *Acta Crystallogr. Sect. B Struct. Sci.*, 2004, **60**, 10-20.
125. S. Alvarez, *Chem. Rev.*, 2015, **115**, 13447-13483.
126. D. B. Straus, S. Hurtado Parra, N. Iotov, J. Gebhardt, A. M. Rappe, J. E. Subotnik, J. M. Kikkawa and C. R. Kagan, *J. Am. Chem. Soc.*, 2016, **138**, 13798-13801.
127. A. R. Srimath Kandada and C. Silva, *J. Phys. Chem. Lett.*, 2020, **11**, 3173-3184.
128. Z. Guo, X. Wu, T. Zhu, X. Zhu and L. Huang, *ACS Nano*, 2016, **10**, 9992-9998.

-
129. S. Kahmann, E. K. Tekelenburg, H. Duim, M. E. Kamminga and M. A. Loi, *Nat. Commun.*, 2020, **11**, 2344.
130. J.-C. Blancon, H. Tsai, W. Nie, C. C. Stoumpos, L. Pedesseau, C. Katan, M. Kepenekian, C. M. M. Soe, K. Appavoo, M. Y. Sfeir, S. Tretiak, P. M. Ajayan, M. G. Kanatzidis, J. Even, J. J. Crochet, A. D. Mohite, *Science*, 2017, **355**, 1288–1292.
131. M. Kepenekian, B. Traore, J. C. Blancon, L. Pedesseau, H. Tsai, W. Nie, C. C. Stoumpos, M. G. Kanatzidis, J. Even, A. D. Mohite, S. Tretiak and C. Katan, *Nano Lett.*, 2018, **18**, 5603–5609.
132. K. Miyata, D. Meggiolaro, M. T. Trinh, P. P. Joshi, E. Mosconi, S. C. Jones, F.; D. Angelis, X.-Y. Zhu, *Sci. Adv.*, 2017, **3**, e1701217.
133. M. Seitz, A. J. Magdaleno, N. Alcazar-Cano, M. Melendez, T. J. Lubbers, S. W. Walraven, S. Pakdel, E. Prada, R. Delgado-Buscalioni and F. Prins, *Nat. Commun.*, 2020, **11**, 2035.
134. L. A. R. Junior, L. L. Castro, L. E. Sousa, G. M. Silva and P. H. O. Neto, *Chem. Phys. Lett.*, 2019, **716**, 162–166.
135. R. Coehoorn, L. Zhang, P. A. Bobbert and H. van Eersel, *Phys. Rev. B*, 2017, **95**.
136. N. J. Jeon, J. H. Noh, W. S. Yang, Y. C. Kim, S. Ryu, J. Seo and S. I. Seok, *Nature*, 2015, **517**, 476–480.
137. N. J. Jeon, H. Na, E. H. Jung, T.-Y. Yang, Y. G. Lee, G. Kim, H.-W. Shin, S. Il Seok, J. Lee and J. Seo, *Nat. Energy*, 2018, **3**, 682–689.
138. T. Leijtens, R. Prasanna, A. Gold-Parker, M. F. Toney and M. D. McGehee, *ACS Energy Lett.*, 2017, **2**, 2159–2165.
139. T.-B. Song, T. Yokoyama, S. Aramaki and M. G. Kanatzidis, *ACS Energy Lett.*, 2017, **4**, 897–903.
140. C. C. Stoumpos, L. Frazer, D. J. Clark, Y. S. Kim, S. H. Rhim, A. J. Freeman, J. B. Ketterson, J. I. Jang and M. G. Kanatzidis, *J. Am. Chem. Soc.*, 2015, **137**, 6804–6819.

Publications

Paper I

Photodetector Based on Spontaneously Grown Strongly Coupled MAPbBr₃ /N-rGO Hybrids Showing Enhanced Performance

Paper II

Electronic Structure and Trap-States of Two-Dimensional Ruddlesden-Popper Perovskites with Relaxed Goldschmidt Tolerance Factor

Paper III

Free excitons versus self-trapped excitons at different facets of Ruddlesden Popper two-dimensional lead halide perovskite single crystals

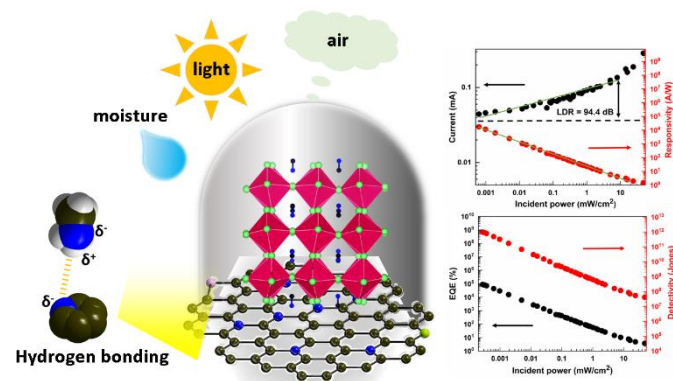
Paper IV

Lead-free double halide perovskite Cs₃BiBr₆ with well-defined crystal structure and high thermal stability for optoelectronics

Papers

Paper I

Photodetector Based on Spontaneously Grown Strongly Coupled MAPbBr₃/N-rGO Hybrids Showing an Enhanced Performance



Photodetector Based on Spontaneously Grown Strongly Coupled MAPbBr₃/N-rGO Hybrids Showing Enhanced Performance

Yingying Tang,[†] Mingli Liang,[†] MinWei Zhang,[†] Alireza Honarfar,^{‡,§} Xianshao Zou,[‡] Mohamed Abdellah,^{‡,§} Tõnu Pullerits,[‡] Kaibo Zheng,^{*,†,‡,§} and Qijin Chi^{*,†,§}

[†]Department of Chemistry, Technical University of Denmark, DK-2800 Kongens Lyngby, Denmark

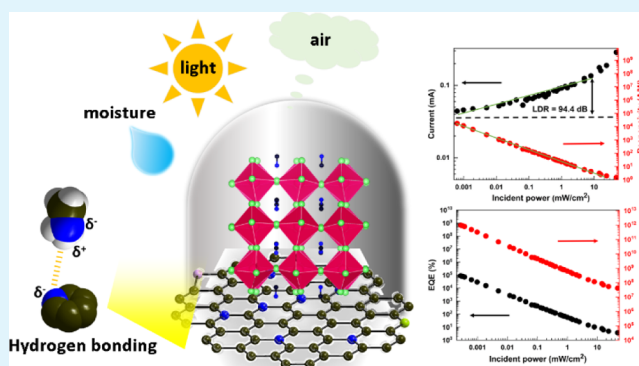
[‡]Department of Chemical Physics and NanoLund, Lund University, Box 124, 22100 Lund, Sweden

[§]Department of Chemistry, Qena Faculty of Science, South Valley University, 83523 Qena, Egypt

Supporting Information

ABSTRACT: Recently, metal-halide perovskites have emerged as a candidate for optoelectronic applications such as photodetectors. However, the poor device performance and instability have limited their future commercialization. Herein, we report the spontaneous growth of perovskite/N-rGO hybrid structures using a facile solution method and their applications for photodetectors. In the hybrid structures, perovskites were homogeneously wrapped by N-rGO sheets through strong hydrogen bonding. The strongly coupled N-rGOs facilitate the charge carrier transportation across the perovskite crystals but also distort the surface lattice of the perovskite creating a potential barrier for charge transfer. We optimize the addition of N-rGO in the hybrid structures to balance interfacial structural distortion and the intercrystal conductivity. High-performance photodetection up to 3×10^4 A/W, external quantum efficiency exceeding 10⁵%, and detectivity up to 10¹² Jones were achieved in the optimal device with the weight ratio between perovskites and N-rGO to be 8:1.5. The underlying mechanism behind the optimal N-rGO addition ratio in the hybrids has also been rationalized via time-resolved spectroscopic studies as a reference for future applications.

KEYWORDS: photodetector, hybrid material, perovskite/N-rGO, hydrogen bonding, time-resolved spectroscopy



INTRODUCTION

Photodetectors are essential in daily life as well as in defence and aerospace applications. In general, good photodetectors should feature high responsivity, detectivity, and quantum efficiency.^{1–6} For example, photodetectors with broad spectral response from UV to infrared can be used in optical imaging, communication, and so forth, while narrow spectral response photodetectors are necessary in biological detection, environment surveillance, and so forth.^{7–9} Metal-halide perovskites have recently emerged at the forefront of light absorber materials because of their tunable optical band gap, large diffusion length, long carrier lifetime, and so forth, showing great potential as building blocks for efficient photodetectors.^{10–15} However, seeking for the suitable charge carrier acceptors for efficient carrier transportation, tuning spectral response, and high stability remains a daunting task restricting the device performance.^{16,17} To obtain a solar-blind UV and visible light photodetector, a fluorine polymer was applied as a protection layer, reaching 7.8 A/W for UV light detection.¹⁸ Polyvinyl pyrrolidone (PVP) modification was processed on the perovskite films, showing a wide spectral response from 405 to 808 nm.¹⁹ Other acceptors like conductive metal

oxides²⁰ or low-dimensional semiconductor materials such as MoS₂ and WS₂ suffer from either the inevitable interfacial structural defects, low conductivity, or ambient instability.^{21,22}

Graphene-based materials have long been considered as very promising charge carrier transporters with outstanding chemical stability and high electric conductivity.^{23–27} Recent reports confirmed that integrating graphene or chemically prepared reduced graphene oxide (rGO) into perovskites did help improve the detectivity and stability of the photodetectors.^{28–30} However, the weak van der Waals bonds between perovskites and graphene would create undesirable interfacial defects with reduced electronic coupling, which consequently inhibit the interfacial charge transfer efficiency. The problem is expected to be mitigated by doping nitrogen in graphene oxide (N-rGO) to create more active sites for better chemical anchoring and electronic coupling. The strategy has previously been successfully used in solar cell devices.^{31–35}

Received: October 17, 2019

Accepted: December 10, 2019

Published: December 10, 2019

Here, we demonstrate that N-doped rGO can also serve as a perfect acceptor in photodetector configuration. We spontaneously form MAPbBr₃/N-rGO (MA = methylammonium) hybrid composites via a facile solution method. The anchoring between N-rGO and perovskites is strengthened via hydrogen bonding with nitrogen activated sites on the N-rGO incorporation into metal halide perovskites lattice instead of simple van der Waals bonding. This regulates the N-rGO/perovskite interface and also reduces the surface defects of perovskites. Consequently, efficient charge transfer between N-rGO and perovskites can be seen by time-resolved spectroscopy. Photodetectors are then fabricated based on such MAPbBr₃/N-rGO hybrid composites, where the partition between the N-rGO and perovskites in the hybrid structure has been optimized. We observed the lattice distortion of perovskites induced by the integration of strongly-coupled N-rGO creating potential barrier for interfacial charge transfer. The optimal ratio between MAPbBr₃ and N-rGO addition was obtained to be 8:1.5 (wt %), which balances the structural distortion and the intercrystal conductivity to generate the highest photocurrent. The optimized device exhibited a high responsivity of 3×10^4 A/W, external quantum efficiency (EQE) of 10⁵%, and detectivity up to 10¹² Jones.

MATERIAL AND METHODS

All the chemical reagents were of analytical grade as received without further purification. Lead (II) bromide (PbBr₂, 99%), methylamine (CH₃NH₂, 33 wt %), and hydrobromic acid (HBr, ≥ 48%) were purchased from Sigma-Aldrich. γ -Butyrolactone was purchased from LiChrosolv. Diethyl ether (≥99.9%) and ethanol (99.96%) were purchased from AnalaR NORMAPURACS.

Preparation of N-rGO. A mixture of lysine and graphene oxide in a molar ratio of 1:1 was added into an autoclave, which was put into an oven at 160 °C for 6 h for the hydrothermal treatment. The reaction mixture was taken out and cooled down to room temperature. The as-synthesized products were washed with Milli-Q water three times to remove unreacted reagents. The N-rGO was freeze-dried under vacuum and grounded in ball mill for use. The N-rGO displays sheet-like morphology (Figure S1a), and in the X-ray powder diffraction (XRD) pattern (Figure S1b), two strong and broad characteristic peaks can be observed at 26.1 and 43.3° arising from the (002) and (100) planes of graphene sheets, respectively. Then 3 mg/mL N-rGO in γ -butyrolactone was prepared for use.

Preparation of MABr. Methylamine (20 mL) and hydrobromic acid (25 mL) were mixed in a 250 mL round-bottom flask. Before stirring for 2 h at 0 °C (ice-water bath), absolute ethanol (50 mL) was added to the mixture. The resulting solution was evaporated at 40 °C via rotary evaporation. After that, the white precipitate of MABr was obtained by washing the oil-like solution three times with diethyl ether. The product was dissolved in ethanol and recrystallized from diethyl ether. Finally, the purified MABr crystals were dried under vacuum at room temperature for 48 h.

Preparation of MAPbBr₃/N-rGO. The formation process of hybrid MAPbBr₃/N-rGO materials is displayed in Figure S2. MABr was first added into 3 mg/mL N-rGO in 2 mL of γ -butyrolactone and ultrasonicated for 5 min. Then, it was heated under 60 °C for 5 min. PbBr₂ was added into above solution with stirring for 10 min under 60 °C. Therefore, a series of MAPbBr₃/N-rGO with mass ratios of 8:0.25, 8:0.5, 8:1, 8:1.5, and 8:2 were obtained. For the preparation of pure MAPbBr₃, 3 mg/mL N-rGO solution in γ -butyrolactone was replaced by γ -butyrolactone. Additionally, we also investigated different kinds of graphene materials, as shown in Figure S3.

Fabrication of the Photodetector. Prototype optoelectronic devices were prepared in-house. ITO electrodes were prepared by the ultrasonic cleaning in acetone, ethanol, and Milli-Q water, each for 15 min successfully. Then, ITO electrodes were treated by ozone for 20 min. A certain amount of MAPbBr₃/N-rGO solution (containing 0.6

mg MAPbBr₃), pure N-rGO (containing 0.6 mg N-rGO), and pure MAPbBr₃ (containing 0.6 mg MAPbBr₃) was deposited on the device surface by drop-casting, which form uniform ultrathin films, followed by annealing at 70 °C. All the photoelectrochemical characterizations were performed on the Autolab workstation in a two-electrode configuration. All measurements were conducted by illuminating the backside of the electrodes.

Scanning electron microscope (SEM) characterizations were carried out on FEI Quanta FEG 200 ESEM. Also, energy dispersive X-ray spectroscopy (EDX) measurements were performed on Inspec S. Al foils and PELCO Tabs™ carbon conductive tabs were used as substrates in SEM tests. The phases and purities of all samples were also characterized by XRD with Cu K α_1 ($\lambda = 1.5406$ Å) radiation. X-ray photoelectron spectroscopy (XPS) (Thermo Scientific) was performed to analyze the compositions of samples, with Al K α (1486 eV) as the excitation X-ray source. The pressure of the analysis chamber was maintained at 2×10^{-10} mbar during measurements. For sample preparation of time-resolved infrared spectroscopy (TRIR), microcrystals (MCs) were diluted with KBr, and were pelleted. The distance between the light source and the sample was held constant (25 cm). All characterizations were carried out at room temperature. Photoluminescence (PL) spectra were scanned on a photoluminescence spectrometer (FLS980, Edinburgh Instruments Ltd.) from 380 to 900 nm with 1 nm increments and 1 s integration time, under an excitation wavelength of 360 nm. Transient absorption experiments were performed by using a femtosecond pump probe setup. Laser pulses (800 nm, 80 fs pulse length, 1 kHz repetition rate) were generated by using a regenerative amplifier (Spitfire XP Pro) seeded by using a femtosecond oscillator (Mai Tai SP, both Spectra Physics). The pump pulses at 350 nm were generated by using an optical parametric amplifier (Topas, Light Conversion). The used excitation photon fluxes are 3×10^{12} photons/cm²/pulse. For the probe, we used the supercontinuum generation from a thin CaF₂ plate. For the ultrafast transient mid-IR absorption spectroscopy, the 1 mJ, 45 fs output of a 1 kHz Ti:Sapphire amplifier (Spitfire Pro, Spectra-Physics) was split into two separate commercial optical parametric amplifiers (TOPAS-C, Light Conversion), which generate the visible pump 410 nm and the mid-IR probe (1850–2200 cm⁻¹) pulses. Prior to reaching the sample, the probe beam was split into equal intensity probe and reference beams using a wedged ZnSe window. All beams are focused with a single $f = 10$ cm off axis parabolic mirror to a ~ 70 μ m spot size in the sample. The pump intensity changed on the sample via density filter. The probe and reference beams were dispersed by using a commercial monochromator (Triax 190, HORIBA Jobin Yvon) equipped with a 75 groove/mm grating and detected on a dual array, 2×64 pixel mercury cadmium telluride detector (InfraRed Associated, Inc). The instrument response function for the experiments was approximately 100 fs. The sample was mounted in a Harrick flow cell. Fourier-transform infrared spectroscopy (FTIR) imaging was also conducted in the same set up with TRIR. Solid-state ¹H nuclear magnetic resonance (NMR) was performed on Ascend 600 installed with the CP-MAS solid-state probe. The chemical shifts are relative to TMS (0 ppm) using a secondary reference of neat adamantane (1.91 ppm). The magnetic field is 14.1 T with $\nu_L(1H) = 600.165$ MHz. Each spectrum consists of 32 transient scans with an interscan delay of 10 s.

RESULTS AND DISCUSSION

Here, hybrid MAPbBr₃/N-rGO composites have been prepared by a facile solution method (Figure S2). N-rGO nanosheets are initially dispersed into γ -butyrolactone via stirring and ultrasonication. MABr was then added into the N-rGO solution followed by the addition of PbBr₂ solution with the creation of the N-rGO sheets wrapped MAPbBr₃ MCs. On the contrast, such method is not applicable for GO and histidine-rGO where their coverage on perovskites is negligible (Figure S3). The possible interpretation could be the MA⁺ ion has already interacted with the N-rGO via hydrogen bonding

N–H...N in the MABr/N-rGO precursor solution.^{36,37} Consequently, MAPbBr₃ should be initiated via the formation of small perovskite seeds weakly coupled with the N-rGO sheets after Pb²⁺ ions have been introduced. The crystallization of the MAPbBr₃ perovskite was facilitated by the following annealing process.^{38,39} The morphology and size of the as-synthesized hybrid N-rGO/perovskites were characterized by SEM with elemental composition mapped by energy-dispersive EDX, as shown in Figure 1.

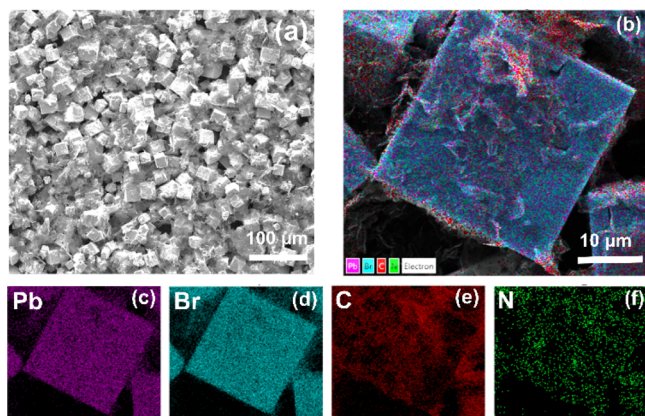


Figure 1. (a) SEM characterization of MAPbBr₃/N-rGO hybrid composite with a typical weight ratio between MAPbBr₃ and N-rGO. (b–f) EDX elemental mapping of the corresponding (c) Pb, (d) Br, (e) C, and (f) N, respectively.

The N-rGO/perovskite hybrids exhibit homogenous integration of N-rGO on MAPbBr₃ cubic MCs networks as displayed in Figures 1a and S4. The mean size of the MCs (10–20 μm) is much uniform than the pristine MAPbBr₃ MCs (5–25 μm, Figure S5), indicating the hindering of crystal growth by graphene coating. The EDX mapping (Figure 1b–f) visualize the composite of MAPbBr₃ and N-rGO with even

distribution of Pb and Br elements over the MCs (Figure 1c,d). C and N elements reside both at the surface of the MAPbBr₃ MCs and the interspaces among the crystals (Figure 1e,f), which demonstrate the interconnection among MAPbBr₃ MCs via N-rGOs.

In order to further characterize the influence of N-rGO addition on the perovskites' formation, we first compare the crystal structures between MAPbBr₃ with and without N-rGO using XRD. As shown in Figure 2a, the diffraction peaks at $2\theta = 14.9, 21.1, 30.1, 33.7, 37.1, 43.1, 45.8, 48.5, 53.5, 55.8,$ and 58.1° correspond to the diffraction from (001), (110), (002), (210), (211), (220), (003), (310), (222), (320), and (321) planes of MAPbBr₃ (space group $Pm\bar{3}m$), respectively. From the Figure 2b, we could clearly observe the main diffraction peak of MAPbBr₃ corresponding to (001) crystalline plane shifts from 14.951° toward the smaller diffraction angle of 14.937° after coating with N-rGO, indicating lattice expansion. Other diffraction peaks such as (110), (210), and (002) are displayed in Figure S6, where blue shift of the XRD peaks could also be observed. Meanwhile, for different ratios of the hybrids, XRD spectra display blue shift compared to MAPbBr₃. The Rietveld refinement results further confirm the lattice constant increase from 5.9204 to 5.9259 Å with N-rGO coating as shown in Figure 2c,d.

The electronic structures of MAPbBr₃ with and without N-rGO are also probed by XPS, as shown in Figure 3a. In N-rGO (Figure 3b), N 1s spectra at 399, 400.1, and 401.5 eV, originate from pyridinic N, pyrrolic N, and graphitic N, respectively.¹¹ As shown in Figures 3c and S7–13, the N 1s core level spectrum in MAPbBr₃ at 402.28 eV is assigned to N atoms in MA⁺ ions of the perovskite. The XPS spectra of N-rGO/perovskite are shown in Figure 3d. The peak at 402.5 eV is almost identical from MA ions in pure perovskite, but peaks at 399.5, 400.8, and 401.8 eV from pyridinic N, pyrrolic N, and graphitic N are all slightly shifted to higher binding energy compared with pure perovskite, as summarized in Table S1. This indicates the modified charge transfer degree for those N

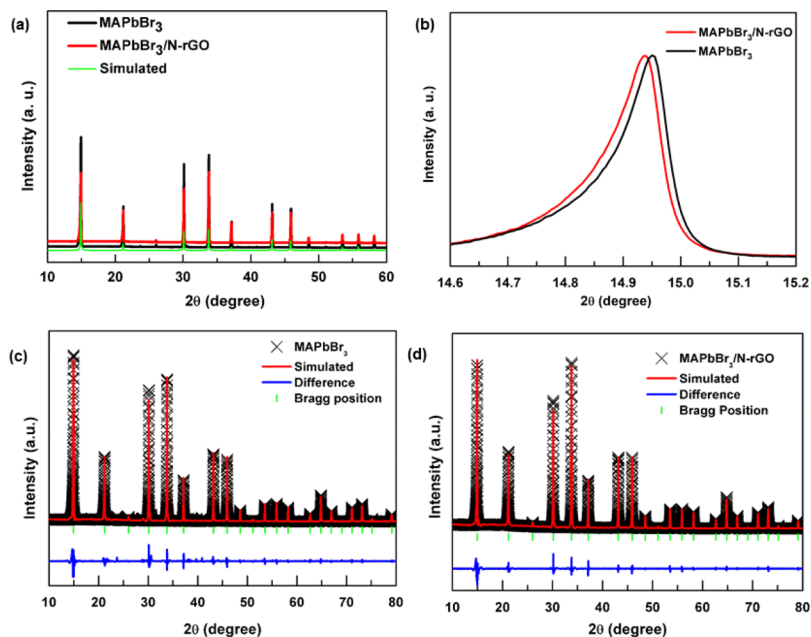


Figure 2. XRD patterns of (a) MAPbBr₃ and MAPbBr₃/N-rGO, and the reference sample of cubic MAPbBr₃ (ICSD, #252415). (b) Magnified XRD spectra. (c,d) Refinement of the pure perovskite and the hybrid material.

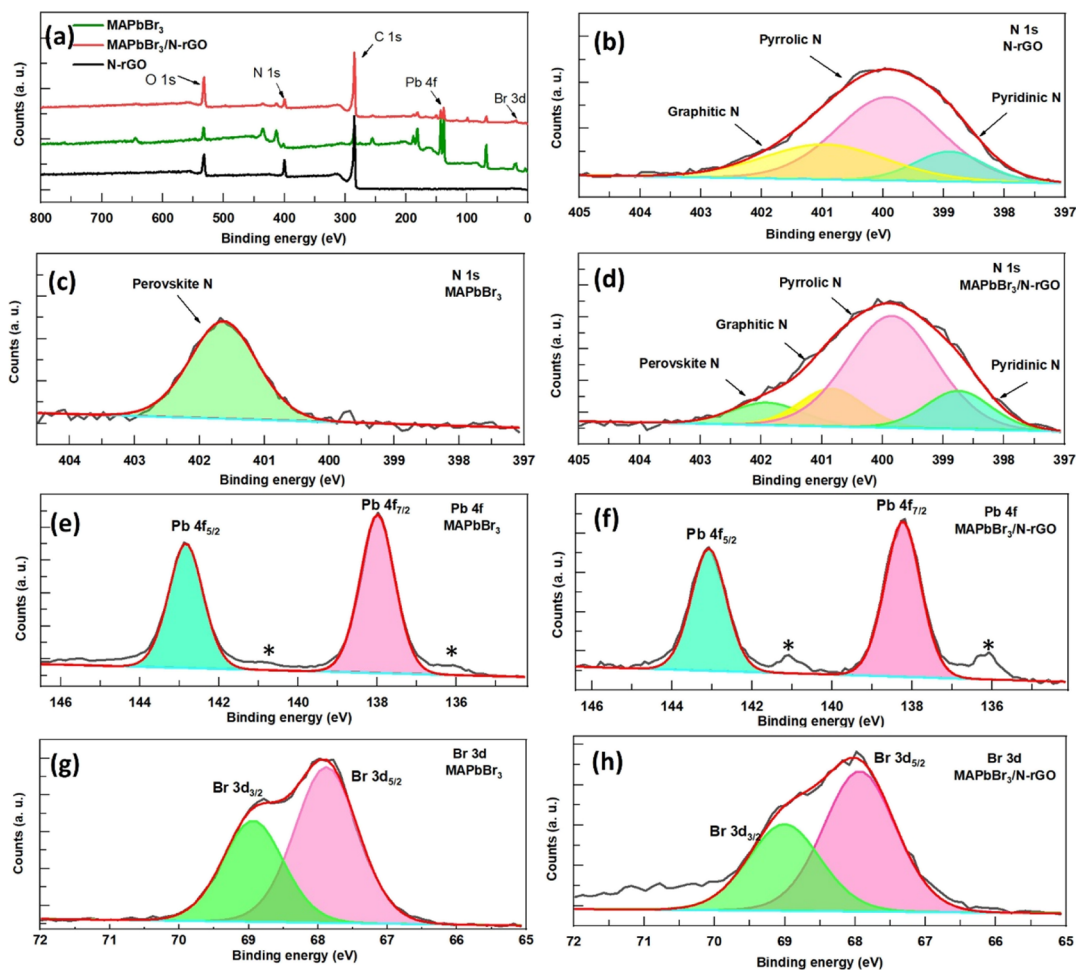


Figure 3. XPS characteristics: (a) survey spectra; (b) N 1s spectra for N-rGO; (c) N 1s, (e) Pb 4f, (g) Br 3d spectra for MAPbBr₃; (d) N 1s, (f) Pb 4f, (h) Br 3d spectra for MAPbBr₃/N-rGO. Star characteristics in the Pb 4f core-level in (e,f) represent Pb²⁺ satellite peaks.

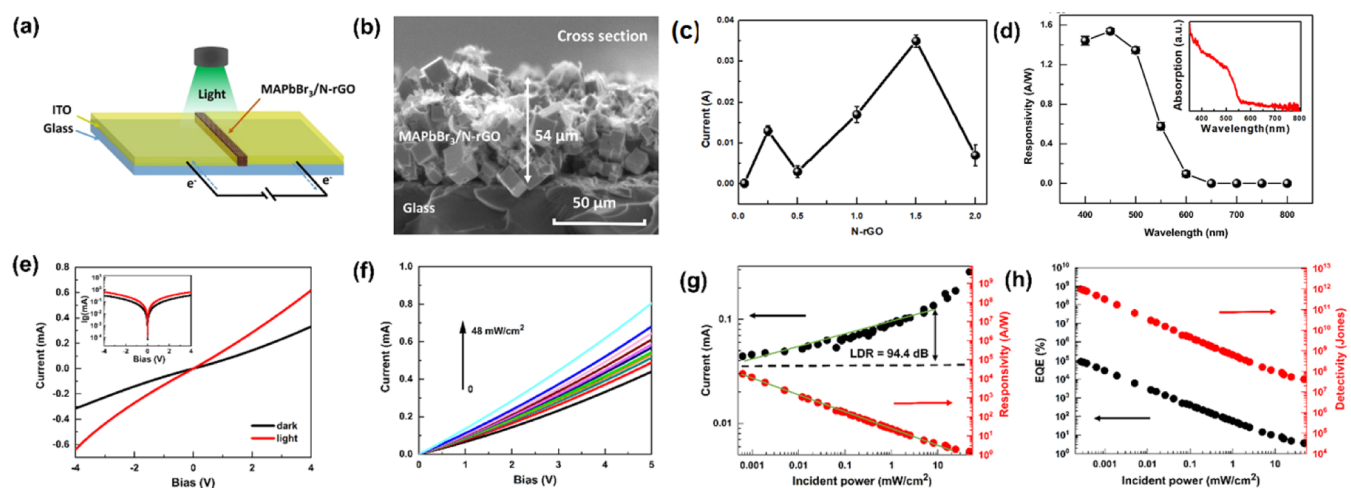


Figure 4. (a) Schematic illustration of the photodetector device with the gap between two ITO plates to be 40 μm . (b) Cross-sectional SEM image of the photodetector. (c) Photocurrent of different ratios of perovskite and N-rGO under white light, 58.6 mW/cm^2 . (d) Wavelength-dependent photocurrent responsivity of MAPbBr₃/N-rGO hybrids at bias of 4 V. Inset: the absorption for the MAPbBr₃/N-rGO. (e–h) Photoresponse of MAPbBr₃/N-rGO in photodetector based on ITO/glass at wavelength of 500 nm. (e) Photocurrent under dark and light. (f) I – V characteristics under light illumination with different power density. (g) Photocurrent and responsivity vs incident power under 4 V bias. (h) EQE and detectivity vs incident power under bias of 4 V.

atoms induced by the hydrogen bond formation to halide ions in perovskites.⁴⁰

Both Pb 4f peaks and Br 3d peaks of MAPbBr₃/N-rGO hybrid composite display a blue shift compared with those of the neat perovskites, indicating the strengthened Pb–Br

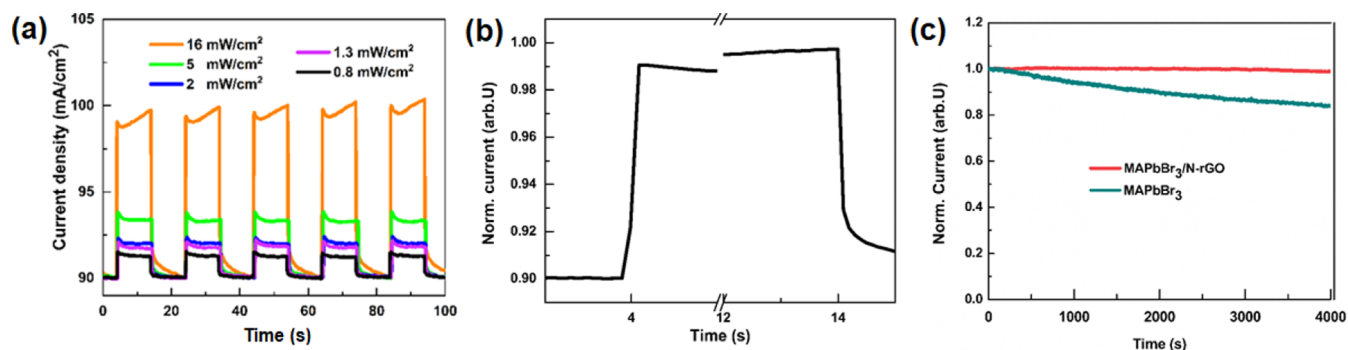


Figure 5. Periodic photoresponse behavior of MAPbBr₃/N-rGO under a strong power density of 500 nm wavelength light: (a) photocurrent under various of voltage and light intensity. (b) Normalized high-resolution photoresponse for rise and decay time. (c) Stability of the photodetector based on pure perovskite and hybrid materials at room temperature under moisture of 60%.

interaction (Figure 3e–h). This also confirms the lattice distortion after introduction of N-rGO leading to the bonding rearrangement (Tables S2 and S3).⁴¹ It is not possible to form other types of interaction such as chemical bonding between N-rGO and MAPbBr₃, as this has been illustrated in previous works.^{42,43}

The photodetector based on the above hybrid materials was then fabricated with MAPbBr₃/N-rGO casted onto two neighboring ITO electrodes, as illustrated in Figure 4a (also Figure S14). The distance between the electrodes is 40 μm while the thickness of the MAPbBr₃/N-rGO layer on the electrode is about 54 μm, as shown in Figures 4b and S15. In order to engineer the ratio of N-rGO in the N-rGO/perovskite hybrids for optimal device performance, we varied the mass ratios between perovskite and N-rGO and in the hybrids (8:0, 8:0.25, 8:0.5, 8:1, 8:1.5, 8:2 denoted as MAPbBr₃, PNrGO_{0.25}, PNrGO_{0.5}, PNrGO₁, PNrGO_{1.5}, and PNrGO₂, respectively). The morphologies of these composites are independent of the N-rGO/perovskite ratio as evidenced in Figure S4 except that minority of larger crystals start to occur with smaller N-rGO ratio. The structures of different ratios of materials were characterized by XRD, displayed in Figure S16, which are also crystallized into the cubic phase and consistent with the structure in Figure 2. XPS results, as shown in Figures S7–13, confirmed the co-existence of MAPbBr₃ and N-rGO in the hybrid materials.

Figure 4c revealed the influence of the N-rGO ratio on the photocurrents of the photodetectors under white light illumination. The photocurrent of the pure perovskite is negligible as shown in Figure S17. A drastically enhancement on photocurrent can be observed after N-rGO addition with the maximum value of 35 mA in PNrGO_{1.5}, which is two orders of magnitude higher than that of the neat perovskite devices (0.15 mA). Further increase of the N-rGO ratio leads to a deteriorated performance. Slight deviation of the trend from sample PNrGO_{0.25} could be attributed by the better coverage of the N-rGO on perovskites at this specific addition ratio (Figure S4).

In addition to the large photocurrent, PNrGO_{1.5} also exhibits other superior photodetection characteristics, as summarized in Figure 4. First, the response of the photodetector complies well with the optical absorption spectrum, indicating the main contribution of photocurrent from the perovskites (Figure 4d). The linearity of the *I*–*V* curves under both illuminated and dark status manifests the ohmic contact between the perovskites and the ITO electrode (Figure 4e). In

addition, the photocurrent clearly increases with the increment of power density, as shown in Figure 4f.

From the light-intensity-dependent photocurrent in Figure 4g, we can extract the linear dynamic range (LDR) to be 94.4 dB and the responsivity (*R*) to be 3.6×10^4 A/W according to eqs 1 and 2,⁴⁴ which is among the highest in all state-of-art perovskite-based photodetectors (Table S5). Here, *I*_{PC} and *I*_{dark} is the current measure with or without illumination, while *P*_{irra} is the irradiation power density and *S* is the effective area of the device. In eq 2, *L*_{upper} and *L*_{lower} are upper and lower limit currents. Moreover, the detectivity (*D*^{*}) and EQE according to eqs 3 and 4, electrons/incident photons of the device, can reach as high as 0.98×10^{12} Jones and $\sim 0.9 \times 10^5\%$, respectively, as depicted in Figure 4h. Here, *c* is the speed of light and λ stands for the wavelength of light source, while *q* is the charge of one electron. For the calculation of the detectivity in previous work, noise current is usually used, which includes shot noise and thermal noise.^{45,46} When the shot noise is dominant, which is decided by dark current, *D* can be expressed by eq 4.⁴⁷ In contrast, the photo-response from both the neat N-rGO and the neat perovskite-based devices is negligible (Figure S17). Figure 5a demonstrates the good reproducibility of photo-response during the repeating illumination cycles. The rise and fall time of the hybrid material is measured to be 30 and 100 ms, respectively (Figure 5b), which is comparable to the previously reported graphene-MAPbBr₃I photodetector.⁴⁸ In addition, at high light intensity illumination, the photodetector is at a saturated state, which makes it decays with a long time.

$$R = (I_{PC} - I_{dark}) / (P_{irra} \cdot S) \quad (1)$$

$$\text{LDR} = 20 \log(L_{upper} / L_{lower}) \quad (2)$$

$$\text{EQE} = R \cdot hc / (e\lambda) \quad (3)$$

$$D^* = RS^{1/2} / (q \cdot I_{dark})^{1/2} \quad (4)$$

One expected advantage of the N-rGO addition is to improve the photostability, which is confirmed in the device aging test in Figure 5c. After 4000 s aging in atmosphere, drastic degradation of photocurrent ($\sim 17\%$) can be found in neat MAPbBr₃ based photodetector, whereas the performance of the MAPbBr₃/N-rGO-based device stays constant. The enhancement of the photostability can be attributed to (1) N-rGO sheets prevent penetration of water molecules into perovskites. (2) Preformed hydrogen bonding between MA⁺ and N atoms on N-rGO sheets during the synthesis (Figure

S18) inhibits their interaction with water molecules, which has been considered as the main origin of the perovskite degradation.^{49–51} (3) hydrogen bonding between MA⁺ and N atoms on N-rGO together (i.e., N–H···N) with the intra hydrogen bonding (i.e. N–H···Br) in MAPbBr₃ increases the activation energy of MA⁺ migration and therefore diminish the following deprotonation processes. Furthermore, solid-state ¹H NMR was also performed to verify the interaction between the N-rGO and perovskite, as shown in Figure 6. From the ¹H

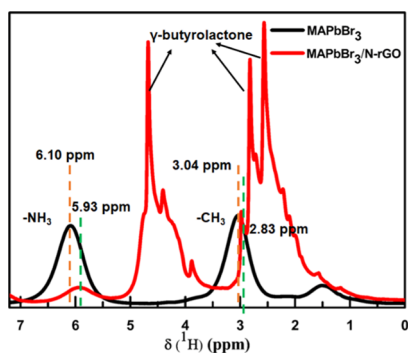


Figure 6. ¹H solid-state NMR spectra at room temperature.

solid-state NMR spectra, we could find out the difference between MAPbBr₃/N-rGO and MAPbBr₃. According to the literature, the peaks at 6.10 and 3.04 ppm can be attributed to NH₃ and CH₃ in pure MAPbBr₃, respectively. However, in MAPbBr₃/N-rGO, those peaks appeared to have shift to the low field at 5.93 and 2.83 ppm [some narrow ¹H peaks adding to the board band are due to the dried N-rGO (Figure S18b) and γ -butyrolactone].⁵² The 0.17 ppm downshift of the peak-

related NH₃ group in MAPbBr₃/N-rGO compared to MAPbBr₃ indicates the shortening of the hydrogen bonding as well as the stronger hydrogen binding interaction in the MAPbBr₃/N-rGO.⁵³ This is a direct evidence for the interfacial conjugation between rGO and perovskite via strong hydrogen bonding.

In order to further rationalize the effect of N-rGO addition, photo-induced charge carrier dynamics was investigated via both steady state and time-resolved spectroscopies. The absorption band edge of MAPbBr₃/N-rGO sample exhibits a pronounced blue shift of ~ 20 nm compared with neat MAPbBr₃. This refers to a widening of the optical band gap from 2.23 to 2.28 eV according to the Tauc plots (inset of the Figure 7a). One possible interpretation can be the so called Burstein–Moss shift induced by the charge transfer from graphene to the semiconductor so that states close to the band edge are partially populated.⁵⁴ However, such assumption can be excluded in our case as the $E_{F-N-rGO}$ (-4.4 eV) is located within the band gap of MAPbBr₃.⁵⁵ Alternatively, the enlarged band gap in MAPbBr₃/N-rGO can be attributed to structure distortion of perovskite because of N-rGO coverage. This is directly evidenced by the shift of the X-ray diffraction peak toward the smaller angle corresponding to lattice expansion (Figure 1b). In fact, the dangling amino groups on the N-rGO can replace the MA⁺ cations and intercalate into the void sites among the PbBr₆⁴⁻ octahedra. Such amino groups anchor with the octahedral networks via hydrogen bonds (~ 13 kJ/mol for N–H···N, ~ 8 kJ/mol for N–H···O) with larger strength than conventional van der Waals force (< 5 kJ/mol).⁵⁶ On the other hand, the hydrogen bonding from N-rGO should still be weaker than those in the intrinsic interaction in the perovskite lattice [i.e. the hydrogen bonding between organic cations (e.g.

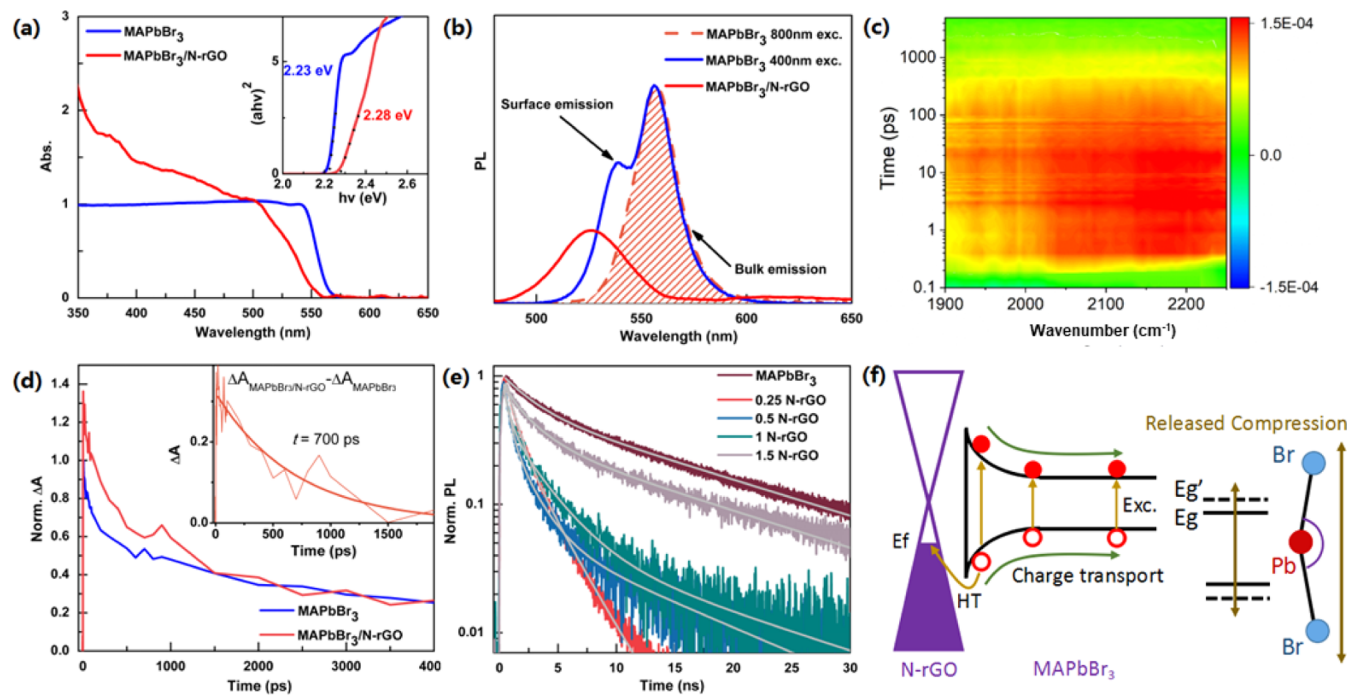


Figure 7. (a) Steady-state absorption spectrum. Inset: Tauc plot representing the band gap of MAPbBr₃ and MAPbBr₃/N-rGO, respectively. (b) Steady-state PL spectrum for MAPbBr₃ and MAPbBr₃/N-rGO excited at 400 and 800 nm, respectively. (c) Time-resolved infrared absorption spectra after 400 nm excitation for MAPbBr₃ crystals. (d) Normalized bleaching kinetics of MAPbBr₃ and MAPbBr₃/N-rGO probed at 400 nm excitation. The inset shows the differential curves of bleaching kinetics between MAPbBr₃/N-rGO and MAPbBr₃. (e) Transient PL excited at 400 nm. (f) Schematic view of the mechanism for the charge transport in MAPbBr₃/N-rGO.

MA⁺) and lead halide network, ~ 25 kJ/mol]⁵⁷ due to the large rigidity of N-rGO which restricts the spatial location of H site for maximal interaction with the halide atoms. Consequently, the intrinsic octahedral tilting induced by the cation related hydrogen bonding in perovskites would be suppressed by graphene coverage, which results in a wider band gap according to both theoretical calculations and experimental observation as shown in Figure 7f.⁵⁸ We speculate that during the spontaneous growth process, the hydrogen bonding has already existed in the mixture of MABr and N-rGO, which makes an effective interaction between MAPbBr₃ and N-rGO after the introduction of PbBr₂. The band edge emission of MAPbBr₃/N-rGO samples is also blue-shifted accordingly, as shown in Figure 7b. The doublet PL emission band of the neat MAPbBr₃ crystals features the coexistence of the surface emission (blue side) as well as bulk emission (red side) with different optical transition energy.⁵⁹ The surface component is drastically diminished at the two-photon absorption condition with 800 nm fs laser excitation (orange dashed area), where the penetration depth L is one order of magnitude larger than one-photon absorption ($L = 1/a = 140$ nm, a : absorption coefficient at 400 nm).

The primary condition of photocurrent generation in perovskite/N-rGO composites should be the transportation of photo-generated charge carriers from perovskite to N-rGO by either charge transfer or energy transfer. In order to distinguish these two processes, we used TRIR to probe the excited state dynamics. Figure 7c shows the time evolution of TRIR spectra after 400 nm excitation of MAPbBr₃ crystals. The broad featureless positive signal is a fingerprint of photo-generated free carriers in the lead halide perovskites representing the intraband absorption transition of excited charges carriers.⁶⁰ The decay of such absorption bands refers to the radiative/nonradiative recombination of the excited charges carriers, as shown in Figure 7d. After being attached to N-rGO, the spectral feature in TRIR keeps the same but with faster decay rate indicating an extra excited state depopulation pathway in the MAPbBr₃. This demonstrates that there should be charge transfer (probably hole transfer according to the band alignment) instead of energy transfer from perovskites to N-rGO after photoexcitation. We fit the hole transfer time from the differential decay signal between MAPbBr₃ and MAPbBr₃/N-rGO samples to be 700 ps (inset of Figure 7d). This further confirms the hole transfer from perovskite to N-rGO as the electron transfer is usually much faster in a ps time range.

The PL quenching observed in the time-resolved photoluminescence (TRPL) measurement confirms the interfacial charge transfer dynamics, as shown in Figure 7e. The PL kinetics of MAPbBr₃/N-rGOs decay faster compared with neat MAPbBr₃ crystals. We can use multi-exponential functions to fit those PL decays as summarized in Table 1. The PL decays

of MAPbBr₃/N-rGOs can be fitted by three components with the lifetimes of sub-ns, 1–2 ns, and 10–15 ns, respectively, while only the last two components can be extracted from neat MAPbBr₃ sample. It should be noted that the excitation fluence during the TRPL measurement was kept to be low ($\sim 10^{11}$ ph/cm²/pulse) to avoid any high order recombination process (e.g., Auger recombination). The lifetime of the slow component (10–15 ns) resembles the typical radiative recombination in bulk MAPbBr₃ perovskites.⁶¹ The middle component can be attributed to surface emission as discussed above with faster recombination rates. The fastest components only occur in MAPbBr₃/N-rGO samples with the similar lifetime to the value obtained from TRIR results and thus can be assigned to the hole transfer process. Such slow hole transfer time in the subnanosecond region is due to the addition charge carrier diffusion time in the perovskite crystals before it can reach the interface for hole transfer. This has also been observed in perovskite film samples.⁶² We noticed the hole transfer times first decrease and then increase with the increment of the N-rGO ratio. This means the hole injection (HT) from MAPbBr₃ to N-rGO is first enhanced with the addition of N-rGO up to 0.5 ratio and then diminished when more N-rGO is introduced. The initial enhancement of the HT can be easily understood as the increased coverage of N-rGO on the perovskite surface. However, the more the interplay between N-rGO and perovskite, the more lattice compression is released, leading to the wider band gap on the surface. A surface barrier would then be created inhibiting the HT, as illustrated in Figure 6f, which explained the observation in TRPL.

We argued that the generation of photocurrent in MAPbBr₃/N-rGO photodetectors is dominated by both intrinsic conductivity of the microcrystal film and interfacial separation of photo-generated charge carriers. Embedding graphene among the perovskite crystals reduced the resistance induced by the inter-crystal barriers. As a result, both dark and photo-current monotonic increases with the N-rGO ratios (Figures 4c, S19 and Table S4). However, the interfacial charge separation would be sacrificed by overloading of N-rGO according to the above discussion. Therefore, as shown in Table S4, the detectivities with different ratios of N-rGO are calculated based on the dark current, through which a large detectivity of the photodetectors was obtained in PNrGO_{1.5} reflecting the optimal balance between the above two factors. The unusual behavior in PNrGO_{0.25} may be derived from the incomplete coverage of N-rGO on the perovskite, which could also be explained by the TRPL.

CONCLUSIONS

To summarize, a facile, productive, and reproducible method was developed, in which MAPbBr₃/N-rGO composites were in situ synthesized by the assistance of hydrogen-bonding interaction. Particularly, the hydrogen bonding guarantees the efficient and homogenous loading of N-rGO on the perovskites. The photodetectors fabricated using the N-rGO coated MAPbBr₃ exhibits significantly enhanced stability under light illumination in ambient conditions. More importantly, we systematically investigated the photophysical influence of N-rGO addition on the photodetection performance. The optimal ratio between N-rGO and perovskites of 8:1.5 wt % in the device has been found with the high responsivity of 3.6×10^4 A/W, EQE of $\sim 10^5\%$, and detectivity up to $\sim 10^{12}$ Jones. The underlying photophysics has been rationalized by time-

Table 1. Multi-Exponential Fitting Parameters for TRPL Kinetics

sample	A_1	τ_1 (ns)	A_2	τ_2 (ns)	A_3	τ_3 (ns)	τ_{avg} (ns)
MAPbBr ₃			0.171	2.5	0.829	15.4	13.2
PNrGO _{0.25}	0.186	0.71	0.746	2.1	0.069	11.0	2.5
PNrGO _{0.5}	0.161	0.45	0.380	1.8	0.459	11.2	5.9
PNrGO ₁	0.098	0.51	0.536	2.8	0.367	14.7	6.9
PNrGO _{1.5}	0.017	0.74	0.175	2.5	0.808	15.4	12.9

resolved spectroscopic studies. The generation of photocurrent in MAPbBr₃/N-rGO photodetectors are dominated by both intrinsic conductivity of the microcrystals film and interfacial separation of photo-generated charge carriers. The former is simply enhanced by the increment of N-rGO networking in the hybrid while the latter is dominated by both electronic coupling and interfacial lattice distortion between N-rGO and perovskite. The maximum detectivity of the photodetectors PNrGO_{1.5} refers to the optimal balance between the above factors. These findings indicate that our synthesized MAPbBr₃/N-rGO composites could be a candidate to be employed in the photocatalytic as well as optoelectronic applications after careful interfacial engineering.

■ ASSOCIATED CONTENT

Supporting Information

The Supporting Information is available free of charge at <https://pubs.acs.org/doi/10.1021/acsami.9b18598>.

Powder XRD patterns, SEM images, XPS spectra, FTIR, photoionization cross sections, Tauc plots, and current–time curves (PDF)

■ AUTHOR INFORMATION

Corresponding Authors

*E-mail: kzheng@kemi.dtu.dk (K.Z.).

*E-mail: cq@kemi.dtu.dk (Q.C.).

ORCID

Alireza Honarfar: 0000-0002-1852-3059

Tõnu Pullerits: 0000-0003-1428-5564

Kaibo Zheng: 0000-0002-7236-1070

Qijin Chi: 0000-0003-4523-2609

Author Contributions

Y.T. and M.L. contributed equally. The manuscript was written through contributions of all authors. All authors have given approval to the final version of the manuscript.

Notes

The authors declare no competing financial interest.

■ ACKNOWLEDGMENTS

This work was supported by the Villum Foundation, Independent Research Fund Denmark-Nature Sciences (DFF-FNU, project no DFF-7014-00302), Independent Research Fund Denmark-Sapere Aude starting grant (no. 7026-00037A) and Swedish Research Council VR starting grant (no. 2017-05337), and the Chinese Scholarship Council for the PhD scholarship to M.L. (no. 201706650012).

■ REFERENCES

- (1) Koppens, F. H. L.; Mueller, T.; Avouris, P.; Ferrari, A. C.; Vitiello, M. S.; Polini, M. Photodetectors Based on Graphene, Other Two-dimensional Materials and Hybrid Systems. *Nat. Nanotechnol.* **2014**, *9*, 780–793.
- (2) Fan, P.; Chettiar, U. K.; Cao, L.; Afshinmanesh, F.; Engheta, N.; Brongersma, M. L. An Invisible Metal–semiconductor Photodetector. *Nat. Photonics* **2012**, *6*, 380–385.
- (3) Siegmund, B.; Mischok, A.; Benduhn, J.; Zeika, O.; Ullbrich, S.; Nehm, F.; Böhm, M.; Spoltore, D.; Fröh, H.; Körner, C.; Leo, K.; Vandewal, K. Organic Narrowband Near-infrared Photodetectors Based on Intermolecular Charge-transfer Absorption. *Nat. Commun.* **2017**, *8*, 15421.
- (4) Michel, J.; Liu, J.; Kimerling, L. C. High-performance Ge-on-Si Photodetectors. *Nat. Photonics* **2010**, *4*, 527–534.

- (5) Chen, X. L.; Lu, X. B.; Deng, B. C.; Sinai, O.; Shao, Y. H.; Li, C.; Yuan, S. F.; Tran, V.; Watanabe, K. J.; Taniguchi, T.; Naveh, D.; Yang, L.; Xia, F. N. Widely Tunable Black Phosphorus Mid-infrared Photodetector. *Nat. Commun.* **2017**, *8*, 1672.

- (6) Yu, W. J.; Vu, Q. A.; Oh, H.; Nam, H. G.; Zhou, H. L.; Cha, S.; Kim, J.-Y.; Carvalho, A.; Jeong, M.; Choi, H.; Neto, A. H. C.; Lee, Y. H.; Duan, X. F. Unusually Efficient Photocurrent Extraction in Monolayer van der Waals Heterostructure by Tunneling Through Discretized Barriers. *Nat. Commun.* **2016**, *7*, 13278.

- (7) Zhou, W.; Peng, Y.; Yin, Y.; Zhou, Y.; Zhang, Y.; Tang, D. Broad spectral response photodetector based on individual tin-doped CdS nanowire. *AIP Adv.* **2014**, *4*, 123005.

- (8) Shen, L.; Zhang, Y.; Bai, Y.; Zheng, X.; Wang, Q.; Huang, J. A Filterless, Visible-blind, Narrow-band, and Near-infrared Photodetector with a Gain. *Nanoscale* **2016**, *8*, 12990–12997.

- (9) Han, M. G.; Park, K.-B.; Bulliard, X.; Lee, G. H.; Yun, S.; Leem, D.-S.; Heo, C.-J.; Yagi, T.; Sakurai, R.; Ro, T.; Lim, S.-J.; Sul, S.; Na, K.; Ahn, J.; Jin, Y. W.; Lee, S. Narrow-Band Organic Photodiodes for High-Resolution Imaging. *ACS Appl. Mater. Interfaces* **2016**, *8*, 26143–26151.

- (10) Wang, H.; Kim, D. H. Perovskite-based Photodetectors: Materials and Devices. *Chem. Soc. Rev.* **2017**, *46*, 5204–5236.

- (11) Saidaminov, M. I.; Adinolfi, V.; Comin, R.; Abdelhady, A. L.; Peng, W.; Dursun, I.; Yuan, M. J.; Hoogland, S.; Sargent, E. H.; Bakr, O. M. Planar-integrated Single-crystalline Perovskite Photodetectors. *Nat. Commun.* **2015**, *6*, 8724.

- (12) Feng, J.; Gong, C.; Gao, H.; Wen, W.; Gong, Y.; Jiang, X.; Zhang, B.; Wu, Y.; Wu, Y.; Fu, H.; Jiang, L.; Zhang, X. Single-crystalline Layered Metal-halide Perovskite Nanowires for Ultra-sensitive Photodetectors. *Nat. Electron.* **2018**, *1*, 404–410.

- (13) Saraf, R.; Maheshwari, V. Self-Powered Photodetector Based on Electric-Field-Induced Effects in MAPbI₃ Perovskite with Improved Stability. *ACS Appl. Mater. Interfaces* **2018**, *10*, 21066–21072.

- (14) Shaikh, P. A.; Shi, D.; Retamal, J. R. D.; Sheikh, A. D.; Haque, M. A.; Kang, C.-F.; He, J.-H.; Bakr, O. M.; Wu, T. Schottky Junctions on Perovskite Single Crystals: Light-modulated Dielectric Constant and Self-biased Photodetection. *J. Mater. Chem. C* **2016**, *4*, 8304–8312.

- (15) Alwadai, N.; Haque, M. A.; Mitra, S.; Flemman, T.; Pak, Y.; Wu, T.; Roqan, I. High-Performance Ultraviolet-to-Infrared Broadband Perovskite Photodetectors Achieved via Inter-/Intraband Transitions. *ACS Appl. Mater. Interfaces* **2017**, *9*, 37832–37838.

- (16) Liang, R.-Z.; Babics, M.; Savikhin, V.; Zhang, W.; Le Corre, V. M.; Lopatin, S.; Kan, Z.; Firdaus, Y.; Liu, S.; McCulloch, I.; Toney, M. F.; Beaujuge, P. M. Carrier Transport and Recombination in Efficient “All-Small-Molecule” Solar Cells with the Nonfullerene Acceptor IDTBR. *Adv. Energy Mater.* **2018**, *8*, 1800264.

- (17) Miao, J.; Zhang, F. Recent Progress on Highly Sensitive Perovskite Photodetectors. *J. Mater. Chem. C* **2019**, *7*, 1741–1791.

- (18) Guo, Y.; Liu, C.; Tanaka, H.; Nakamura, E. Air-Stable and Solution-Processable Perovskite Photodetectors for Solar-Blind UV and Visible Light. *J. Phys. Chem. Lett.* **2015**, *6*, 535–539.

- (19) Zhao, F.; Xu, K.; Luo, X.; Liang, Y.; Peng, Y.; Lu, F. Toward High Uniformity of Photoresponse Broadband Hybrid Organic–Inorganic Photodiode Based on PVP-Modified Perovskite. *Adv. Opt. Mater.* **2018**, *6*, 1700509.

- (20) Liu, H.; Zhang, X.; Zhang, L.; Yin, Z.; Wang, D.; Meng, J.; Jiang, Q.; Wang, Y.; You, J. A High-performance Photodetector Based on an Inorganic Perovskite–ZnO Heterostructure. *J. Mater. Chem. C* **2017**, *5*, 6115–6122.

- (21) Ma, C.; Shi, Y.; Hu, W.; Chiu, M.-H.; Liu, Z.; Bera, A.; Li, F.; Wang, H.; Li, L.-J.; Wu, T. Heterostructured WS₂/CH₃NH₃PbI₃ Photoconductors with Suppressed Dark Current and Enhanced Photodetectivity. *Adv. Mater.* **2016**, *28*, 3683–3689.

- (22) Wang, Y.; Fullon, R.; Acerce, M.; Petoukhoff, C. E.; Yang, J.; Chen, C.; Du, S.; Lai, S. K.; Lau, S. P.; Voiry, D.; O’Carroll, D.; Gupta, G.; Mohite, A. D.; Zhang, S.; Zhou, H.; Chhowalla, M. Solution-Processed MoS₂/Organolead Trihalide Perovskite Photodetectors. *Adv. Mater.* **2017**, *29*, 1603995.

- (23) Zhu, N.; Han, S.; Gan, S.; Ulstrup, J.; Chi, Q. Graphene Paper Doped with Chemically Compatible Prussian Blue Nanoparticles as Nanohybrid Electrocatalyst. *Adv. Funct. Mater.* **2013**, *23*, 5297–5306.
- (24) Gan, S.; Zhong, L.; Wu, T.; Han, D.; Zhang, J.; Ulstrup, J.; Chi, Q.; Niu, L. Spontaneous and Fast Growth of Large-Area Graphene Nanofilms Facilitated by Oil/Water Interfaces. *Adv. Mater.* **2012**, *24*, 3958–3964.
- (25) Novoselov, K. S.; Fal'ko, V. I.; Colombo, L.; Gellert, P. R.; Schwab, M. G.; Kim, K. A Roadmap for Graphene. *Nature* **2012**, *490*, 192–200.
- (26) Hafez, H. A.; Kovalev, S.; Deinert, J.-C.; Mics, Z.; Green, B.; Awari, N.; Chen, M.; Germanskiy, S.; Lehnert, U.; Teichert, J.; Wang, Z.; Tielrooij, K.-J.; Liu, Z.; Chen, Z.; Narita, A.; Müllen, K.; Bonn, M.; Gensch, M.; Turchinovich, D. Extremely Efficient Terahertz High-harmonic Generation in Graphene by Hot Dirac Fermions. *Nature* **2018**, *561*, 507–511.
- (27) Zhou, K.-G.; Vasu, K. S.; Cherian, C. T.; Neek-Amal, M.; Zhang, J. C.; Ghorbanfekr-Kalashami, H.; Huang, K.; Marshall, O. P.; Kravets, V. G.; Abraham, J.; Su, Y.; Grigorenko, A. N.; Pratt, A.; Geim, A. K.; Peeters, F. M.; Novoselov, K. S.; Nair, R. R. Electrically Controlled Water Permeation Through Graphene Oxide Membranes. *Nature* **2018**, *559*, 236–240.
- (28) Chen, Z.; Kang, Z.; Rao, C.; Cheng, Y.; Liu, N.; Zhang, Z.; Li, L.; Gao, Y. Improving Performance of Hybrid Graphene–Perovskite Photodetector by a Scratch Channel. *Adv. Mater. Opt. Electron.* **2019**, *5*, 1900168.
- (29) Li, J.; Yuan, S.; Tang, G.; Li, G.; Liu, D.; Li, J.; Hu, X.; Liu, Y.; Li, J.; Yang, Z.; Liu, S. F.; Liu, Z.; Gao, F.; Yan, F. High-Performance, Self-Powered Photodetectors Based on Perovskite and Graphene. *ACS Appl. Mater. Interfaces* **2017**, *9*, 42779–42787.
- (30) Lee, Y.; Kwon, J.; Hwang, E.; Ra, C.-H.; Yoo, W. J.; Ahn, J.-H.; Park, J. H.; Cho, J. H. High-Performance Perovskite–Graphene Hybrid Photodetector. *Adv. Mater.* **2015**, *27*, 41–46.
- (31) Hadadian, M.; Correa-Baena, J.-P.; Goharshadi, E. K.; Ummadisingu, A.; Seo, J.-Y.; Luo, J.; Gholipour, S.; Zakeeruddin, S. M.; Saliba, M.; Abate, A.; Grätzel, M.; Hagfeldt, A. Enhancing Efficiency of Perovskite Solar Cells via N-doped Graphene: Crystal Modification and Surface Passivation. *Adv. Mater.* **2016**, *28*, 8681–8686.
- (32) Li, X.; Wang, H.; Robinson, J. T.; Sanchez, H.; Diankov, G.; Dai, H. Simultaneous Nitrogen Doping and Reduction of Graphene Oxide. *J. Am. Chem. Soc.* **2009**, *131*, 15939–15944.
- (33) Park, J.; Kim, S. Nitrogen Modified-Reduced Graphene Oxide Supports for Catalysts for Fuel Cells and Their Electrocatalytic Activity. *J. Electrochem. Soc.* **2014**, *161*, F518–F524.
- (34) Zhang, X.; Wang, Q.; Jin, Z.; Chen, Y.; Liu, H.; Wang, J.; Li, Y.; Liu, S. F. Graphdiyne Quantum Dots for Much Improved Stability and Efficiency of Perovskite Solar Cells. *Adv. Mater. Interfaces* **2018**, *5*, 1701117.
- (35) Li, J.; Jiu, T.; Chen, S.; Liu, L.; Yao, Q.; Bi, F.; Zhao, C.; Wang, Z.; Zhao, M.; Zhang, G.; Xue, Y.; Lu, F.; Li, Y. Graphdiyne as a Host Active Material for Perovskite Solar Cell Application. *Nano Lett.* **2018**, *18*, 6941–6947.
- (36) El-Mellouhi, F.; Bentría, E.; Marzouk, A.; Rashkeev, S. N.; Kais, S.; Alharbi, F. H. Hydrogen Bonding: a Mechanism for Tuning Electronic and Optical Properties of Hybrid Organic–inorganic Frameworks. *npj Comput. Mater.* **2016**, *2*, 16035.
- (37) Svane, K. L.; Forse, A. C.; Grey, C. P.; Kieslich, G.; Cheetham, A. K.; Walsh, A.; Butler, K. T. How Strong Is the Hydrogen Bond in Hybrid Perovskites? *J. Phys. Chem. Lett.* **2017**, *8*, 6154–6159.
- (38) Hu, X.; Zhang, X.; Liang, L.; Bao, J.; Li, S.; Yang, W.; Xie, Y. High-Performance Flexible Broadband Photodetector Based on Organolead Halide Perovskite. *Adv. Funct. Mater.* **2014**, *24*, 7373–7380.
- (39) Chen, Y.; He, M.; Peng, J.; Sun, Y.; Liang, Z. Structure and Growth Control of Organic–Inorganic Halide Perovskites for Optoelectronics: From Polycrystalline Films to Single Crystals. *Adv. Sci.* **2016**, *3*, 1500392.
- (40) Varadwaj, P. R.; Varadwaj, A.; Marques, H. M.; Yamashita, K. Significance of Hydrogen Bonding and Other Noncovalent Interactions in Determining Octahedral Tilting in the $\text{CH}_3\text{NH}_3\text{PbI}_3$ Hybrid Organic–inorganic Halide Perovskite Solar Cell Semiconductor. *Sci. Rep.* **2019**, *9*, 50.
- (41) Liu, M.; Zhong, G.; Yin, Y.; Miao, J.; Li, K.; Wang, C.; Xu, X.; Shen, C.; Meng, H. Aluminum-Doped Cesium Lead Bromide Perovskite Nanocrystals with Stable Blue Photoluminescence Used for Display Backlight. *Adv. Sci.* **2017**, *4*, 1700335.
- (42) Ou, Q.; Zhang, Y.; Wang, Z.; Yuwono, J. A.; Wang, R.; Dai, Z.; Li, W.; Zheng, C.; Xu, Z.-Q.; Qi, X.; Duhm, S.; Medhekar, N. V.; Zhang, H.; Bao, Q. Strong Depletion in Hybrid Perovskite p–n Junctions Induced by Local Electronic Doping. *Adv. Mater.* **2018**, *30*, 1705792.
- (43) Ou, Q.-D.; Li, C.; Wang, Q.-K.; Li, Y.-Q.; Tang, J.-X. Recent Advances in Energetics of Metal Halide Perovskite Interfaces. *Adv. Mater. Interfaces* **2017**, *4*, 1600694.
- (44) Ding, J.; Du, S.; Zuo, Z.; Zhao, Y.; Cui, H.; Zhan, X. High Detectivity and Rapid Response in Perovskite CsPbBr_3 Single-Crystal Photodetector. *J. Phys. Chem. C* **2017**, *121*, 4917–4923.
- (45) Bao, C.; Chen, Z.; Fang, Y.; Wei, H.; Deng, Y.; Xiao, X.; Li, L.; Huang, J. Low-Noise and Large-Linear-Dynamic-Range Photodetectors Based on Hybrid-Perovskite Thin-Single-Crystals. *Adv. Mater.* **2017**, *29*, 1703209.
- (46) Li, F.; Wang, H.; Kufer, D.; Liang, L.; Yu, W.; Alarousu, E.; Ma, C.; Li, Y.; Liu, Z.; Liu, C.; Wei, N.; Wang, F.; Chen, L.; Mohammed, O. F.; Fratolocchi, A.; Liu, X.; Konstantatos, G.; Wu, T. Ultrahigh Carrier Mobility Achieved in Photoresponsive Hybrid Perovskite Films via Coupling with Single-Walled Carbon Nanotubes. *Adv. Mater.* **2017**, *29*, 1602432.
- (47) Dou, L. T.; Yang, Y.; You, J. B.; Hong, Z. R.; Chang, W.-H.; Li, G.; Yang, Y. Solution-processed hybrid perovskite photodetectors with high detectivity. *Nat. Commun.* **2014**, *5*, 5404.
- (48) Wang, Y.; Zhang, Y.; Lu, Y.; Xu, W.; Mu, H.; Chen, C.; Qiao, H.; Song, J.; Li, S.; Sun, B.; Cheng, Y.-B.; Bao, Q. Hybrid Graphene–Perovskite Phototransistors with Ultrahigh Responsivity and Gain. *Adv. Opt. Mater.* **2015**, *3*, 1389–1396.
- (49) Hernández-Soto, H.; Weinhold, F.; Francisco, J. S. Radical Hydrogen Bonding: Origin of Stability of Radical-molecule Complexes. *J. Chem. Phys.* **2007**, *127*, 164102.
- (50) Golec, B.; Nawara, K.; Gorski, A.; Thummel, R. P.; Herbich, J.; Waluk, J. Combined Effect of Hydrogen Bonding Interactions and Freezing of Rotameric Equilibrium on the Enhancement of Photostability. *Phys. Chem. Chem. Phys.* **2018**, *20*, 13306–13315.
- (51) Zhu, Z.; Hadjiev, V. G.; Rong, Y.; Guo, R.; Cao, B.; Tang, Z.; Qin, F.; Li, Y.; Wang, Y.; Hao, F.; Venkatesan, S.; Li, W.; Baldelli, S.; Guloy, A. M.; Fang, H.; Hu, Y.; Yao, Y.; Wang, Z.; Bao, J. Interaction of Organic Cation with Water Molecule in Perovskite MAPbI_3 : From Dynamic Orientational Disorder to Hydrogen Bonding. *Chem. Mater.* **2016**, *28*, 7385–7393.
- (52) National Center for Biotechnology Information. PubChem Database. gamma-Butyrolactone, CID=7302, <https://pubchem.ncbi.nlm.nih.gov/compound/gamma-Butyrolactone> (accessed Dec 18, 2019).
- (53) Petrova, M.; Muhamadejev, R.; Vigante, B.; Duburs, G.; Liepinsh, E. Intramolecular hydrogen bonds in 1,4-dihydropyridine derivatives. *R. Soc. Open Sci.* **2018**, *5*, 180088.
- (54) Yang, J.; Zhao, X.; Shan, X.; Fan, H.; Yang, L.; Zhang, Y.; Li, X. Blue-Shift of UV Emission in ZnO/graphene Composites. *J. Alloys Compd.* **2013**, *556*, 1–5.
- (55) Jun, G. H.; Jin, S. H.; Lee, B.; Kim, B. H.; Chae, W.-S.; Hong, S. H.; Jeon, S. Enhanced Conduction and Charge-selectivity by N-doped Graphene Flakes in the Active Layer of Bulk-Heterojunction Organic Solar Cells. *Energy Environ. Sci.* **2013**, *6*, 3000–3006.
- (56) Wen, X.; Wu, J.; Gao, D.; Lin, C. Interfacial Engineering with Amino-functionalized Graphene for Efficient Perovskite Solar Cells. *J. Mater. Chem. A* **2016**, *4*, 13482–13487.

(57) Lee, J. H.; Lee, J.-H.; Kong, E.-H.; Jang, H. M. The Nature of Hydrogen-bonding Interaction in the Prototypic Hybrid Halide Perovskite, Tetragonal CH₃NH₃PbI₃. *Sci. Rep.* **2016**, *6*, 21687.

(58) Kong, L.; Liu, G.; Gong, J.; Hu, Q.; Schaller, R. D.; Dera, P.; Zhang, D.; Liu, Z.; Yang, W.; Zhu, K.; Tang, Y.; Wang, C.; Wei, S.-H.; Xu, T.; Mao, H.-k. Simultaneous Band-gap Narrowing and Carrier-lifetime Prolongation of Organic-inorganic Trihalide Perovskites. *Proc. Natl. Acad. Sci. U.S.A.* **2016**, *113*, 8910–8915.

(59) Yang, B.; Zhang, F.; Chen, J.; Yang, S.; Xia, X.; Pullerits, T.; Deng, W.; Han, K. Ultrasensitive and Fast All-Inorganic Perovskite-Based Photodetector via Fast Carrier Diffusion. *Adv. Mater.* **2017**, *29*, 1703758.

(60) Tang, Y.; Cao, X.; Honarfar, A.; Abdellah, M.; Chen, C.; Avila, J.; Asensio, M.-C.; Hammarström, L.; Sa, J.; Canton, S. E.; Zheng, K.; Pullerits, T.; Chi, Q. Inorganic Ions Assisted the Anisotropic Growth of CsPbCl₃ Nanowires with Surface Passivation Effect. *ACS Appl. Mater. Interfaces* **2018**, *10*, 29574–29582.

(61) Zheng, K.; Židek, K.; Abdellah, M.; Messing, M. E.; Al-Marri, M. J.; Pullerits, T. Trap States and Their Dynamics in Organometal Halide Perovskite Nanoparticles and Bulk Crystals. *J. Phys. Chem. C* **2016**, *120*, 3077–3084.

(62) Leng, J.; Liu, J.; Zhang, J.; Jin, S. Decoupling Interfacial Charge Transfer from Bulk Diffusion Unravels Its Intrinsic Role for Efficient Charge Extraction in Perovskite Solar Cells. *J. Phys. Chem. Lett.* **2016**, *7*, 5056–5061.

Supporting Information

Email list for co-authors

- 1) Yingying Tang, y.tang2@uva.nl
- 2) Mingli Liang, milia@kemi.dtu.dk
- 3) MinWei Zhang, zhang66106911@sohu.com
- 4) Alireza Honarfar, alireza.honarfar@chemphys.lu.se
- 5) Xianshao Zou, xianshao.zou@chemphys.lu.se
- 6) Mohamed Abdellah, mohamed.abdellah@chemphys.lu.se
- 7) Kaibo Zheng, kzheng@kemi.dtu.dk, kaibo.zheng@chemphys.lu.se
- 8) Tõnu Pullerits, tonu.pullerits@chemphys.lu.se
- 9) Qijin Chi, cq@kemi.dtu.dk

Supporting Information

Photodetector Based on Spontaneously Grown Strongly Coupled MAPbBr₃/N-rGO Hybrids Showing an Enhanced Performance

Yingying Tang,^{†#} Mingli Liang,^{†#} MinWei Zhang,[†] Alireza Honarfar,[‡] Xianshao Zou,[‡]

Mohamed Abdellah,[‡] Tõnu Pullerits,[‡] Kaibo Zheng,^{†‡} and Qijin Chi[†]

[†]Department of Chemistry, Technical University of Denmark, DK-2800 Kongens
Lyngby, Denmark.

[‡]Department of Chemical Physics and NanoLund, Lund University, Box 124, 22100,
Lund, Sweden

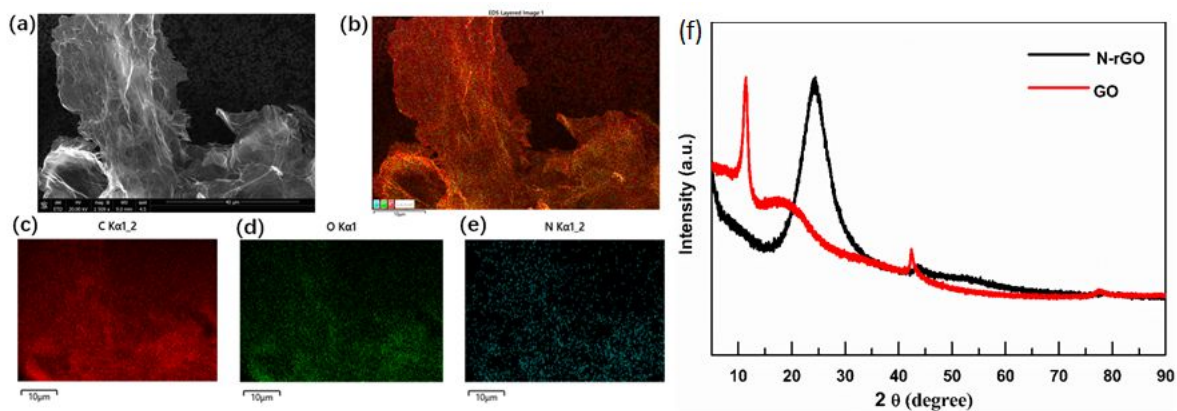


Figure S1. SEM images for N-rGO (a) and (b-e) the EDX elemental mapping of the corresponding C, O, and N, respectively. (f) XRD pattern for the GO precursor and N-rGO.

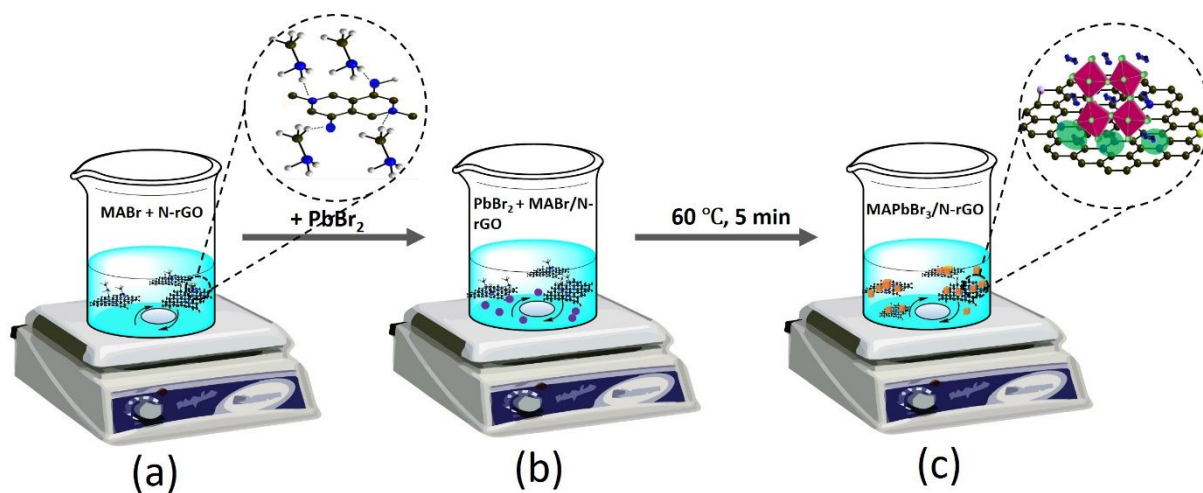


Figure S2. Schematic illustration for the in situ synthesis of MAPbBr₃/N-rGO. a, b) Illustration of the addition of MABr and PbBr₂, which leads to the formation of hydrogen bonding between MABr and N-rGO. c) The formation of MAPbBr₃ cubes on N-rGO sheets. Not drawn to scale.

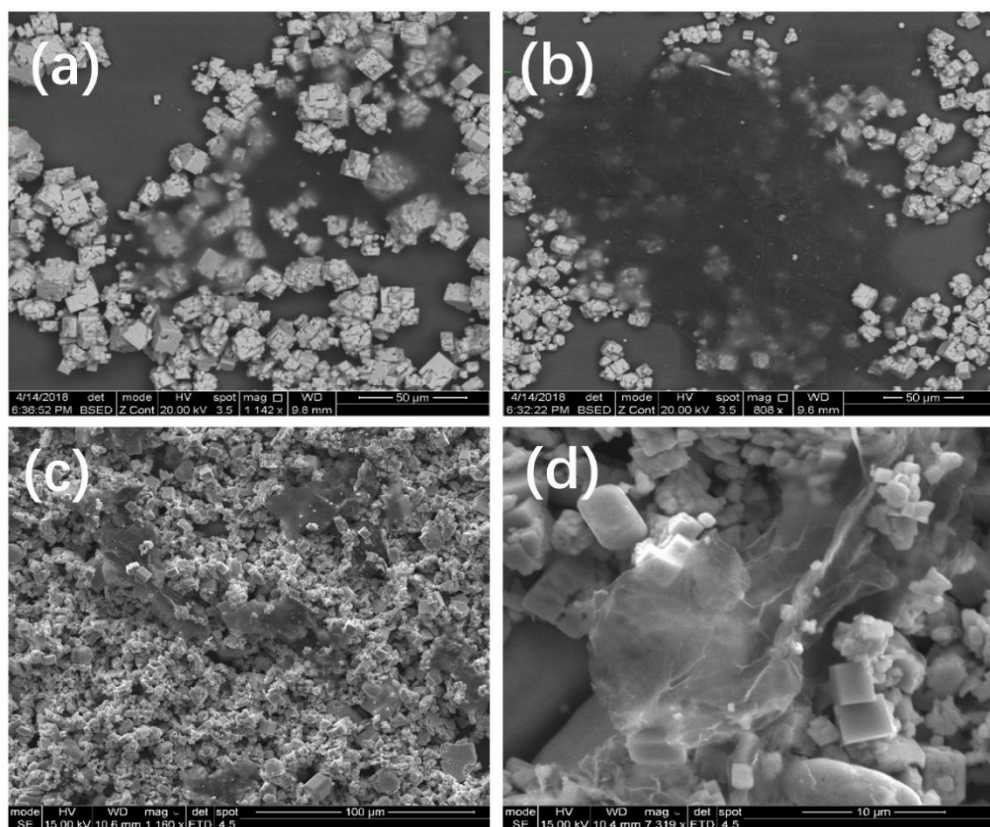


Figure S3. SEM images for MAPbBr₃ hybridized with different kinds of graphene-based materials: a and b) GO, c and d) histidine-rGO.

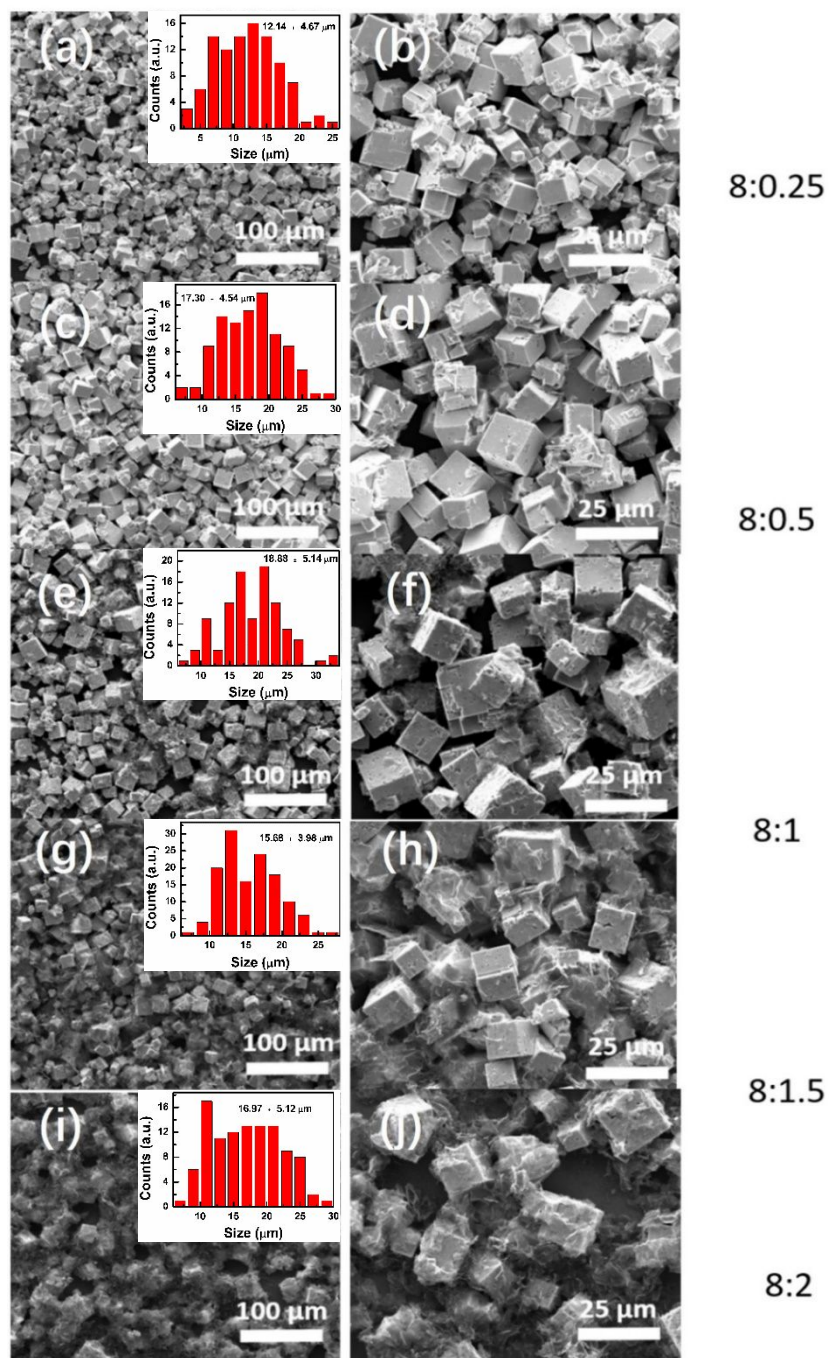


Figure S4. SEM images of MAPbBr₃/N-rGO with different precursor ratios: a, b) 8:0.25; c, d) 8:0.5; e, f) 8:1; g, h) 8:1.5; i, j) 8:2.

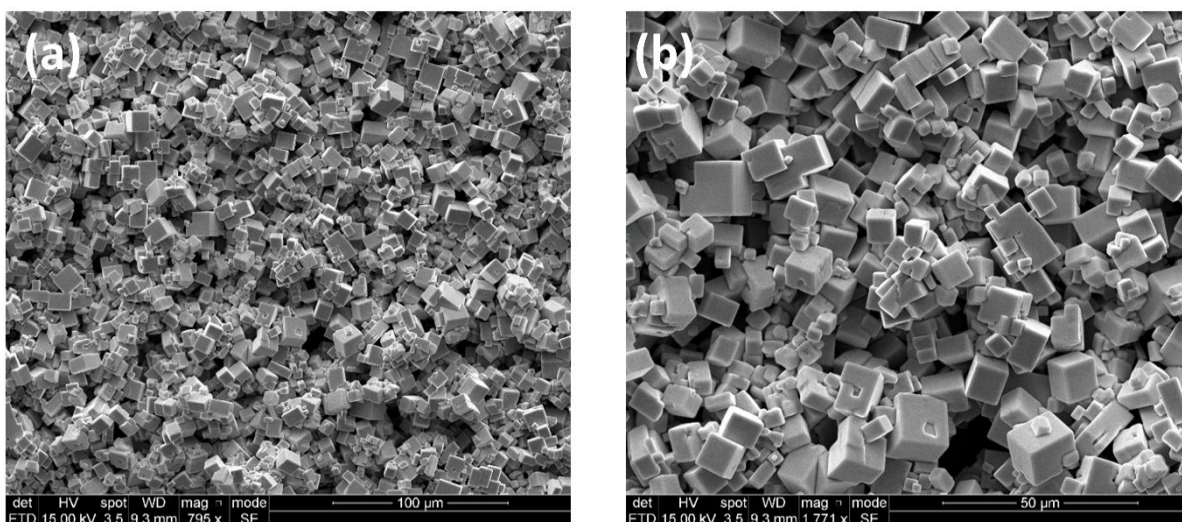


Figure S5. a, b) SEM images of MAPbBr₃ microcrystals.

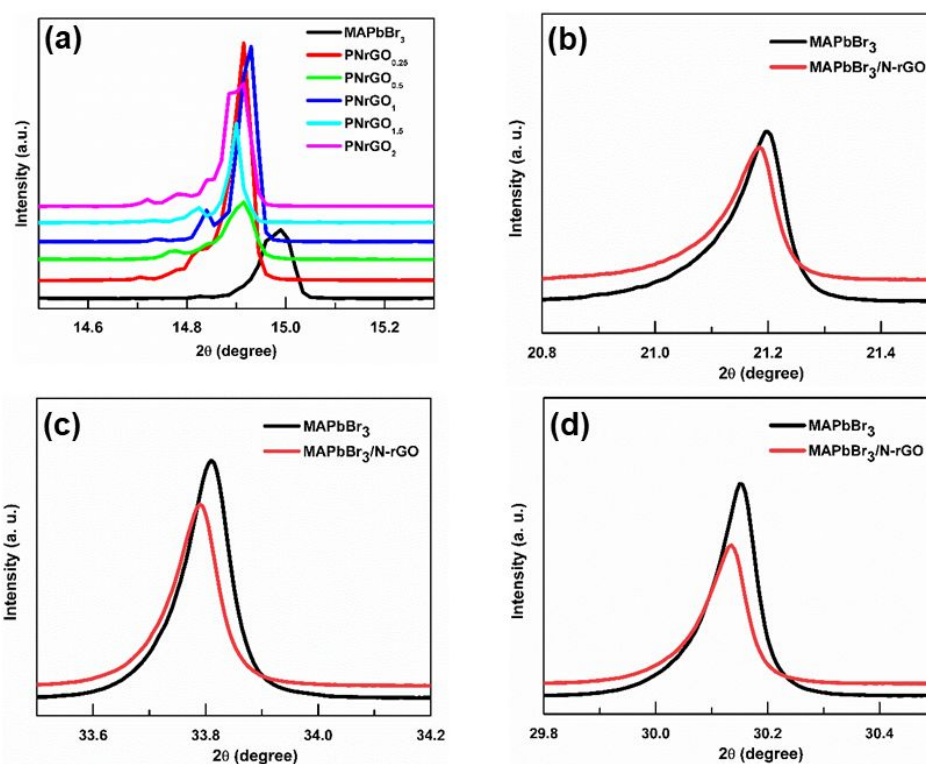


Figure S6. XRD spectra for (a) MAPbBr₃, PNRGO_{0.25}, PNRGO_{0.5}, PNRGO₁, PNRGO_{1.5}, and PNRGO₂, respectively. Magnified XRD spectra for (b) (110) (c) (210), (d) (002) crystalline planes.

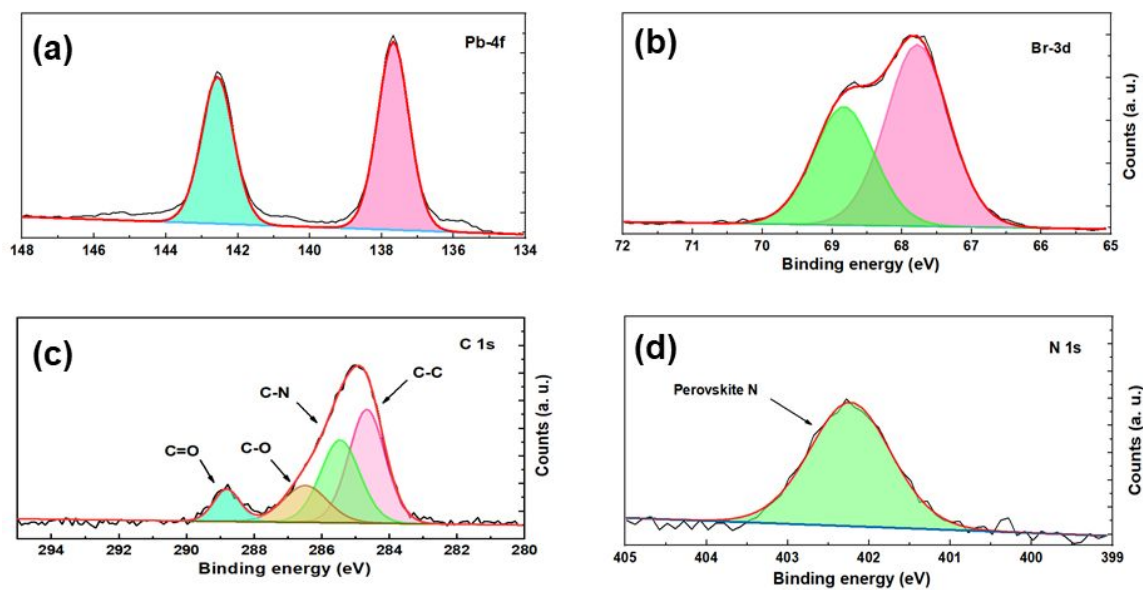


Figure S7. XPS characteristics: a) Pb 4f, b) Br 3d, c) C 1s, d) N 1s spectra for MAPbBr₃.

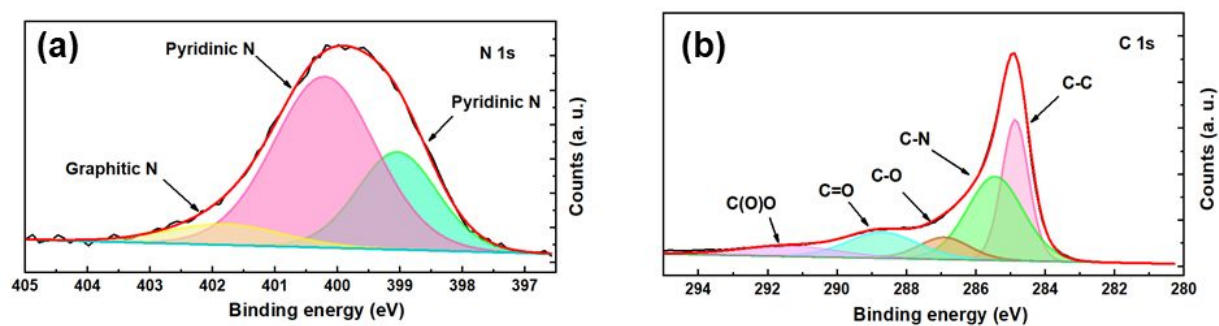


Figure S8. XPS characteristics: a) C 1s, b) N 1s spectra for N-rGO.

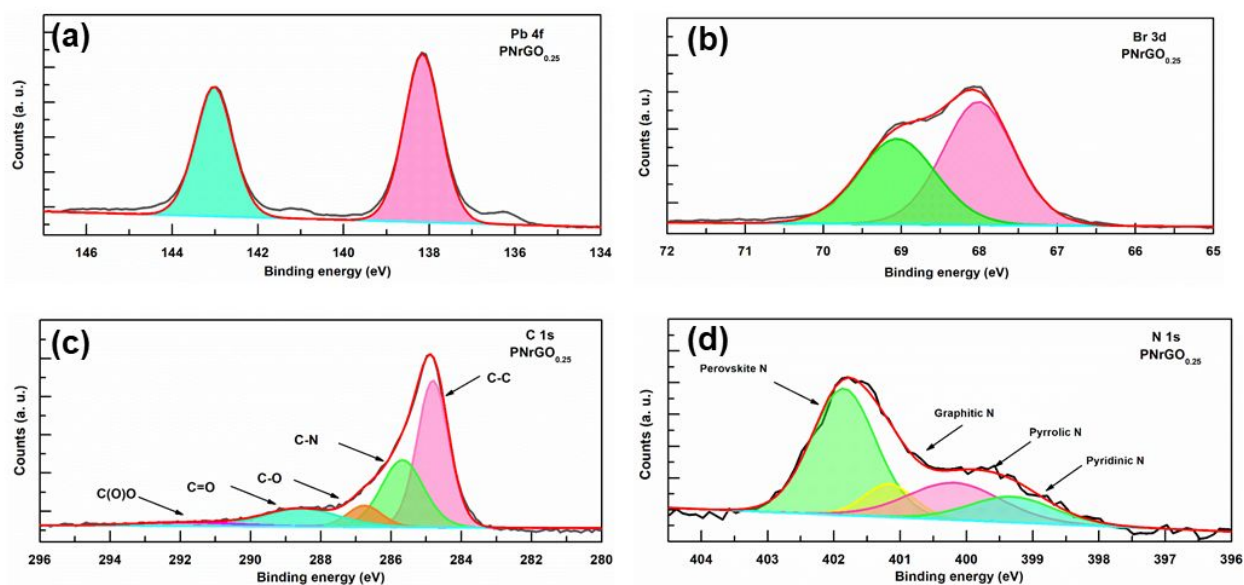


Figure S9. XPS characteristics: a) Pb 4f, b) Br 3d, c) C 1s, d) N 1s spectra for PNRGO_{0.25}.

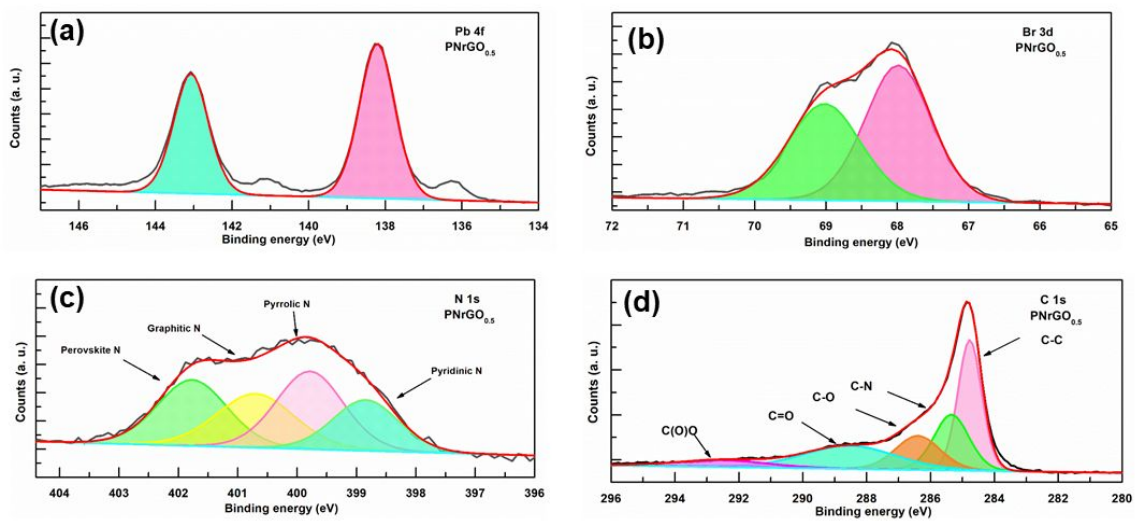


Figure S10. XPS characteristics: a) $\text{Pb } 4f$, b) $\text{Br } 3d$, c) $\text{N } 1s$, d) $\text{C } 1s$ spectra for $\text{PNrGO}_{0.5}$.

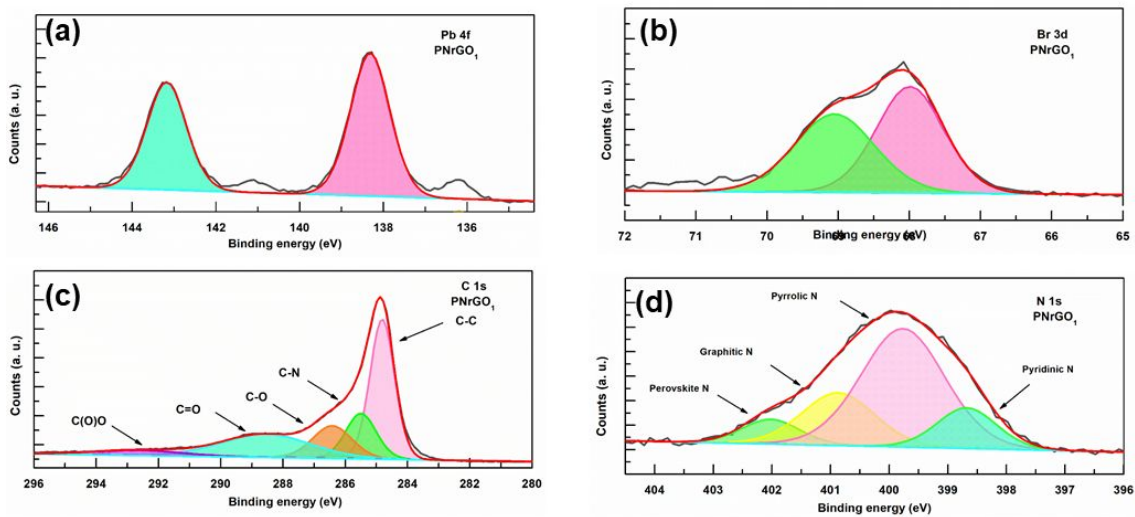


Figure S11. XPS characteristics: a) $\text{Pb } 4f$, b) $\text{Br } 3d$, c) $\text{C } 1s$, d) $\text{N } 1s$ spectra for PNrGO_1 .

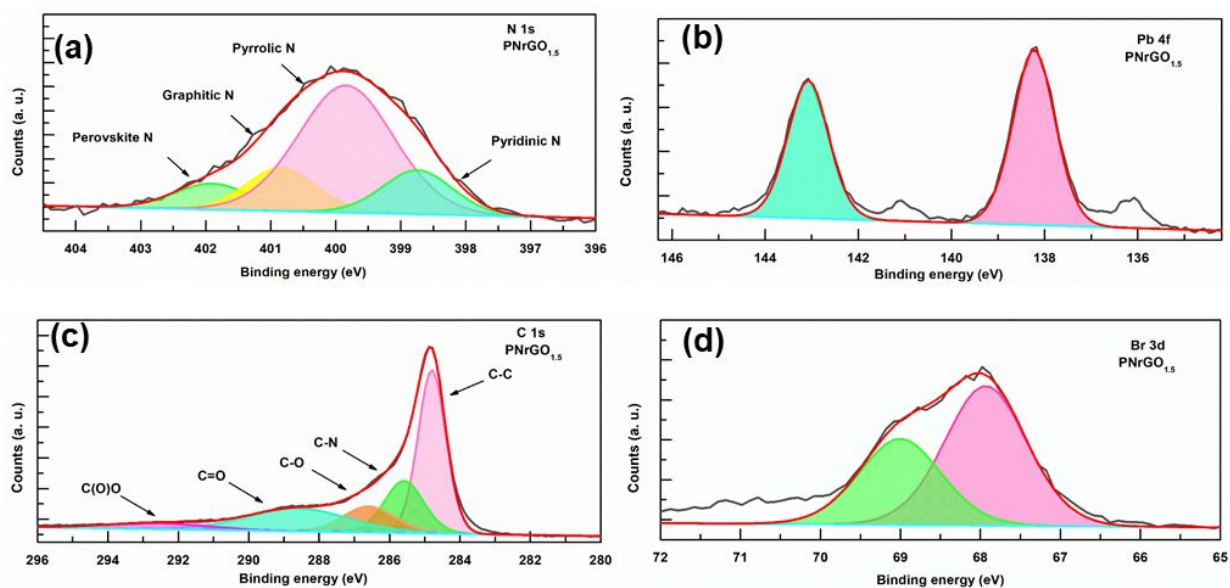


Figure S12. XPS characteristics: a) N 1s, b) Pb 4f, c) C 1s, d) Br 3d spectra for $\text{PNrGO}_{1.5}$.

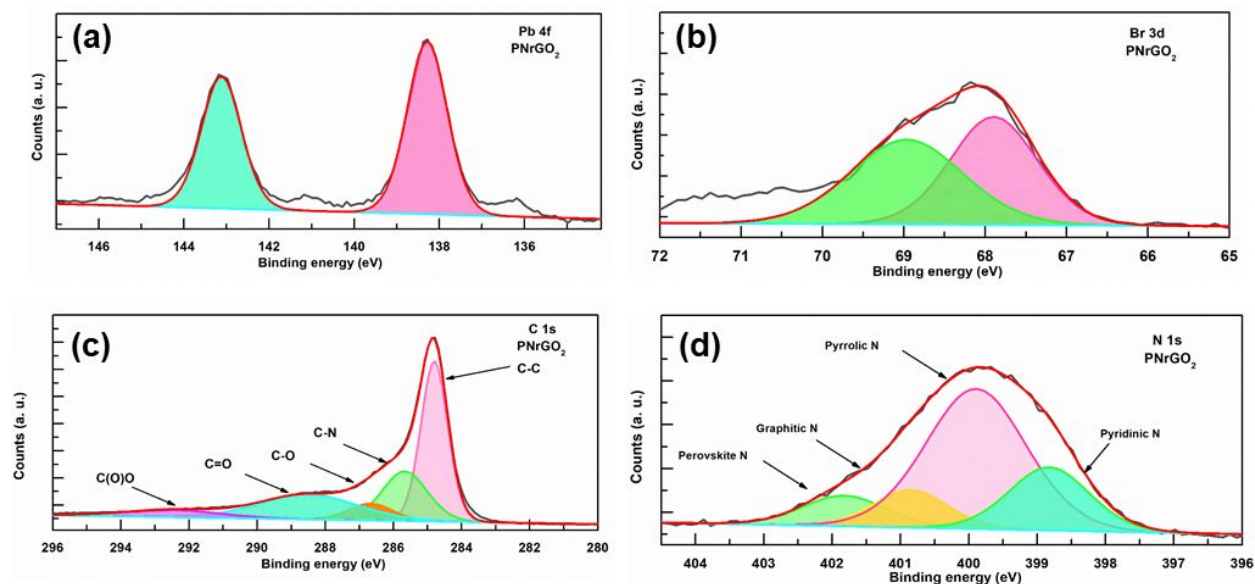


Figure S13. XPS characteristics: a) Pb 4f, b) Br 3d, c) C 1s, d) N 1s spectra for PNrGO_2 .

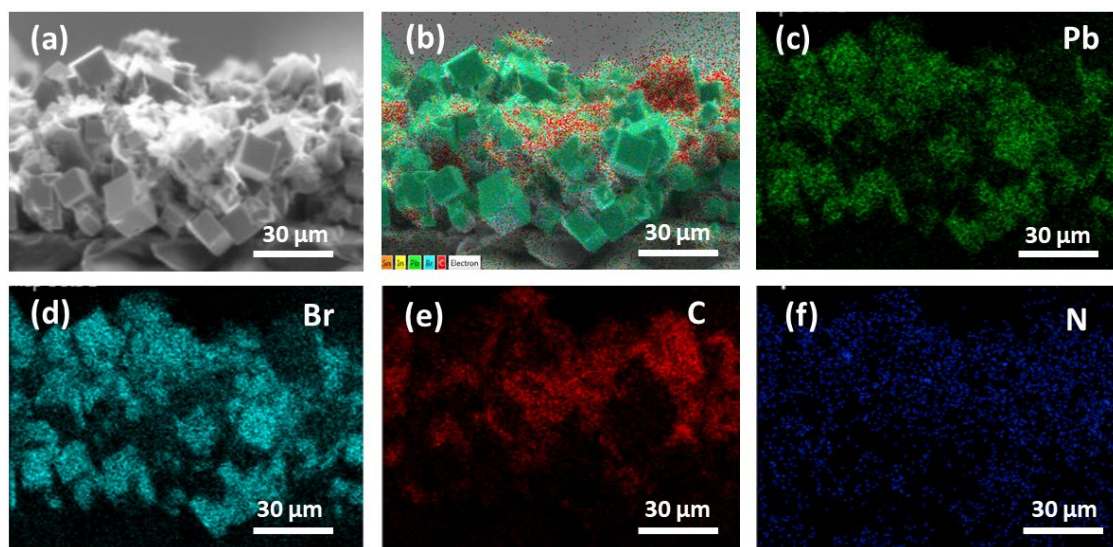


Figure S14. a) Cross-sectional SEM image of the photodetector and b-f) the EDX elemental mapping of the corresponding Pb, Br, C, and N, respectively.

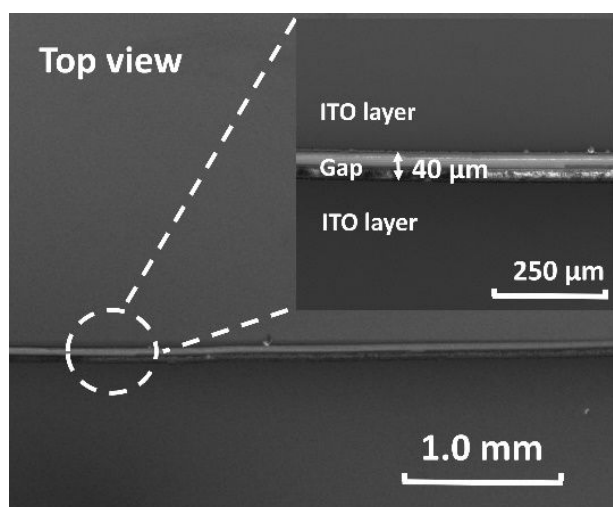


Figure S15. SEM image of the blank ITO electrode. Inset: zoom-in of the gap of the electrode.

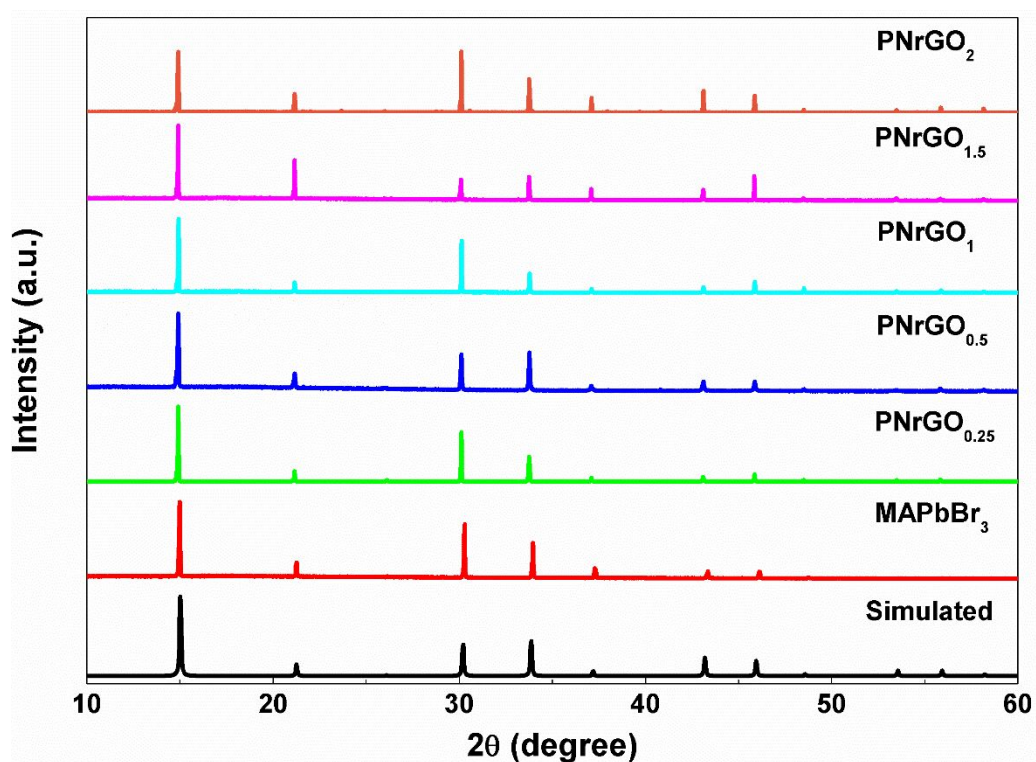


Figure S16. XRD patterns for MAPbBr₃, PNrGO_{0.25}, PNrGO_{0.5}, PNrGO_{1.0}, PNrGO_{1.5}, PNrGO_{2.0}.

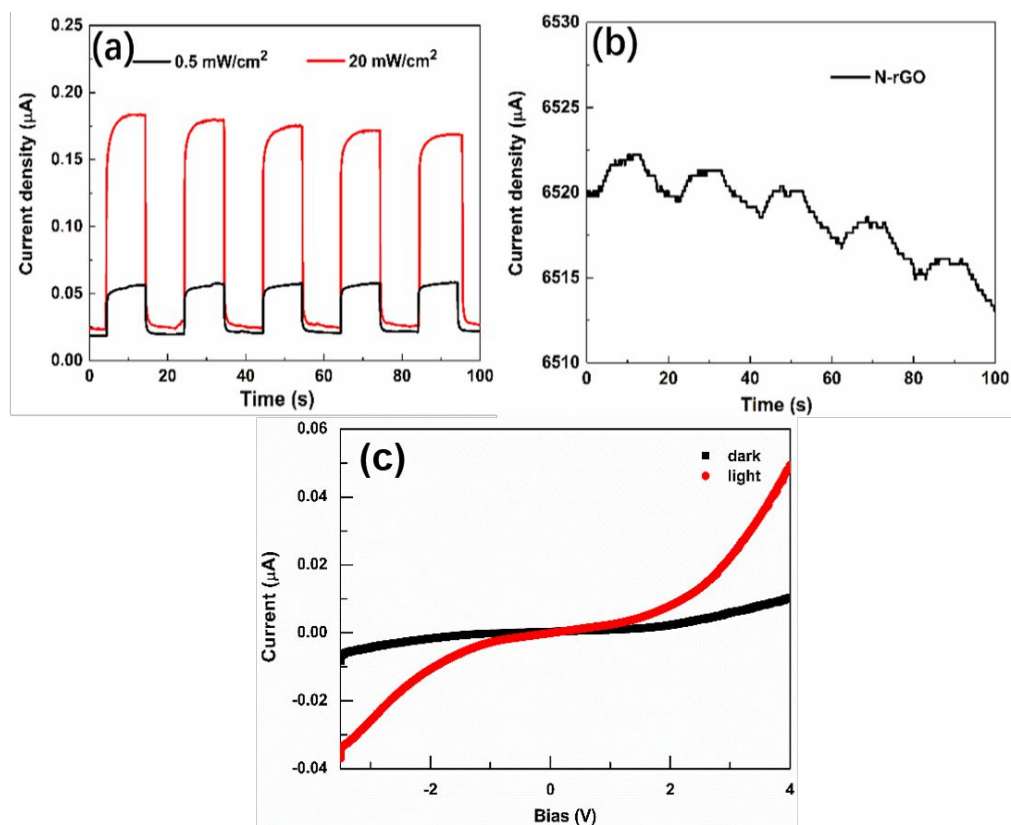


Figure S17. Photocurrent response under 500 nm wavelength light on and off for a) the pure perovskite, MAPbBr₃ and b) N-rGO at voltage of 4V. (c) I-V for pure perovskite under 500 nm wavelength illumination.

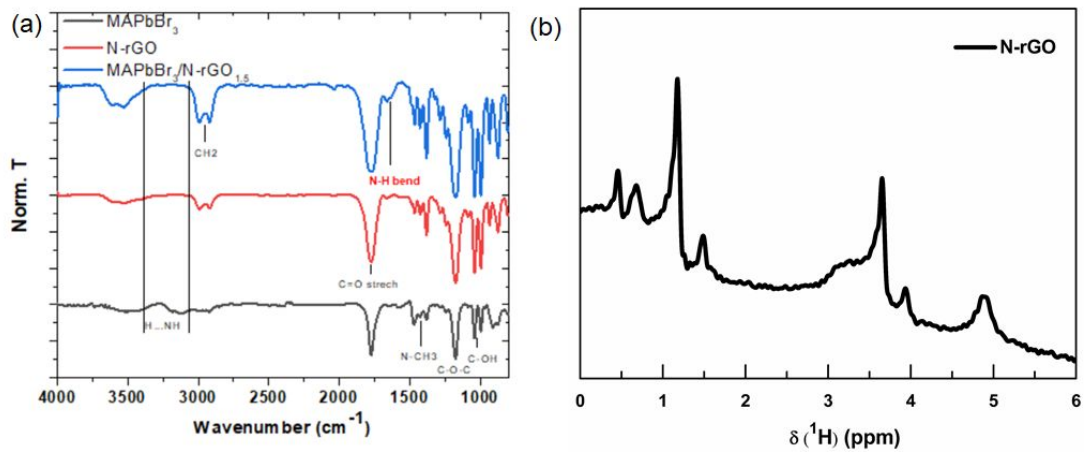


Figure S18. (a) Fourier transform infrared spectra for samples of MAPbBr₃, N-rGO, MAPbBr₃/N-rGO. (b) Solid-state ¹H NMR spectra for N-rGO.

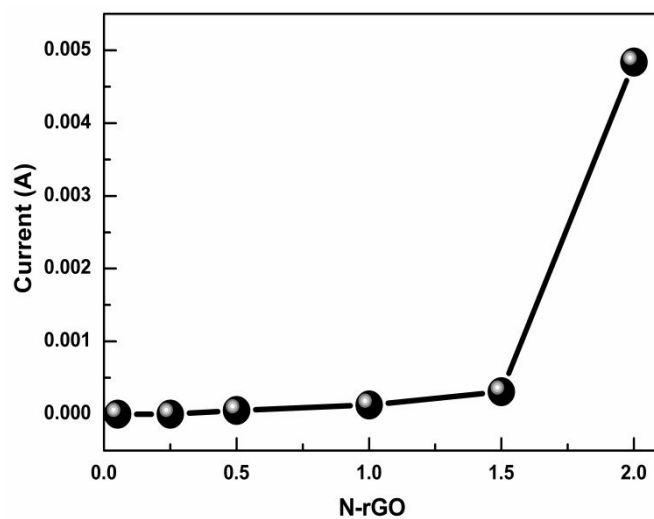


Figure S19. Dark current for different ratios of N-rGO in perovskites.

Table S1. A comparison of N 1s spectrum for N-rGO, MAPbBr₃, and MAPbBr₃/ N-rGO.

N	pyridinic N (eV)	pyrrolic N (eV)	graphitic N (eV)	MA⁺ (eV)
N-rGO	399	400.1	401.5	-
MAPbBr ₃	-	-	-	402.28
PNrGO _{0.25}	399.35	400.22	401.19	401.88
PNrGO _{0.5}	398.84	399.81	400.73	401.79
PNrGO ₁	398.70	399.76	400.87	402.02
PNrGO _{1.5}	398.81	400.02	401.40	402.22
PNrGO ₂	398.84	399.90	400.89	401.83

Table S2. A comparison of Pb 4f and Br 3d spectrum for N-rGO, MAPbBr₃, and MAPbBr₃/ N-rGO.

	Pb 4f_{7/2} (eV)	Pb 4f_{5/2} (eV)	Br 3d_{5/2} (eV)	Br 3d_{3/2} (eV)
MAPbBr ₃	137.99	142.86	67.88	68.93
PNrGO _{0.25}	138.19	143.00	68.03	69.05
PNrGO _{0.5}	138.20	143.10	67.98	69.03
PNrGO ₁	138.32	143.20	67.99	69.07
PNrGO _{1.5}	138.18	143.10	67.94	69.03
PNrGO ₂	138.31	143.13	67.90	68.97

Table S3. A comparison of C spectrum for N-rGO, MAPbBr₃, and MAPbBr₃/ N-rGO.

C	C-C (eV)	C-N (eV)	C-O (eV)	C=O (eV)	C(O)O (eV)
N-rGO	284.8	285.5	287	288.9	291.9
MAPbBr ₃	284.5	285.5	286.5	288.8	-
PNrGO _{0.25}	284.83	285.70	286.76	288.60	291.91
PNrGO _{0.5}	284.79	285.35	286.44	288.59	292.74
PNrGO ₁	284.83	285.52	286.48	288.64	292.91
PNrGO _{1.5}	284.84	285.61	286.65	288.67	292.74
PNrGO ₂	284.83	285.70	286.65	285.70	284.83

Table S4. Dark current and detectivities for the pure perovskite MAPbBr₃, hybrid perovskite/N- rGO materials, PNrGO_{0.25}, PNrGO_{0.5}, PNrGO₁, PNrGO_{1.5}, PNrGO₂.

	MAPbBr ₃	PNrGO _{0.25}	PNrGO _{0.5}	PNrGO ₁	PNrGO _{1.5}	PNrGO ₂
I _{dark} (A)	1.5×10 ⁻⁸	7.2×10 ⁻⁷	4.9×10 ⁻⁵	7.5×10 ⁻⁵	2.9×10 ⁻⁴	4.9×10 ⁻³
D*(Jones)	8.26×10 ⁹	1.03×10 ¹¹	2.88×10 ⁹	1.32×10 ¹⁰	1.39×10 ¹⁰	6.79×10 ⁸

Table S5. Parameters for perovskite-based photodetectors.

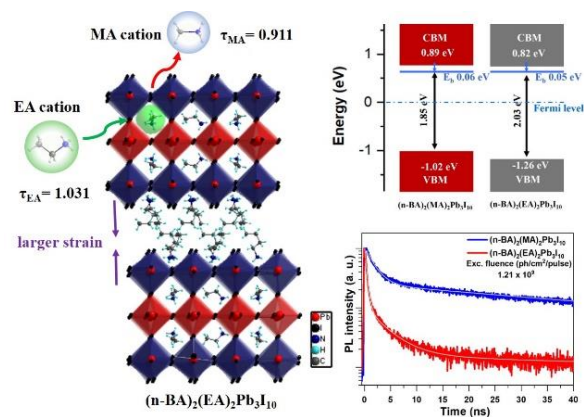
Device Structure	Material structure	Rise/decay time (ms)	EQE (%)	Detectivity (Jones)	Responsivity (A W ⁻¹)	Ref.
ITO/MAPbBr ₃ /Au	Film	81/890 μs	-	1.3×10 ¹³	1.6 × 10 ⁷	1
Au/C ₄ H ₉ NH ₃ PbI ₄ /Au	Single crystals	1.7/3.9 μs	-	2.4×10 ¹³	38	2
Au/ graphene-MAPbI ₃ /Au	Film	-	~5×10 ⁴	10 ⁹	180	3
Au/Si-	Nanowire	55 s/75 s	-	-	2.6 × 10 ⁶	4
SiO ₂ /MAPbI ₃ /graphene/Au	Islands	120/750	-	-	6.0 × 10 ⁵	5
Au/ graphene-MAPbBr ₂ I /Au						
ITO/CsPbBr ₃ /ITO	Microcrystal	0.5/1.6	2×10 ⁷	10 ¹³	6.0 × 10 ⁴	6
Au/CsPbI ₃ /Au	Nanocrystals	0.05/0.15	0.9×10 ⁶	5.17×10 ¹³	2.92× 10 ³	7
Au/CsPbBr ₃ /Au	Porous film	0.35/1.26	658	-	2.7	8
Pt/ CsPbBr ₃ /Au	Single crystal	230/60	6	1.7×10 ¹¹	0.028	9
ITO/MAPbBr ₃ -N-rGO/ITO	Microcrystal	30/100	10 ⁵	10 ¹²	3.6 × 10 ⁴	This work

References

- (1) Yang, Z. Q.; Deng, Y. H.; Zhang, X. W.; Wang, S.; Chen, H. Z.; Yang, S.; Khurgin, J.; Fang, N. X.; Zhang, X. Ma; R. M. High - Performance Single - Crystalline Perovskite Thin - Film Photodetector. *Adv. Mater.* **2018**, *30*, 1704333.
- (2) Wang, K.; Wu, C. C.; Yang, D.; Jiang, Y. Y.; Priya, S. Quasi-Two-Dimensional Halide Perovskite Single Crystal Photodetector. *ACS Nano* **2018**, *12*, 4919-4929.
- (3) Lee, Y.; Kwon, J.; Hwang, E.; Ra, C. -H.; Yoo, W. J.; Ahn, J. -H.; Park, J. H.; Cho, J. H. High - Performance Perovskite - Graphene Hybrid Photodetector. *Adv. Mater.* **2015**, *27*, 41-46.
- (4) Spina, M.; Lehmann, M.; Náfrádi, B.; Bernard, L.; Bonvin, E.; Gaál, R.; Magrez, A.; Forró, L.; Horváth, E. Microengineered $\text{CH}_3\text{NH}_3\text{PbI}_3$ Nanowire/Graphene Phototransistor for Low-Intensity Light Detection at Room Temperature. *Small* **2015**, *11*, 4824-4828.
- (5) Wang, Y. S.; Zhang, Y. P.; Lu, Y.; Xu, W. D.; Mu, H. R.; Chen, C. Y.; Qiao, H.; Song, J. C.; Li, S. J.; Sun, B. Q.; Cheng, Y. -B.; Bao, Q. L. Hybrid Graphene-Perovskite Phototransistors with Ultrahigh Responsivity and Gain. *Adv. Optical Mater.* **2015**, *3*, 1389-1396.
- (6) Yang, B.; Zhang, F. Y.; Chen, J. S.; Yang, S. Q.; Xia, X. S.; Pullerits, T.; Deng, W. Q.; Han, K. L. Ultrasensitive and Fast All-Inorganic Perovskite-Based Photodetector via Fast Carrier Diffusion. *Adv. Mater.* **2017**, *29*, 1703758.
- (7) Yang, T.; Zheng, Y. P.; Du, Z. T.; Liu, W. N.; Yang, Z. B.; Gao, F. M.; Wang, L.; Chou, K. -C.; Hou, X. M.; Yang, W. Y. Superior Photodetectors Based on All-Inorganic Perovskite CsPbI_3 Nanorods with Ultrafast Response and High Stability. *ACS Nano* **2018**, *12*, 1611-1617.
- (8) Xue, J.; Gu, Y.; Shan, Q.; Zou, Y.; Song, J.; Xu, L.; Dong, Y.; Li, J.; Zeng, H. Constructing Mie-Scattering Porous Interface-Fused Perovskite Films to Synergistically Boost Light Harvesting and Carrier Transport. *Angew. Chem. Int. Ed.* **2017**, *56*, 5232-5236.
- (9) Saidaminov, M. I.; Haque, M. A.; Almutlaq, J.; Sarmah, S.; Miao, X. -H.; Begum, R.; Zhumekenov, A. A.; Dursun, I.; Cho, N.; Murali, B.; Mohammed, O. F.; Wu, T.; Bakr, O. M. Inorganic Lead Halide Perovskite Single Crystals: Phase - Selective Low - Temperature Growth, Carrier Transport Properties, and Self - Powered Photodetection. *Adv. Opt. Mater.* **2017**, *5*, 1600704.

Paper II

Electronic Structure and Trap-States of Two-Dimensional Ruddlesden-Popper Perovskites with Relaxed Goldschmidt Tolerance Factor



Electronic Structure and Trap States of Two-Dimensional Ruddlesden–Popper Perovskites with the Relaxed Goldschmidt Tolerance Factor

Mingli Liang,¹ Weihua Lin,¹ Zhenyun Lan, Jie Meng, Qian Zhao, Xianshao Zou, Ivano E. Castelli, Tõnu Pullerits, Sophie E. Canton,* and Kaibo Zheng*



Cite This: *ACS Appl. Electron. Mater.* 2020, 2, 1402–1412



Read Online

ACCESS |



Metrics & More



Article Recommendations



Supporting Information

ABSTRACT: Two-dimensional Ruddlesden–Popper perovskites (2D RPPs) have been considered as promising building blocks for optoelectronic applications owing to optical properties comparable to the ones of 3D perovskites, together with superior stability. In addition, the more flexible structure adopted by such perovskites leads to a relaxation of the Goldschmidt tolerance factor (τ) requirement. Herein, we compare the crystalline and electronic structures, as well as the photophysics of two 2D perovskite single crystals $(n\text{-BA})_2(\text{MA})_2\text{Pb}_3\text{I}_{10}$ (BMAPI) and $(n\text{-BA})_2(\text{EA})_2\text{Pb}_3\text{I}_{10}$ (BEAPI) ($n\text{-BA} = n\text{-butylamine}$) containing small A-cations (MA, methylammonium) and large A-cations (EA, ethylammonium), respectively. The latter presents a relaxed τ ($\tau_{\text{EA}} > 1$) compared with the requirement of a stable phase in 3D perovskites ($\tau < 1$). Such relaxed τ is beneficial from the structural flexibility of the long organic cation bilayer and the pronounced lattice distortions in the 2D perovskite structures. We further elucidate how the greater lattice distortions concurrently modulate the electronic structure as well as trap densities in these 2D RPPs. The electronic band gap (E_g) of BEAPI (2.08 ± 0.03 eV) is ~ 0.17 eV larger than the one of BMAPI (1.91 ± 0.03 eV). This is mainly because of a shift in the valence band maximum associated with the expansion of the Pb–I bond length in BEAPI. In addition, the overall trap state densities for BMAPI and BEAPI are calculated to be $\sim 2.18 \times 10^{16}$ and $\sim 3.76 \times 10^{16}$ cm^{-3} , respectively, as extracted from the time-resolved photoluminescence studies. The larger trap density in BEAPI can be attributed to the stronger interfacial lattice distortion that sets in when large EA cations are contained into the inorganic crystal lattice.

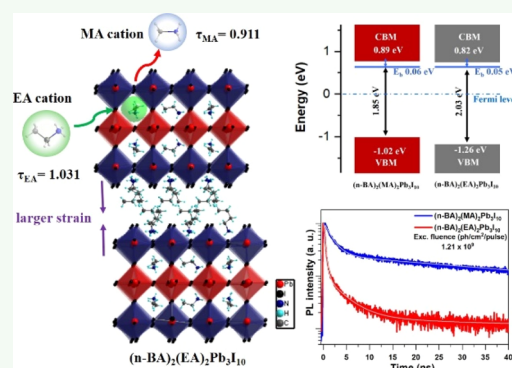
KEYWORDS: two-dimensional Ruddlesden–Popper perovskites, Goldschmidt tolerance factor, lattice distortions, electronic structure, trap densities

INTRODUCTION

Over the past decade, metal halide perovskite materials have occurred as a forefront kind of innovative materials suited for the next generation of cost-efficient optoelectronic devices. This is due to their advantageous physical properties, such as strong light absorption, slow charge carrier recombination rate, and high carrier mobility.^{1–8} The certified efficiencies of the perovskite photovoltaic devices have been improved from 3.8 to 25.2% within the past 10 years.^{9,10} In addition, these materials also show good prospects for advanced applications, such as light-emitting diodes, photodetectors for various wavelength regions as well as lasing devices.^{11–22} However, the conventional three-dimensional (3D) lead halide perovskites holding the chemical formula of APbX_3 (here A refers to a cation, X refers a halide) suffer from structural instability triggered by exposure to moisture. This problem can be potentially solved by utilizing 2D Ruddlesden–Popper perovskite (RPP) derivatives, with generic formula of

$(\text{B})_2(\text{A})_{n-1}\text{Pb}_n\text{X}_{3n+1}$ (where A refers to the same small cation, B refers an long chain organic spacing cation, n is the number of lead halide octahedra layers).^{23–26} 2D RPPs are constructed by repeating inorganic perovskite layers and organic spacing cations, so that they exhibit an enhanced structural flexibility compared with 3D perovskites.^{27–29} Their electronic band gap (E_g) is determined by the thickness of the inorganic perovskite layers (i.e., the value of n), thereby extending greatly the diversity of their properties and possible applications.

In general, the formation of 3D APbX_3 perovskites is governed by the Goldschmidt tolerance factor (τ), a



Received: March 5, 2020

Accepted: April 23, 2020

Published: April 23, 2020



geometrical parameter related to the ionic radii of the elemental constituents, defined as follows

$$\tau = \frac{r_A + r_X}{\sqrt{2}(r_{Pb} + r_X)} \quad (1)$$

where r_A , r_{Pb} , and r_X are the effective radii of the A-cations, the Pb^{2+} , and the halogen X ions, respectively. In principle, τ needs to fall into the range from 0.8 to 1.0 for the stable cubic or distorted 3D perovskite structures to be formed.^{30,31} In this scenario, only a limited number of small A-cations, such as the cesium cation (Cs^+), the methylammonium (MA), and the formamidinium (FA) cations could be employed to realize the Pb-based perovskite lattice.³² However, it has been recently realized that the strong restriction of the τ range can be relaxed in 2D RPPs, which allows larger A-cations, such as ethylammonium (EA) and guanidinium (GA) to fill the inorganic $[PbI_3]^-$ cages. The 2D RPPs that have been reported so far include $EA_4Pb_3X_{10}$ ($X = Cl, Br, \text{ or } I$),^{33,34} $(n\text{-}BA)_2(EA)_2Pb_3I_{10}$ ($n\text{-}BA = n\text{-}butylamine$),³⁵ $(n\text{-}PA)_2(GA)Pb_2I_7$ ($n\text{-}PA = n\text{-}pentylammonium$),³⁶ and $(n\text{-}HA)_2(GA)Pb_2I_7$ ($n\text{-}HA = n\text{-}hexylammonium$).³⁷ Compared to the 2D RPPs using the usual A cations (i.e., Cs^+ , MA, or FA), they all exhibit greater structural distortions identified through elongated Pb–X bond lengths and tilted X–Pb–X bond angles in the $[PbX_6]^{4-}$ octahedron motif.

In this paper, we systematically study the effect of the lattice distortions on the electronic structure and photo-physical properties of 2D RPPs as a function of the relaxed tolerance factor. We target two benchmark single crystals with similar molecular composition, namely, $(n\text{-}BA)_2(MA)_2Pb_3I_{10}$ (BMAPI) and $(n\text{-}BA)_2(EA)_2Pb_3I_{10}$ (BEAPI). We confirmed a relaxed τ in BEAPI. The larger electronic band gap (E_g) of BEAPI compared to the one of BMAPI has been rationalized by the elongated Pb–I bond length. In addition, time-resolved photoluminescence (TRPL) studies of the two compounds reveal long-lived trap states in both of them. We observe dynamic trap filling under repetitive laser pulse excitation. By modeling the trap filling process, we can evaluate the trap state density of these two compounds to be $\sim 3.76 \times 10^{16} \text{ cm}^{-3}$ for BEAPI and $\sim 2.18 \times 10^{16} \text{ cm}^{-3}$ for BMAPI. The larger trap density in the EA-based 2D RPP can be attributed to the more severe lattice distortion. These results provide robust references for the intrinsic properties of new type of 2D perovskites with relaxed tolerance factor toward materials engineering and for further implementations into improved devices.

MATERIAL AND METHODS

PbI_2 (99%), methanamine hydriodide (98%, MAI), ethylamine hydriodide (98%, EAI), n -butylammonium iodide (98%, n -BAI), hypophosphorous acid solution (50%, in water), and hydroiodic acid (57%, in water) have been utilized without further treatment. All of the chemicals were supplied by Sigma-Aldrich.

Synthesis of BMAPI and BEAPI Single Crystals. The single crystals of the two compounds BMAPI and BEAPI were prepared by the temperature lowering method of PbI_2 , MAI/EAI, and n -BAI in 5 mL hydroiodic acid. The precursor solution contained PbI_2 (1.5 mmol, 0.691 g), EAI (3.0 mmol, 0.519 g), and n -BAI (2.0 mmol, 0.402 g) for BEAPI; PbI_2 (1.5 mmol, 0.691 g), MAI (2.5 mmol, 0.395 g), and n -BAI (2.0 mmol, 0.402 g) for BMAPI. The mixtures were placed into glass bottles (20 mL), and 0.25 mL of hypophosphorous acid was added to prevent the hydroiodic acid from being oxidized. Afterward, the glass bottles were sealed and stirred at room temperature to induce the formation of red colored precipitates. Completely clear solutions were obtained after reaction for few

minutes at 80 °C as precursor. Bulk single crystals were grown from such solution at a cooling rate of 0.5 °C/day starting from 55 °C. The schematic diagram of the synthesis process and the obtained crystals are shown in Figure S1. The purity of these two crystals was characterized by powder X-ray diffraction (XRD) studies (Figure S2).

Single Crystal Crystallography. Crystallographic data for these two single crystals were collected on SuperNova Dual Wavelength CCD diffractometer (Agilent Technologies) equipped with a graphite-monochromatic Mo $K\alpha$ radiation ($\lambda = 0.71073 \text{ \AA}$) at the room temperature ($\sim 298 \text{ K}$) with the detailed procedures and following data treatment identical to our previous work.³⁸ The detailed crystallographic data with structural refinement parameters for these two compounds are provided in Table S1 with the final crystallographic data in CIF and checked CIF results also given (in the Supporting Information). The Pb–I bond lengths and I–Pb–I angles are listed in Tables S2 and S3, respectively.

Spectroscopy Studies. The absorption spectra were measured by a UV–vis–NIR absorption spectrophotometer (PerkinElmer, Lambda 1050). Powder XRD patterns were measured on a Rigaku MiniFlex II diffractometer using Mo $K\alpha$ radiation ($\lambda = 1.5406 \text{ \AA}$). The Raman measurements (InduRAM, HORIBA Jobin Yvon) were performed with excitation at around 795 nm. X-ray photoelectron spectroscopy (XPS) (Thermo Scientific) was employed to study the elemental composition and the electronic structure of the compounds, with an X-ray photon energy of 1486 eV (Al $K\alpha$ X-ray source). The steady-state PL spectra were acquired on a spectrometer (Avantes AvaSpec-2048) under an excitation wavelength of 405 nm. The TRPL measurements were performed by time-correlated single photon counting (PicoHarp) using a pulsed diode laser (Wavelength: 438 nm; Frequency: 2.5 MHz; Pulse duration: 40 ps; A long-pass filter from 450 nm) and a fast avalanche photodiode. It is important to note that during all photophysical measurements the bulk crystals were exfoliated with scotch tapes in order to expose fresh surfaces.

Computational Method. All calculations were implemented in the framework of density functional theory (DFT), using the Atomistic Simulation Environment (ASE), Vienna ab initio simulation package (VASP), and GPAW codes.^{39–42} The structures were optimized using VASP and the generalized gradient approximation PBEsol exchange–correlation functional.⁴³ The electronic wave functions were calculated by using projected augmented wave (PAW).⁴⁴ The cutoff energy for the plane-wave basis was set to be 500 eV. The Brillouin zone samplings were carried out with a Γ -center $5 \times 1 \times 5$ k -point mesh. The atomic forces were relaxed to be less than 0.01 \AA^{-1} . Because of the well-known issue with the underestimation of the band gap, the GLLB-SC exchange–correlation functional has been used to calculate the electronic properties.⁴⁵ Thanks to the explicit calculation of the derivative discontinuity, it has been shown that this functional gives a very good estimation of the band gap at a reasonable computational cost.^{46,47} The Brillouin zone samplings were carried out using a Γ -center point mesh, with density of 8 k -point/ \AA . Spin–orbit coupling (SOC) corrections were included.

RESULTS AND DISCUSSION

Relaxed Tolerance Factor and Intraoctahedral Distortions in the 2D RPPs. In general, the 3D $APbX_3$ perovskites are stable only when their τ -value falls between 0.8 and 1.0.^{30,31,48} For instance, MA with an effective radius of 217 pm has a τ -value of 0.911; thus, $MAPbI_3$ is easy to crystallize in the stable perovskite phase. However, $EAPbI_3$ tends to crystallize in an orthorhombic space group $Pna2_1$ (no. 33) at room temperature and cannot form a traditional continuous 3D perovskite lattice (Figure S3).⁴⁹ This is due to the larger effective radius of EA ($r_{EA} = 274 \text{ pm}$), which leads to a τ -value of 1.031. Interestingly, BEAPI can exist at room temperature. This indicates that the conventional τ -value threshold can be relaxed if the target compound is expected to adopt a 2D structure rather than a 3D structure. Fu, et al.

attributed this phenomenon to the fact that the strain accumulation caused by larger A-cations is compensated by the separating flexible organic layers.³⁷ The organic spacing cations act as “buffers” to the compression imposed on the rigid inorganic layers. The large strain accumulation is directly reflected by the increased distortion of the $[\text{PbI}_6]^{4-}$ octahedron that form the inorganic layers. To get detailed insight into the lattice distortion, the $[\text{PbI}_6]^{4-}$ octahedral structures in BMAPI and BEAPI were systematically compared.

In order to ensure the accuracy of the structural comparisons and exclude the impact from nonstructural factors, we have collected their single crystal data at room temperature (~ 298 K). BMAPI crystallizes in the orthorhombic space groups $Aba2$ (no. 41), while BEAPI crystallizes in the orthorhombic space groups $Cmc2_1$ (no. 36). Despite the different space groups, they both belong to the homologous series of 2D RPPs phases $(\text{B})_2(\text{A})_{n-1}\text{Pb}_n\text{X}_{3n+1}$ with $n = 3$ and identical periodic layered structure (Figure 1a,b). In their lattices, the organic cations are

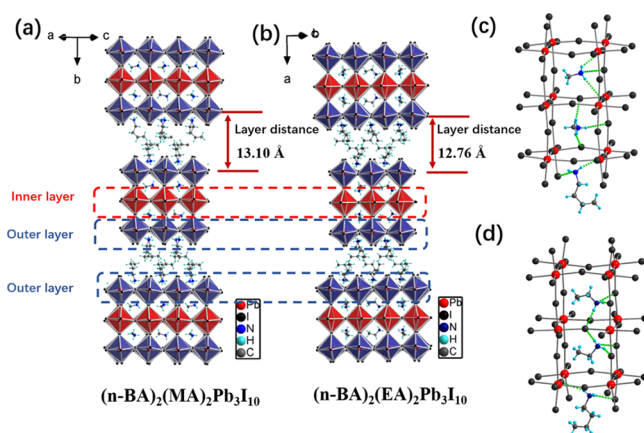


Figure 1. Detailed structure of (a) BMAPI and (b) BEAPI, where the inner layers (red) consist of “slightly distorted” while the outer layers (blue) consist of “largely distorted” octahedra; strong hydrogen bonding in (c) BMAPI and (d) BEAPI is indicated in green.

intercalated into the 2D octahedron layered quantum wells through the inorganic units via $\text{N}-\text{H}\cdots\text{I}$ hydrogen bonds.⁵⁰ The green dashed lines in Figure 1c,d represent the strong $\text{N}-\text{H}\cdots\text{I}$ hydrogen bonds. The corresponding bond lengths and angles are shown in Table S4. The three inorganic monolayers in the 2D quantum wells can be classified into an inner layer (red) and two outer layers (blue).

It is clear that all of the $[\text{PbI}_6]^{4-}$ octahedra in BMAPI and BEAPI are distorted. The characteristic Pb–I bond lengths present in the two compounds are indicated in Figure 2a. For BMAPI, the longest and shortest Pb–I bond lengths are 3.3040(12) and 3.0521(15) Å, respectively, with a difference of ~ 0.25 Å. For BEAPI, the longest and shortest Pb–I bonds are [3.457(2) Å, red dotted lines] and [3.010(2) Å] so that the difference now reaches ~ 0.45 Å (Table S1). Furthermore, their I–Pb–I bond angles are also tilted. The minimum I–Pb–I trans-angles of BMAPI and BEAPI are only $175.72(5)^\circ$ and $167.94(4)^\circ$, respectively, which are both far from 180° (Table S2). A quantitative comparison of the lattice distortion in the two compounds can be performed by evaluating the intra-octahedral distortions parameters,^{51,52} consisting of the average metal–halide (Pb–I) the bond distance parameter ($\langle D \rangle$), distance distortion parameter (ζ), tilting distortion parameter

(Δ), torsional distortion parameter (Θ), and angle distortion parameter (Σ) which are defined as follows

$$\langle D \rangle = \left(\sum_{i=1}^6 d_i \right) / 6 \quad (2)$$

$$\zeta = \sum_{i=1}^6 |d_i - \langle D \rangle| \quad (3)$$

$$\Delta = \sum_{i=1}^6 \left(\frac{d_i - \langle D \rangle}{\langle D \rangle} \right)^2 \quad (4)$$

$$\Theta = \sum_{i=1}^{24} |60 - \theta_i| \quad (5)$$

$$\Sigma = \sum_{i=1}^{12} |90 - \varphi_i| \quad (6)$$

The d_i are the individual Pb–I bond distances in the $[\text{PbI}_6]^{4-}$ octahedron. θ_i are the angles of the 24 unique projections of the I–Pb–I angles to the triangular faces of the $[\text{PbI}_6]^{4-}$ octahedron along its pseudo-3-fold axis. φ_i are the 12 cis-angles of I–Pb–I around the Pb atom. Among these five parameters, $\langle D \rangle$, ζ , and Δ are related to the distortions of Pb–I bond length. Θ represents the distortion of the $[\text{PbI}_6]^{4-}$ geometry from perfectly octahedral symmetry (O_h) to trigonal prismatic symmetry (D_{3h}), a process known as the Bailar trigonal twist.⁵² Σ is the sum of the $|90 - \varphi_i|$, which a general measure of the deviation from an ideal octahedron. In principle, the larger values of these parameters indicate the greater degree of $[\text{PbI}_6]^{4-}$ intra-octahedral distortions, shown in Figure 2b–f with specific values listed in Table S5. Comparing the values of the five parameters provides a global overview into the $[\text{PbI}_6]^{4-}$ octahedra distortions. As expected, the values of the five parameters are identical for the $[\text{PbI}_6]^{4-}$ octahedra from the two outer layers for both complexes because they are in the same chemical coordination environment.

First, as shown in Figure 2b, the $\langle D \rangle$ values of BEAPI are much larger than those of BMAPI. This is due to the large EA cations filling the $[\text{PbI}_3]^-$ cages, which increases the strain accumulation of the inorganic layers, thereby elongating the Pb–I bonds. Moreover, the $\langle D \rangle$ value of the outer layers is higher than that of the inner layers in BMAPI. The reverse holds in BEAPI. This is mainly due to a very short Pb2–I6 bond of only 3.010(2) Å. The two parameters ζ and Δ describe the uniformity of the six Pb–I bond lengths in a $[\text{PbI}_6]^{4-}$ octahedron. As seen in Figure 2c,d, the ζ and Δ values of the outer layers are much larger than those of the inner layer. It is attributed to the strain relaxation occurring at the $[\text{PbI}_6]^{4-}$ octahedra in the outer layer, due to lower geometric constraint, aided by the structural flexibility of the long organic spacing cations outside the cages that accommodate the $[\text{PbI}_6]^{4-}$ octahedral distortions. The same situation is also reflected by the two angle-dependent Θ and Σ parameters. Figure 2e,f shows a greater trigonal angular distortion of the $[\text{PbI}_6]^{4-}$ octahedra in BEAPI. Overall, the five parameters are all larger for BEAPI than for compared to BMAPI. This is in line with the distance between the two inorganic layers being ~ 13.10 Å for BMAPI and ~ 12.76 Å for BEAPI as a sign of compression in the latter (Figure 1a,b).

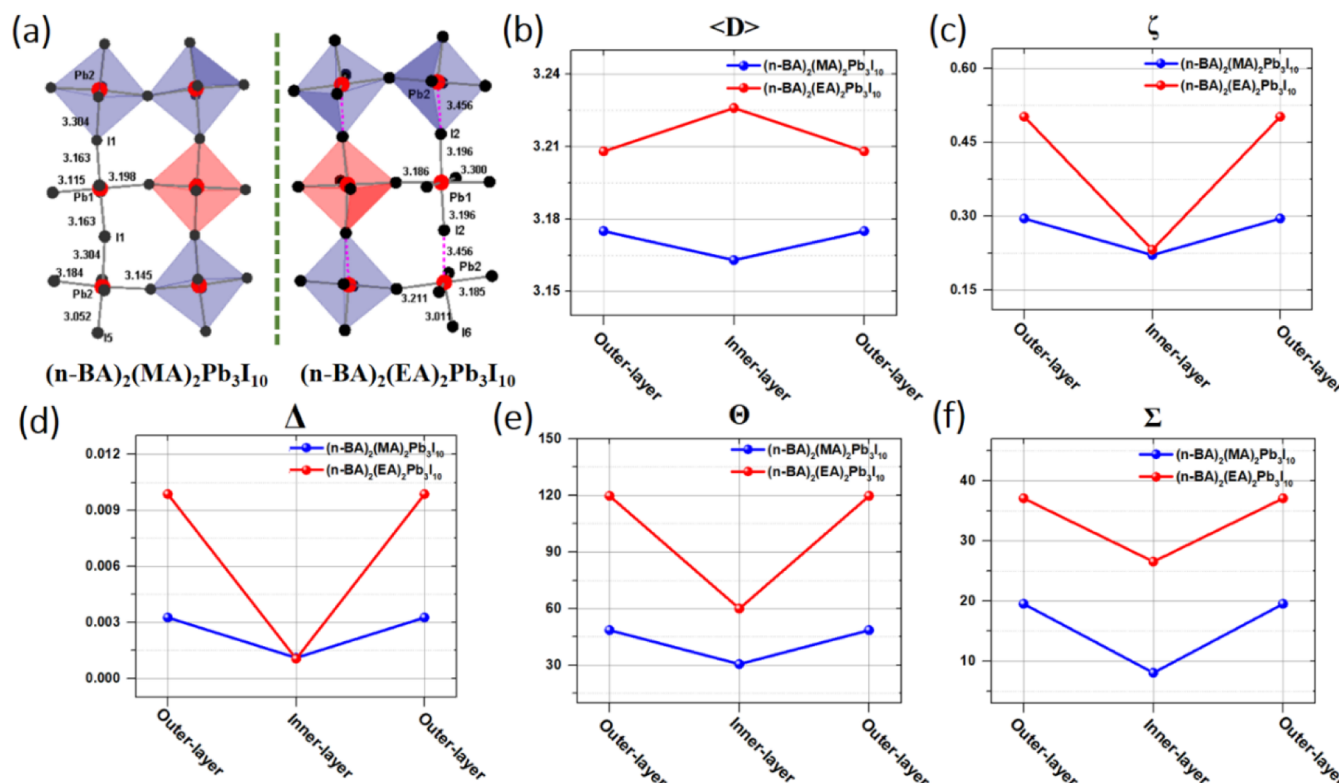


Figure 2. (a) Inorganic lattice and the $[\text{PbI}_6]^{4-}$ octahedral distortions in BMAPI and BEAPI; the magnitude of $[\text{PbI}_6]^{4-}$ octahedral distortion parameters: (b) bond distance parameter ($\langle D \rangle$), (c) distance distortion parameter (ζ), (d) tilting distortion parameter (Δ), (e) torsional distortion parameter (Θ), and (f) angle distortion parameter (Σ).

To summarize, we find both an increase in $[\text{PbI}_6]^{4-}$ octahedral distortions and an increase in compression for organic layers in BEAPI, which all account for the stable accommodation of larger EA cations in the $[\text{PbI}_3]^-$ cages. However, we found that 2D RPP ($n\text{-BA}$ as the spacing cation) with even larger A-cations like GA (with a τ -value of 1.039) is not stable any more.

Vibrational Modes of the MA and EA Cations in the $[\text{PbI}_3]^-$ Cages. In order to compare the vibrational modes of the MA and EA cations in the $[\text{PbI}_3]^-$ cages of the two compounds, we measured the Raman spectra of the crystals with an excitation around 795 nm, which was chosen to avoid strong background photoluminescence. The measurement range was determined such that the internal vibrations of the organic cations dominated over the mixed modes involving the organic cations and inorganic units.⁵³ To clearly identify the vibrational modes of the EA cation, we also compared our experimental results with the theoretical calculations performed for the isolated cation (Figure S4). As shown in Figures 3 and S5, the peaks observed at 1468.0 cm^{-1} for BMAPI and 1467.2 cm^{-1} for BEAPI can be assigned to the symmetric NH_3 deformation. The peaks at 1571.6 cm^{-1} for BMAPI and 1568.3 cm^{-1} for BEAPI are attributed to the asymmetric NH_3 deformation.^{53,54} Only a small red shift of these peaks can be noted between the two compounds, a finding which complies with their similar average bond lengths of $\text{N}\cdots\text{I}$ hydrogen bonds (Table S4). The average $\text{N}\cdots\text{I}$ hydrogen bond distance in BEAPI [2.934(10) Å] is only slightly smaller than that in BMAPI [3.092(10) Å]. This implies that the NH_3 unit in BEAPI interacts slightly more with the $[\text{PbI}_3]^-$ cages. The peak of BMAPI at 960 cm^{-1} can be assigned to the MA rocking mode. In contrast, the EA rocking peak appears at

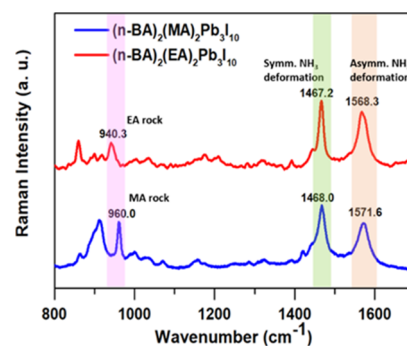


Figure 3. Raman spectrum of BMAPI and BEAPI.

940.3 cm^{-1} , with a large red shift of ~ 20 cm^{-1} . This suggests that the rocking degree of freedom of the EA cations in $[\text{PbI}_3]^-$ cages is limited due to their larger sizes.⁵⁵

Impact of the Relaxed Tolerance Factor on the Electronic Band-Edge Properties. In general, the changes in the lattice structure induce an alteration of the physical properties in semiconductors, especially the electronic band-edge properties. We first measured the optical band gaps (E_{opt}) of both BMAPI and BEAPI. The UV-vis absorption spectra of BEAPI (Figure 4a) show the absorption band edge at ~ 611 nm, which is blue-shifted by ~ 59 nm compared with BMAPI (located at ~ 670 nm). This difference refers to a widening of E_{opt} from 1.85 ± 0.01 to 2.03 ± 0.01 eV according to the Tauc plots, respectively (inset of the Figure 4a). It is well known that the electronic band gap E_g the semiconductors is actually the sum of E_{opt} and the exciton binding energy (E_b).⁵⁶ Therefore, we measured the E_b of the 2D RPP using temperature-dependent PL (for details of E_b calculation see S5).⁵⁷ The

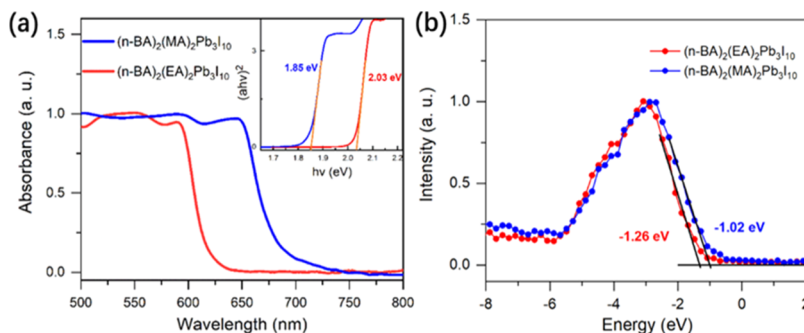


Figure 4. (a) Steady-state absorption spectrum. Insert: Tauc plot representing the band gap of BMAPI and BEAPI, respectively. (b) XPS valence band spectra for the BMAPI and BEAPI.

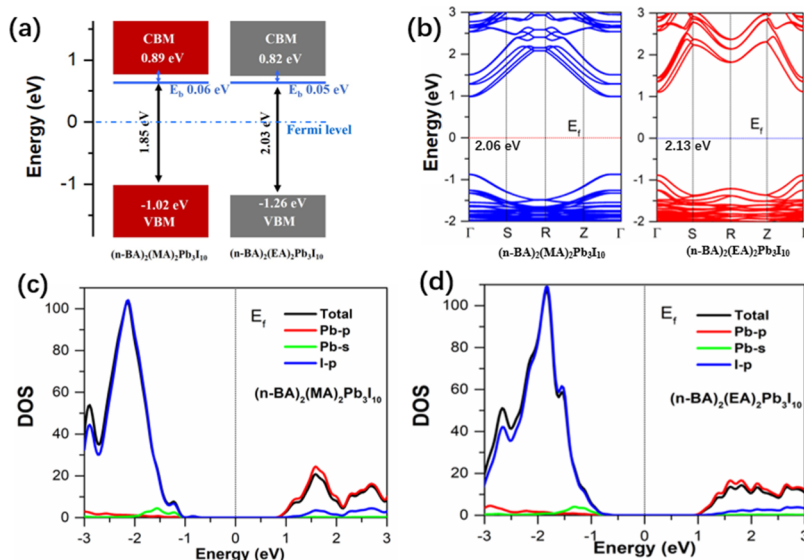


Figure 5. (a) Band alignment between BMAPI and BEAPI, the zero energy level corresponds to the Fermi level; (b) band structure of two compounds with SOC calculated from the experimental crystallographic structure; the PDOS diagrams of (c) BMAPI and (d) BEAPI. The Fermi energy is set to zero; MA/EA and *n*-BA mainly interact with the inorganic framework via hydrogen bonding and are not shown in the figure for clarity.

calculated E_b of BMAPI and BEAPI are 65.8 ± 10 and 46.4 ± 10 meV, respectively. Therefore, the final E_g -values are 1.91 ± 0.03 and 2.08 ± 0.03 eV for BMAPI and BEAPI, respectively. We note that the calculated E_b values are smaller than the results obtained with other methods, which is probably due to the minor contribution of the shallow traps on the dissociation of the excitons.^{58,59} However, the present relative comparison between the two samples should be still valid.

The energy positions of the valence band maximum (VBM) with respect to the Fermi level (zero energy) are then established from the XPS spectra displayed in Figure 4b. A clear up-shift of the VBM in BEAPI (-1.26 ± 0.03 eV) by ~ 0.24 eV is observed in comparison with BMAPI (-1.02 ± 0.03 eV). It should be noted that it is very close to the difference of E_{opt} . As the definition of electronic band gap E_g is the difference between the energies of the conduction band minimum (CBM) and VBM [that is, $E_g = E(\text{CBM}) - E(\text{VBM})$], we can now locate the CBM levels of two compounds as shown in Figure 5a.

In order to elucidate the nature of the band gap and the correlation between the electronic and geometric structures in these two materials, the DFT band structures, including SOC corrections, were calculated based on the crystal structures determined experimentally, as shown in Figure 5b. The lowest

energy of the CBs and highest energy of the VBs of BMAPI and BEAPI are all located at the Γ points, meaning the direct band gap character of these semiconductors. These bands are mostly composed of I p, Pb p, and Pb 6s states, respectively, as previously shown for other hybrid perovskite materials.^{27,60} We found consistency between the experimental and computational values of the gap: the calculated gaps are 2.06 and 2.13 eV for BMAPI and BEAPI, respectively, while the experimental values are 1.91 and 2.08 eV. The projections of the density of states (PDOS) on the different constituent atoms indicate that the VBMs for both compounds are mainly due to the I 5p and Pb 6s orbitals, whereas the CBMs mainly originate from the I 5p and Pb 6p orbitals (Figure 5c,d).

From the XPS spectra shown in Figure 6a, we can clearly see that the binding energy of the Pb 4f core levels is lower in BMAPI than in BEAPI (with a shift ~ 0.2 eV). This means that the electronic density at the Pb center is higher in BMAPI than in BEAPI, owing to the more pronounced delocalization of the outer charges caused by a shorter Pb–I distance. On the other hand, the XPS spectra of the I 3d core level are identical in two compounds (Figure 6b) indicating similar chemical environments around the I atoms. A possible reason could be the contribution of N–H \cdots I hydrogen bonding between N and I

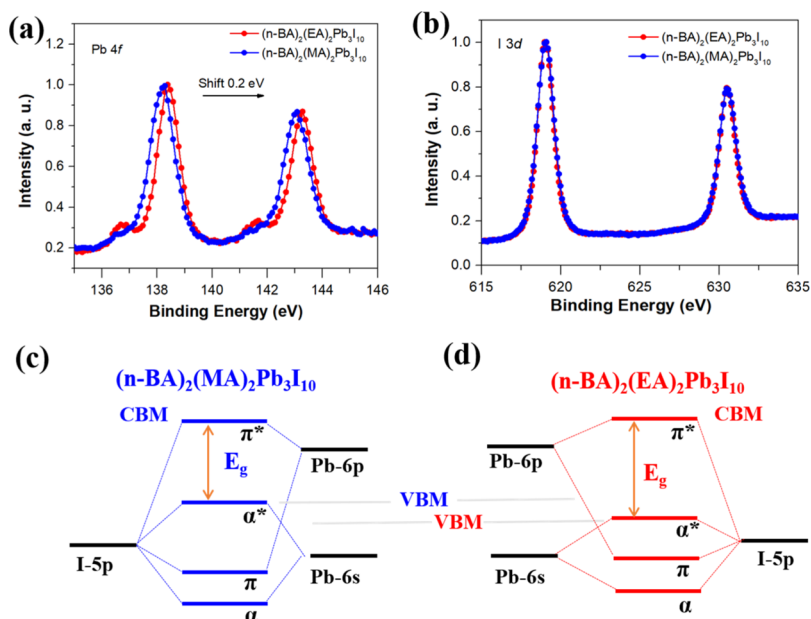


Figure 6. XPS core level emission of (a) Pb 4f doublet and (b) I 3d doublet; and the lone-pair model with stereochemical activity of the s^2 electrons in the (c) BMAPI and (d) BEAPI.

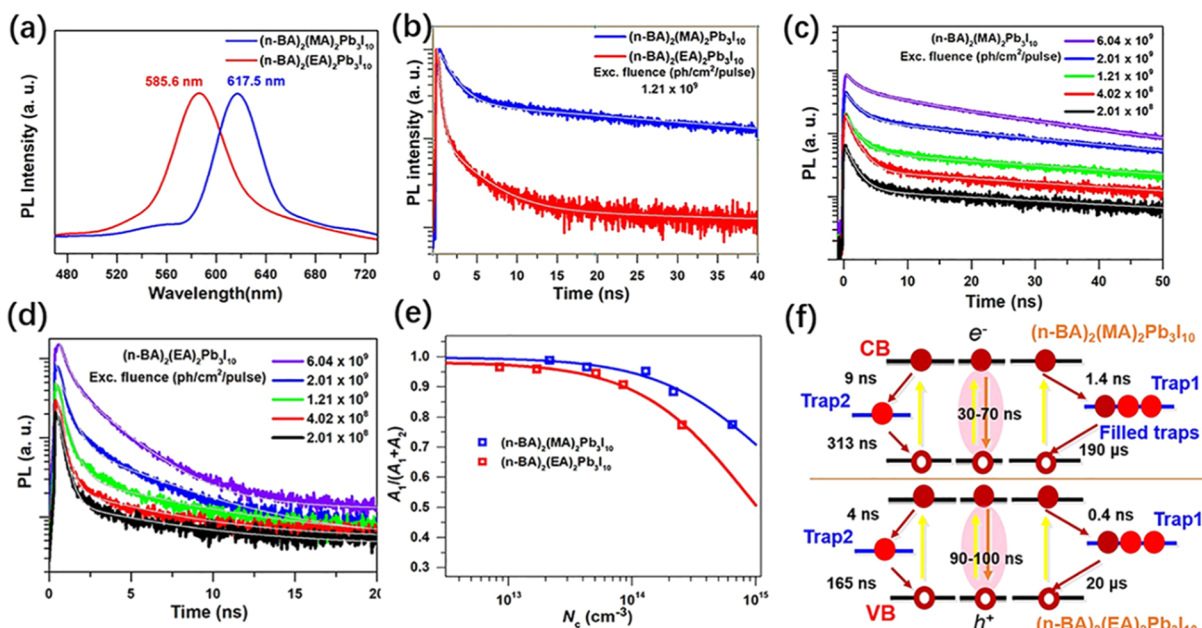


Figure 7. (a) Steady-state PL and (b) transient PL of BMAPI and BEAPI crystals. PL decay kinetics with different excitation fluence for (c) BMAPI and (d) BEAPI. (e) Amplitude ratios $A_1/(A_1 + A_2)$ extracted from the multiexponential fitting of the decays vs the initial charge carrier densities N_c for two compounds. (f) Illustration of the trap-mediated charge recombination in the two compounds.

that could balance the charge reorganization within the Pb–I covalent bond.

Based on the DOS calculations for BMAPI and BEAPI and other published results, the VBM of lead iodide perovskites mainly consists of the anti-bonding combination between the Pb 6s and I 5p orbitals, while their CBM consists of the slightly anti-bonding combination of the Pb 6p and I 5p orbitals.⁶¹ In other words, the electronic band edges of these two compounds are determined by the bonding in the $[\text{PbI}_6]^{4-}$ octahedral unit. The orbitals of the organic molecules are either too deep in the VB or too high in the CB, so that they do not participate to the electronic band edges.^{27,61} The

electronic band edge models of EA and MA materials are illustrated in Figure 6a,b. We notice that the 6s and 6p orbitals from Pb^{2+} are mixed despite the fact that, in a perfect metal octahedron MX_6 , this should not happen based on stringent selection rules associated with symmetry upon inversion. However, as a lone-pair metal cation, Pb^{2+} possesses a pair of $6s^2$ electrons in its valence shell. This ion is usually observed to be off-centered within the X_6 cage,^{62,63} which is quantified through the distortion parameters of the $[\text{PbI}_6]^{4-}$ octahedron discussed above. A well-accepted explanation for the off-centering of Pb^{2+} distortion is that the lone-pair is stereochemically active. The resulting covalent hybridization of the

6s and 6p orbitals of Pb^{2+} causes a nonspherical electronic distribution.⁶¹

Structurally, the Pb–I bond distance ($\langle D \rangle$ parameter) of BMAPI is shorter than that for BEAPI. This reflects a stronger interaction, hence a larger degree of charge delocalization over the I 5p and Pb 6s orbitals. As such, the energy difference between the bonding orbitals (σ) and anti-bonding orbitals (σ^*) increases. Therefore, the VBM position of BMAPI is higher than that of BEAPI. In contrast, unlike the hybridization mode between I 5p and Pb 6s orbitals, I 5p and Pb 6p orbitals are hybridized into bonding orbitals (π) and anti-bonding orbitals (π^*), with the CBM being less affected by Pb–I bond distance. Hence, in Figure 6a,b the CBM positions of BMAPI and BEAPI are almost identical.

Impact of the Relaxed Tolerance Factor on the Trap-Mediated Charge Recombination. The different lattice distortions associated with the relaxed tolerance factor are also expected to affect the photo-physical properties of the two compounds, as shown in Figure 7. First, the steady-state PL spectrum of BEAPI (585.6 nm) is clearly blue-shifted compared to the one of BMAPI (617.5 nm) (Figure 7a). This is mainly ascribed to the differences in their E_g . Moreover, we find that the PL lifetime of BEAPI is much shorter than the one of BMAPI (Figure 7b). Under the same excitation fluence (1.21×10^9 ph/cm²/pulse), the average PL lifetime of BMAPI ($t_{\text{average}} = 5.86$ ns) is approximately 6.5-fold longer than that of BEAPI ($t_{\text{average}} = 0.90$ ns) (Tables S6 and S7). Here, it should be noted that in order to avoid the effect of edge emission of the crystal on the PL kinetics during the TRPL measurements, we focused the laser spot only on the flat bulk area of the crystal flakes (Figure S7). We can fit adequately the PL decays using triexponential decays including a fast component (t_1), medium component (t_2), and slow component (t_3). It should be first noted that owing to the low exciton binding energy of our 2D perovskite crystals and the low excitation concentration during the TRPL measurement, the majority of the photo-generated species should be free carriers (see the calculation in S7 and S8). In this scenario, we can associate the slow component to the intrinsic bimolecular recombination. The other two faster components, although very often assigned to nonradiative trap-mediated recombination, can have various origins, such as Auger process, photo-chemically induced reaction, internal energy/charge transfer, or charge carrier recombination induced by different phases or impurities in the samples.^{64–67} First, because the samples are uniform fresh crystal flakes and have excellent powder XRD patterns, the existence of additional phase or impurities can be excluded. Second, the low excitation fluence applied in the experiment guarantee the absence of any Auger recombination process. Third, photo-induced chemical reactions are also unlikely in these stable 2D perovskites.

The PL kinetics exhibit very notable on the excitation intensity (Figure 7c,d). We can clearly observe a prolongation of the PL lifetime with the increment of excitation intensity for both compounds. This behavior is a well-known fingerprint of trap filling/accumulation seen in most perovskite materials. This process occurs when the lifetime of traps is longer than the laser pulse interval time so that some of traps constantly remain filled.⁶⁸ We can globally fit the different PL decays by three exponential components with the same set of lifetimes (t_1 , t_2 and t_3) but with different amplitudes (A_1 , A_2 , and A_3) that are allowed to vary with the laser intensities. As seen in Tables S6 and S7, the ratios $[A_1/(A_1 + A_2)]$ are becoming

smaller with increasing intensity. Such a phenomenon has already been observed in our previous study on 3D perovskite bulk crystals, where the dynamics were extensively rationalized by considering the parallel charge carrier trapping processes by two different types of trap states in the crystal.⁶⁴ One type of traps possessed a long lifetime, which could cause trap filling depending on the excitation condition, while the other type of traps was immune to trap filling due to its faster depopulation time. Here, we use the same model to simulate the PL dynamics in the 2D perovskite crystals. Briefly, the ratio A_1/A_2 can reflect the fraction between photogenerated charge carriers that undergo trapping by two different traps. It should be equal to the initial ratio between unfilled density of traps 1 (n_{uncT1}) and traps 2 (n_{uncT2}): $n_{\text{uncT1}}/n_{\text{uncT2}}$, where such unoccupied traps refer to the equilibrium condition between photo-induced trap filling and trap recovery within two excitation pulse. We can then obtain the density of the filled traps n_T under a certain excitation density (N_c) and a total trap densities (N_T) using the following equations that have been outlined in the previous paper (for the details of the calculation model see S9), where the equilibrium between free carriers and excitons after photoexcitation is calculated by the Saha equation.^{64,68}

$$n_T = -\frac{1}{2}\alpha + \frac{1}{2}\sqrt{\alpha^2 + 4\beta N_T} \quad (7)$$

$$\alpha = \frac{[A + R(A - N_T)]}{\left(1 + \frac{1}{K} + R\right)} \quad (8)$$

$$\beta = \frac{RA}{\left(1 + \frac{1}{K} + R\right)} \quad (9)$$

$$K = \frac{1}{\gamma_0 t_0} \ln \left[1 + \frac{AN_c}{N_T(A + N_T)} \right] \quad (10)$$

$$A = \frac{\nu_x}{\nu_e \nu_h} e^{-E_b/k_b T} \quad (11)$$

Here, R indicates the ratio between the trap population and depopulation rates; γ_0 is the total electronic decay rate except for any trapping processes; t_0 is laser pulse interval time; λ_i refers to the thermal wavelength of each quasiparticles i (free electrons e, holes h and excitons x), and $\nu_i = \lambda_i^3$. We can further obtain the concentration of n_{uncT1} and n_{uncT2} as

$$n_{\text{nucT1}} = N_{T1} - n_{T1} = N_{T1} + \frac{1}{2}\alpha - \frac{1}{2}\sqrt{\alpha^2 + 4\beta N_{T1}} \quad (12)$$

$$n_{\text{nucT2}} = N_{T2} - n_{T2} = N_{T2} + \frac{1}{2}\alpha - \frac{1}{2}\sqrt{\alpha^2 + 4\beta N_{T2}} \quad (13)$$

$$A_1/(A_1 + A_2) = n_{\text{nucT1}}/(n_{\text{nucT1}} + n_{\text{nucT2}}) \quad (14)$$

where N_{T1} , N_{T2} are the initial densities of two type of traps, respectively. The $A_1/(A_1 + A_2)$ ratios versus N_c can then be depicted and fitted using the model within the eqs 12–14. The four fitting parameters are (N_{T1} , N_{T2}), R_1 , and R_2 . From the analysis, we calculated that the depopulation time of traps 2 in BMAPI and BEAPI are about ~ 313 and ~ 165 ns, respectively, which are close to t_0 (250 ns). Therefore, there should be no significant trap filling occurring in their traps 2 because the

depopulation rate is quite fast. The model is then modified for the case where the trap filling occurs only in trap 1 as follows

$$A_1/(A_1 + A_2) = n_{\text{nucT1}}/(n_{\text{nucT1}} + N_{\text{T2}}) \quad (15)$$

Here, the $A_1/(A_1 + A_2)$ ratio equals the ratio between n_{nucT1} and N_{T2} . This model provides an excellent fit for both compounds as shown in Figure 7e. Defining R as the ratio between trap population and depopulation rates, we can calculate that the depopulation time of traps 1 of BMAPI (trapping time ≈ 1.4 ns) and of BEAPI (trapping time ≈ 0.4 ns) are ~ 190 and ~ 20 μs , respectively. The illustrations of the trap-mediated charge recombination are given in Figure 7f. Table 1 summarizes the fitted trap densities of two types of

Table 1. Trap Densities Calculated From the Fitting Shown in Figure 7e

	N_{T1} (10^{15} cm^{-3})	N_{T2} (10^{15} cm^{-3})
$(n\text{-BA})_2(\text{MA})_2\text{Pb}_3\text{I}_{10}$	21.8	0.11
$(n\text{-BA})_2(\text{EA})_2\text{Pb}_3\text{I}_{10}$	37.6	0.59

traps. Compared to N_{T1} , N_{T2} are small and can be neglected. Therefore, the trap-mediated recombination should be dominated by the traps 1 at low excitation density. The N_{T1} values for BMAPI and BEAPI are $\sim 2.18 \times 10^{16}$ and $\sim 3.76 \times 10^{16} \text{ cm}^{-3}$, respectively. They are of the same order of magnitude as the ones reported for 3D perovskites ($2.5 \times 10^{16} \text{ cm}^{-3}$, at 300 K) using identical analysis method.⁶⁸ In general, because of the presence of long organic bilayer and larger lattice distortions in 2D RPPs, the trap densities would be expected to be larger than that of 3D perovskites. However, their similarities could be due to the absence of grain boundaries in the fresh single crystal compared to the film samples. In addition, the N_{T1} of BEAPI is 1.7 times higher than that of BMAPI. Considering the similar single-crystal growth conditions, we believe that such a difference in trap density reflects the larger degree of interfacial lattice distortion in BEAPI where the larger EA cations fill the crystal lattice. As noted above, this is also the main reason for the overall shorter PL lifetime in the EA-based 2D RPPs. In addition, both fast trapping and detrapping times in BEAPI indicate much shallower trap states compared to the MA based 2D RPPs. Globally, the combination of shallower traps together with larger trap density should be the main reason for the overall shorter PL lifetime in the EA-based 2D RPPs. Finally, our previous studies on 3D perovskite crystals suggest the origins of the traps 1 and traps 2 to be the volume traps and surface traps, respectively, due to their different trapping times (i.e., it takes generally longer time for photogenerated carriers to migrate to the surface of the crystals).⁶⁴ However, the defect structures in 2D perovskites should be more complicated owing to the existence of large organic cations, as aspect which requires further exploration.

CONCLUSIONS

In this work, we have successfully synthesized the single crystals of two lead iodide 2D RPPs, BMAPI, and BEAPI. The detailed structural comparison shows that BEAPI with large-size A cations and relaxed τ exhibit increased inorganic layer distortions and compression by long organic bilayers. The larger lattice distortions, especially the increase in the Pb–I bond lengths, further widen the band gap by mainly lowering the position of the VBM, which can be rationalized by the

orbital hybridization theory. In addition, from the TRPL studies, we revealed ultra-long-lived trap states in both two compounds with trap densities of $\sim 2.18 \times 10^{16}$ and $\sim 3.76 \times 10^{16} \text{ cm}^{-3}$ for BMAPI and BEAPI, respectively. We believe that the higher trap densities of BEAPI is due to the more severe lattice distortion leading to a much shorter PL lifetime compared to BMAPI. However, the shorter detrapping time of BEAPI may diminish the trapping process in the sample. The present findings can provide robust reference for future materials engineering and device application based on such 2D RPPs.

ASSOCIATED CONTENT

Supporting Information

The Supporting Information is available free of charge at <https://pubs.acs.org/doi/10.1021/acsaelm.0c00179>.

Crystal data and structure determinations of the samples, values of Pb–I bond distances and I–Pb–I bond angles, schematic diagram of the growth of bulk single crystals, powder XRD data of the samples, the values of five distortion parameters, multiexponential fitting parameters for TRPL kinetics for the samples, details about calculation of E_b using the temperature-dependent photoluminescence method, details about calculations of the absorption coefficients and excitation density of the samples, and detailed model of trap filling and fitting process (PDF)

Crystallographic data of C10H36I10N4Pb3 and C12H40N4Pb3I10 (CIF)

checkCIF/PLATON report and datablock: C10H36I10N4Pb3 and C12H40N4Pb3I10 (PDF)

AUTHOR INFORMATION

Corresponding Authors

Sophie E. Canton – ELI-ALPS, ELI-HU Non-Profit, Ltd., 6720 Szeged, Hungary; orcid.org/0000-0003-4337-8129; Email: Sophie.Canton@eli-alps.hu

Kaibo Zheng – Department of Chemistry, Technical University of Denmark, DK-2800 Kongens Lyngby, Denmark; Chemical Physics and NanoLund, Lund University, 22100 Lund, Sweden; orcid.org/0000-0002-7236-1070; Email: kzheng@kemi.dtu.dk

Authors

Mingli Liang – Department of Chemistry, Technical University of Denmark, DK-2800 Kongens Lyngby, Denmark; orcid.org/0000-0002-1854-7026

Weihua Lin – Chemical Physics and NanoLund, Lund University, 22100 Lund, Sweden

Zhenyun Lan – Department of Energy Conversion and Storage, Technical University of Denmark, DK-2800 Kongens Lyngby, Denmark; orcid.org/0000-0001-7943-5936

Jie Meng – Department of Chemistry, Technical University of Denmark, DK-2800 Kongens Lyngby, Denmark; orcid.org/0000-0002-3813-5221

Qian Zhao – Department of Chemistry, Technical University of Denmark, DK-2800 Kongens Lyngby, Denmark

Xianshao Zou – Chemical Physics and NanoLund, Lund University, 22100 Lund, Sweden

Ivano E. Castelli – Department of Energy Conversion and Storage, Technical University of Denmark, DK-2800 Kongens Lyngby, Denmark; orcid.org/0000-0001-5880-5045

Tõnu Pullerits – *Chemical Physics and NanoLund, Lund University, 22100 Lund, Sweden*; orcid.org/0000-0003-1428-5564

Complete contact information is available at:
<https://pubs.acs.org/10.1021/acsaelm.0c00179>

Author Contributions

[†]M.L. and W.L. contributed equally to this work.

Notes

The authors declare no competing financial interest.

ACKNOWLEDGMENTS

This work was supported by the Independent Research Fund Denmark-Sapere Aude starting grant (no. 7026-00037A) and Swedish Research Council VR starting grant (no. 2017-05337), Swedish Energy Agency and the Chinese Scholarship Council for the PhD scholarship to M.L., W.L., Z.L., M. J., and Q.Z. The ELI-ALPS project (GINOP-2.3.6-15-2015-00001) is supported by the European Union and co-financed by the European Regional Development Fund.

REFERENCES

- (1) Lee, M. M.; Teuscher, J.; Miyasaka, T.; Murakami, T. N.; Snaith, H. J. Efficient Hybrid Solar Cells Based on Meso-Superstructured Organometal Halide Perovskites. *Science* **2012**, *338*, 643–647.
- (2) Etgar, L.; Gao, P.; Xue, Z.; Peng, Q.; Chandiran, A. K.; Liu, B.; Nazeeruddin, M. K.; Grätzel, M. Mesoscopic $\text{CH}_3\text{NH}_3\text{PbI}_3/\text{TiO}_2$ Heterojunction Solar Cells. *J. Am. Chem. Soc.* **2012**, *134*, 17396–17399.
- (3) Bai, S.; Da, P.; Li, C.; Wang, Z.; Yuan, Z.; Fu, F.; Kawecki, M.; Liu, X.; Sakai, N.; Wang, J. T.-W.; Huettner, S.; Buecheler, S.; Fahlman, M.; Gao, F.; Snaith, H. J. Planar Perovskite Solar Cells with Long-Term Stability Using Ionic Liquid Additives. *Nature* **2019**, *571*, 245–250.
- (4) Wu, Z.; Bai, S.; Xiang, J.; Yuan, Z.; Yang, Y.; Cui, W.; Gao, X.; Liu, Z.; Jin, Y.; Sun, B. Efficient Planar Heterojunction Perovskite Solar Cells Employing Graphene Oxide as Hole Conductor. *Nanoscale* **2014**, *6*, 10505–10510.
- (5) Ponceca, C. S.; Savenije, T. J.; Abdellah, M.; Zheng, K.; Yartsev, A.; Pascher, T.; Harlang, T.; Chabera, P.; Pullerits, T.; Stepanov, A.; Wolf, J.-P.; Sundström, V. Organometal Halide Perovskite Solar Cell Materials Rationalized: Ultrafast Charge Generation, High and Microsecond-Long Balanced Mobilities, and Slow Recombination. *J. Am. Chem. Soc.* **2014**, *136*, 5189–5192.
- (6) Burschka, J.; Pellet, N.; Moon, S.-J.; Humphry-Baker, R.; Gao, P.; Nazeeruddin, M. K.; Grätzel, M. Sequential Deposition as a Route to High-Performance Perovskite-Sensitized Solar Cells. *Nature* **2013**, *499*, 316–319.
- (7) Brenner, T. M.; Egger, D. A.; Kronik, L.; Hodes, G.; Cahen, D. Hybrid Organic - Inorganic Perovskites: Low-Cost Semiconductors with Intriguing Charge-Transport Properties. *Nat. Rev. Mater.* **2016**, *1*, 15007.
- (8) Zhao, Y.; Zhu, K. Organic-Inorganic Hybrid Lead Halide Perovskites for Optoelectronic and Electronic Applications. *Chem. Soc. Rev.* **2016**, *45*, 655–689.
- (9) Kojima, A.; Teshima, K.; Shirai, Y.; Miyasaka, T. Organometal Halide Perovskites as Visible-Light Sensitizers for Photovoltaic Cells. *J. Am. Chem. Soc.* **2009**, *131*, 6050–6051.
- (10) National Renewable Energy Laboratory. Best Research-Cell Efficiencies. http://www.nrel.gov/pv/assets/images/efficiency_chart.jpg (accessed Jan 13, 2020).
- (11) Ha, S.-T.; Su, R.; Xing, J.; Zhang, Q.; Xiong, Q. Metal Halide Perovskite Nanomaterials: Synthesis and Applications. *Chem. Sci.* **2017**, *8*, 2522–2536.
- (12) Di, X.; Shen, L.; Jiang, J.; He, M.; Cheng, Y.; Zhou, L.; Liang, X.; Xiang, W. Efficient White LEDs with Bright Green-Emitting

CsPbBr₃ Perovskite Nanocrystal in Mesoporous Silica Nanoparticles. *J. Alloys Compd.* **2017**, *729*, 526–532.

(13) Yao, J.-S.; Ge, J.; Han, B.-N.; Wang, K.-H.; Yao, H.-B.; Yu, H.-L.; Li, J.-H.; Zhu, B.-S.; Song, J.-Z.; Chen, C.; Zhang, Q.; Zeng, H.-B.; Luo, Y.; Yu, S.-H. Ce³⁺-Doping to Modulate Photoluminescence Kinetics for Efficient CsPbBr₃ Nanocrystals Based Light-Emitting Diodes. *J. Am. Chem. Soc.* **2018**, *140*, 3626–3634.

(14) Dai, S.-W.; Hsu, B.-W.; Chen, C.-Y.; Lee, C.-A.; Liu, H.-Y.; Wang, H.-F.; Huang, Y.-C.; Wu, T.-L.; Manikandan, A.; Ho, R.-M.; Tsao, C.-S.; Cheng, C.-H.; Chueh, Y.-L.; Lin, H.-W. Perovskite Quantum Dots with Near Unity Solution and Neat-Film Photoluminescent Quantum Yield by Novel Spray Synthesis. *Adv. Mater.* **2018**, *30*, 1705532.

(15) Yang, B.; Chen, J.; Yang, S.; Hong, F.; Sun, L.; Han, P.; Pullerits, T.; Deng, W.; Han, K. Lead-Free Silver-Bismuth Halide Double Perovskite Nanocrystals. *Angew. Chem., Int. Ed.* **2018**, *57*, 5359–5363.

(16) Saidaminov, M. I.; Adinolfi, V.; Comin, R.; Abdelhady, A. L.; Peng, W.; Dursun, I.; Yuan, M.; Hoogland, S.; Sargent, E. H.; Bakr, O. M. Planar-Integrated Single-Crystalline Perovskite Photodetectors. *Nat. Commun.* **2015**, *6*, 8724.

(17) Zhuo, S.; Zhang, J.; Shi, Y.; Huang, Y.; Zhang, B. Self-Template-Directed Synthesis of Porous Perovskite Nanowires at Room Temperature for High-Performance Visible-Light Photodetectors. *Angew. Chem., Int. Ed.* **2015**, *54*, 5693–5696.

(18) Zhang, F.; Yang, B.; Zheng, K.; Yang, S.; Li, Y.; Deng, W.; He, R. Formamidinium Lead Bromide (FAPbBr₃) Perovskite Microcrystals for Sensitive and Fast Photodetectors. *Nano-Micro Lett.* **2018**, *10*, 43.

(19) Yang, B.; Zhang, F.; Chen, J.; Yang, S.; Xia, X.; Pullerits, T.; Deng, W.; Han, K. Ultrasensitive and Fast All-Inorganic Perovskite-Based Photodetector via Fast Carrier Diffusion. *Adv. Mater.* **2017**, *29*, 1703758.

(20) Pan, W.; Wu, H.; Luo, J.; Deng, Z.; Ge, C.; Chen, C.; Jiang, X.; Yin, W.-J.; Niu, G.; Zhu, L.; Yin, L.; Zhou, Y.; Xie, Q.; Ke, X.; Sui, M.; Tang, J. Cs₂AgBiBr₆ Single-Crystal X-Ray Detectors with a Low Detection Limit. *Nat. Photonics* **2017**, *11*, 726–732.

(21) Yin, L.; Wu, H.; Pan, W.; Yang, B.; Li, P.; Luo, J.; Niu, G.; Tang, J. Controlled Cooling for Synthesis of Cs₂AgBiBr₆ Single Crystals and Its Application for X-Ray Detection. *Adv. Opt. Mater.* **2019**, *7*, 1900491.

(22) Cegielski, P. J.; Giesecke, A. L.; Neutzner, S.; Porschatis, C.; Gandini, M.; Schall, D.; Perini, C. A. R.; Bolten, J.; Suckow, S.; Kataria, S.; Chmielak, B.; Wahlbrink, T.; Petrozza, A.; Lemme, M. C. Monolithically Integrated Perovskite Semiconductor Lasers on Silicon Photonic Chips by Scalable Top-Down Fabrication. *Nano Lett.* **2018**, *18*, 6915–6923.

(23) Raghavan, C. M.; Chen, T.-P.; Li, S.-S.; Chen, W.-L.; Lo, C.-Y.; Liao, Y.-M.; Haider, G.; Lin, C.-C.; Chen, C.-C.; Sankar, R.; Chang, Y.-M.; Chou, F.-C.; Chen, C.-W. Low-Threshold Lasing from 2D Homologous Organic-Inorganic Hybrid Ruddlesden-Popper Perovskite Single Crystals. *Nano Lett.* **2018**, *18*, 3221–3228.

(24) Chen, Y.; Sun, Y.; Peng, J.; Zhang, W.; Su, X.; Zheng, K.; Pullerits, T.; Liang, Z. Tailoring Organic Cation of 2D Air-Stable Organometal Halide Perovskites for Highly Efficient Planar Solar Cells. *Adv. Energy Mater.* **2017**, *7*, 1700162.

(25) Tsai, H.; Nie, W.; Blancon, J.-C.; Stoumpos, C. C.; Asadpour, R.; Harutyunyan, B.; Neukirch, A. J.; Verduzco, R.; Crochet, J. J.; Tretiak, S.; Pedesseau, L.; Even, J.; Alam, M. A.; Gupta, G.; Lou, J.; Ajayan, P. M.; Bedzyk, M. J.; Kanatzidis, M. G.; Mohite, A. D. High-Efficiency Two-Dimensional Ruddlesden-Popper Perovskite Solar Cells. *Nature* **2016**, *536*, 312–316.

(26) Yang, S.; Wu, D.; Gong, W.; Huang, Q.; Zhen, H.; Ling, Q.; Lin, Z. Highly Efficient Room-Temperature Phosphorescence and Afterglow Luminescence from Common Organic Fluorophores in 2D Hybrid Perovskites. *Chem. Sci.* **2018**, *9*, 8975–8981.

(27) Stoumpos, C. C.; Soe, C. M. M.; Tsai, H.; Nie, W.; Blancon, J.-C.; Cao, D. H.; Liu, F.; Traoré, B.; Katan, C.; Even, J.; Mohite, A. D.; Kanatzidis, M. G. High Members of the 2D Ruddlesden-Popper

Halide Perovskites: Synthesis, Optical Properties, and Solar Cells of $(\text{CH}_3(\text{CH}_2)_3\text{NH}_3)_2(\text{CH}_3\text{NH}_3)_4\text{Pb}_3\text{I}_{16}$. *Chem* **2017**, *2*, 427–440.

(28) Saparov, B.; Mitzi, D. B. Organic-Inorganic Perovskites: Structural Versatility for Functional Materials Design. *Chem. Rev.* **2016**, *116*, 4558–4596.

(29) Blancon, J.-C.; Tsai, H.; Nie, W.; Stoumpos, C. C.; Pedesseau, L.; Katan, C.; Kepenekian, M.; Soe, C. M. M.; Appavoo, K.; Sfeir, M. Y.; Tretiak, S.; Ajayan, P. M.; Kanatzidis, M. G.; Even, J.; Crochet, J. J.; Mohite, A. D. Extremely Efficient Internal Exciton Dissociation through Edge States in Layered 2D Perovskites. *Science* **2017**, *355*, 1288–1292.

(30) Charles, B.; Dillon, J.; Weber, O. J.; Islam, M. S.; Weller, M. T. Understanding the Stability of Mixed A-Cation Lead Iodide Perovskites. *J. Mater. Chem. A* **2017**, *5*, 22495–22499.

(31) Li, Z.; Yang, M.; Park, J.-S.; Wei, S.-H.; Berry, J. J.; Zhu, K. Stabilizing Perovskite Structures by Tuning Tolerance Factor: Formation of Formamidinium and Cesium Lead Iodide Solid-State Alloys. *Chem. Mater.* **2016**, *28*, 284–292.

(32) Han, G.; Hadi, H. D.; Bruno, A.; Kulkarni, S. A.; Koh, T. M.; Wong, L. H.; Soci, C.; Mathews, N.; Zhang, S.; Mhaisalkar, S. G. Additive Selection Strategy for High Performance Perovskite Photovoltaics. *J. Phys. Chem. C* **2018**, *122*, 13884–13893.

(33) Mao, L.; Wu, Y.; Stoumpos, C. C.; Traore, B.; Katan, C.; Even, J.; Wasielewski, M. R.; Kanatzidis, M. G. Tunable White-Light Emission in Single-Cation-Templated Three-Layered 2D Perovskites $(\text{CH}_3\text{CH}_2\text{NH}_3)_4\text{Pb}_3\text{Br}_{10-x}\text{Cl}_x$. *J. Am. Chem. Soc.* **2017**, *139*, 11956–11963.

(34) Wang, S.; Liu, X.; Li, L.; Ji, C.; Sun, Z.; Wu, Z.; Hong, M.; Luo, J. An Unprecedented Biaxial Trilayered Hybrid Perovskite Ferroelectric with Directionally Tunable Photovoltaic Effects. *J. Am. Chem. Soc.* **2019**, *141*, 7693–7697.

(35) Han, S.; Liu, X.; Liu, Y.; Xu, Z.; Li, Y.; Hong, M.; Luo, J.; Sun, Z. High-Temperature Antiferroelectric of Lead Iodide Hybrid Perovskites. *J. Am. Chem. Soc.* **2019**, *141*, 12470–12474.

(36) Xu, Z.; Li, Y.; Liu, X.; Ji, C.; Chen, H.; Li, L.; Han, S.; Hong, M.; Luo, J.; Sun, Z. Highly Sensitive and Ultrafast Responding Array Photodetector Based on a Newly Tailored 2D Lead Iodide Perovskite Crystal. *Adv. Opt. Mater.* **2019**, *7*, 1900308.

(37) Fu, Y.; Hautzinger, M. P.; Luo, Z.; Wang, F.; Pan, D.; Aristov, M. M.; Guzei, I. A.; Pan, A.; Zhu, X.; Jin, S. Incorporating Large A Cations into Lead Iodide Perovskite Cages: Relaxed Goldschmidt Tolerance Factor and Impact on Exciton-Phonon Interaction. *ACS Cent. Sci.* **2019**, *5*, 1377–1386.

(38) Liang, M.-L.; Ma, Y.-X.; Hu, C.-L.; Kong, F.; Mao, J.-G. $\text{A}(\text{VO}_2\text{F})(\text{SeO}_3)$ (A = Sr, Ba) and $\text{Ba}(\text{MOF}_2)(\text{TeO}_4)$ (M = Mo, W): first examples of alkali-earth selenites/tellurites with a fluorinated d⁰-TM octahedron. *Dalton Trans.* **2018**, *47*, 1513–1519.

(39) Larsen, A. H.; Mortensen, J. J.; Blomqvist, J.; Castelli, I. E.; Christensen, R.; Dulak, M.; Friis, J.; Groves, M. N.; Hammer, B.; Hargus, C.; Hermes, E. D.; Jennings, P. C.; Jensen, P. B.; Kermode, J.; Kitchin, J. R.; Kolsbjerg, E. L.; Kubal, J.; Kaasbjerg, K.; Lysgaard, S.; Maronsson, J. B.; Maxson, T.; Olsen, T.; Pastewka, L.; Peterson, A.; Rostgaard, C.; Schiøtz, J.; Schütt, O.; Strange, M.; Thygesen, K. S.; Vegge, T.; Vilhelmsen, L.; Walter, M.; Zeng, Z.; Jacobsen, K. W. The Atomic Simulation Environment—A Python Library for Working with Atoms. *J. Phys.: Condens. Matter* **2017**, *29*, 273002.

(40) Kresse, G.; Hafner, J. Ab Initio Molecular Dynamics for Liquid Metals. *Phys. Rev. B: Condens. Matter Mater. Phys.* **1993**, *47*, 558–561.

(41) Mortensen, J. J.; Hansen, L. B.; Jacobsen, K. W. Real-Space Grid Implementation of the Projector Augmented Wave Method. *Phys. Rev. B: Condens. Matter Mater. Phys.* **2005**, *71*, 035109.

(42) Enkovaara, J.; Rostgaard, C.; Mortensen, J. J.; Chen, J.; Dulak, M.; Ferrighi, L.; Gavnholt, J.; Glinsvad, C.; Haikola, V.; Hansen, H. A.; Kristoffersen, H. H.; Kuisma, M.; Larsen, A. H.; Lehtovaara, L.; Ljungberg, M.; Lopez-Acevedo, O.; Moses, P. G.; Ojanen, J.; Olsen, T.; Petzold, V.; Romero, N. A.; Stausholm-Møller, J.; Strange, M.; Tritsarlis, G. A.; Vanin, M.; Walter, M.; Hammer, B.; Häkkinen, H.; Madsen, G. K. H.; Nieminen, R. M.; Nørskov, J. K.; Puska, M.; Rantala, T. T.; Schiøtz, J.; Thygesen, K. S.; Jacobsen, K. W. Electronic

Structure Calculations with GPAW: A Real-Space Implementation of the Projector Augmented-Wave Method. *J. Phys.: Condens. Matter* **2010**, *22*, 253202.

(43) Perdew, J. P.; Ruzsinszky, A.; Csonka, G. I.; Vydrov, O. A.; Scuseria, G. E.; Constantin, L. A.; Zhou, X.; Burke, K. Restoring the Density-Gradient Expansion for Exchange in Solids and Surfaces. *Phys. Rev. Lett.* **2008**, *100*, 136406.

(44) Blöchl, P. E. Projector Augmented-Wave Method. *Phys. Rev. B: Condens. Matter Mater. Phys.* **1994**, *50*, 17953–17979.

(45) Kuisma, M.; Ojanen, J.; Enkovaara, J.; Rantala, T. T. Kohn-Sham Potential with Discontinuity for Band Gap Materials. *Phys. Rev. B: Condens. Matter Mater. Phys.* **2010**, *82*, 115106.

(46) Castelli, I. E.; Hüser, F.; Pandey, M.; Li, H.; Thygesen, K. S.; Seger, B.; Jain, A.; Persson, K. A.; Ceder, G.; Jacobsen, K. W. New light-harvesting materials using accurate and efficient bandgap calculations. *Adv. Energy Mater.* **2015**, *5*, 1400915.

(47) Castelli, I. E.; García-Lastra, J. M.; Thygesen, K. S.; Jacobsen, K. W. Bandgap Calculations and Trends of Organometal Halide Perovskites. *APL Mater.* **2014**, *2*, 081514.

(48) Becker, M.; Klüner, T.; Wark, M. Formation of Hybrid ABX_3 Perovskite Compounds for Solar Cell Application: First-Principles Calculations of Effective Ionic Radii and Determination of Tolerance Factors. *Dalton Trans.* **2017**, *46*, 3500–3509.

(49) Gao, P.; Bin Mohd Yusoff, A. R.; Nazeeruddin, M. K. Dimensionality Engineering of Hybrid Halide Perovskite Light Absorbers. *Nat. Commun.* **2018**, *9*, 5028.

(50) Varadwaj, P. R.; Varadwaj, A.; Marques, H. M.; Yamashita, K. Significance of Hydrogen Bonding and Other Noncovalent Interactions in Determining Octahedral Tilting in the $\text{CH}_3\text{NH}_3\text{PbI}_3$ Hybrid Organic-Inorganic Halide Perovskite Solar Cell Semiconductor. *Sci. Rep.* **2019**, *9*, 50.

(51) Lufaso, M. W.; Woodward, P. M. Jahn-Teller Distortions, Cation Ordering and Octahedral Tilting in Perovskites. *Acta Crystallogr., Sect. B: Struct. Sci.* **2004**, *60*, 10–20.

(52) Alvarez, S. Distortion Pathways of Transition Metal Coordination Polyhedra Induced by Chelating Topology. *Chem. Rev.* **2015**, *115*, 13447–13483.

(53) Pérez-Osorio, M. A.; Lin, Q.; Phillips, R. T.; Milot, R. L.; Herz, L. M.; Johnston, M. B.; Giustino, F. Raman Spectrum of the Organic-Inorganic Halide Perovskite $\text{CH}_3\text{NH}_3\text{PbI}_3$ from First Principles and High-Resolution Low-Temperature Raman Measurements. *J. Phys. Chem. C* **2018**, *122*, 21703–21717.

(54) Quarti, C.; Grancini, G.; Mosconi, E.; Bruno, P.; Ball, J. M.; Lee, M. M.; Snaith, H. J.; Petrozza, A.; De Angelis, F. The Raman Spectrum of the $\text{CH}_3\text{NH}_3\text{PbI}_3$ Hybrid Perovskite: Interplay of Theory and Experiment. *J. Phys. Chem. Lett.* **2014**, *5*, 279–284.

(55) Xie, L.-Q.; Zhang, T.-Y.; Chen, L.; Guo, N.; Wang, Y.; Liu, G.-K.; Wang, J.-R.; Zhou, J.-Z.; Yan, J.-W.; Zhao, Y.-X.; Mao, B.-W.; Tian, Z.-Q. Organic-Inorganic Interactions of Single Crystalline Organolead Halide Perovskites Studied by Raman Spectroscopy. *Phys. Chem. Chem. Phys.* **2016**, *18*, 18112–18118.

(56) Zheng, K.; Zhu, Q.; Abdellah, M.; Messing, M. E.; Zhang, W.; Generalov, A.; Niu, Y.; Ribaud, L.; Canton, S. E.; Pullerits, T. Exciton Binding Energy and the Nature of Emissive States in Organometal Halide Perovskites. *J. Phys. Chem. Lett.* **2015**, *6*, 2969–2975.

(57) Chen, Z.; Yu, C.; Shum, K.; Wang, J. J.; Pfenninger, W.; Vockic, N.; Midgley, J.; Kenney, J. T. Photoluminescence Study of Polycrystalline CsSnI_3 Thin Films: Determination of Exciton Binding Energy. *J. Lumin.* **2012**, *132*, 345–349.

(58) Blancon, J.-C.; Stier, A. V.; Tsai, H.; Nie, W.; Stoumpos, C. C.; Traoré, B.; Pedesseau, L.; Kepenekian, M.; Katsutani, F.; Noe, G. T.; Kono, J.; Tretiak, S.; Crooker, S. A.; Katan, C.; Kanatzidis, M. G.; Crochet, J. J.; Even, J.; Mohite, A. D. Scaling law for excitons in 2D perovskite quantum wells. *Nat. Commun.* **2018**, *9*, 2254.

(59) Baranowski, M.; Plochocka, P. Excitons in Metal-Halide Perovskites. *Adv. Energy Mater.* **2020**, 1903659.

(60) Katan, C.; Pedesseau, L.; Kepenekian, M.; Rolland, A.; Even, J. Interplay of Spin-Orbit Coupling and Lattice Distortion in Metal

Substituted 3D Tri-Chloride Hybrid Perovskites. *J. Mater. Chem. A* **2015**, *3*, 9232–9240.

(61) Zhu, Q.; Zheng, K.; Abdellah, M.; Generalov, A.; Haase, D.; Carlson, S.; Niu, Y.; Heimdal, J.; Engdahl, A.; Messing, M. E.; Pullerits, T.; Canton, S. E. Correlating Structure and Electronic Band-Edge Properties in Organolead Halide Perovskites Nanoparticles. *Phys. Chem. Chem. Phys.* **2016**, *18*, 14933–14940.

(62) Waghmare, U. V.; Spaldin, N. A.; Kandpal, H. C.; Seshadri, R. First-Principles Indicators of Metallicity and Cation off-Centricity in the IV-VI Rocksalt Chalcogenides of Divalent Ge, Sn, and Pb. *Phys. Rev. B: Condens. Matter Mater. Phys.* **2003**, *67*, 125111.

(63) Payne, D. J.; Egdell, R. G.; Walsh, A.; Watson, G. W.; Guo, J.; Glans, P. A.; Learmonth, T.; Smith, K. E. Electronic Origins of Structural Distortions in Post-Transition Metal Oxides: Experimental and Theoretical Evidence for a Revision of the Lone Pair Model. *Phys. Rev. Lett.* **2006**, *96*, 157403.

(64) Zheng, K.; Židek, K.; Abdellah, M.; Messing, M. E.; Al-Marri, M. J.; Pullerits, T. Trap States and Their Dynamics in Organometal Halide Perovskite Nanoparticles and Bulk Crystals. *J. Phys. Chem. C* **2016**, *120*, 3077–3084.

(65) Zheng, K.; Židek, K.; Abdellah, M.; Chen, J.; Chábera, P.; Zhang, W.; Al-Marri, M. J.; Pullerits, T. High Excitation Intensity Opens a New Trapping Channel in Organic-Inorganic Hybrid Perovskite Nanoparticles. *ACS Energy Lett.* **2016**, *1*, 1154–1161.

(66) de Quilettes, D. W.; Vorpahl, S. M.; Stranks, S. D.; Nagaoka, H.; Eperon, G. E.; Ziffer, M. E.; Snaith, H. J.; Ginger, D. S. Impact of Microstructure on Local Carrier Lifetime in Perovskite Solar Cells. *Science* **2015**, *348*, 683–686.

(67) Abdellah, M.; Židek, K.; Zheng, K.; Chábera, P.; Messing, M. E.; Pullerits, T. Balancing Electron Transfer and Surface Passivation in Gradient CdSe/ZnS Core-Shell Quantum Dots Attached to ZnO. *J. Phys. Chem. Lett.* **2013**, *4*, 1760–1765.

(68) Stranks, S. D.; Burlakov, V. M.; Leijtens, T.; Ball, J. M.; Goriely, A.; Snaith, H. J. Recombination Kinetics in Organic-Inorganic Perovskites: Excitons, Free Charge, and Subgap States. *Phys. Rev. Appl.* **2014**, *2*, 034007.

Supporting Information

Electronic Structure and Trap-States of Two-Dimensional Ruddlesden-Popper Perovskites with Relaxed Goldschmidt Tolerance Factor

Mingli Liang^{†,1}, Weihua Lin^{‡,1}, Zhenyun Lan[#], Jie Meng[†], Qian Zhao[†], Xianshao Zou[‡], Ivano E. Castelli[#], Tönu Pullerits[‡], Sophie E. Canton^{*,^} and Kaibo Zheng^{*,†,‡}

[†]*Department of Chemistry, Technical University of Denmark, DK-2800 Kongens Lyngby, Denmark;*

[‡]*Chemical Physics and NanoLund, Lund University, Box 124, 22100 Lund, Sweden;*

[#]*Department of Energy Conversion and Storage, Technical University of Denmark, DK-2800 Kongens Lyngby, Denmark;*

[^]*ELI-ALPS, ELI-HU Non-Profit, Ltd., Dugonics ter 13, Szeged 6720, Hungary;*

*Sophie E.Canton, Sophie.Canton@eli-alps.hu

*Kaibo Zheng, kzheng@kemi.dtu.dk

Table S1. Crystal data and structure determinations of the BMAPI and BEAPI.

Table S2. Bond distances (Angstroms) of Pb-I for the BMAPI and BEAPI.

Table S3. I-Pb-I angles (deg) for the BMAPI and BEAPI.

Table S4. Selected strong N-H···I hydrogen bond distances (H···I, Angstroms) angles (deg) for the BMAPI and BEAPI.

Table S5. The values of five distortion parameters of BMAPI and BEAPI.

Table S6. Multi-exponential fitting parameters for TRPL kinetics of BMAPI.

Table S7. Multi-exponential fitting parameters for TRPL kinetics of BEAPI.

Table S8. Excitation density of BMAPI and BEAPI with different laser photon flux.

Table S9. The calculated values of ratio of the free carriers x .

Table S10. Trap densities obtained from the fitting.

Figure S1. A schematic diagram of the growth of the bulk single crystals, and the resulting two title single crystals.

Figure S2. The powder XRD spectra of (a) BMAPI and (b) BEAPI.

Figure S3. A diagram for the formation processes of perovskite phase MAPbI_3 and non-perovskite phase EAPbI_3 .

Figure S4. Comparison between experimental Raman spectra of BEAPI and the calculation of isolated EA cation.

Figure S5. The vibration modes of MA and EA in BMAPI and BEAPI.

S5. Calculation of E_b using temperature dependent photoluminescence method.

Figure S6. The temperature dependent PL spectra of (a) BMAPI and (c) BEAPI; $\ln(I_0/I(T)-1)$ vs. $1/k_B T$ plot of temperature dependent PL of (b) BMAPI and (d) BEAPI.

S7. Calculations of the absorption coefficients and excitation density of two compounds.

Figure S7. The fresh crystal flakes of (a) BMAPI and (b) BEAPI were used for PL kinetics measurements.

S8. Calculation of the free carrier ratio after photo-excitation.

S9. Detailed model of trap filling and fitting process.

Table S1. Crystal data and structure determinations of the BMAPI and BEAPI.

Formula	BMAPI	BEAPI
Formula Weight	2103.00	2131.05
Space group	<i>Aba2</i>	<i>Cmc2₁</i>
<i>a</i> (Å)	8.9365(10)	52.098(5)
<i>b</i> (Å)	51.969(5)	8.9769(9)
<i>c</i> (Å)	8.8754(9)	8.9902(9)
α (deg)	90	90
β (deg)	90	90
γ (deg)	90	90
<i>V</i> (Å ³)	4121.9(7)	4204.5(7)
<i>Z</i>	4	4
μ (Mo <i>Ka</i>) (mm ⁻¹)	19.721	19.366
GOF on <i>F</i> ²	1.029	1.066
<i>R</i> ₁ , <i>wR</i> ₂ [<i>I</i> > 2σ(<i>I</i>)] ^a	0.0711, 0.1262	0.0856, 0.1990
<i>R</i> ₁ , <i>wR</i> ₂ (all data) ^a	0.1595, 0.1600	0.1632, 0.2611

$$^a R_1 = \sum ||F_o| - |F_c| / \sum |F_o|, wR_2 = \{ \sum w[(F_o)^2 - (F_c)^2]^2 / \sum w[(F_o)^2]^2 \}^{1/2}$$

Table S2. Bond distances (Angstroms) of Pb-I for the BMAPI and BEAPI.

BMAPI			
Pb(1)-I(4)#1	3.115(5)	Pb(2)-I(3)#4	3.145(3)
Pb(1)-I(4)	3.115(5)	Pb(2)-I(2)#2	3.159(3)
Pb(1)-I(1)#1	3.1633(11)	Pb(2)-I(3)	3.184(3)
Pb(1)-I(1)	3.1634(11)	Pb(2)-I(2)	3.185(3)
Pb(1)-I(4)#2	3.199(5)	Pb(2)-I(1)	3.3040(12)
Pb(1)-I(4)#3	3.199(5)	Pb(2)-I(5)	3.0521(15)
BEAPI			
Pb(1)-I(5)#1	3.186(4)	Pb(2)-I(6)	3.010(2)
Pb(1)-I(2)	3.1950(16)	Pb(2)-I(3)	3.183(3)

Pb(1)-I(2)#2	3.1950(16)	Pb(2)-I(1)	3.184(3)
Pb(1)-I(5)	3.213(4)	Pb(2)-I(1)#4	3.202(3)
Pb(1)-I(4)	3.270(3)	Pb(2)-I(3)#5	3.211(3)
Pb(1)-I(4)#3	3.299(4)	Pb(2)-I(2)	3.457(2)

Symmetry transformations used to generate equivalent atoms:

For BMAPI: #1 -x+1, -y, z; #2 -x+3/2, y, z+1/2; #3 x-1/2, -y, z+1/2; #4 -x+1/2, y, z+1/2.

For BEAPI: #1 -x+2, -y+1, z-1/2; #2 -x+2, y, z; #3 -x+2, -y+2, z+1/2; #4 x, -y+2, z-1/2; #5 x, -y+1, z-1/2.

Table S3. I-Pb-I angles (deg) for the BMAPI and BEAPI.

BMAPI			
I(4)#1-Pb(1)-I(4)	90.1(3)	I(5)-Pb(2)-I(3)#4	92.71(10)
I(4)#1-Pb(1)-I(1)#1	90.57(9)	I(5)-Pb(2)-I(2)#2	90.54(10)
I(4)-Pb(1)-I(1)#1	91.00(8)	I(3)#4-Pb(2)-I(2)#2	89.50(10)
I(4)#1-Pb(1)-I(1)	91.00(8)	I(5)-Pb(2)-I(3)	93.84(9)
I(4)-Pb(1)-I(1)	90.57(9)	I(3)#4-Pb(2)-I(3)	89.17(2)
I(1)#1-Pb(1)-I(1)	177.8(2)	I(2)#2-Pb(2)-I(3)	175.48(6)
I(4)#1-Pb(1)-I(4)#2	179.4(3)	I(5)-Pb(2)-I(2)	91.23(9)
I(4)-Pb(1)-I(4)#2	89.331(10)	I(3)#4-Pb(2)-I(2)	175.72(5)
I(1)#1-Pb(1)-I(4)#2	89.29(9)	I(2)#2-Pb(2)-I(2)	88.78(2)
I(1)-Pb(1)-I(4)#2	89.16(8)	I(3)-Pb(2)-I(2)	92.25(10)
I(4)#1-Pb(1)-I(4)#3	89.331(10)	I(5)-Pb(2)-I(1)	175.69(6)
I(4)-Pb(1)-I(4)#3	179.4(3)	I(3)#4-Pb(2)-I(1)	90.21(8)
I(1)#1-Pb(1)-I(4)#3	89.16(8)	I(2)#2-Pb(2)-I(1)	86.31(8)
I(1)-Pb(1)-I(4)#3	89.29(9)	I(3)-Pb(2)-I(1)	89.37(8)
I(4)#2-Pb(1)-I(4)#3	91.2(3)	I(2)-Pb(2)-I(1)	85.77(8)
BEAPI			
I(5)#1-Pb(1)-I(2)	90.15(9)	I(1)-Pb(2)-I(2)	82.28(7)
I(5)#1-Pb(1)-I(2)#2	90.15(9)	I(6)-Pb(2)-I(3)	89.84(9)
I(2)-Pb(1)-I(2)#2	172.06(13)	I(6)-Pb(2)-I(1)	87.89(9)
I(5)#1-Pb(1)-I(5)	92.26(5)	I(3)-Pb(2)-I(1)	91.81(9)
I(2)-Pb(1)-I(5)	93.96(7)	I(6)-Pb(2)-I(1)#4	90.00(9)
I(2)#2-Pb(1)-I(5)	93.96(7)	I(3)-Pb(2)-I(1)#4	178.70(9)
I(5)#1-Pb(1)-I(4)	87.27(10)	I(1)-Pb(2)-I(1)#4	89.47(3)
I(2)-Pb(1)-I(4)	86.05(7)	I(6)-Pb(2)-I(3)#5	91.73(9)
I(2)#2-Pb(1)-I(4)	86.05(7)	I(3)-Pb(2)-I(3)#5	89.35(3)

I(5)-Pb(1)-I(4)	179.53(12)	I(1)-Pb(2)-I(3)#5	178.77(9)
I(5)#1-Pb(1)-I(4)#3	175.27(10)	I(1)#4-Pb(2)-I(3)#5	89.37(9)
I(2)-Pb(1)-I(4)#3	89.52(8)	I(2)-Pb(2)-I(3)	97.40(7)
I(2)#2-Pb(1)-I(4)#3	89.52(8)	I(2)-Pb(2)-I(6)	167.94(4)
I(5)-Pb(1)-I(4)#3	92.47(11)	I(2)-Pb(2)-I(1)#4	82.98(7)
I(4)-Pb(1)-I(4)#3	88.00(4)	I(2)-Pb(2)-I(3)#5	97.96(7)

Symmetry transformations used to generate equivalent atoms:

For BMAPI: #1 -x+1, -y, z; #2 -x+3/2, y, z+1/2; #3 x-1/2, -y, z+1/2; #4 -x+1/2, y, z+1/2.

For BEAPI: #1 -x+2, -y+1, z-1/2; #2 -x+2, y, z; #3 -x+2, -y+2, z+1/2; #4 x, -y+2, z-1/2; #5 x, -y+1, z-1/2; #5 x, -y+1, z-1/2.

Table S4. Selected strong N-H \cdots I hydrogen bond distances (H \cdots I, Angstroms) angles (deg) for the BMAPI and BEAPI.

BMAPI		
N(1)-H(1A)-I(2)	3.065(10) (Å)	132.19(7) (°)
N(1)-H(1B)-I(1)	2.985(10)	164.43(7)
N(1)-H(1C)-I(5)	3.002(10)	142.74(7)
N(2)-H(2A)-I(4)	3.234(10)	144.16(7)
N(2)-H(2B)-I(3)	3.147(10)	149.52(7)
N(2)-H(2C)-I(2)	3.120(10)	133.45(7)
Average	3.092(10)	
BEAPI		
N(1)-H(1B)-I(6)	2.988(10)	146.94(7)
N(1)-H(1C)-I(3)	2.924(10)	154.89(7)
N(7)-H(7A)-I(5)	2.857(10)	157.12(7)
N(7)-H(7B)-I(2)	3.039(10)	142.56(7)
N(7)-H(7C)-I(2)	2.862(10)	136.91(7)
Average	2.934(10)	

Table S5 The values of five distortion parameters of BMAPI and BEAPI.

BMAPI	$\langle D \rangle$	ζ	Δ	Θ	Σ
Outer layer	3.18	0.29	3.3×10^{-3}	48.5	19.5
Inner layer	3.16	0.22	1.1×10^{-3}	30.5	8.1
Outer layer	3.18	0.29	3.3×10^{-3}	48.5	19.5
BEAPI	$\langle D \rangle$	ζ	Δ	Θ	Σ
Outer layer	3.21	0.50	9.9×10^{-3}	119.7	37.1
Inner layer	3.23	0.23	1.1×10^{-3}	60.1	26.5
Outer layer	3.21	0.50	9.9×10^{-3}	119.7	37.1

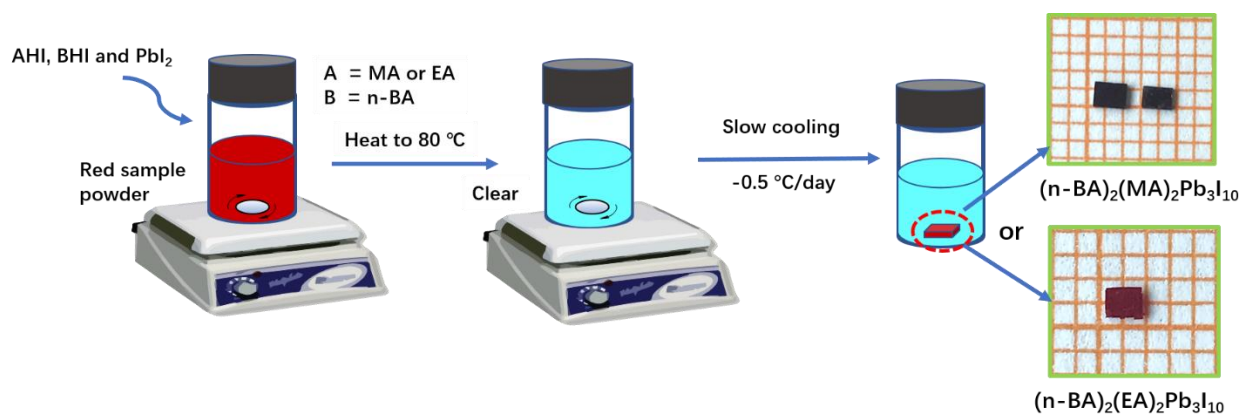


Figure S1. A schematic diagram of the growth of the bulk single crystals, and the resulting the two title single crystals (~1.5 - 2.0 mm).

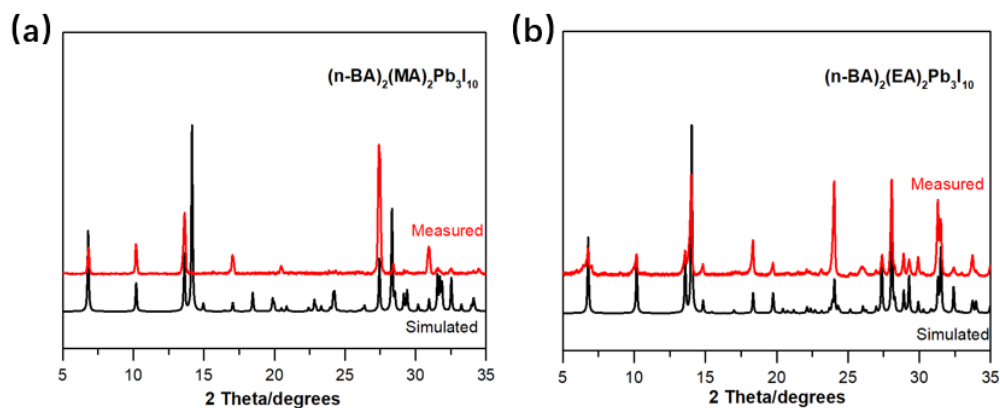


Figure S2. The powder XRD spectra of (a) BMAPI and (b) BEAPI.

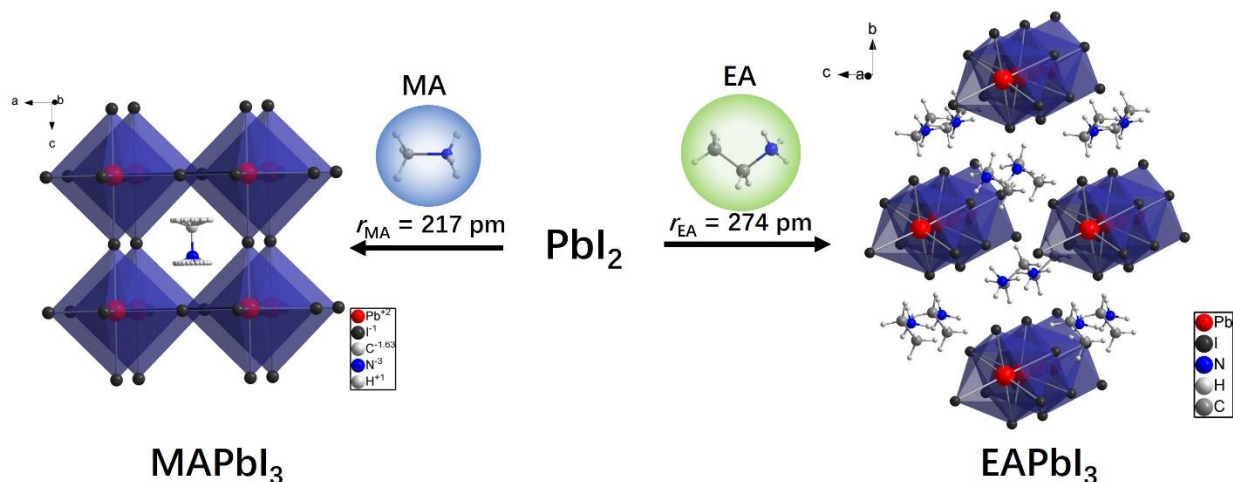


Figure S3. A diagram for the formation processes of perovskite phase MAPbI_3 (Reproduced with permission from ref 1, Copyright 2018 American Chemical Society) and non-perovskite phase EAPbI_3 (Reproduced with permission from ref 2, Copyright 2015 Royal Society of Chemistry).

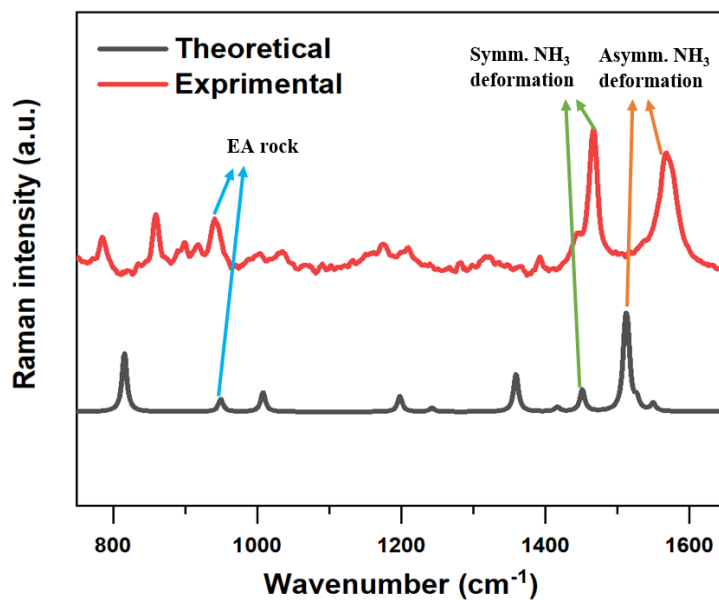


Figure S4. Comparison between experimental Raman spectra of BEAPI and the calculation of isolated EA cation. The experimental peaks of EA cation at 943, 1467 and 1560 cm^{-1} could be assigned to the vibrational modes of EA rock, symmetric NH_3 deformation and asymmetric NH_3 deformation. The stronger electron static correlation between the surface states and adsorbed molecules in our sample could lead to stronger Van Der Waals interactions, which changes the force constant of the adsorbed molecules and further results in Raman peak shifts.

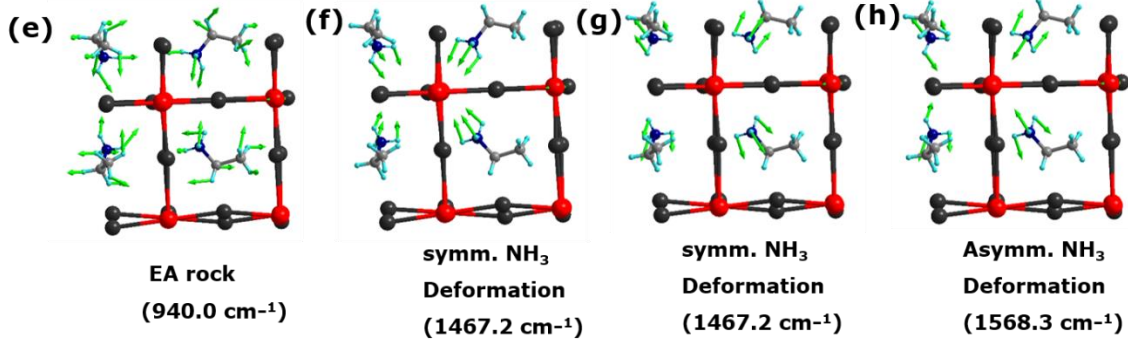
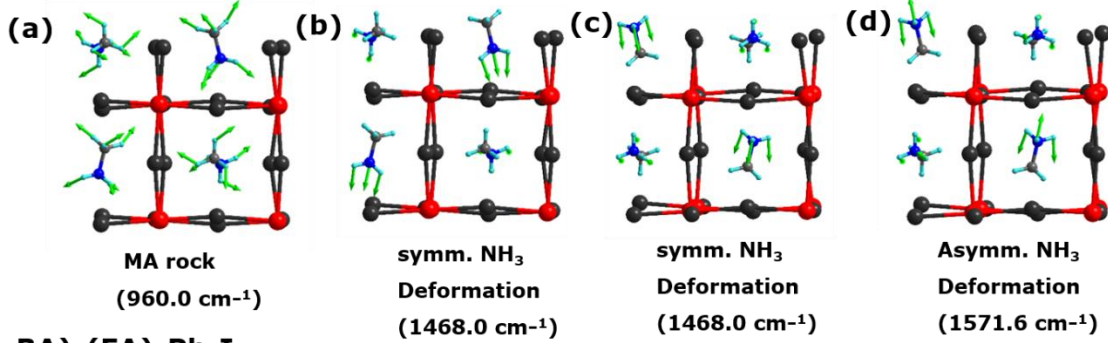


Figure S5. The vibration modes of MA and EA in BMAPI and BEAPI.

S5. Calculation of E_b using temperature dependent photoluminescence method.

PL spectra of these two fresh title compounds were measured at temperatures ranging 100-260 K in a cryostat, liquid nitrogen as the coolant, and the integrated PL intensities $I(T)$ were calculated (Figure s5a, s5c). Here, the PL intensity decreased with increased temperatures due to the thermal dissociation of excitons at higher temperatures, the temperature dependent PL intensity can be expressed as follows:

$$I(T) = \frac{I_0}{1 + Ae^{(-E_b/k_B T)}} \quad (6)$$

In which, I_0 is the PL intensity at low temperature, and k_B is the Boltzmann constant. From the linear fitting of $\ln(I_0/I(T)-1)$ and $1/k_B T$ plot, we can obtain their E_b as the slopes.³ The E_b of BMAPI and BEAPI are 65.8 ± 10 meV and 46.4 ± 10 meV, respectively (Figure s5b, s5d). In general, the PL peaks of two samples both exhibit blue shifts over the increasing temperature range, which

should be due to the dominating effect from the lattice expansion. There also remain some impurity emission peaks as background, which should come from the substrate and do not affect the E_b calculation.

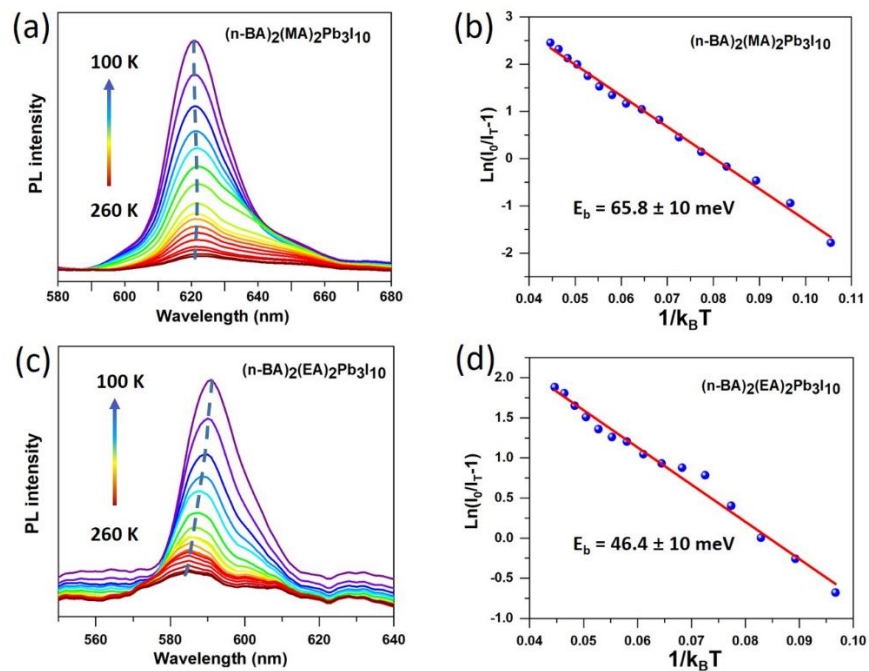


Figure S6. The temperature dependent PL spectra of (a) BMAPI and (c) BEAPI at temperature from 100-260 K; $\ln(I_0/I(T)-1)$ vs. $1/k_B T$ plot of temperature dependent PL of (b) BMAPI and (d) BEAPI.

Table S6. Multi-exponential fitting parameters for TRPL kinetics of BMAPI.

Excitation Fluence (photon/pulse/cm ²)	A ₁ (%)	t ₁ (ns)	A ₂ (%)	t ₂ (ns)	A ₃ (%)	t ₃ (ns)	t _{average} (ns)
6.04×10 ⁹	56.1	1.64 (±0.01)	16.2	10.29 (±0.12)	27.7	34.61 (±0.08)	12.17
2.01×10 ⁹	72.2	1.53 (±0.01)	9.4	10.53 (±0.18)	18.4	49.85 (±0.11)	11.27
1.21×10 ⁹	89.3	1.35 (±0.01)	4.4	9.52 (±0.20)	6.3	67.16 (±0.19)	5.86
4.02×10 ⁸	93.3	1.23(±0.01)	3.2	8.71 (±0.36)	3.5	76.42 (±0.49)	4.10

2.01×10^8	94.3	1.28 (± 0.01)	1.0	6.37 (± 0.15)	4.7	70.67 (± 0.27)	4.59
--------------------	------	---------------------	-----	---------------------	-----	----------------------	------

Table S7. Multi-exponential fitting parameters for TRPL kinetics of BEAPI.

Excitation Fluence (photon/pulse/cm ²)	A ₁ (%)	t ₁ (ns)	A ₂ (%)	t ₂ (ns)	A ₃ (%)	t ₃ (ns)	t _{average} (ns)
6.04×10^9	77.2	0.496 (± 0.002)	22.5	2.44 (± 0.01)	0.3	86.7 (± 1.2)	1.19
2.01×10^9	90.4	0.426 (± 0.001)	9.2	3.41 (± 0.03)	0.4	96.1 (± 2.3)	1.08
1.21×10^9	94.3	0.390 (± 0.001)	5.4	4.20 (± 0.06)	0.3	101.5 (± 2.9)	0.90
4.02×10^8	95.8	0.369 (± 0.002)	3.9	4.53 (± 0.10)	0.3	100.2 (± 5.2)	0.83
2.01×10^8	96.2	0.367 (± 0.002)	3.4	4.89 (± 0.16)	0.4	93.4 (± 5.6)	0.89

S7. Calculations of the absorption coefficients and excitation density of two compounds.

To calculate the excitation density of the two samples, we first measured their absorption coefficients using the laser. The perovskite crystals were torn into thin flakes that were placed on a quartz substrate and used for measurements (Figure S7). From Scanning Electron Microscope (SEM) measurement, the section thicknesses of BMAPI and BEAPI are approximately 680 and 600 nm, respectively. The absorbance (A) can be calculated by the following formula:

$$A = \log (I_0/I_1) \quad (1)$$

Here, I_0 is incident light intensity and I_1 is the transmitted light intensity. The A values of BMAPI and BEAPI are 0.73 and 0.25, respectively. The absorption coefficient $\varepsilon = A/l$, where l is the path length of the light, which is equal to the thickness of the crystal. So, we obtain $\varepsilon = 1.07 \times 10^5$ and $4.2 \times 10^4 \text{ cm}^{-1}$ for BMAPI and BEAPI, respectively. The excitation density n can be calculated as photon flux f in photons/cm² multiplied by absorption coefficient ε : $n = f\varepsilon$, Table S8 summarizes the corresponding excitation density at different laser photon flux in the TRPL measurements:

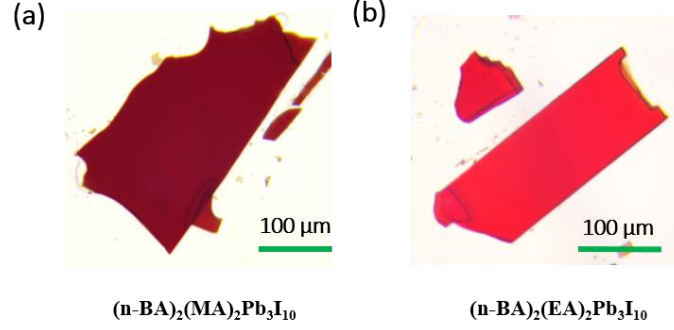


Figure S7. The fresh crystal flakes of (a) BMAPI and (b) BEAPI were used for TRPL kinetics measurements. The laser spot was focused on a bulk area during the measurements.

Table S8 Excitation density of BMAPI and BEAPI with different laser photon flux.

Excitation Fluence (photon/pulse/cm ²)	Excitation Intensity (cm ⁻³) of BMAPI	Excitation Intensity (cm ⁻³) of BEAPI
6.04×10^9	6.46×10^{14}	2.54×10^{14}
2.01×10^9	2.15×10^{14}	8.44×10^{13}
1.21×10^9	1.29×10^{14}	5.08×10^{13}
4.02×10^8	4.30×10^{13}	1.69×10^{13}
2.01×10^8	2.15×10^{13}	8.44×10^{12}

S8 Calculation of the free carrier ratio after photo-excitation

After photoexcitation by the laser pulse, the free carriers and weak coupled excitons actually coexist in the crystal under a thermodynamics equilibrium. The ratio between these two species is a fixed term resembling the ion-electron balance in a hot plasma, which depends strongly on the exciton binding energy as well as the excitation concentration. Therefore, we can use a classic Saha-Langmuir theory to calculate approximately the ratio of the free carriers X (i.e. fraction of the free carriers among all the excited species) in the system:

$$\frac{x^2}{1-x} = \frac{1}{n} \left(\frac{2\pi m k_B T}{h^2} \right)^{1.5} e^{-\frac{E_b}{k_B T}} \quad (12)$$

where E_b refers to the exciton binding energy, m is the exciton effective mass, T is the temperature

and n is the excitation concentration. The following table summarizes the calculated x ratio of the two samples under the excitation condition of the PL decay measurements. Apparently, during our measurement, the majority of the excited species in the 2D perovskite crystals are free carriers and the contribution of the exciton can be mostly neglected.

Table S9. The calculated values of ratio of the free carriers x .

Excitation Intensity (cm^{-3}) of BMAPI	x	Excitation Intensity (cm^{-3}) of BEAPI	x
6.46×10^{14}	0.949	2.54×10^{14}	0.994
2.15×10^{14}	0.982	8.44×10^{13}	0.998
1.29×10^{14}	0.989	5.08×10^{13}	0.999
4.30×10^{13}	0.996	1.69×10^{13}	0.999
2.15×10^{13}	0.998	8.44×10^{12}	0.999

S9. Detailed model of trap filling and fitting process.

The detailed calculation procedures of the model have been described in the reference⁴. In brief, the equilibrium between free carriers and excitons can be described using the Saha equation. When photodoping (i.e accumulated trap filling) is present, the Saha equation can be generalized as the following equation expressing the concentrations of electrons (n_e), holes (n_h) and excitons (n_x) corresponding to the overall untrapped photogenerated species density N :

$$n_h = -\frac{(A - n_T)}{2} + \frac{1}{2}\sqrt{(A + N_T)^2 + 4AN} \quad (2)$$

$$n_e = n_h - n_T \quad (3)$$

where $A = v_x/(v_h v_e) \exp[-E_b/(k_B T)]$, λ_i is the thermal wavelength of the species i and $v_i = \lambda_i^{-3}$, n_T is concentration of filled traps and N_T is the concentration of total traps.

Here, we assume that n_T varies little and is only dependent on the average concentration of electrons $\overline{n_e(t)} = \frac{1}{t_0} \int_0^{t_0} n_e(t) dt$ during the PL recording time t_0 between the repetition pulses. Then, we get the following rate equations:

$$\frac{dn_T}{dt} = R_{pop}(N_T - n_T)\overline{n_e(t)} - R_{dep}(N_T^2 + n_T\overline{n_e(t)}) = 0 \quad (4)$$

where R_{pop} and R_{dep} are the recombination rates of trap population and depopulation, respectively. Taking equations (2) and (3) we can obtain the average concentration of electrons as:

$$\overline{n_e(t)} = \frac{1}{t_0} \int_0^{t_0} n_e(t) \approx K(A + n_T), K = \frac{1}{\gamma_0 t_0} \ln \left[1 + \frac{AN(0)}{N_T(A + N_T)} \right] \quad (5)$$

Here $N(0)$ can be simplified as the initial excitation density N_c . γ_0 is the total rate of electronic decay not involving the traps. Substitution of equation (5) into (4) gives:

$$n_T = -\frac{1}{2}\alpha + \frac{1}{2}\sqrt{\alpha^2 + 4\beta N_T} \quad (6)$$

$$\alpha = \frac{[A + R(A - N_T)]}{\left(1 + \frac{1}{K} + R\right)} \quad (7)$$

$$\beta = \frac{RA}{\left(1 + \frac{1}{K} + R\right)} \quad (8)$$

$$K = \frac{1}{\gamma_0 t_0} \ln \left[1 + \frac{AN_c}{N_T(A + N_T)} \right], R = R_{pop}/R_{dep} \quad (9)$$

which are the equations 7~10 in the main text.

During the fitting of the trapping model, we first assume that both traps exhibit filling but due to different trap population and depopulation rates, the ratio of unoccupied trap densities between two type of traps varies with different excitation intensity. Therefore we can plot $A_1/(A_1+A_2) \sim N_c$ data and fit with the expression combination equation 12-14 in the main text.

$$\frac{A_1}{A_1+A_2} = \frac{n_{uncT1}}{n_{uncT1}+n_{uncT2}} = \frac{N_{T1} + \frac{1}{2}\alpha_1 - \frac{1}{2}\sqrt{\alpha_1^2 + 4\beta_1 N_{T1}}}{(N_{T1} + \frac{1}{2}\alpha_1 - \frac{1}{2}\sqrt{\alpha_1^2 + 4\beta_1 N_{T1}}) + (N_{T2} + \frac{1}{2}\alpha_2 - \frac{1}{2}\sqrt{\alpha_2^2 + 4\beta_2 N_{T2}})} \quad (10)$$

Here, n_{uncT1} and n_{uncT2} are the concentrations of filled traps 1 and 2, respectively. N_{T1} and N_{T2} are the original concentrations of trap 1 and trap 2, respectively. In this work, A of BMAPI and BEAPI were calculated as $1.42 \times 10^{15} \text{ cm}^{-3}$ and $5.10 \times 10^{15} \text{ cm}^{-3}$, respectively, the PL recording time t_0 was $2.5 \times 10^{-7} \text{ s}$, and γ_0 was taken as the rate of the charge recombination not contributing to the trap filling process (i.e. the slow component in the PL kinetics, as shown in Table S6 and S7). We first set all the four fitting parameters (N_{T1} , N_{T2} , R_1 , and R_2) while analyzing these two compounds. The best fitting results are shown in Table S9. In this table, R_2 of BMAPI and BEAPI are 34.8 and 41.1, respectively. Considering that R is the ratio between trap population and

depopulation rates, we can then estimate the depopulation time of their traps 2 using the trap population time obtained in the PL kinetics (from the lifetime of the second component ~9 and ~4 ns, respectively) to be ~313 and ~165 ns, respectively. These depopulation time of traps 2 are not much different from the interval between the pulses in our measurement (250 ns). Therefore we conclude that no considerable trap filling should occur in their traps 2 since the depopulation rate is too fast.⁵ The model is then modified for the case where trap filling occurs only in trap1 as follows:

$$\frac{A_1}{A_1+A_2} = \frac{n_{\text{uncT1}}}{n_{\text{uncT1}}+N_{\text{T2}}} = \frac{N_{\text{T1}} + \frac{1}{2}\alpha_1 - \frac{1}{2}\sqrt{\alpha_1^2+4\beta_1N_{\text{T1}}}}{(N_{\text{T1}} + \frac{1}{2}\alpha_1 - \frac{1}{2}\sqrt{\alpha_1^2+4\beta_1N_{\text{T1}}}) + N_{\text{T2}}} \quad (11)$$

Here the $A_1/(A_1+A_2)$ represents the ratio between the unoccupied density of trap 1 and the original density of trap 2. We first set all the three fitting parameters (N_{T1} , N_{T2} , and R) free for the values from the equation (10) as shown in Table S9. Then, we fit the equation (11) to get the new parameters (Table S9).

Table S10. Trap densities obtained from the fitting.

Model	Compounds	R ₁	R ₂	N_{T1} (10 ¹⁵ cm ⁻³)	N_{T2} (10 ¹⁵ cm ⁻³)
				³⁾	
$\frac{A_1}{A_1+A_2} = \frac{n_{\text{uncT1}}}{n_{\text{uncT1}}+n_{\text{uncT2}}}$	BMAPI	1.4×10^5	34.8	6.0	0.08
	BEAPI	5.3×10^4	41.1	7.4	0.18
$\frac{A_1}{A_1+A_2} = \frac{n_{\text{uncT1}}}{n_{\text{uncT1}}+N_{\text{T2}}}$	BMAPI	1.4×10^5	/	21.8	0.11
	BEAPI	5.1×10^4	/	37.6	0.59

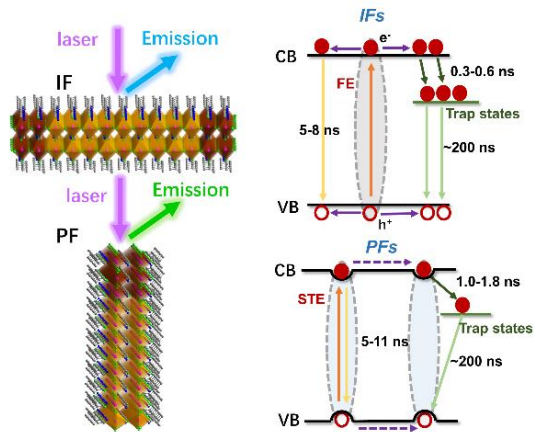
Reference

- (1) Spanopoulos, I.; Ke, Wei.; Stoumpos, C. C.; Schueller, E. C.; Kontsevoi, O. Y.; Seshadri, R.; Kanatzidis, M. G. Unraveling the chemical nature of the 3D "hollow" hybrid halide perovskites. *J. Am. Chem. Soc.* **2018**, *140*, 5728–5742.

- (2) Safdari, M.; Fischer, A.; Xu, B.; Kloo, L.; Gardner, J. M. Structure and function relationships in alkylammonium lead(ii) iodide solar cells. *J. Mater. Chem. A* **2015**, *3*, 9201–9207.
- (3) Chen, Z.; Yu, C.; Shum, K.; Wang, J. J.; Pfenninger, W.; Vockic, N.; Midgley, J.; Kenney, J. T. Photoluminescence Study of Polycrystalline CsSnI₃ Thin Films: Determination of Exciton Binding Energy. *J. Lumin.* **2012**, *132*, 345–349.
- (4) Stranks, S. D.; Burlakov, V. M.; Leijtens, T.; Ball, J. M.; Goriely, A.; Snaith, H. J. Recombination Kinetics in Organic-Inorganic Perovskites: Excitons, Free Charge, and Subgap States. *Phys. Rev. Appl.* **2014**, *2*, 034007.
- (5) Zheng, K.; Žídek, K.; Abdellah, M.; Messing, M. E.; Al-Marri, M. J.; Pullerits, T. Trap States and Their Dynamics in Organometal Halide Perovskite Nanoparticles and Bulk Crystals. *J. Phys. Chem. C* **2016**, *120*, 3077–3084.

Paper III

Free excitons versus self-trapped excitons at different facets of Ruddlesden Poppers two-dimensional lead halide perovskite single crystals





Free excitons versus self-trapped excitons at different facets of Ruddlesden Poppers two-dimensional lead halide perovskite single crystals

Received 00th January 20xx,
Accepted 00th January 20xx

Mingli Liang,^{a†} Weihua Lin,^b Qian Zhao,^a Xianshao Zou,^b Zhenyun Lan,^c Jie Meng,^a Qi Shi,^b Sophie E. Canton^d, Tönu Pullerits,^b and Kaibo Zheng^{a,b,*}

DOI: 10.1039/x0xx00000x

www.rsc.org/

Sub-band gap broad photoluminescence has been widely observed in Ruddlesden Poppers two-dimensional (2D) lead halide perovskites (LHPs). However, the occurrence of such broad emission varies among different 2D structures. Whether the formation of self-trapped excitons (STEs) or in-gap defect states account for such broad emission is still under debate. In this paper, we studied the photoluminescence features from different facets of three 2D LHP single crystals with various spacing cations (i.e., iso-butylamine, n-butylamine, n-pentylamine). Our results show that self-trapped excitons do induce sub-bandgap emission, which depend highly on the local structures of the single crystals. In the bulk area with no boundary of the 2D inorganic layers, the STEs are less likely to be formed, whereas free excitons (FEs) dominate due to the weak electron-phonon coupling in a more symmetric lattice. In the facet perpendicular to the 2D inorganic layers, large distortion of the lead halide octahedra due to the accumulation of the strain along the 2D layers enhance the electron-phonon coupling, and therefore the formation of STEs is favourable. The spacing cations also influence the structure of the bulk and edge areas. Spacing cations that maintain the local structure rigidity (i.e., n-butylamine) promote the lattice distortion in the edge area and facilitate the formation of STEs. The time-resolved PL studies indicate that photo-generated FE in the bulk area can move freely within the 2D plane and display the trapping and trap filling by the intrinsic defects of the 2D perovskites. STEs at the edge area are more or less susceptible to further trapping due to their restricted spatial localization. However, with increasing STE density, the STE diffusion is enhanced, and the defect trapping process is enabled. Our findings revealed the severe dependence of STE formation and their dynamics in 2D LHPs on the local structure.

Introduction

Ruddlesden Poppers (RP) two-dimensional lead halide perovskites (2D LHPs) have become increasingly prevalent over the past several years. Compared with the traditional 3D APbX₃ (where A is a small cation, X is a halide) perovskites, they show unique advantages with higher stability to moisture, more tuneable electronic structures, and larger defect tolerance, etc.¹⁻⁵ These merits render them as promising building block materials in solar cells, light-emitting diodes (LEDs), and photodetectors.⁶⁻¹⁴ The general formula of 2D RP LHPs is (B)₂(A)_{n-1}Pb_nX_{3n+1}, where B is a long chain organic amine cation, A refers to the small amine cation, n is the number of octahedral layers. Inorganic semiconductor quantum wells (QWs) with a certain thickness (n) are isolated periodically by organic spacing layers. Such unique microscopic structure induces electronic

structure properties that differ from their 3D counterparts. Among them, one of the most concerning topics is the identification of the species. Generally speaking, Wannier excitons are believed to be generated in semiconductor 2D quantum wells due to the dielectric confinement with the exciton binding energy (E_b) depending on the well thickness.¹⁵ 2D perovskites, on the other hand, possess much softer lattice and more complex vibrational structures due to the intercalation of the organic spacing cations.¹⁶ Consequently, photo-induced local lattice distortion can occur due to strong electron-phonon coupling leading to the formation of so-called self-trapped excitons (STEs).¹⁷⁻²⁰ One fingerprint of such STE formation in 2D perovskites is a broad sub-bandgap emission with a large Stokes shift.²¹ However, the observation of such broad emission depends on the sample parameters such as n values and molecular composition.²² Recent photoluminescence (PL) microscopic study on single 2D perovskite flakes even disagrees with the assignment of such broad emission to STE.²³ The photophysics in 2D perovskites has also been reported to be modulated by the local structures. Low-energy emission was observed to originate from the edge state of single-crystal (SC) flakes, which was interpreted by the formation of low energy edge states (LES).²⁴ DFT calculation indicates the formation of such LES is induced by the asymmetric relaxation of the interface strain to trigger the surface reorganization.²⁵⁻²⁶ In this regard, the photo-generated species in the bulk volume and at the edge area can be different due to the difference in local electronic structures. Therefore,

^a Department of Chemistry, Technical University of Denmark, DK-2800 Kongens Lyngby, Denmark. Email: kzheng@kemi.dtu.dk

^b Department of Chemical Physics and NanoLund, Lund University, Box 124, 22100, Lund, Sweden.

^c Department of Energy Conversion and Storage, Technical University of Denmark, DK-2800 Kongens Lyngby, Denmark.

^d ELI-ALPS, ELI-HU Non-Profit, Ltd., Dugonics ter 13, Szeged 6720, Hungary. Email: Email: Sophie.Canton@eli-alps.hu

Electronic Supplementary Information (ESI) available: [details of any supplementary information available should be included here]. See DOI: 10.1039/x0xx00000x

identifying the photo-generated species and clarifying the corresponding dynamics within various local structures is essential to characterize the actual photophysics in 2D perovskite materials.

In this paper, we investigated emissive state dynamics to identify the photo-generated species at two different surface facets of 2D RP lead bromide perovskite SCs with three spacing cations [i.e., iso-butylamine (iso-BA), n-butylamine (n-BA) and n-pentylamine (n-PA)] corresponding to in-plane and perpendicular facets with the 2D inorganic lattice layers, respectively. The difference in spacing cations controls the energies of LES by modulating the interface strain relaxation, which is confirmed by the structural characterization. The temperature-dependent PL measurements at two facets indicate that STEs are dominated at the perpendicular facet (PF) while free excitons (FE) are generated at the in-plane facet (IF). The STE formation is strongly affected by the spacing cations where n-PA with less interface lattice strain generates shallower STE at the PFs after photoexcitation. Furthermore, the time-resolved PL study discovered that the STEs at the PFs are more localized than FEs in bulk and exempt from the intrinsic defect state trapping. However, when the excitation density is increased, the large STE concentration will lead to the flattening of the lattice deformation and thereby facilitate the STE diffusion. The defect trapping is then re-enabled. Our results provide direct confirmation of STE formation in 2D perovskites but specify their location to be more at the PFs. FE versus STE at different parts of 2D perovskite will then trigger distinct photophysical behaviours.

Experimental Section

Materials

PbBr₂ (98 %), methenamine hydrobromide (98 %, MABr), iso-butylamine (99 %, iso-BA), n-butylamine (99.5 %, n-BA), n-pentylamine (99.5 %, n-PA), ethanol (99.8%) and hydrobromic acid (HBr, 47 % in water) have been utilized without further treatment. All the chemicals were supplied by Sigma-Aldrich.

Synthesis of long-chain amine bromides

The long-chain amine bromides of them were manufactured by adding equal stoichiometric ratio of iso-BA, n-BA and n-PA to dilute aqueous HBr (25% in mixed ethanol and water) under strong stirring in an ice-water bath. The white products of them were acquired by rotary evaporation at 60 °C. After that, a lot of white crystals of long-chain amine bromides (iso-BABr, n-BABr, and n-PABr) were obtained by washing three times with ethanol and vacuum drying for 24h.

Synthesis of 2D RP LHP single crystals

(iso-BA)₂(MA)Pb₂Br₇ (iso-BAPB), (n-BA)₂(MA)Pb₂Br₇ (n-BAPB) and (n-PA)₂(MA)Pb₂Br₇ (n-PAPB) SCs obtained by the temperature lowering method of PbBr₂ (2.5 mmol), MABr (1.5 mmol), iso-BABr/ n-BABr/ n-PABr (3.0 mmol) in 5 ml HBr (47 % in water). The mixtures were placed into glass bottles (20 ml). Afterwards, the glass bottles were sealed and stirred at room temperature for 30 minutes to induce the formation of yellow precipitates. Completely clear solutions were obtained after reaction for few minutes at 80 °C as precursor. Bulk SCs were grown from such solution at a cooling rate of 0.5 °C/day

starting from 50 °C. The obtained centimetre-scaled crystals and their powder X-ray diffraction (PXRD) spectra are shown in Figure 2a.

Characterizations

Single crystal XRD measurements were performed on SuperNova Dual Wavelength CCD diffractometer (Agilent Technologies, Mo-K α with $\lambda = 0.71073$ Å) at the room temperature (~298 K). Further structural solves and refinements by full-matrix least-squares fitting on F^2 using SHELX-97, the details are the same with our recent work.²⁷ PXRD data were collected on a Rigaku MiniFlex 136 II diffractometer using Cu-K α radiation with $\lambda = 1.5406$ Å. The UV-vis absorption spectra were measured on PerkinElmer (Lambda 1050) with a UV-Vis-NIR absorption spectrophotometer. Steady-state PL spectra were acquired on a Avantes AvaSpec-2048 spectrometer under an excitation wavelength of 375 nm. The time-resolved photoluminescence (TRPL) measurements were performed with time-correlated single photon counting (TCSPC, Picoharp) using pulsed diode laser (Wavelength: 375 nm; Frequency: 2.5 MHz; Pulse duration: 8 ps;) and a fast avalanche photodiode; when measuring TRPL spectra of IFs and PFs, a long-pass filter from 400 nm and a long-pass filter from 470 nm are used, respectively.

Results and Discussion

Local lattice distortions and structural origin of the edge state in 2D perovskite SCs.

According to the theoretical calculation, the edge states in 2D RP perovskites are mainly induced by the relaxation of the interface strain along the 2D inorganic layer nucleating the surface reorganization, while such strain along the direction perpendicular to the 2D layer can be released by the spacing cations.²⁵ As demonstrated by an example structure of (B)₂(A)_{n-1}Pb_nX_{3n+1} (n=2) (Figure 1), PbX₆ octahedra are extended by the co-corner links along (200) facet forming the largest crystal facet in the macroscopic crystal. Along the (002), (110), and (111) facets, the organic spacing layers and the inorganic QWs are superimposed, which makes the crystal grow slowly. Therefore, these facets correspond to the small crystal facets in the macroscopic crystal (Figure 1a and 1b). The lattice strain along the direction vertical to the (200) facet can be released into the organic spacing cations every two periodic layers (Figure 1c).

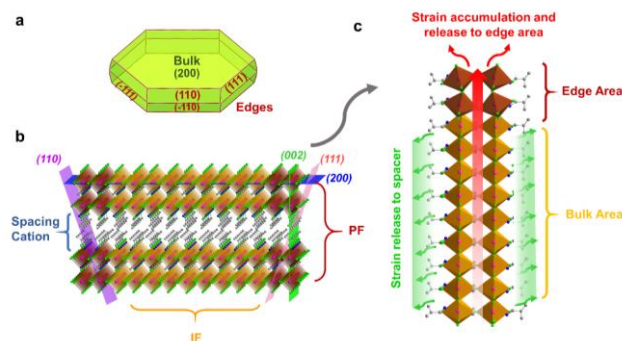


Figure 1. A macroscopic morphology of crystal morphology of a 2D RP perovskite (a), which is simulated by Mercury based on our structural data in supporting information; schematics show the definition of IF and PF(b) and the directions of strain accumulation release (c).

Thus, no significant structural difference should occur between the surface of the IF and the bulk volume area. We can then consider the (200) surface facet as a bulk-behaved structure. On the other hand, lattice strain continuously accumulates along the (002), (110), and (111) directions and releases at the surface boundary. Thus, the surface lattice structure along them should be different from the inner bulk state, resulting in the so-called edge area where LES are found (Figure 1c).²⁴

Since the LES formation is induced by the accumulation and relaxation of strain-related elastic energy, spacing cations are expected to play a critical role in modulating the LES. They can offer additional paths to relax the accumulated strain as mentioned above.^{28,29} Therefore, in this work, we have synthesized three benchmark 2D perovskites SCs with various spacing cations, iso-BAPB, n-BAPB, and n-PAPB. They all belong to the typical 2D RP phase perovskites $(B)_2(A)_{n-1}Pb_nX_{3n+1}$ with $n=2$. Specifically, n-BAPB and n-PAPB are crystallized in the orthorhombic space group of *Ccc2* (No. 37, Table 1), while the space group of iso-BAPB is determined as the monoclinic space group of *Cc* (No. 9) as its β angle (90.789(7)°) is far away from 90° (Table 1). The single crystal powder XRD patterns in Figure 2a have been well refined to reproduce the fine 2D layered structure as shown in Figure 2b-2d. Among them, n-PAPB exhibit the biggest inter-inorganic layer spacing of 15.22 Å due to the longest spacing cations. However, iso-BAPB and n-BAPB have a similar spacing distance of 13.45 Å and 13.49 Å, respectively. This may be due to the considerable steric hindrance of iso-BA that prevents the interdigitation of two opposing spacing cations compared with n-BA.

Although it is difficult to directly characterize the local structure of each surface facet, we can still estimate the accumulation of strain-related elastic energy by quantifying the octahedron distortion. Pb^{2+} , as a lone-pair metal cation, is usually observed to be off-centered within the X_6 octahedral cage caused by the second-order Jahn-Teller (SOJT) effects.^{30,31} This phenomenon is also common in 2D LHPs.³²⁻³⁴ For instance, in a $PbBr_6$ octahedron of iso-BAPB, the longest Pb-Br bond is 3.061(9) Å and the shortest Pb-Br bond is only 2.884(5) Å, and their Br-Pb-Br cis-angles also deviate from 90° (Table S1 and S2). Herein, we can use three parameters, namely the tilting distortion parameter (Δ), the angle distortion parameter (Σ), and the out-of-center distortion parameter (Δ_{od}), to quantitatively compare $PbBr_6$ octahedral distortions of the iso-BAPB, n-BAPB, and n-PAPB. Δ and Σ represent the distortion degree of the Pb-Br bond lengths and Br-Pb-Br cis-angles, respectively.^{29,35} Δ_{od} describes the degree of deviation of Pb atom from an ideal octahedral center.³⁰ The calculation equations for Δ and Σ are listed below (Eq. 1 and 2). And the calculation method of Δ_{od} is given in S1.

$$\Delta = \sum_{i=1}^6 \left(\frac{d_i - \langle D \rangle}{\langle D \rangle} \right)^2 \quad (1)$$

$$\Sigma = \sum_{i=1}^{12} |90 - \varphi_i| \quad (2)$$

Table 1. Crystal data and structure determinations of the iso-BAPB, n-BAPB and n-PAPB.

Samples	iso-BAPB	n-BAPB	n-PAPB
Formula	1154.11	1154.11	1199.20
Space group	<i>Cc</i>	<i>Ccc2</i>	<i>Ccc2</i>
a (Å)	39.173(4)	8.3262(7)	8.3250(6)
b (Å)	8.3835(5)	39.247(4)	42.717(4)
c (Å)	8.3225(5)	8.3629(8)	8.3250(8)
α (deg)	90	90	90
β (deg)	90.789(7)	90	90
γ (deg)	90	90	90
V (Å ³)	2732.9(4)	2732.8(5)	2960.5(4)
Z	4	4	4
(Mo $K\alpha$) (mm ⁻¹)	22.537	22.538	20.811
GOF on F^2	1.031	1.065	1.046
$R1^a$	0.0892	0.0789	0.0633
$wR2$ [$I > 2\sigma$] (I) ^a	0.2080	0.1935	0.1406

$$^a R1 = \sum ||F_o| - |F_c|| / \sum |F_o|, wR2 = \{ \sum w[(F_o)^2 - (F_c)^2]^2 / \sum w[(F_o)^2]^2 \}^{1/2}$$

where the d_i are the individual Pb-Br bond distances in a the $PbBr_6$ octahedron. $\langle D \rangle$ is the average Pb-Br bond length, the φ_i are the twelve cis-angles of Br-Pb-Br around the Pb atom. The calculation results of these three parameters are shown in the Figure 2e-2g. It is worth noting that there are two types of Pb^{2+} ions in iso-BAPB (i.e., Pb1 and Pb2) since it crystallizes in a low symmetry monoclinic space group. In this work, we took their average parameter value to represent the $PbBr_6$ distortion of it. The distortion analysis revealed that Δ and Δ_{od} values of n-PAPB are much larger than that of iso-PAPB and n-BAPB. On the other hand, the value of Σ in iso-BAPB is the largest one (19.97°), while the values of n-BAPB (15.95°) and n-PAPB (14.86°) are relatively close. Overall, we can conclude that the $PbBr_6$ octahedron of n-BAPB has least distortion while store the strain-related elastic energy to the largest extent, while that of n-PAPB has strongest distortion to relax the interface lattice strain. In this scenario, we can expect that n-BAPB should exhibit pronounced LES with lowest energy while it's more difficult for n-PAPB to form LES due to the less lattice deformation on the edge.

Formation of the STE vs. FE (free excitons) in three SCs at different facets.

After characterizing the local structures of the SCs, we measured the steady-state PL spectra at both PF and IF of the three SCs as discussed above, respectively. Figure 3a illustrates the configuration of the PL measurement on 2D perovskite SCs using a 375 nm CW laser with beam size ~ 0.12 mm². Such beam size is much smaller than the area of each faceted surface, ensuring that the PL signals are solely contributed by the incident beam area. In addition, the laser penetration depths are calculated to be about 71, 72, and 79 nm for iso-BAPB, n-BAPB, and n-PAPB, respectively (for the details of the method see S2). Compared with centimeter-scaled crystals, such small penetration depths indicate that PL emission from the surface can be detected. Figure 3b shows the PL spectra from two facets of three SCs at room temperature. The emission from different facets

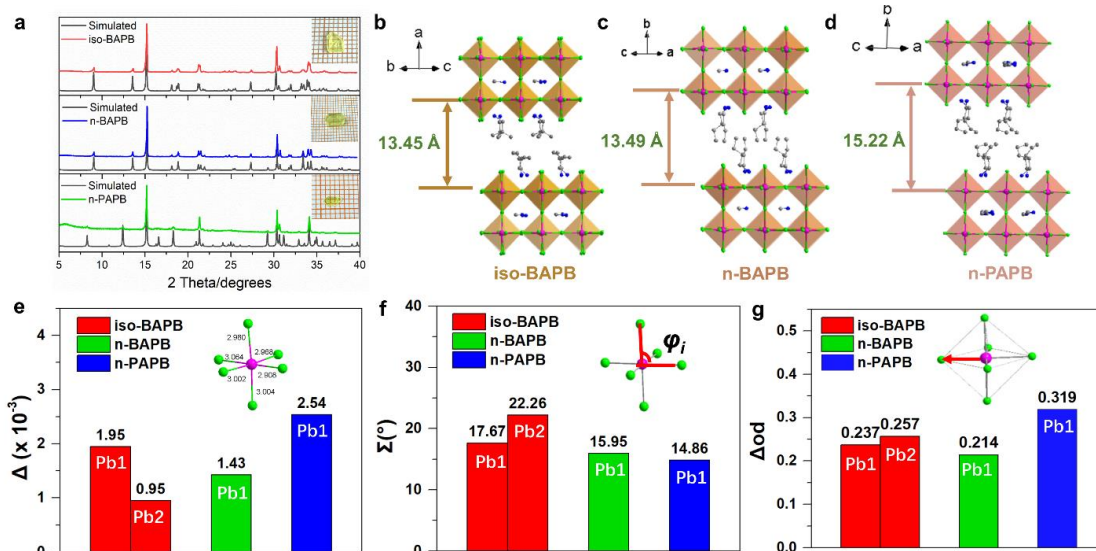


Figure 2. Powder XRD (a) and crystal structures of the three SCs (b, c, d), and their three distorted parameters of PbBr₆ octahedron (e, f, g).

in iso-BAPB and n-BAPB exhibit clear single bands, but PL at PF drastically red-shift compared to that of IF by 85.0 nm (~0.45 eV), 81.6 nm (~0.43 eV), respectively. In n-PAPB, two emission peaks occur at the PF while the low-energy emission is less red-shifted (75.1 nm, ~0.41 eV) compared with the other two samples.

The difference in PL emission at two facets firstly should not be mainly induced by the lattice distortion as the shifting energy (i.e., 0.4–0.45 eV) is much larger than the value that octahedral distortion induced bandgap modification can provide.^{36–38} On the contrary, the origin of the spatially distributed low-energy emission in 2D RP LHPs has been frequently debated in recent years. The red-shift broad emission is usually assigned to STEs. Figure 3c is a schematic of the energy level structure of STE, in which, once electrons and holes are photogenerated, they will quickly self-trap from a mobile state to a more stable self-trapping state. Moreover, self-trapping energy (E_{st}) is defined as the energy loss of exciton in this process.²⁰ However, recent PL microscopic studies argued that low-energy emission in 2D RP LHPs should be more related to the mid-bandgap trap states trapping the diffusing FEs.²³

In order to determine the physical process responsible for the emission in the three samples, we conducted the temperature-

dependent PL at IFs and PFs with temperatures from 100 to 280K for three samples (Figure 4). For n-PAPB, the PL intensity of the IF decreases with increasing temperature due to the dissociation of the exciton into free charges (Figure 4c). On the other hand, the dual emission peaks occur all over the temperature region at the PF, whereas the respective population high-energy PL becomes more dominant at low temperature (Figure 4f). This phenomenon is against the traditional exciton trapping mechanism where the emission from trap state and band-edge exciton states are competing and modulated by the thermal equilibrium between the trapping and detrapping of the excited carriers. In this scenario, the high-energy band-edge exciton emission should be diminished at low temperature as no sufficient thermal energy can be provided to deactivate the trapped charge carriers. On the other hand, we believe the low-energy emission at the PF should be attributed to STEs as in perovskite they are formed by the electron-LO phonon coupling via the Fröhlich interaction as shown in Figure 3c, which should be dominate at room temperature.³⁹ Furthermore, the line-shapes of PL spectra in n-BAPB and iso-BAPB remain constant with the temperature at both IFs and PFs, indicating more stabilized STE in those samples. In addition, we also obtained their respective E_b by fitting the temperature-dependent PL peak intensities (for the details of the method see S3).

In order to verify our assumption, we calculate the electron-phonon coupling strength from the FWHMs of temperature-dependent PL spectra using the following model:^{39,40}

$$\Gamma(T) = \Gamma_0 + \Gamma_{ac} + \Gamma_{LO}$$

$$= \Gamma_0 + \gamma_{ac}T + \gamma_{LO}N_{LO}(T) + \gamma_{imp}e^{-E_b/k_B T} \quad (3)$$

Here, Γ_0 is a temperature-independent inhomogeneous broadening contributing, which arises from scattering due to disorder and imperfections. Γ_{ac} and Γ_{LO} are homogeneous broadening terms, which result from acoustic and Fröhlich scattering, with charge-carrier phonon coupling strengths of γ_{ac} and γ_{LO} , respectively. $N_{LO}(T) = 1/(e^{E_{LO}/k_B T} - 1)$, where the E_{LO} is an

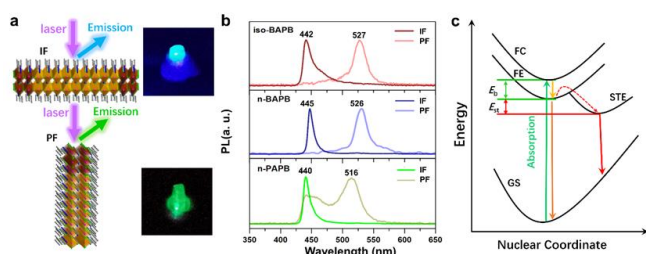


Figure 3. Schematics of PL measurements (a); PL spectra of bulk and edge states of the three SCs (b), and the schematic of the energy level structure of STE (c) (FC is free carrier state; FE is free exciton state; GS is ground state; E_{st} is self-trapping energy)

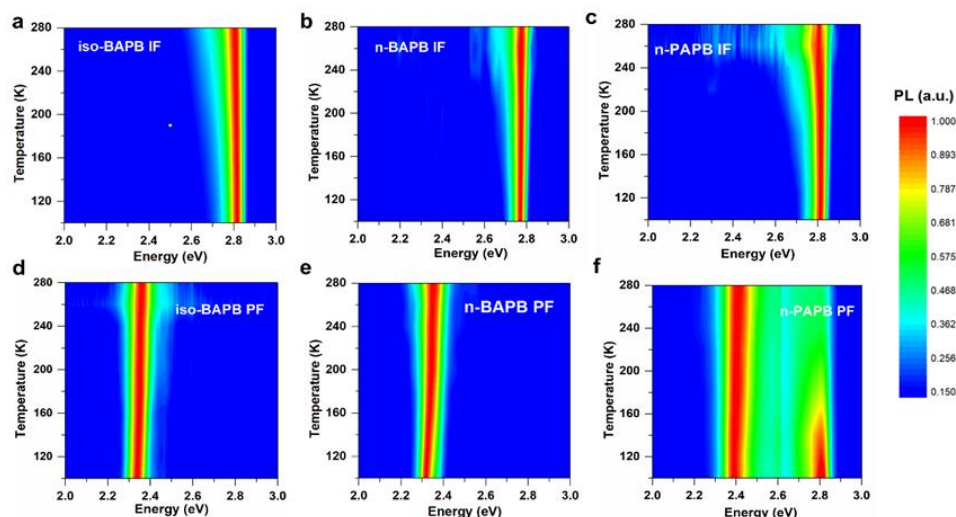


Figure 4. Temperature-dependent PL spectral colour plots of IFs and PFs of the three SCs.

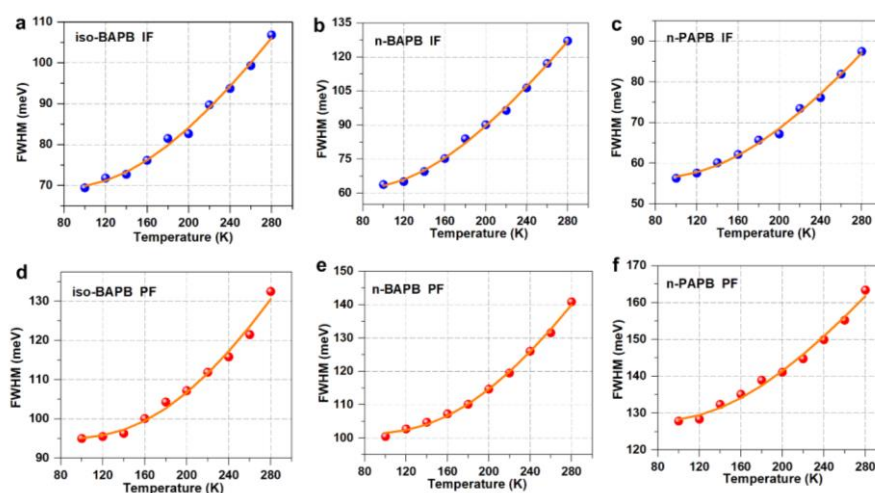


Figure 5. FWHM of the temperature-dependent PL for the IFs and PFs of the three SCs, and the solid orange lines fit equation 4.

energy representative of the frequency for the weakly dispersive LO phonon branch, and k_B is Boltzmann constant. Γ_{imp} is inhomogeneous broadening due to the ionized impurities. It is worth noting that Γ_{ac} and Γ_{imp} can be considered to be approximately equal to zero at higher temperatures (> 100 K). Hence, we model the linewidth broadening of these three SCs using equation 4 (Figure 5), and the linewidth parameters are shown in table 2.

$$\Gamma(T) = \Gamma_0 + \gamma_{\text{LO}} N_{\text{LO}}(T) \quad (4)$$

The fitted ELO values are much larger than the vibration mode of Pb-Br stretching (18 meV), which is believed to dominate the Fröhlich interaction in 3D perovskites.^{39,41} In 2D RP perovskites, however, E_{LO} only provides an effective value, which cannot be associated to specific phonon modes due to the complex vibrational structure.⁴² In fact, recent studies on mono-layered 2D perovskites ($n=1$) also revealed such larger ELO values (i.e. 35–40 meV) indicating the participation of the vibrational modes of spacing organic cations with large vibration energy in the Fröhlich interaction.^{43–44} Such slow

Table 2. Extracted linewidth parameters.

Bulk state	Γ_0 (meV)	γ_{LO} (meV)	E_{LO} (meV)
iso-BAPB	69.1	251.5	49.5
n-BAPB	61.3	359.9	45.1
n-PAPB	56.1	218.3	50.3
Edge state	Γ_0 (meV)	γ_{LO} (meV)	E_{LO} (meV)
iso-BAPB	94.8	452.5	63.1
n-BAPB	101.1	434.1	60.3
n-PAPB	127.5	233.4	49.6

vibration modes usually can be referred to the rotation or bending of large molecular moieties (e.g. NH_3^+).¹⁷ More importantly, the coupling strength γ_{LO} at the PFs are remarkably larger than those at IFs in three samples except for n-PAPB. The stronger PF electron-phonon coupling drives the formation of STE in our 2D perovskite SCs. On the other hand, the relatively weaker coupling of excitons or charge carriers with lattice

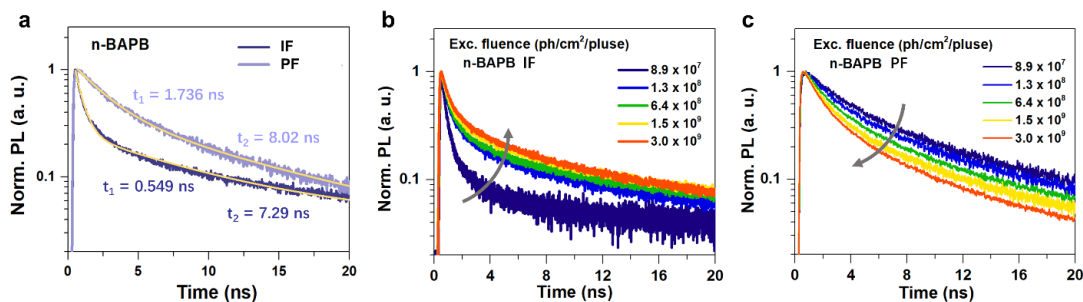


Figure 6. TRPL kinetics of IFs and PFs of n-BAPB.

deformation at the PF of n-PAPB explains the less stabilized STE as mentioned above.

Dynamics of STE vs. FE emission in three SCs at different facets.

In order to further distinguish the photophysics at IFs and PFs, we studied the PL dynamics at two facets of three samples. Figure 6a shows the PL decays at IFs and PFs of n-BAPB using 375 nm excitation at an excitation fluence of 1.3×10^8 photon/pulse/cm². The PL lifetime at the PF is longer than the IF. We can fit the PL kinetics using triexponential decays with one fast component (t_1), a medium component (t_2), and a slow component (t_3) (Table S6). The slow components t_3 feature a small amplitude that can be neglected. Here t_1 and t_2 can be assigned to the trapping related nonradiative recombination and radiative recombination of the photoexcited charge carriers, respectively, in the crystals according to our previous research.^{29, 45} t_2 of IF and PF in n-BAPB are almost identical around 8 ns while the t_1 at edge state (~ 1.7 ns) is much longer than at bulk state (~ 0.5 ns). The PL lifetimes of the bulk state increase with the excitation intensity as illustrated in Figure 6b. This behavior has been explained by trap filling/accumulation, which is widely observed in

2D and 3D perovskite single and microcrystals.⁴⁵⁻⁴⁶ It occurs if the trap depopulation time is longer than the time interval between the laser pulses, and consequently, partial traps are still filled when the new excitation pulse comes. We can obtain trap density of the bulk states to be 2.9×10^{16} cm⁻³ by globally fitting the intensity-dependent PL kinetics using a dynamic trap-filling model (for the details of the method see S5).⁴⁶ More importantly, such behavior indicates that of the photo-generated species at the IFs should be free carriers transporting freely along the perovskite lattices to fill the traps. In fact, we can estimate the fraction of free carriers in the photo-generated species using the Saha-Langmuir theory between 84% to 99% at the IFs of our samples (for the details of the method see S4). On the contrary, the PL kinetics decay faster with the increasing excitation intensity at the PFs, indicating a different charge recombination schematic (Figure 7). We can first exclude the occurrence of high order multi-exciton recombination because the PL intensity exhibits linear dependence on the excitation intensity, as shown in insert pictures of Figure 7a-7c. The deviation of intensity-dependent PL kinetics at edge state can be well interpreted by the STE model. Unlike in 3D perovskite or IFs in 2D perovskite where the electron-phonon coupling generate mainly large polaron, a larger degree of lattice distortion at the PFs of 2D perovskites tends to form

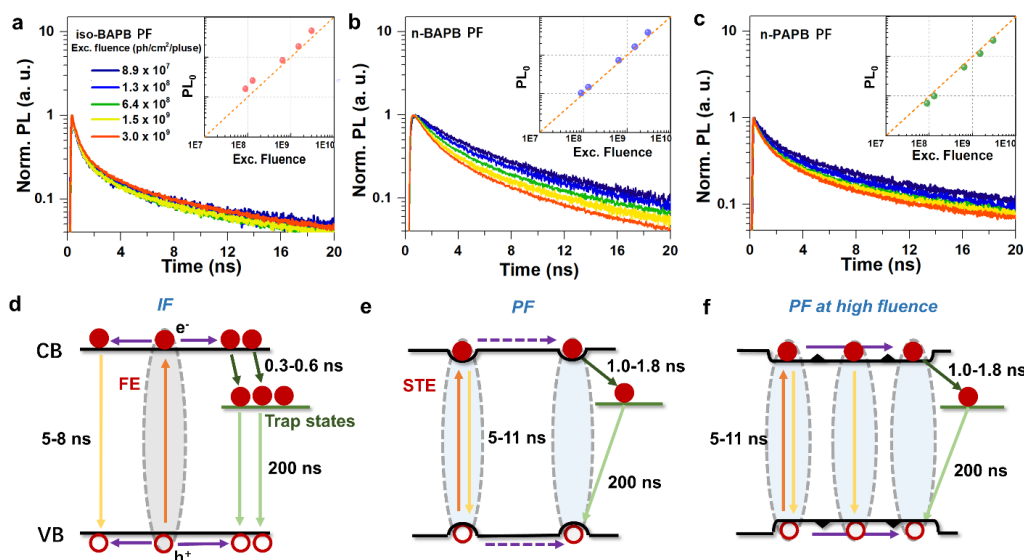


Figure 7. PL decay kinetics with different excitation fluence for the PFs of these three SCs (a-c), insets: PL intensities change with fluence intensity; Illustrations of the charge recombination processes in these three SCs (d-f).

small polarons that move through site to site hopping.^{19,47-48} The intrinsic trap density of the n-BAPB SCs calculated above provides a mean interval distance among the trap states to be 32 nm. It is difficult for the small polaron at the PFs to diffuse to the trap state at low excitation density and undergoes a trapping process. Therefore the dominant excited state depopulation pathway is the STE radiative recombination as shown in Figure 7e. The increasing excitation intensity would increase the STE density at the PFs, flatten the lattice deformation which reduced the potential barrier for the movement of the STEs as illustrated in Figure 7f. This may enhance the diffusivity of the STE hopping. Such polaron concentration dependence has been observed in OPV materials interpreted by the change of spatial confinement.⁴⁹⁻⁵⁰ In our samples, the improved motion of the STEs at the PFs increases the possibility of fast trapping by the defect states, and thereby the PL lifetime is shortened as illustrated in Figure 7f. In addition, we estimated the relative PLQY by divide the integrated area of the PL decays over the excitation fluence as shown in Figure S6. The relative PLQY at the PFs decreases with the increasing excitation intensity supporting our argumentation that extra carrier trapping has been introduced at high excitation density.

Figure 7a-7c depict the intensity-dependent PL kinetics at the PFs of all three SCs. The detailed exponential fitting of those PL kinetics can be found in the table S7. We can observe the shortening of the PL lifetime in both n-BAPB and n-PAPB. In iso-BAPB, however, the PL decay is as fast as that in n-BAPB and n-PAPB at high excitation intensity whereas remains independent of excitation intensity. One of the possible reasons is the larger trap density found in iso-BAPB SCs. Using the analogous analysis mentioned above, we can calculate the intrinsic trap density of iso-BA to be $4.7 \times 10^{16} \text{ cm}^{-3}$, about 1.6 times larger than n-BA leading to the mean distance between traps to be 27 nm. This facilitates the trapping of diffused STE along 2D perovskite lattice as illustrated in Figure 7f.

Conclusions

In conclusion, we investigated the local structure and PL emission dynamics at different surface facets of 2D RP lead bromide perovskite SCs with three spacing cations (i.e., n-BA, iso-BA, and n-PA). Structural analysis of three SCs reveals the different degrees of octahedral distortion (i.e., n-PAPB > iso-BAPB > n-BAPB) due to spacers' different of the spacer to relax the internal lattice strain. We then conducted the PL measurement at two surface facets with the direction along (IF) and perpendicular (PF) to the 2D inorganic layer, respectively. The former can be considered the bulk area, while the latter refers to the edge area as the strain accumulation along the inorganic layer would be released to induce structural distortion at this facet. The PL spectra at IF of three SCs exhibit typical pure band-edge emission bands while the emission at the PF is drastically red-shifted. In addition, at the PF of n-PAPB the band edge emission and the red-shifted emission occurs concurrently with the ratio of the band-edge emission over low-energy emission increasing at low temperature. Such behaviour indicates the low-energy emission should be attributed more to the STE than conventional defect emission since the STE formation would be diminished at low T due to reduced electron-LO phonon coupling. The dual emission bands in n-

PAPB can be explained by the lower self-trapping energy compared with the other two SCs, which is consistent with the structural analysis. The Fröhlich coupling strength (γ_{LO}) extracted from the linewidth of temperature-dependent PL spectra is higher at the PF than that of the IF further supports the STE at the PFs. We also found a longer PL lifetime at the IFs than the PFs. In addition, PL decays slower with the increasing excitation density at IFs with opposite behaviour at PFs. This can be well interpreted by the different photophysics of photo-generated FE at the bulk area and STE at the edge area. FE can move freely along the 2D perovskites and get trapped by the intrinsic defect states, leading to the fast PL quenching. At high excitation intensity, trapping filling dominates due to the long trap lifetime (~200 ns) and the PL lifetime becomes longer due to the passivation of the nonradiative recombination processes. The STEs at PFs are more localized due to the lattice deformation and therefore are more shielded from the defect states. The large STE concentration would flatten the lattice deformation at high excitation density and improve the STE diffusivity. Consequently, more excitons can be quenched by the defect trapping after diffusion. Our findings confirmed the origin of the LES in 2D RP perovskites to be the STE. Such STE are more localized compared with the FE at the perpendicular edge area. The STE formation is also strongly influenced by the spacing cations in the 2D lattice. That conclusion can guide the materials engineering and device application in the future.

Conflicts of interest

There are no conflicts to declare.

Acknowledgements

This work was supported by the Independent Research Fund Denmark-Sapere Aude starting grant (no. 7026-00037A) and Swedish Research Council VR starting grant (no. 2017-05337), and the Chinese Scholarship Council for the PhD scholarship to M. L, W. L., Z. L., M. J., and Q. Z.

References

1. Y. Chen, Y. Sun, J. Peng, J. Tang, K. Zheng and Z. Liang, *Adv. Mater.*, 2018, **30**, 1703487.
2. T. J. Savenije, C. S. Ponseca, Jr., L. Kunneman, M. Abdellah, K. Zheng, Y. Tian, Q. Zhu, S. E. Canton, I. G. Scheblykin, T. Pullerits, A. Yartsev and V. Sundstrom, *J. Phys. Chem. Lett.*, 2014, **5**, 2189-2194.
3. C. C. Stoumpos, D. H. Cao, D. J. Clark, J. Young, J. M. Rondinelli, J. I. Jang, J. T. Hupp and M. G. Kanatzidis, *Chem. Mater.*, 2016, **28**, 2852-2867.
4. K. Zheng and T. Pullerits, *J. Phys. Chem. Lett.*, 2019, **10**, 5881-5885.
5. L. Mao, C. C. Stoumpos and M. G. Kanatzidis, *J. Am. Chem. Soc.*, 2019, **141**, 1171-1190.
6. H. Tsai, W. Nie, J. C. Blancon, C. C. Stoumpos, R. Asadpour, B. Harutyunyan, A. J. Neukirch, R. Verduzco, J. J. Crochet, S. Tretiak, L. Pedesseau, J. Even, M. A. Alam, G. Gupta, J. Lou, P. M. Ajayan, M. J. Bedzyk and M. G. Kanatzidis, *Nature*, 2016, **536**, 312-316.

7. X. Gong, O. Voznyy, A. Jain, W. Liu, R. Sabatini, Z. Piontkowski, G. Walters, G. Bappi, S. Nokhrin, O. Bushuyev, M. Yuan, R. Comin, D. McCamant, S. O. Kelley and E. H. Sargent, *Nat. Mater.*, 2018, **17**, 550-556.
8. J. Wang, J. Li, S. Lan, C. Fang, H. Shen, Q. Xiong and D. Li, *ACS Nano*, 2019, **13**, 5473-5484.
9. Y. Fu, W. Zheng, X. Wang, M. P. Hautzinger, D. Pan, L. Dang, J. C. Wright, A. Pan and S. Jin, *J. Am. Chem. Soc.*, 2018, **140**, 15675-15683.
10. A. Kojima, K. Teshima, Y. Shirai, T. Miyasaka, *J. Am. Chem. Soc.*, 2009, **131**, 6050-6051.
11. E. R. Dohner, E. T. Hoke and H. I. Karunadasa, *J. Am. Chem. Soc.*, 2014, **136**, 1718-1721.
12. K. Thirumal, W. K. Chong, W. Xie, R. Ganguly, S. K. Muduli, M. Sherburne, M. Asta, S. Mhaisalkar, T. C. Sum, H. S. Soo and N. Mathews, *Chem. Mater.*, 2017, **29**, 3947-3953.
13. L. Qian, Y. Sun, M. Sun, Z. Fang, L. Li, D. Xie, C. Li and L. Ding, *J. Mater. Chem. C*, 2019, **7**, 5353-5358.
14. Y. Xu, M. Wang, Y. Lei, Z. Ci and Z. Jin, *Adv. Ener. Mater.*, 2020, **10**, 1700414.
15. J. C. Blancon, A. V. Stier, H. Tsai, W. Nie, C. C. Stoumpos, B. Traore, L. Pedesseau, M. Kepenekian, F. Katsutani, G. T. Noe, J. Kono, S. Tretiak, S. A. Crooker, C. Katan, M. G. Kanatzidis, J. J. Crochet, J. Even and A. D. Mohite, *Nat. Commun.*, 2018, **9**, 2254.
16. D. B. Straus and C. R. Kagan, *J. Phys. Chem. Lett.*, 2018, **9**, 1434-1447.
17. D. B. Straus, S. Hurtado Parra, N. Iotov, J. Gebhardt, A. M. Rappe, J. E. Subotnik, J. M. Kikkawa and C. R. Kagan, *J. Am. Chem. Soc.*, 2016, **138**, 13798-13801.
18. A. R. Srimath Kandada and C. Silva, *J. Phys. Chem. Lett.*, 2020, **11**, 3173-3184.
19. Z. Guo, X. Wu, T. Zhu, X. Zhu and L. Huang, *ACS Nano*, 2016, **10**, 9992-9998.
20. S. Li, J. Luo, J. Liu and J. Tang, *J. Phys. Chem. Lett.*, 2019, **10**, 1999-2007.
21. M. D. Smith and H. I. Karunadasa, *Acc. Chem. Res.*, 2018, **51**, 619-627.
22. D. Cortecchia, S. Neutzner, A. R. Srimath Kandada, E. Mosconi, D. Meggiolaro, F. De Angelis, C. Soci and A. Petrozza, *J. Am. Chem. Soc.*, 2017, **139**, 39-42.
23. S. Kahmann, E. K. Tekelenburg, H. Duim, M. E. Kamminga and M. A. Loi, *Nat. Commun.*, 2020, **11**, 2344.
24. J.-C. Blancon, H. Tsai, W. Nie, C. C. Stoumpos, L. Pedesseau, C. Katan, M. Kepenekian, C. M. M. Soe, K. Appavoo, M. Y. Sfeir, S. Tretiak, P. M. Ajayan, M. G. Kanatzidis, J. Even, J. J. Crochet, A. D. Mohite, *Science*, 2017, **355**, 1288-1292.
25. M. Kepenekian, B. Traore, J. C. Blancon, L. Pedesseau, H. Tsai, W. Nie, C. C. Stoumpos, M. G. Kanatzidis, J. Even, A. D. Mohite, S. Tretiak and C. Katan, *Nano Lett.*, 2018, **18**, 5603-5609.
26. K. Wang, C. Wu, Y. Jiang, D. Yang, K. Wang, S. Priya, *Sci. Adv.* 2019, **5**, 1-10.
27. M.-L. Liang, Y.-X. Ma, C.-L. Hu, F. Kong and J.-G. Mao, *Chem. Mater.*, 2020, **32**, 9688-9695.
28. Y. Fu, M. P. Hautzinger, Z. Luo, F. Wang, D. Pan, M. M. Aristov, I. A. Guzei, A. Pan, X. Zhu and S. Jin, *ACS Cent. Sci.*, 2019, **5**, 1377-1386.
29. M. Liang, W. Lin, Z. Lan, J. Meng, Q. Zhao, X. Zou, I. E. Castellì, T. Pullerits, S. E. Canton and K. Zheng, *ACS Appl. Elect. Mater.*, 2020, **2**, 1402-1412.
30. P. S. Halasyamani, *Chem. Mater.*, 2004, **16**, 3586-3592.
31. Q. Zhu, K. Zheng, M. Abdellah, A. Generalov, D. Haase, S. Carlson, Y. Niu, J. Heimdahl, A. Engdahl, M. E. Messing, T. Pullerits and S. E. Canton, *Phys. Chem. Chem. Phys.*, 2016, **18**, 14933-14940.
32. E. R. Dohner, A. Jaffe, L. R. Bradshaw and H. I. Karunadasa, *J. Am. Chem. Soc.*, 2014, **136**, 13154-13157.
33. L. Mao, Y. Wu, C. C. Stoumpos, B. Traore, C. Katan, J. Even, M. R. Wasielewski and M. G. Kanatzidis, *J. Am. Chem. Soc.*, 2017, **139**, 11956-11963.
34. L. Mao, W. Ke, L. Pedesseau, Y. Wu, C. Katan, J. Even, M. R. Wasielewski, C. C. Stoumpos and M. G. Kanatzidis, *J. Am. Chem. Soc.*, 2018, **140**, 3775-3783.
35. X. Li, Y. Fu, L. Pedesseau, P. Guo, S. Cuthriell, I. Hadar, J. Even, C. Katan, C. C. Stoumpos, R. D. Schaller, E. Harel and M. G. Kanatzidis, *J. Am. Chem. Soc.*, 2020, **142**, 11486-11496.
36. L. Zhang, L. Wu, K. Wang and B. Zou, *Adv. Sci. (Weinh)*, 2019, **6**, 1801628.
37. M. Li, T. Liu, Y. Wang, W. Yang and X. Lü, *Matter Radiat. Extremes*, 2020, **5**.
38. A. Jaffe, Y. Lin, C. M. Beavers, J. Voss, W. L. Mao and H. I. Karunadasa, *ACS Cent. Sci.*, 2016, **2**, 201-209.
39. A. D. Wright, C. Verdi, R. L. Milot, G. E. Eperon, M. A. Perez-Osorio, H. J. Snaith, F. Giustino, M. B. Johnston and L. M. Herz, *Nat. Commun.*, 2016, **7**.
40. Q. Shi, S. Ghosh, P. Kumar, L. C. Folkers, S. K. Pal, T. Pullerits, K. J. Karki, *J. Phys. Chem. C*, 2018, **122**, 21817-21823.
41. X. Lao, Z. Yang, Z. Su, Y. Bao, J. Zhang, X. Wang, X. Cui, M. Wang, X. Yao and S. Xu, *J. Phys. Chem. C*, 2019, **123**, 5128-5135.
42. J. D. Ziegler, J. Zipfel, B. Meisinger, M. Menahem, X. Zhu, T. Taniguchi, K. Watanabe, O. Yaffe, D. A. Egger and A. Chernikov, *Nano Lett.*, 2020, **20**, 6674-6681.
43. J. M. Urban, G. Chehade, M. Dyksik, M. Menahem, A. Surrente, G. Trippe-Allard, D. K. Maude, D. Garrot, O. Yaffe, E. Deleporte, P. Plochocka and M. Baranowski, *J. Phys. Chem. Lett.*, 2020, **11**, 5830-5835.
44. D. Feldstein, R. Perea-Causin, S. Wang, M. Dyksik, K. Watanabe, T. Taniguchi, P. Plochocka and E. Malic, *J. Phys. Chem. Lett.*, 2020, **11**, 9975-9982.
45. K. Zheng, K. Židek, M. Abdellah, M. E. Messing, M. J. Al-Marri and T. Pullerits, *J. Phys. Chem. C*, 2016, **120**, 3077-3084.
46. S. D. Stranks, V. M. Burlakov, T. Leijtens, J. M. Ball, A. Goriely and H. J. Snaith, *Phys. Rev. Appl.*, 2014, **2**.
47. K. Miyata, D. Meggiolaro, M. T. Trinh, P. P. Joshi, E. Mosconi, S. C. Jones, F.; D. Angelis, X.-Y. Zhu, *Sci. Adv.*, 2017, **3**, e1701217.
48. M. Seitz, A. J. Magdaleno, N. Alcazar-Cano, M. Melendez, T. J. Lubbers, S. W. Walraven, S. Pakdel, E. Prada, R. Delgado-Buscalioni and F. Prins, *Nat. Commun.*, 2020, **11**, 2035.
49. L. A. Ribeiro Junior, L. L. e Castro, L. E. de Sousa, G. M. e Silva and P. H. de Oliveira Neto, *Chem. Phys. Lett.*, 2019, **716**, 162-166.
50. R. Coehoorn, L. Zhang, P. A. Bobbert and H. van Eersel, *Phys. Rev. B*, 2017, **95**.

Free excitons versus self-trapped excitons at different facets of Ruddlesden Poppers two-dimensional lead halide perovskite single crystals

Mingli Liang[†], Weihua Lin[‡], Qian Zhao[†], Xianshao Zou[‡], Zhenyun Lan[#], Jie Meng[†], Qi Shi[‡], Sophie E. Canton[^], Tönu Pullerits[‡] and Kaibo Zheng^{*,†,‡}

[†]*Department of Chemistry, Technical University of Denmark, DK-2800 Kongens Lyngby, Denmark;*

[‡]*Chemical Physics and NanoLund, Lund University, Box 124, 22100 Lund, Sweden;*

[#]*Department of Energy Conversion and Storage, Technical University of Denmark, DK-2800 Kongens Lyngby, Denmark;*

[^]*ELI-ALPS, ELI-HU Non-Profit, Ltd., Dugonics ter 13, Szeged 6720, Hungary;*

*Corresponding Author

Kaibo Zheng: kzheng@kemi.dtu.dk

Supporting Information

Table S1. Bond distances (Angstroms) of Pb-Br for the iso-BAPB, n-BAPB and n-PAPB.

Table S2. Br-Pb-Br angles (deg) for the iso-BAPB, n-BAPB and n-PAPB.

Table S3 Excitation density of iso-BAPB, n-BAPB and n-PAPB with different laser photon flux.

Table S4 The calculated values of ratio of the free carriers x.

Table S5 Multi-exponential fitting parameters for TRPL kinetics of iso-BAPB, n-BAPB and n-PAPB under the excitation fluence of 1.3×10^8 photon/pulse/cm².

Table S6 Trap Densities obtained from the fitting.

Table S7 Multi-exponential fitting parameters for TRPL kinetics of iso-BAPB, n-BAPB and n-PAPB PFs.

S1: Calculation of the out-of-center distortions (Δ_{od}) method.

S2 Calculations of the penetration depths and excitation density of the three compounds.

S3. Calculation of E_b using temperature dependent photoluminescence method.

S4. Calculation of the free carrier ratio after photo-excitation

S5. Detailed model of trap filling and fitting process.

Table S1. Bond distances (Angstroms) of Pb-Br for the iso-BAPB, n-BAPB and n-PAPB.

(iso-BA) ₂ (MA)Pb ₂ Br ₇ (iso-BAPB)			
Pb(1)-Br(4)	2.884(5)	Pb(2)-Br(10)	2.951(5)
Pb(1)-Br(9)	2.979(3)	Pb(2)-Br(7)#1	2.981(3)
Pb(1)-Br(9)#1	2.988(3)	Pb(2)-Br(7)	2.992(3)
Pb(1)-Br(3)	3.009(3)	Pb(2)-Br(6)	3.017(3)
Pb(1)-Br(3)#2	3.016(3)	Pb(2)-Br(6)#2	3.025(3)
Pb(1)-Br(5)	3.061(9)	Pb(2)-Br(5)	3.071(9)
(n-BA) ₂ (MA)Pb ₂ Br ₇ (n-BAPB)			
Pb(1)-Br(6)	2.908(4)	Pb(1)-Br(3)	3.002(8)
Pb(1)-Br(4)	2.968(9)	Pb(1)-Br(3)#2	3.004(6)
Pb(1)-Br(4)#1	2.980(7)	Pb(1)-Br(2)	3.0636(9)
(n-PA) ₂ (MA)Pb ₂ Br ₇ (n-PAPB)			
Pb(1)-Br(4)	2.890(3)	Pb(1)-Br(3)#2	2.998(6)
Pb(1)-Br(3)	2.925(7)	Pb(1)-Br(5)	3.034(5)
Pb(1)-Br(5)#1	2.967(4)	Pb(1)-Br(2)	3.0697(8)

Symmetry transformations used to generate equivalent atoms:

For iso-BAPB: #1 x,-y+1,z+1/2; #2 x,-y+2,z+1/2

For n-BAPB: #1 -x,y,z+1/2; #2 -x+1,y,z-1/2

For n-PAPB: #1 -x,y,z+1/2; #2 -x+1,y,z-1/2

Table S2. Br-Pb-Br angles (deg) for the iso-BAPB, n-BAPB and n-PAPB.

iso-BAPB			
Br(4)-Pb(1)-Br(9)	90.09(13)	Br(10)-Pb(2)-Br(7)#1	89.54(12)
Br(4)-Pb(1)-Br(9)#1	93.44(13)	Br(10)-Pb(2)-Br(7)	95.31(12)
Br(9)-Pb(1)-Br(9)#1	90.29(3)	Br(7)#1-Pb(2)-Br(7)	90.46(3)
Br(4)-Pb(1)-Br(3)	86.23(12)	Br(10)-Pb(2)-Br(6)	92.08(12)
Br(9)-Pb(1)-Br(3)	89.45(9)	Br(7)#1-Pb(2)-Br(6)	177.21(12)
Br(9)#1-Pb(1)-Br(3)	179.58(13)	Br(7)-Pb(2)-Br(6)	91.65(8)
Br(4)-Pb(1)-Br(3)#2	89.41(12)	Br(10)-Pb(2)-Br(6)#2	86.53(11)
Br(9)-Pb(1)-Br(3)#2	178.21(9)	Br(7)#1-Pb(2)-Br(6)#2	89.15(8)
Br(9)#1-Pb(1)-Br(3)#2	91.45(9)	Br(7)-Pb(2)-Br(6)#2	178.11(14)
Br(3)-Pb(1)-Br(3)#2	88.81(3)	Br(6)-Pb(2)-Br(6)#2	88.68(3)
Br(4)-Pb(1)-Br(5)	174.77(9)	Br(10)-Pb(2)-Br(5)	173.14(13)

Br(9)-Pb(1)-Br(5)	92.33(16)	Br(7)#1-Pb(2)-Br(5)	89.24(16)
Br(9)#1-Pb(1)-Br(5)	91.18(13)	Br(7)-Pb(2)-Br(5)	91.45(13)
Br(3)-Pb(1)-Br(5)	89.16(12)	Br(6)-Pb(2)-Br(5)	88.88(15)
Br(3)#2-Pb(1)-Br(5)	88.03(15)	Br(6)#2-Pb(2)-Br(5)	86.70(13)
n-BAPB			
Br(6)-Pb(1)-Br(4)	91.2(3)	Br(4)#1-Pb(1)-Br(3)#2	176.2(3)
Br(6)-Pb(1)-Br(4)#1	90.4(2)	Br(3)-Pb(1)-Br(3)#2	90.12(6)
Br(4)-Pb(1)-Br(4)#1	90.36(5)	Br(6)-Pb(1)-Br(2)	179.4(6)
Br(6)-Pb(1)-Br(3)	91.2(3)	Br(4)-Pb(1)-Br(2)	89.3(3)
Br(4)-Pb(1)-Br(3)	176.3(2)	Br(4)#1-Pb(1)-Br(2)	89.2(2)
Br(4)#1-Pb(1)-Br(3)	86.9(3)	Br(3)-Pb(1)-Br(2)	88.2(3)
Br(6)-Pb(1)-Br(3)#2	92.0(2)	Br(3)#2-Pb(1)-Br(2)	88.3(2)
Br(4)-Pb(1)-Br(3)#2	92.5(3)		
n-PAPB			
Br(4)-Pb(1)-Br(3)	91.3(3)	Br(5)#1-Pb(1)-Br(5)	89.68(4)
Br(4)-Pb(1)-Br(5)#1	90.1(2)	Br(3)#2-Pb(1)-Br(5)	85.6(3)
Br(3)-Pb(1)-Br(5)#1	94.5(3)	Br(4)-Pb(1)-Br(2)	179.1(4)
Br(4)-Pb(1)-Br(3)#2	90.8(2)	Br(3)-Pb(1)-Br(2)	88.6(3)
Br(3)-Pb(1)-Br(3)#2	90.22(4)	Br(5)#1-Pb(1)-Br(2)	89.0(2)
Br(5)#1-Pb(1)-Br(3)#2	175.2(3)	Br(3)#2-Pb(1)-Br(2)	90.1(2)
Br(4)-Pb(1)-Br(5)	89.7(3)	Br(5)-Pb(1)-Br(2)	90.5(3)
Br(3)-Pb(1)-Br(5)	175.7(2)		

Symmetry transformations used to generate equivalent atoms:

For iso-BAPB: #1 $x, -y+1, z+1/2$; #2 $x, -y+2, z+1/2$

For n-BAPB: #1 $-x, y, z+1/2$; #2 $-x+1, y, z-1/2$

For n-PAPB: #1 $-x, y, z+1/2$; #2 $-x+1, y, z-1/2$

S1: Calculation of the out-of-center distortions (Δ_{od}) method.

When the lone-pair cations (e.g. Sn^{2+} , Pb^{2+} , Bi^{3+} , etc.) and d^0 transition metals (e.g. Nb^{5+} , V^{5+} , Mo^{6+} , etc.) form a polyhedron with oxygen or halide ions, the primary distortive cause can be attributed to second-order Jahn-Teller (SOJT) effects (electronic effects). The most common is the formation of a distorted MX_6 octahedron (see Figure S1), in which the metal ions (M) deviate from the center position where they should be. The magnitudes of out-of-center distortions could be calculated by the following method:¹

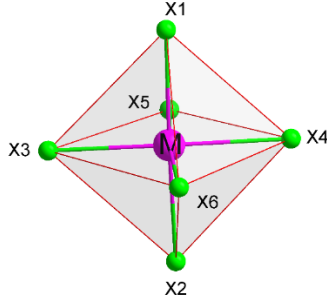


Figure S1. A distorted MX_6 octahedron

We can first define three trans bond angles based on figure S1 are as follows: $\theta_1 = \angle \text{X1-M-X2}$, $\theta_2 = \angle \text{X3-M-X4}$, $\theta_3 = \angle \text{X5-M-X6}$. Then, taking the difference in the associated bond lengths and dividing by the cosine of each angle results in the magnitude of the out-of-center distortion:

$$\Delta_{\text{od}} = [|(M-X1) - (M-X2)| \div |\cos \theta_1|] + [|(M-X3) - (M-X4)| \div |\cos \theta_2|] + [|(M-X5) - (M-X6)| \div |\cos \theta_3|] \quad (1)$$

When its value falls between 0.00-0.05, it can be considered that the MX_6 octahedron has no distortion. Similarly, 0.05-0.40 range corresponds weak distortion; 0.40-0.80 range corresponds moderate distortion; $\Delta_{\text{od}} > 0.80$ range corresponds strong distortion. In this work, the PbBr_3 octahedra in all three compounds have weak distortions.

S2 Calculations of the penetration depths and excitation density of the three compounds.

To calculate the penetration depths and excitation density of these samples, we first measured their absorption coefficients using the laser. In order to ensure that the laser spot is completely illuminated on the samples, we prepared a sufficiently large film according to the method in the literature. (REF) And after the absorption measurements, we used AFM to determine the thickness of the film (Figure S2). The absorbance (A) can be calculated by the following formula:

$$A = \log (I_0/I_1) \quad (2)$$

Here, I_0 is incident light intensity and I_1 is outgoing light intensity. After measuring the A values at 375 nm of the iso-BAPB, n-BAPB and n-PAPB are about 0.37, 0.39 and 0.33, respectively. The absorption coefficient $\varepsilon = 2.303A/l$, where l is the path length of the light which equals to the thickness of the crystal. So, we obtain $\varepsilon = 1.40 \times 10^5$, 1.38×10^5 and $1.27 \times 10^5 \text{ cm}^{-1}$ for iso-BAPB, n-BAPB and n-PAPB, respectively. The penetration depths of them at 375 nm are about 71, 73 and 79 nm, respectively ($\delta = 1/\varepsilon$). The excitation density n can be calculated as photon flux f in photons/ cm^2 multiplied by absorption coefficient ε : $n = f\varepsilon$, Table S3 summarizes the corresponding excitation density at different laser photon flux in TRPL measurements:

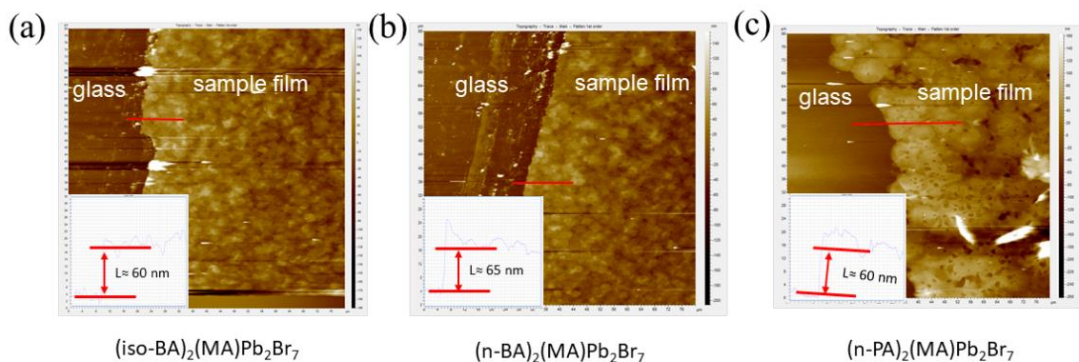


Figure S2. The AFM pictures of iso-BAPB (a), n-BAPB (b) and n-PAPB (c) films with the thickness values.

Table S3 Excitation density of iso-BAPB, n-BAPB and n-PAPB with different laser photon flux.

Excitation Fluence (photon/pulse/cm ²)	Excitation Intensity (cm ⁻³) of iso-BAPB	Excitation Intensity (cm ⁻³) of n-BAPB	Excitation Intensity (cm ⁻³) of n-PAPB
8.9×10^7	1.25×10^{13}	1.23×10^{13}	1.13×10^{13}
1.3×10^8	1.82×10^{13}	1.79×10^{13}	1.65×10^{13}
6.4×10^8	8.96×10^{13}	8.83×10^{13}	8.13×10^{13}
1.5×10^9	2.10×10^{14}	2.07×10^{14}	1.91×10^{14}
3.0×10^9	4.20×10^{14}	4.14×10^{14}	3.81×10^{14}

S3. Calculation of E_b using temperature dependent photoluminescence method.

PL spectra of these three compounds were measured at temperatures ranging 100-280 K in a cryostat (Figure S3), liquid nitrogen as the coolant, and the integrated PL intensities $I(T)$ were calculated. Here the PL intensity decreased with increased temperatures due to the thermal dissociation of excitons at higher temperatures, the temperature dependent PL intensity can be expressed as follows:²

$$I(T) = \frac{I_0}{1 + Ae^{(-E_b/k_B T)}} \quad (3)$$

In which, I_0 is the PL intensity at low temperature, and k_B is the Boltzmann constant. From the linear fitting of $\ln(I_0/I(T)-1)$ and $1/k_B T$ plot, we can obtain their E_b as the slopes (Figure S4).

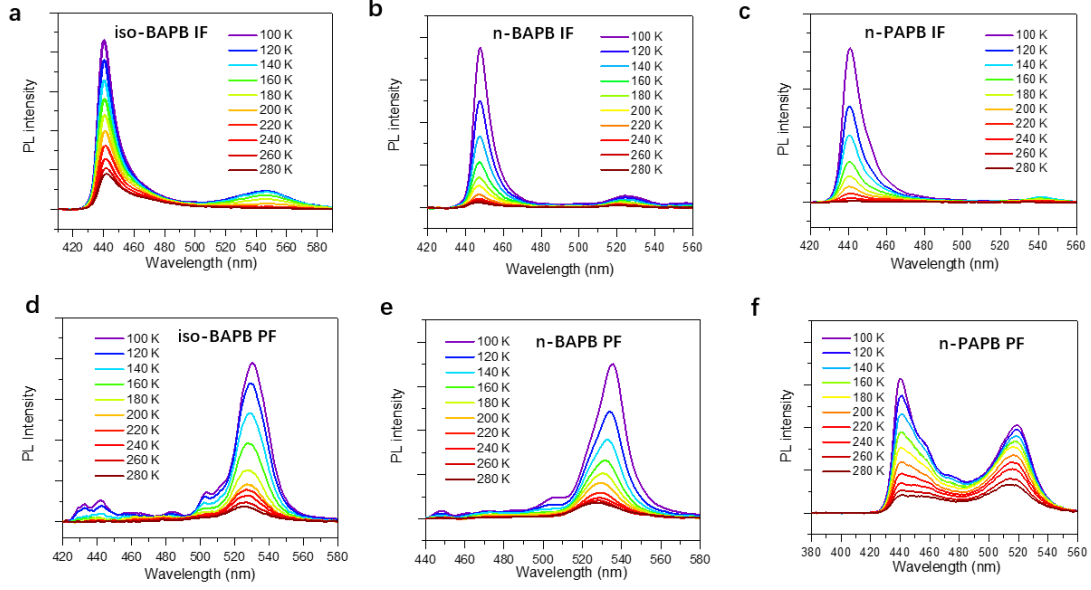


Figure S3 Temperature-dependent PL spectra of IFs and PFs of the three SCs.

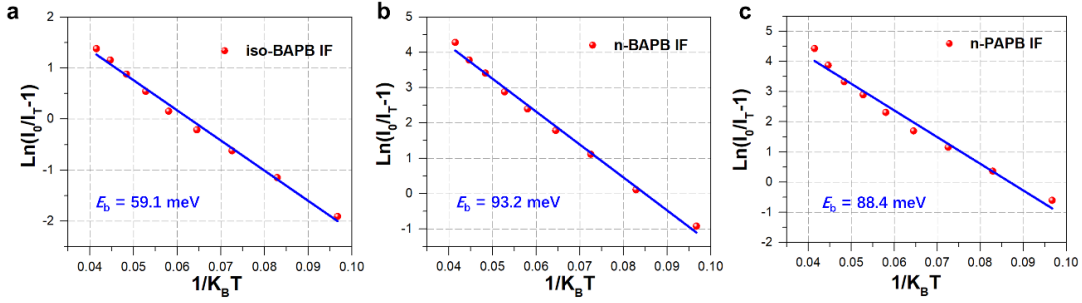


Figure S4. The E_b values of IFs were extracted by fitting to the Arrhenius equation.

S4. Calculation of the free carrier ratio after photo-excitation

After photoexcitation by the laser pulse, actually the free carriers and weak coupled excitons coexist in the crystal under a thermodynamics equilibrium. The ratio between two species is a fixed term resembling the ion-electron balance in a hot plasma, which depends strongly on the exciton binding energy as well as the excitation concentration. Therefore, we can use a classic Saha-Langmuir theory to roughly calculate the ratio of the free carriers X (i.e. fraction of the free carriers among all the excited species) in the system:

$$\frac{x^2}{1-x} = \frac{1}{n} \left(\frac{2\pi m k_B T}{h^2} \right)^{1.5} e^{-\frac{E_b}{k_B T}} \quad (4)$$

Where E_b refers to the exciton binding energy, m is the exciton effective mass, T is the temperature and n is the excitation concentration. The following table summarized the calculated x ratio of three samples under the excitation condition in PL decay measurement (Table S4). Apparently, during our measurement, the majority of

the excited species in the 2D perovskite crystals is free carriers and the contribution of the exciton can almost be negligible.

Table S4. The calculated values of ratio of the free carriers x .

Samples	Excitation Intensity (cm^{-3})	x
iso-BAPB IF	$0.125 - 4.20 \times 10^{14}$	$0.998 - 0.946$
n-BAPB IF	$0.123 - 4.14 \times 10^{14}$	$0.993 - 0.839$
n-PAPB IF	$0.113 - 3.81 \times 10^{14}$	$0.995 - 0.868$

Table S5 Multi-exponential fitting parameters for TRPL kinetics of iso-BAPB, n-BAPB and n-PAPB under the excitation fluence of 1.3×10^8 photon/pulse/ cm^2 .

IFs	$A_1(\%)$	t_1 (ns)	$A_2(\%)$	t_2 (ns)	$A_3(\%)$	t_3 (ns)
iso-BAPB	88.4	$0.398 (\pm 0.001)$	8.2	$8.15 (\pm 0.02)$	3.4	$84.4 (\pm 0.2)$
n-BAPB	87.9	$0.549 (\pm 0.001)$	9.8	$7.29 (\pm 0.03)$	2.3	$75.6 (\pm 0.2)$
n-PAPB	93.4	$0.492 (\pm 0.002)$	5.6	$5.98 (\pm 0.03)$	1.0	$76.3 (\pm 0.4)$
PFs	$A_1(\%)$	t_1 (ns)	$A_2(\%)$	t_2 (ns)	$A_3(\%)$	t_3 (ns)
iso-BAPB	84.1	$0.481 (\pm 0.002)$	13.6	$5.05 (\pm 0.02)$	2.3	$52.2 (\pm 0.2)$
n-BAPB	68.0	$1.736 (\pm 0.006)$	48.7	$8.02 (\pm 0.04)$	3.3	$50.7 (\pm 0.2)$
n-PAPB	71.9	$1.123 (\pm 0.006)$	23.7	$10.24 (\pm 0.02)$	4.4	$98.9 (\pm 0.4)$

S5. Detailed model of trap filling and fitting process.

The detailed calculation procedures of the model have been described in the reference.³ In brief, the equilibrium between free carriers and excitons can be described using the Saha equation. When photodoping (i.e accumulated trap filling) is present, the Saha equation can be generalized as the following equation expressing the concentrations of electrons (n_e), holes (n_h) and excitons (n_x) corresponding to the overall untapped photogenerated species density N :

$$N_h = -\frac{(A - n_T)}{2} + \frac{1}{2}\sqrt{(A + N_T)^2 + 4AN} \quad (5)$$

$$n_e = n_h - n_T \quad (6)$$

where $A = v_x/(v_h v_e) \exp[-E_b/(k_B T)]$ and $v_i = \lambda_i^3$, λ_i is the thermal wavelength of the species i . n_T is concentration of filled traps and N_T is the concentration of total traps.

Here we assume that n_T varies little and is only dependent on average concentration of electrons $\overline{n_e(t)} = \frac{1}{t_0} \int_0^{t_0} n_e(t) dt$ during the PL recording time t_0 among the repetition pulses. Then we can get the

following rate equations:

$$\frac{dn_T}{dt} = R_{pop}(N_T - n_T)\overline{n_e(t)} - R_{dep}(N_T^2 + n_T\overline{n_e(t)}) = 0 \quad (7)$$

where R_{pop} and R_{dep} are the recombination rates of trap population and depopulation, respectively. Taking equations (5) and (6) we can obtain the average concentration of electrons as:

$$\overline{n_e(t)} = \frac{1}{t_0} \int_0^{t_0} n_e(t) \approx K(A + n_T), K = \frac{1}{\gamma_0 t_0} \ln \left[1 + \frac{AN(0)}{N_T(A + N_T)} \right] \quad (8)$$

Here $N(0)$ can be simplified as initial excitation density N_c . γ_0 is the total rate of electronic decay not involving traps. Substitution of equation (8) into (7) gives:

$$n_T = -\frac{1}{2}\alpha + \frac{1}{2}\sqrt{\alpha^2 + 4\beta N_T} \quad (9)$$

$$\alpha = \frac{[A + R(A - N_T)]}{\left(1 + \frac{1}{K} + R\right)} \quad (10)$$

$$\beta = \frac{RA}{\left(1 + \frac{1}{K} + R\right)} \quad (11)$$

$$K = \frac{1}{\gamma_0 t_0} \ln \left[1 + \frac{AN_c}{N_T(A + N_T)} \right], R = R_{pop}/R_{dep} \quad (12)$$

During the fitting of the trapping model, we first assume that both traps exhibit filling but due to different trap population and depopulation rates, the ratio of unoccupied trap densities between two type of traps varies with different excitation intensity. Therefore we can plot $A_1/(A_1+A_2) \sim N_c$ data and fit with the expression combination equations 9-12.

$$\frac{A_1}{A_1+A_2} = \frac{n_{uncT1}}{n_{uncT1}+n_{uncT2}} = \frac{N_{T1} + \frac{1}{2}\alpha_1 - \frac{1}{2}\sqrt{\alpha_1^2+4\beta_1N_{T1}}}{(N_{T1} + \frac{1}{2}\alpha_1 - \frac{1}{2}\sqrt{\alpha_1^2+4\beta_1N_{T1}}) + (N_{T2} + \frac{1}{2}\alpha_2 - \frac{1}{2}\sqrt{\alpha_2^2+4\beta_2N_{T2}})} \quad (13)$$

Here n_{uncT1} and n_{uncT2} are the concentration of filled traps 1 and 2, respectively. N_{T1} and N_{T2} are the concentrations of original concentration of trap 1 and trap 2, respectively. In this work, A of (iso-BA)₂(MA)Pb₂Br₇ and (n-BA)₂(MA)Pb₂Br₇ were approximately equal to $0.97 \times 10^{15} \text{ cm}^{-3}$, respectively, PL recording time t_0 was $2.5 \times 10^{-7} \text{ s}$, and γ_0 was taken as the rate of the charge recombination not contributing to the trap filling process, We first set all the four fitting parameters (N_{T1} , N_{T2} , R_1 , and R_2) while analyzing these two compounds. The best fitting results as shown in Table S6. In this table, R_2 of (iso-BA)₂(MA)Pb₂Br₇ and (iso-BA)₂(MA)Pb₂Br₇ are 15.5 and 36.7, respectively. Considering R is the ratio between trap population and depopulation rates, we can then roughly estimate the depopulation time of thier traps 2 using the trap population time obtained in PL kinetics (lifetime of the second component 5.05 and $\sim 8.02 \text{ ns}$, respectively) to be ~ 80 and $\sim 290 \text{ ns}$, respectively. These depopulation time of traps 2 are not much different from the interval between the pulses in our measurement (250 ns). Therefore we conclude that no considerable trap filling should occur in their

traps 2 since the depopulation rate is too fast.⁴ The model is then modified for the case that trap filling occurs only in trap1 as follows:

$$\frac{A_1}{A_1+A_2} = \frac{n_{\text{uncT1}}}{n_{\text{uncT1}}+N_{\text{T2}}} = \frac{N_{\text{T1}} + \frac{1}{2}\alpha_1 - \frac{1}{2}\sqrt{\alpha_1^2+4\beta_1N_{\text{T1}}}}{(N_{\text{T1}} + \frac{1}{2}\alpha_1 - \frac{1}{2}\sqrt{\alpha_1^2+4\beta_1N_{\text{T1}}}) + N_{\text{T2}}} \quad (14)$$

Here the $A_1/(A_1+A_2)$ represents the ratio between unoccupied density of trap 1 and original density of trap 2. We first set all the three fitting parameters (N_{T1} , N_{T2} , and R) free for the values from the equation (10). Then, we fit the equation (11) (Figure S5c) to get the new parameters (Table S6).

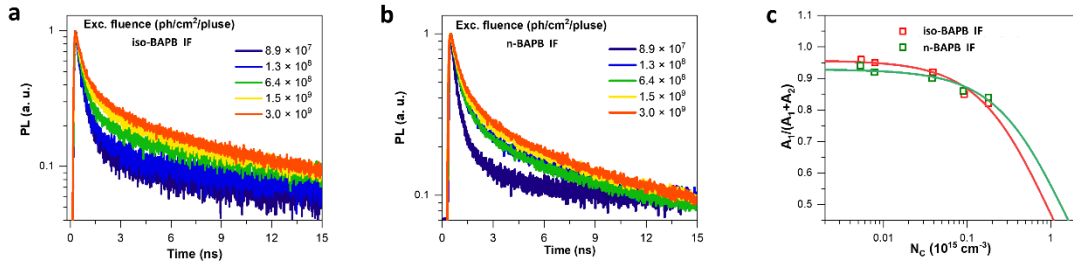


Figure S5. PL decay kinetics with different excitation fluence for the IFs of iso-BAPB and n-BAPB (a, b); dependence of the amplitude ratios $A_1/(A_1 + A_2)$ in the multi-exponential fitting of the decays on the initial charge densities N_c for the IFs of iso-BAPB and n-BAPB (c).

Table S6. Trap Densities obtained from the fitting.

Model	IFs	R_1	R_2	$N_{\text{T1}} (10^{15} \text{ cm}^{-3})$	$N_{\text{T2}} (10^{15} \text{ cm}^{-3})$
$\frac{A_1}{A_1+A_2} = \frac{n_{\text{uncT1}}}{n_{\text{uncT1}}+n_{\text{uncT2}}}$	(iso-BA) ₂ (MA)Pb ₂ Br ₇	2.3×10^5	15.5	11.7	0.23
	(n-BA) ₂ (MA)Pb ₂ Br ₇	2.7×10^4	36.7	9.1	0.57
$\frac{A_1}{A_1+A_2} = \frac{n_{\text{uncT1}}}{n_{\text{uncT1}}+N_{\text{T2}}}$	(iso-BA) ₂ (MA)Pb ₂ Br ₇	1.4×10^5	/	46.9	2.08
	(n-BA) ₂ (MA)Pb ₂ Br ₇	5.1×10^4	/	29.1	2.19

Table S7 Multi-exponential fitting parameters for TRPL kinetics of iso-BAPB, n-BAPB and n-PAPB PFs.

iso-BAPB						
Exc. Fluence photon/pulse/cm ²	t_1 (ns)	A_1 (%)	t_2 (ns)	A_2 (%)	t_3 (ns)	A_3 (%)
3.0×10^9	0.481(±0.001)	70.1	5.05(±0.02)	24.6	47.6(±0.1)	5.3

1.5×10^9	0.481(± 0.001)	72.0	5.05(± 0.02)	23.7	53.6(± 0.2)	4.3
6.4×10^8	0.481(± 0.001)	72.3	5.05(± 0.02)	23.0	49.4(± 0.3)	4.7
1.3×10^8	0.481(± 0.002)	73.9	5.05(± 0.02)	21.9	70.7(± 0.4)	4.2
8.9×10^7	0.481(± 0.002)	75.0	5.05(± 0.03)	20.8	53.7(± 0.7)	4.2
n-BAPB						
Exc. Fluence photon/pulse/cm²	t₁ (ns)	A₁ (%)	t₂ (ns)	A₂ (%)	t₃(ns)	A₃ (%)
3.0×10^9	1.736(± 0.003)	74.1	8.02(± 0.02)	22.8	54.2(± 0.3)	3.1
1.5×10^9	1.736(± 0.006)	68.0	8.02(± 0.04)	28.7	50.7(± 0.4)	3.3
6.4×10^8	1.736(± 0.002)	48.8	8.02(± 0.09)	45.1	69.6(± 0.7)	6.1
1.3×10^8	1.736(± 0.003)	42.4	8.02(± 0.06)	51.6	54.5(± 0.7)	3.9
8.9×10^7	1.736(± 0.006)	28.6	8.02(± 0.23)	63.8	68.9(± 0.8)	7.6
n-PAPB						
Exc. Fluence photon/pulse/cm²	t₁ (ns)	A₁ (%)	t₂ (ns)	A₂ (%)	t₃(ns)	A₃ (%)
3.0×10^9	1.123(± 0.003)	70.8	10.24(± 0.02)	27.5	112.4(± 0.3)	4.5
1.5×10^9	1.123(± 0.006)	66.5	10.24(± 0.04)	28.3	98.9(± 0.4)	5.2
6.4×10^8	1.123(± 0.002)	62.5	10.24(± 0.09)	31.6	87.7(± 0.6)	5.9
1.3×10^8	1.123(± 0.003)	58.3	10.24(± 0.06)	35.1	85.7(± 0.6)	6.6
8.9×10^7	1.123(± 0.003)	51.8	10.24(± 0.06)	40.7	108.0(± 0.9)	7.5

Table S8 Relative PLQY (%) at PFs of three samples (PL decay Aera/Exc. Fluence)

Samples Exc. Fluence	iso-BAPB PF	n-BAPB PF	n-PAPB PF
8.9×10^7	0.00167	0.03288	0.01074
1.3×10^8	0.00154	0.02422	0.00984
6.4×10^8	0.00069	0.01062	0.00705
1.5×10^9	0.00065	0.00745	0.00672
3.0×10^9	0.00069	0.00687	0.00626

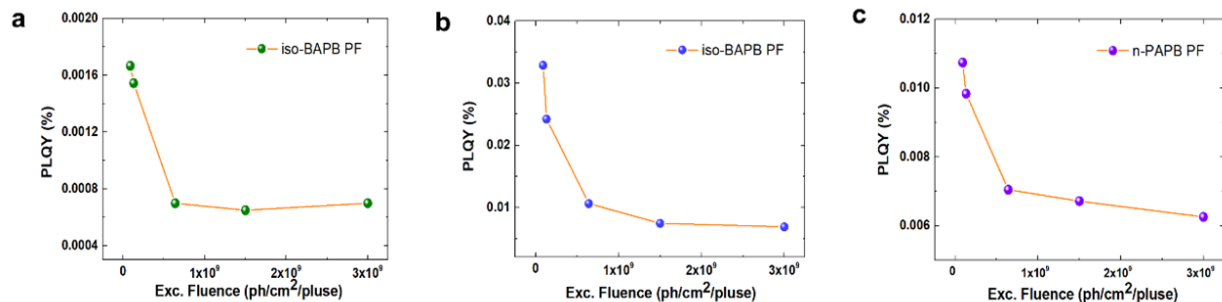


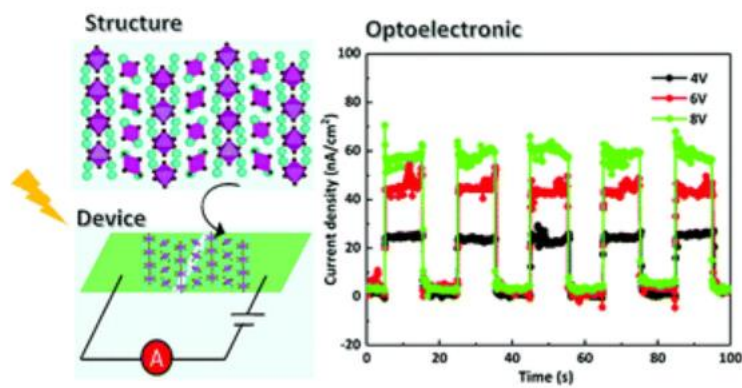
Figure S6 Relative PLQY (%) at PFs of three samples.

Reference

- (1) Halasyamani, P. S. Asymmetric Cation Coordination in Oxide Materials: Influence of Lone-Pair Cations on the Intra-octahedral Distortion in d0 Transition Metals. *Chem. Mater.* **2004**, *16*, 3586-3592.
- (2) Chen, Z.; Yu, C.; Shum, K.; Wang, J. J.; Pfenninger, W.; Vockic, N.; Midgley, J.; Kenney, J. T. Photoluminescence Study of Polycrystalline CsSnI₃ Thin Films: Determination of Exciton Binding Energy. *J. Lumin.* **2012**, *132*, 345–349.
- (3) Stranks, S. D.; Burlakov, V. M.; Leijtens, T.; Ball, J. M.; Goriely, A.; Snaith, H. J. Recombination Kinetics in Organic-Inorganic Perovskites: Excitons, Free Charge, and Subgap States. *Phys. Rev. Appl.* **2014**, *2*, 034007.
- (4) Zheng, K.; Židek, K.; Abdellah, M.; Messing, M. E.; Al-Marri, M. J.; Pullerits, T. Trap States and Their Dynamics in Organometal Halide Perovskite Nanoparticles and Bulk Crystals. *J. Phys. Chem. C* **2016**, *120*, 3077–3084.

Paper IV

Lead-free double halide perovskite Cs_3BiBr_6 with well-defined crystal structure and high thermal stability for optoelectronics





Cite this: *J. Mater. Chem. C*, 2019, 7, 3369

Lead-free double halide perovskite Cs₃BiBr₆ with well-defined crystal structure and high thermal stability for optoelectronics†

Yingying Tang,^a Mingli Liang,^a Bingdong Chang,^b Hongyu Sun,^c Kaibo Zheng,^{ad} Tönu Pullerits^d and Qijin Chi^{id}*^a

Halide perovskites have continued to rise as attractive light absorber materials, mainly driven by their potential wide applications in the fields of solar cells, photodetectors, lasers and others. However, Pb-containing perovskites are poisonous and could cause serious potential problems to our environment. Thus, there is a strong desire to develop lead-free perovskites as environmentally friendly alternatives. Here, we have shown a successful synthesis of a non-toxic single crystalline double-halide perovskite, Cs₃BiBr₆, and analysed its structural characteristics in detail. This perovskite represents a new structure in terms of double-halide perovskites. The crystal structure features isolated BiBr₆ polyhedra forming a zero-dimensional halide perovskite. The bandgap of this compound is measured to be 2.55 eV. High thermal stability is also clearly shown in the Cs₃BiBr₆ single crystal. A photodetector based on this compound is fabricated and tested, which exhibits an impressive detectivity of 0.8 × 10⁹ Jones and low dark current under 400 nm light illumination. Overall, our results show that the Cs₃BiBr₆ perovskite as a lead-free perovskite has interesting structures and promising properties for optoelectronic devices.

Received 31st October 2018,
Accepted 25th January 2019

DOI: 10.1039/c8tc05480k

rsc.li/materials-c

Introduction

Halide perovskites have been at the forefront of new-emerging energy materials due to their great potential in the design and fabrication of new-generation optoelectronic devices, such as solar cells,¹ photodetectors,^{2–5} light-emitting devices,^{6,7} field-effect transistors^{8,9} and lasers.^{10,11} Power conversion efficiency (PCE) of ABX₃ (A = monovalent cation, B = divalent metal, and X = halides)-based solar cells has largely increased from 3.8% to 22.6%, and it aims towards 30% in the future.^{12–16} Although they possess unique photo-physical properties such as tunable wavelength, high photoluminescence quantum yield (PLQY), large carrier diffusion length, long carrier lifetime *etc.*, the current most efficient materials are Pb-containing perovskites. Pb is detrimental to the environment and the human body, potentially causing memory problems and intellectual disability. Therefore, there is a strong desire to replace toxic Pb with a

benign element such as Sn, Ge, Bi *etc.* without drastically reducing the conversion efficiency. However, due to the high-energy-lying 5s orbitals of Sn²⁺, its oxidation into Sn⁴⁺ would undoubtedly lead to drastic performance reduction.^{17–19} As for Ge-based perovskites, their poor performance makes them lag far behind the other two alternatives.^{20–22}

Among the various alternatives, Bi-based halide perovskites have undergone rapid development. The recently emerged double perovskites, A₂BB'X₆, in which B is a monovalent metal and B' is a trivalent metal, have been demonstrated to be stable and environmentally friendly. Visible to near-infrared absorption of Cs₂SnI₆ nanocrystals exhibited high mobility after being fabricated into field-effect transistors.²³ Solar cells based on Cs₂AgBiBr₆ thin films show a PCE of 2.5%, which represents the highest efficiency among non-lead perovskites.²⁴ Especially for the double perovskite single crystal, a detectable dose rate in the Cs₂AgBiBr₆ single crystal, 59.7 nGy_{air}S⁻¹, was reported to be as low as that of CH₃NH₃PbBr₃ arising from the suppressed ion migration.²⁵

Besides A₂BB'X₆, the development of the series of A₃B₂X₉ materials is on a par with them. Blue (CH₃NH₃)₃Bi₂Br₉ quantum dots with a high PLQY of 12% were successfully synthesized.²⁶ As for their all-inorganic counterparts, a PLQY of 19.4% was realized in Cs₃Bi₂Br₉, exhibiting quite good photostability and moisture stability as well.²⁷ Besides Cs₃Bi₂Br₉, the structure of Cs₃BiBr₆ was also reported to be possible in the literature and

^a Department of Chemistry, Technical University of Denmark, DK-2800 Kongens Lyngby, Denmark. E-mail: cq@kemi.dtu.dk; Fax: +45 45883136; Tel: +45 45252032

^b DTU Danchip, Technical University of Denmark, 2800 Kongens Lyngby, Denmark

^c Department of Micro- and Nanotechnology, Technical University of Denmark, 2800 Kongens Lyngby, Denmark

^d Department of Chemical Physics and NanoLund, Lund University, Box 124, 22100, Lund, Sweden

† Electronic supplementary information (ESI) available. See DOI: 10.1039/c8tc05480k

predicted to have different optical properties compared with $\text{Cs}_3\text{Bi}_2\text{Br}_9$. However, the pure phase of Cs_3BiBr_6 has yet to be achieved and the fine structure remains unknown.²⁸

In this work, we demonstrate the synthesis and structural analysis of a single crystal of Cs_3BiBr_6 for the first time, which crystallizes in the form of isolated BiBr_6 octahedra within a three-dimensional (3D) framework. A photodetector based on this perovskite was fabricated, showing a high detectivity of around 0.8×10^9 Jones under ambient conditions. This material has thus successfully substituted Pb^{2+} with Bi^{3+} in the perovskites. Moreover, it enriches the structural family of non-lead perovskites and holds potential for optoelectronic applications.

Experimental section

Chemicals

All chemical reagents were at least of analytical grade and used as received without further purification. Bismuth bromide (BiBr_3 , 99%), cesium bromide (CsBr , 99.9%), hydrobromic acid (HBr , 48%), and *N,N*-dimethylformamide (DMF, 99.8%) were all purchased from Sigma-Aldrich.

Synthesis and crystal growth of Cs_3BiBr_6

In a typical batch synthesis, BiBr_3 (0.0894 g, 0.2 mmol), CsBr (0.1038 g, 0.49 mmol) and HBr (2.5 mL) were mixed in a beaker, which was then transferred into an oven at 110 °C for 2 h. Finally, light yellow crystals were obtained after cooling to room temperature naturally. During the synthesis of the single crystal, if the amount of CsBr was much lower than BiBr_3 , $\text{Cs}_3\text{Bi}_2\text{Br}_9$ was obtained. Therefore, controlling the ratio between the two raw materials is a key factor to obtain the single crystals of Cs_3BiBr_6 .

X-ray crystallographic studies

Small crystals of Cs_3BiBr_6 ($\sim 0.1 \text{ mm} \times 0.1 \text{ mm} \times 0.05 \text{ mm}$) were selected and mounted on glassy fibers for single-crystal XRD measurements. Data collections were performed on a Bruker APEX-II CCD diffractometer equipped with graphite monochromated $\text{Mo K}\alpha$ radiation ($\lambda = 0.71073 \text{ \AA}$) at 293 K. The data sets were corrected for Lorentz and polarization factors as well as for absorption by using a multi-scan method.²⁹ The structure was solved using direct methods and refined by full-matrix least-squares fitting on F^2 by SHELX-97.³⁰ All non-H atoms were refined using anisotropic thermal parameters. The final refined structural parameters were checked by using the PLATON program.³¹ Crystallographic data and structural refinements are summarized in Table S1 in the ESI†. The final refined atomic positions and structural parameters are further provided in the ESI† (Tables S2–S4). Rietveld refinement of the powder XRD data was performed by using the Fullprof program.

Material characterization

X-ray photoelectron spectroscopy (XPS) (Thermo Scientific) was performed to analyze the compositions of samples, with Al-K α (1486 eV) as the excitation X-ray source. The pressure of the analysis chamber was maintained at 2×10^{-10} mbar during measurements.

All characterizations were carried out at room temperature. Scanning electron microscopy (SEM) and energy dispersive X-ray spectroscopy (EDX) characterizations were carried out on an FEI Quanta FEG 200 ESEM. The absorption behaviours of the samples were studied using the UV-Vis spectrometer from Agilent Technologies (Santa Clara, USA). Absorption (α/S) data were converted from diffuse reflectance spectra using the Kubelka–Munk function, $\alpha/S = (1 - R)^2/2R$, where R is the reflectance coefficient and α and S are the absorption and scattering coefficients.³² All the photoelectronic characterizations were performed on the Autolab workstation. The phase and purity of all samples were characterized *via* powder XRD with $\text{Cu K}\alpha 1$ ($\lambda = 1.5406 \text{ \AA}$) radiation. Thermogravimetric analysis (TGA) was performed in the Mettler Toledo, Star^E System (Columbus, OH, USA) with a GC 100 gas controller in a nitrogen atmosphere at a heating rate of 10 °C min^{-1} . It should be noted that all the measurements were performed at room temperature.

Fabrication of photodetectors

Prototype optoelectronic devices were prepared in-house. ITO electrodes were prepared by ultrasonic cleaning in acetone, ethanol, and Milli-Q water successively. Cs_3BiBr_6 single crystals were dissolved into DMF and then a certain amount of solution was deposited on the device surface by drop-casting, followed by annealing at 100 °C. The working area was 0.004 cm^2 .

Results and discussion

X-ray analysis indicates clearly that the compound of Cs_3BiBr_6 crystallizes in the orthorhombic system of space group *Pbcm* with $a = 8.689(2) \text{ \AA}$, $b = 13.628(1) \text{ \AA}$, and $c = 27.694(9) \text{ \AA}$ (Table S1, ESI†). There are two Bi atoms, three Cs atoms, and seven Br atoms in an asymmetric unit. Two independent Bi atoms are located at their Wyckoff position of 4c and 4d, respectively. As shown in Fig. 1a and b, each Bi atom is coordinated by six Br atoms, forming BiBr_6 octahedra. All of the BiBr_6 octahedra are distorted, as illustrated by the bond lengths and angles in Table S3 (ESI†). The 3D framework of Cs_3BiBr_6 is displayed in Fig. 1c, where all BiBr_6 octahedra are isolated from each other forming a 0D perovskite structure. Cs^+ cations filled up the spaces left by the unconnected BiBr_6 octahedra. In particular, Bi1 locates at the mirror plane while Bi1 and Cs3 form a pseudo-triangular tunnel, which is filled up by Cs2 atoms (Fig. S1a, ESI†). In contrast, Bi1, Bi2 and Cs3 form a square tunnel, where Cs1 atoms are located forming a traditional ABX_3 structure. In order to better understand the structural characteristics of this compound, a relationship among Cs_3BiBr_6 , CsPbBr_3 ,³³ $\text{Cs}_2\text{AgBiBr}_6$ and Cs_4PbBr_6 ,³⁴ is discussed, as displayed in Fig. 2. It is known that if one Pb atom is substituted by Ag and the neighboring one is substituted by Bi in CsPbBr_3 , the perovskite $\text{Cs}_2\text{AgBiBr}_6$ forms, where all BiBr_6 octahedra are separated by Cs^+ and Ag^+ . This comparison has generally been used to illustrate the relationship between CsPbBr_3 and $\text{Cs}_2\text{AgBiBr}_6$. Despite this, there is a clear statement for the relationship between Cs_3BiBr_6 and $\text{Cs}_2\text{AgBiBr}_6$, where Ag in $\text{Cs}_2\text{AgBiBr}_6$ is substituted by Cs3 in Cs_3BiBr_6 . At the same time, a difference arises, which is that after the incorporation

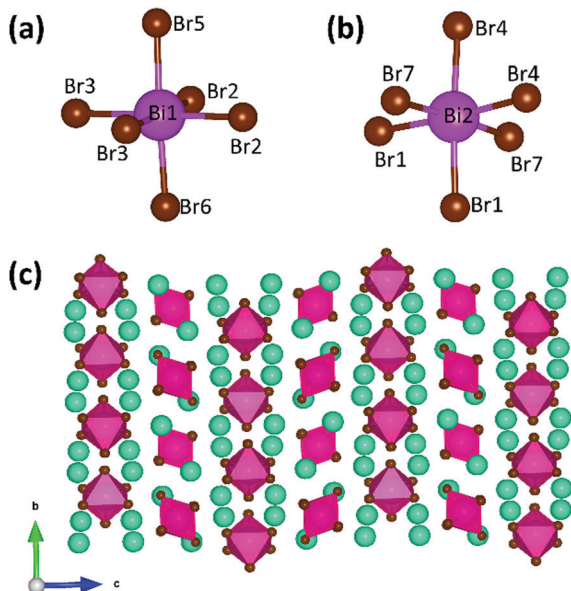


Fig. 1 View of structural characteristics for Cs_3BiBr_6 . Bromide-coordination environment for (a) Bi1 and (b) Bi2. (c) 3D framework on the bc plane. Color codes: Cs, green; Bi, purple; and Br, brown.

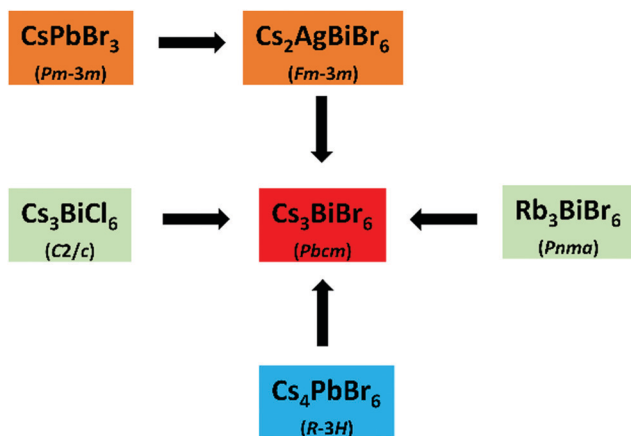


Fig. 2 Chemical and structural relationship among a series of perovskites.

of Cs3, the crystallographic symmetry of Cs_3BiBr_6 is lower than that in $\text{Cs}_2\text{AgBiBr}_6$, leading to a distinct structural characteristic in Cs_3BiBr_6 . Meanwhile, we could also clearly observe the similarity of Cs_3BiBr_6 with that of Cs_4PbBr_6 , where one monovalent Cs^+ and one divalent Pb^{2+} are simultaneously substituted by a trivalent Bi atom. Both structures are characteristic of isolated MX_6 octahedra, despite being crystallized in different crystal systems. Even compared to its isomers of Cs_3BiCl_6 and Rb_3BiBr_6 (Table S5, ESI[†]),^{35–37} different crystallographic systems and structures are found. This further reminds us that much more attention is needed for the phase checking of a new material if using the known phase as a reference (Fig. S2, ESI[†]).

The purity of samples was confirmed *via* powder X-ray diffraction (Fig. 3a). The dominant diffraction peaks of $2\theta = 13.66^\circ, 20.09^\circ, 22.06^\circ, 29.19^\circ, 30.08^\circ, 32.22^\circ, 39.08^\circ, 44.98^\circ,$ and 56.43° could be identified to be the crystal planes of (112),

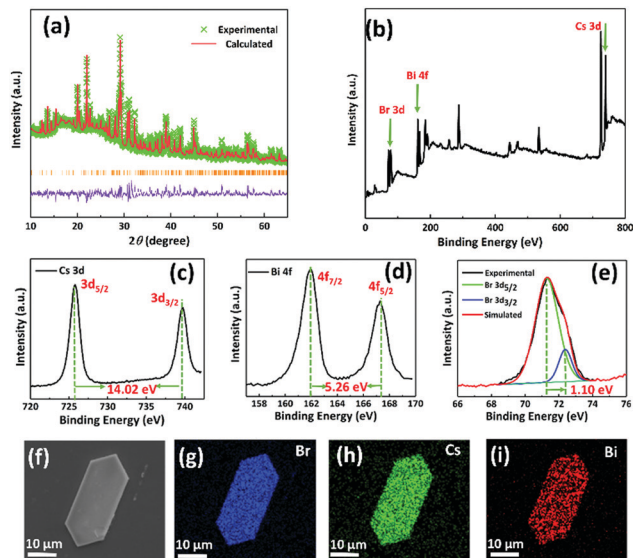


Fig. 3 (a) Rietveld refinement of the experimental powder XRD pattern of Cs_3BiBr_6 and calculated XRD patterns using a single crystal. XPS spectra: (b) survey spectrum, (c) Cs 3d, (d) Bi 4f, and (e) Br 3d. (f) Electron micrograph of the microstructure for single crystal Cs_3BiBr_6 . (g–i) EDX mapping of the elemental distribution: (g) Br, (h) Cs, and (i) Bi.

(115), (130), (044), (233), (312), (334), (329) and (367), respectively. Furthermore, we used the Fullprof software to check the purity in detail. The Rietveld refinement results show the good agreement between observed (cross) and fitted (solid lines) diffraction patterns with the resulting χ^2 of 4.40. This consistency between the experimental and simulated XRD patterns confirms the phase purity of the studied material. Besides, we further confirmed the valence state and the element distribution by XPS measurements (Fig. 3b–e). From the XPS results, we could observe the signals of Cs ($3d_{5/2}, 3d_{3/2}$, separated spin-orbital components $\Delta = 14.02$ eV), Bi ($4f_{7/2}, 4f_{5/2}$, $\Delta = 5.26$ eV) and Br ($3d_{5/2}, 3d_{3/2}$, $\Delta = 1.10$ eV), which indicates their valence (+1, +3, −1, respectively) to be consistent with the formula and confirms the existence of all elements in this material (Fig. 3c–e). Besides, the morphology of the as-synthesized single crystal was measured *via* SEM, where a smooth surface was observed on the single crystal (Fig. 3f). Elemental composition was mapped by energy dispersive X-ray (EDX) spectroscopy to study the elemental distribution (Fig. 3g–i). All elements of Cs, Bi, and Br were observed and distributed uniformly on the surface of the single crystal.

To analyze the optical properties of Cs_3BiBr_6 , the UV-Vis absorption spectrum was measured. Cs_3BiBr_6 displays an absorption edge at about 485 nm, and the bandgap of the compound was calculated to be 2.55 eV according to the Tauc plot (the inset of Fig. 4). Meanwhile, we also conducted DFT calculations to evaluate the bandgap, which was found to be ~ 3.2 eV (Fig. S3, ESI[†]). The slight difference with the experimental values is attributed to the limitation of the DFT methods.³⁸ In the PL spectra, two emission peaks appear: one peak at 475 nm is due to the band emission and the other peak at 530 nm is due to the defects (Fig. S4, ESI[†]). Regarding the thermal stability, the samples of Cs_3BiBr_6 single crystals were heated under a

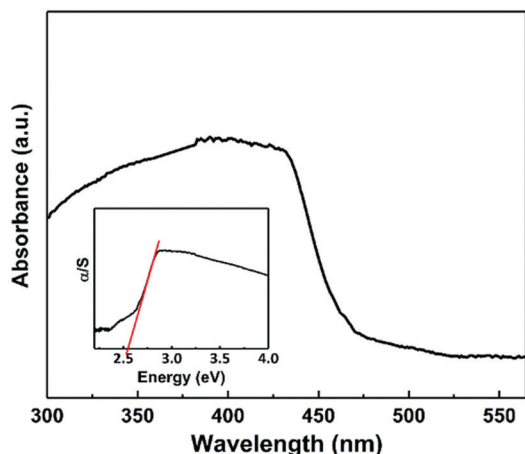


Fig. 4 Absorption spectrum of Cs_3BiBr_6 . Inset: The Tauc plot showing the bandgap of ca. 2.55 eV.

nitrogen atmosphere, as shown in the TGA curve in Fig. S5 (ESI[†]). It can be observed that Cs_3BiBr_6 is stable with increasing temperature up to 425 °C, when the onset of weight loss is observed.^{39,40} As a comparison, $\text{CH}_3\text{NH}_3\text{PbBr}_3$ was also investigated. For $\text{CH}_3\text{NH}_3\text{PbBr}_3$, the loss in the weight of the sample starts from 285 °C, while a plateau is seen in the temperature range of 420–455 °C. This step was attributed to the loss of $\text{CH}_3\text{NH}_3\text{Br}$. Furthermore, a rapid drop in the weight loss curve is clearly seen above 455 °C, indicating further decomposition of the system. This indicates a higher thermal stability of Cs_3BiBr_6 than $\text{CH}_3\text{NH}_3\text{PbBr}_3$.

In order to check the optoelectronic property of Cs_3BiBr_6 , a photodetector was fabricated on ITO electrodes as illustrated in Fig. 5a. The morphology of the film was examined as displayed in Fig. S6 (ESI[†]). Fig. 5b and Fig. S7 (ESI[†]) show the I - V characteristics in the dark and under light illumination at different light densities. Obviously, the photocurrent increases with the increase of the light density and voltage. Under a 6 V bias, an ultralow dark current of 0.3 nA was obtained. Fig. 5c shows the dynamic current-time (i - t) curves for the Cs_3BiBr_6 based photodetectors under repeated switching of 400 nm monochromatic illumination with a light density of 25 mW cm^{-2} . The amperometric i - t curves demonstrate that the device can repeatedly produce stable photocurrent signals in response to periodical light ON and OFF. Upon illumination, the photocurrent increases to 70 nA cm^{-2} by increasing the voltage up to 8 V. Besides, the photoresponse of the detector versus light power density was also measured, as shown in Fig. 5d. With the increase of the power density, the photocurrent also increases, reaching 50 nA cm^{-2} under the light density of 25 mW cm^{-2} at the voltage of 6 V. The above results from i - t curves are consistent with our conclusions from the I - V curves.

Hereafter, we focus on the investigation of responsivity and detectivity of the photodetector. Fig. 5e and f show the responsivity and detectivity of the photodetector versus voltage and light density, respectively. The responsivity (R), which can be understood as an electrical output per optical input, is calculated by the following equation:⁴¹

$$R = (I_{\text{PC}} - I_{\text{dark}}) / (P_{\text{irra}} \cdot S) \quad (1)$$

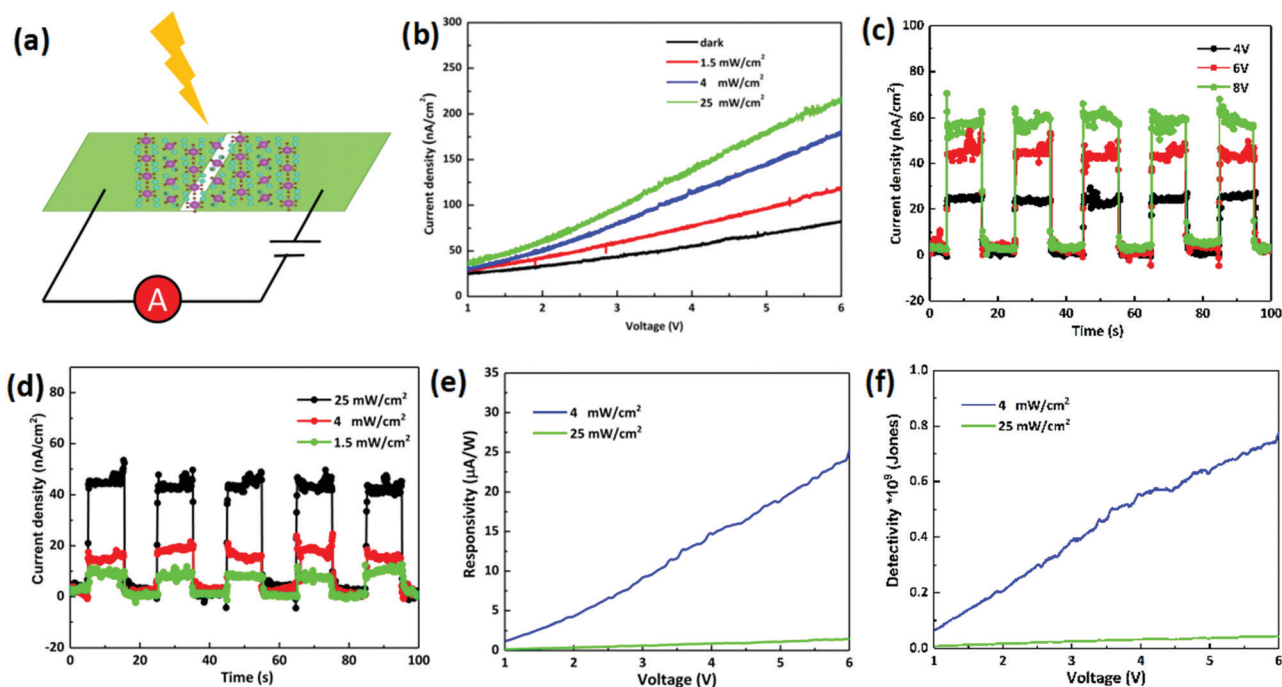


Fig. 5 (a) Schematic view of the photodetector based on Cs_3BiBr_6 . (b) I - V characteristics at different power densities. (c) Photocurrent responses under various bias voltages with fixed light density of 25 mW cm^{-2} . (d) Photocurrent responses at various light densities at a fixed bias voltage of 6 V. (e) Comparison of the responsivity at two different light densities. (f) Comparison of the detectivity at two different light densities.

where I_{PC} and I_{dark} are currents measured with and without illumination, respectively. P_{irra} is the irradiation power density and S is the effective working area of the detector. Detectivity (D^*) as a figure of merit evaluating the ability to detect weak light can be calculated using eqn (2).

$$D^* = R/(2e \times I_{dark})^{1/2} \quad (2)$$

At the voltage of 6 V, the responsivity of this material can reach $\sim 25 \mu\text{A W}^{-1}$ at a light density of 4 mW cm^{-2} . And its detectivity was calculated to be around 0.8×10^9 Jones. External quantum efficiency (EQE) was calculated to be 0.008% at a voltage of 6 V and a power density of 4 mW cm^{-2} according to the equation $\text{EQE} = R \cdot hc/(e\lambda)$ (Fig. S8, ESI†). After exposing to 400 nm light illumination, the rise and decay time of the device was extracted to be 50 ms and 60 ms, respectively (Fig. S9, ESI†). Meanwhile, we also checked the photo-detection ability of this material toward white light, as shown in Fig. S10 (ESI†). It is clear that the device behaves similarly to that under 400 nm light, although a weak responsivity was observed. At a 6 V bias, the responsivity towards white light was only $0.2 \mu\text{A W}^{-1}$, much lower than that under 400 nm wavelength light. In Fig. S11 (ESI†), the stability of the photodetector is shown.

Conclusions

In summary, we have successfully synthesized non-toxic single crystals of a perovskite, Cs_3BiBr_6 . The crystal structure of the perovskite was analyzed for the first time revealing a system of non-overlapping BiBr_6 polyhedra. A photodetector based on this perovskite was fabricated, exhibiting a good detectivity of 0.8×10^9 Jones under 400 nm light illumination, demonstrating the potential of the material for its application in optoelectronic devices. Besides, the crystals display high stability against temperature and moisture. Finally, this work offers an example of the utilization of non-toxic perovskites for photo-detection. It further facilitates the development of lead-free perovskites toward environment friendly energy conversion devices.

Conflicts of interest

There are no conflicts to declare.

Acknowledgements

This work was supported by the Villum Foundation, the Independent Research Fund Denmark-Nature Sciences (DFF-FNU, Project No. DFF-7014-00302), the Independent Research Fund Denmark-Sapere Aude starting grant (No. 7026-00037A) and the Swedish Research Council VR starting grant (No. 2017-05337), the KAW foundation, the Crafoord foundation and the Swedish Energy Agency. We thank Christian Engelbrekt for his help in using optical sources.

Notes and references

- 1 N. Arora, M. Ibrahim Dar, A. Hinderhofer, N. Pellet, F. Schreiber, S. M. Zakeeruddin and M. Grätzel, *Science*, 2017, **358**, 768–771.
- 2 H. R. Xia, J. Li, W. T. Sun and L. M. Peng, *Chem. Commun.*, 2014, **50**, 13695.
- 3 R. Dong, Y. J. Fang, J. Chae, J. Dai, Z. G. Xiao, Q. F. Dong, Y. B. Yuan, A. Centrone, X. C. Zeng and J. S. Huang, *Adv. Mater.*, 2015, **27**, 1912–1918.
- 4 Z. J. Tan, Y. Wu, H. Hong, J. B. Yin, J. C. Zhang, L. Lin, M. Z. Wang, X. Sun, L. Z. Sun, Y. C. Huang, K. H. Liu, Z. F. Liu and H. L. Peng, *J. Am. Chem. Soc.*, 2016, **138**, 16612–16615.
- 5 M. I. Saidaminov, V. Adinolfi, R. Comin, A. L. Abdelhady, W. Peng, I. Dursun, M. Yuan, S. Hoogland, E. H. Sargent and O. M. Bakr, *Nat. Commun.*, 2015, **6**, 8724.
- 6 P. Schulz, E. Edri, S. Kirmayer, G. Hodes, D. Cahen and A. Kahn, *Energy Environ. Sci.*, 2014, **7**, 1377–1381.
- 7 G. R. Li, Z.-K. Tan, D. W. Di, M. L. Lai, L. Jiang, J. H.-W. Lim, R. H. Friend and N. C. Greenham, *Nano Lett.*, 2015, **15**, 2640–2644.
- 8 X. Y. Chin, D. Cortecchia, J. Yin, A. Bruno and C. Soci, *Nat. Commun.*, 2015, **6**, 7383.
- 9 S. P. Senanayak, B. Y. Yang, T. H. Thomas, N. Giesbrecht, W. C. Huang, E. Gann, B. Nair, K. Goedel, S. Guha, X. Moya, C. R. McNeill, P. Docampo, A. Sadhanala, R. H. Friend and H. Sirringhaus, *Sci. Adv.*, 2017, **3**, e1601935.
- 10 S. D. Stranks, S. M. Wood, K. Wojciechowski, F. Deschler, M. Saliba, H. Khandelwal, J. B. Patel, S. J. Elston, L. M. Herz, M. B. Johnston, A. P. H. J. Schenning, M. G. Debije, M. K. Riede, S. M. Morris and H. J. Snaith, *Nano Lett.*, 2015, **15**, 4935–4941.
- 11 G. C. Xing, N. Mathews, S. S. Lim, N. Yantara, X. F. Liu, D. Sabba, M. Grätzel, S. Mhaisalkar and T. C. Sum, *Nat. Mater.*, 2014, **13**, 476–480.
- 12 A. Kojima, K. Teshima, Y. Shirai and T. Miyasaka, *J. Am. Chem. Soc.*, 2009, **131**, 6050–6051.
- 13 M. M. Lee, J. Teuscher, T. Miyasaka, T. N. Murakami and H. J. Snaith, *Science*, 2012, **338**, 643–647.
- 14 M. Liu, M. B. Johnston and H. J. Snaith, *Nature*, 2013, **501**, 395–398.
- 15 N. J. Jeon, J. H. Noh, W. S. Yang, Y. C. Kim, S. Ryu, J. Seo and S. I. Seok, *Nature*, 2015, **517**, 476–480.
- 16 N. J. Jeon, H. Na, E. H. Jung, T.-Y. Yang, Y. G. Lee, G. Kim, H.-W. Shin, S. Il Seok, J. Lee and J. Seo, *Nat. Energy*, 2018, **3**, 682–689.
- 17 T. Leijtens, R. Prasanna, A. Gold-Parker, M. F. Toney and M. D. McGehee, *ACS Energy Lett.*, 2017, **2**, 2159–2165.
- 18 T.-B. Song, T. Yokoyama, S. Aramaki and M. G. Kanatzidis, *ACS Energy Lett.*, 2017, **4**, 897–903.
- 19 E. J. Yeom, S. S. Shin, W. S. Yang, S. J. Lee, W. P. Yin, D. Kim, J. H. Noh, T. K. Ahn and S. Il Seok, *J. Mater. Chem. A*, 2017, **5**, 79–86.
- 20 C. C. Stoumpos, L. Frazer, D. J. Clark, Y. S. Kim, S. H. Rhim, A. J. Freeman, J. B. Ketterson, J. I. Jang and M. G. Kanatzidis, *J. Am. Chem. Soc.*, 2015, **137**, 6804–6819.

- 21 I. Kopacic, B. Friesenbichler, S. F. Hoefler, B. Kunert, H. Plank, T. Rath and G. Trimmel, *ACS Appl. Energy Mater.*, 2018, **1**, 343–347.
- 22 T. Krishnamoorthy, H. Ding, C. Yan, W. L. Leong, T. Baikie, Z. Y. Zhang, M. Sherburne, S. Z. Li, M. Asta, N. Mathews and S. G. Mhaisalkar, *J. Mater. Chem. A*, 2015, **3**, 23829–23832.
- 23 L.-Z. Lei, Z.-F. Shi, Y. Li, Z.-Z. Ma, F. Zhang, T.-T. Xu, Y.-T. Tian, D. Wu, X.-J. Lia and G.-T. Du, *J. Mater. Chem. C*, 2018, **6**, 7982–7988.
- 24 A. F. Wang, X. X. Yan, M. Zhang, S. B. Sun, M. Yang, W. Shen, X. Q. Pan, P. Wang and Z. T. Deng, *Chem. Mater.*, 2016, **28**, 8132–8140.
- 25 W. C. Pan, H. D. Wu, J. J. Luo, Z. Z. Deng, C. Ge, C. Chen, X. W. Jiang, W.-J. Yin, G. D. Niu, L. J. Zhu, L. X. Yin, Y. Zhou, Q. G. Xie, X. X. Ke, M. L. Sui and J. Tang, *Nat. Photonics*, 2017, **11**, 726–732.
- 26 M. Leng, Z. Chen, Y. Yang, Z. Li, K. Zeng, K. Li, G. Niu, Y. He, Q. Zhou and J. Tang, *Angew. Chem., Int. Ed.*, 2016, **55**, 15012–15016.
- 27 M. Y. Leng, Y. Yang, K. Zeng, Z. W. Chen, Z. F. Tan, S. R. Li, J. H. Li, B. Xu, D. B. Li, M. P. Hautzinger, Y. P. Fu, T. Y. Zhai, L. Xu, G. D. Niu, S. Jin and J. Tang, *Adv. Funct. Mater.*, 2018, **1**, 1704446.
- 28 S. E. Creutz, E. N. Crites, M. C. De Siena and D. R. Gamelin, *Nano Lett.*, 2018, 1118–1123.
- 29 *CrystalClear, version 1.3.5*, Rigaku Corp., The Woodlands, TX, 1999.
- 30 G. M. Sheldrick, *Crystallographic Software Package, SHELXTL, version 5.1*, Bruker AXS, Madison, WI, 1998.
- 31 A. L. Spek, *J. Appl. Crystallogr.*, 2003, **36**, 7.
- 32 G. Kortüm, *Reflectance Spectroscopy*, Springer-Verlag, New York, 1969.
- 33 S. Hirotsu, J. Harada, M. Iizumi and K. Gesi, *J. Phys. Soc. Jpn.*, 1974, **37**, 1393–1398.
- 34 M. I. Saidaminov, J. Almutlaq, S. Sarmah, I. Dursun, A. A. Zhumeckenov, R. Begum, J. Pan, N. Cho, O. F. Mohammed and O. M. Bakr, *ACS Energy Lett.*, 2016, **1**, 840–845.
- 35 M. Shimizu, M. Koshimizu, Y. Fujimoto, T. Yanagida, S. Ono and K. Asai, *Opt. Mater.*, 2016, **61**, 115–118.
- 36 F. Lazarini, *Acta Crystallogr., Sect. B: Struct. Crystallogr. Cryst. Chem.*, 1978, **34**, 2288–2290.
- 37 C. W. M. Timmermans and G. Blasse, *Phys. Status Solidi*, 1983, **b118**, 353.
- 38 M.-L. Liang, Y.-X. Ma, C.-L. Hu, F. Kong and J.-G. Mao, *Dalton*, 2018, **47**, 1513.
- 39 M. Y. Leng, Y. Yang, K. Zeng, Z. W. Chen, Z. F. Tan, S. R. Li, J. H. Li, B. Xu, D. B. Li, M. P. Hautzinger, Y. P. Fu, T. Y. Zhai, L. Xu, G. D. Niu, S. Jin and J. Tang, *Adv. Funct. Mater.*, 2018, **28**, 1704446.
- 40 L. Zhou, Y.-F. Xu, B.-X. Chen, D.-B. Kuang and C.-Y. Su, *Small*, 2018, **14**, 1703762.
- 41 J. X. Ding, S. J. Du, Z. Y. Zuo, Y. Zhao, H. Z. Cui and X. Y. Zhan, *J. Phys. Chem. C*, 2017, **121**, 4917–4923.

Electronic Supplementary Information (ESI)†

Lead-free double-halide perovskite Cs₃BiBr₆ with well-defined crystal structure and high thermal stability for optoelectronics

Yingying Tang,^a Mingli Liang,^a Bingdong Chang,^b Hongyu Sun,^c Kaibo Zheng,^{a,d} Tönu Pullerits,^d Qijin Chi^{*a}

a. Department of Chemistry, Technical University of Denmark, DK-2800 Kongens Lyngby, Denmark

b. DTU Danchip, Technical University of Denmark, 2800 Kongens Lyngby, Denmark

c. Department of Micro- and Nanotechnology, Technical University of Denmark, 2800 Kongens Lyngby, Denmark

d. Department of Chemical Physics and NanoLund, Lund University, Box 124, 22100, Lund, Sweden

* To whom correspondence should be addressed. E-mail: cq@kemi.dtu.dk; Phone: +45 45252032

Contents:

Table S1. Crystal data and structure refinements for the Cs₃BiBr₆.

Table S2. Atomic coordinates and equivalent isotropic displacement parameters for Cs₃BiBr₆.

Table S3. Bond lengths (Å) and angles (deg) for Cs₃BiBr₆.

Table S4. Anisotropic displacement parameters for Cs₃BiBr₆.

Table S5. Crystallographic and electronic parameters for the known perovskites.

Fig. S1 View of the structures constructed by (a) Bi1 and (b) Bi2, respectively.

Fig. S2 Comparison of XRD pattern for Cs₃BiBr₆, Rb₃BiBr₆, Cs₃BiCl₆.

Fig. S3 TGA curves of Cs₃BiBr₆ and CH₃NH₃PbBr₃.

Fig. S4 (a) Electron micrograph of the microstructure for the photodetector. (b)-(d) Energy dispersive X-ray (EDX) mapping of the element distribution: (b) Br, (c) Cs, (d) Bi.

Fig. S5 EQE versus voltage under light illumination of 4 mW/cm² and 25 mW/cm².

Fig. S6 The high-resolution I-t curve of Cs₃BiBr₆ devices towards 400 nm illumination with a powder intensity of 25 mW/cm².

Fig. S7 Photoresponse of Cs₃BiBr₆ under white light illumination with power density of 350 mW/cm².

Fig. S8 EQE versus voltage under light illumination of 4 mW/cm² and 25 mW/cm².

Fig. S9 The high-resolution I-t curve of Cs₃BiBr₆ devices towards 400 nm illumination with a powder intensity of 25 mW/cm².

Fig. S10 Photoresponse of Cs₃BiBr₆ under white light illumination with power density of 350 mW/cm².

Fig. S11 The stability for the photodetector under light illumination.

Table S1. Crystal data and structure refinements for the Cs₃BiBr₆.

formula	Cs ₃ BiBr ₆
fw	1087.11
T, K	room temp
λ, Å	0.71073
space group	<i>Pbcm</i>
a, Å	8.689(2)
b, Å	13.628(1)
c, Å	27.694(9)
α, deg	90
β, deg	90
γ, deg	90
V, Å ³	3279.5(6)
Z	8
D _{calcd} , g cm ⁻³	4.404
μ, mm ⁻¹	31.89
GOF on F ²	1.062
R1,wR2 [<i>I</i> > 2σ(<i>I</i>)] ^a	0.0495, 0.1412
R1,wR2(all data)	0.0794, 0.1603

$$^a R1 = \sum ||F_o| - |F_c|| / \sum |F_o|, wR2 = \{ \sum w[(F_o)^2 - (F_c)^2]^2 / \sum w[(F_o)^2]^2 \}^{1/2}$$

Table S2. Atomic coordinates ($\times 10^4$) and equivalent isotropic displacement parameters ($\text{Å}^2 \times 10^3$) for Cs₃BiBr₆. U(eq) is defined as one third of the trace of the orthogonalized Uij tensor.

Atom	x	y	z	U(eq)
Bi(1)	7451(1)	806(1)	2500	22(1)
Bi(2)	-2141(1)	-2500	0	21(1)
Cs(3)	3140(1)	-939(1)	1546(1)	35(1)
Cs(2)	8180(1)	-2461(1)	1615(1)	37(1)
Br(5)	6001(1)	-1075(1)	2500	31(1)
Br(6)	8801(1)	2722(1)	2500	30(1)
Br(7)	-2221(2)	-4191(1)	588(1)	57(1)
Br(4)	294(1)	-1717(1)	582(1)	47(1)
Br(3)	9470(1)	202(1)	1752(1)	48(1)
Br(2)	5486(1)	1392(1)	1720(1)	46(1)
Br(1)	-4459(1)	-3387(1)	-581(1)	51(1)
Cs(1)	-2566(1)	-5855(1)	-493(1)	70(1)

Table S3. Bond lengths (Å) and angles (deg) for Cs₃BiBr₆.

Bi(1)-Br(3)	2.8360(9)	Bi(1)-Br(3)#1	2.8360(8)
Bi(1)-Br(5)	2.8557(11)	Bi(1)-Br(6)	2.8628(11)
Bi(1)-Br(2)	2.8671(8)	Bi(1)-Br(2)#1	2.8671(8)
Bi(2)-Br(7)	2.8233(8)	Bi(2)-Br(7)#2	2.8233(8)
Bi(2)-Br(1)	2.8484(9)	Bi(2)-Br(1)#2	2.8484(9)
Bi(2)-Br(4)	2.8655(9)	Bi(2)-Br(4)#2	2.8655(9)
Cs(3)-Br(1)#5	3.5117(10)	Cs(3)-Br(3)#4	3.5927(11)
Cs(3)-Br(6)#6	3.6278(9)	Cs(3)-Br(5)	3.6329(10)
Cs(3)-Br(7)#7	3.6528(11)	Cs(3)-Br(4)	3.7906(10)
Cs(3)-Br(2)	3.8048(11)	Cs(3)-Br(2)#6	3.8593(11)
Cs(2)-Br(4)#10	3.5490(10)	Cs(2)-Br(2)#6	3.5602(11)
Cs(2)-Br(6)#11	3.5980(10)	Cs(2)-Br(5)	3.6266(10)
Cs(2)-Br(7)#10	3.7120(11)	Cs(2)-Br(3)#11	3.8028(11)
Cs(2)-Br(3)	3.8167(10)	Cs(2)-Br(1)#5	3.8463(12)
Cs(2)-Bi(2)#10	4.4827(5)	Cs(1)-Br(4)#15	3.7600(11)
Cs(1)-Br(4)#9	3.8610(13)	Cs(1)-Br(2)#3	3.8665(13)
Cs(1)-Br(3)#3	4.0110(15)	Cs(1)-Br(1)#16	4.0743(15)
Cs(1)-Br(7)#9	4.1682(17)	Cs(1)-Cs(1)#17	5.2503(15)
Cs(1)-Cs(3)#9	5.2774(9)	Cs(1)-Cs(3)#3	5.3291(9)
Cs(1)-Cs(2)#18	5.4278(10)	Br(3)-Bi(1)-Br(3)#1	93.79(5)
Br(3)-Bi(1)-Br(5)	90.73(3)	Br(3)-Bi(1)-Br(6)	90.63(3)
Br(5)-Bi(1)-Br(6)	178.01(3)	Br(3)-Bi(1)-Br(2)	84.22(3)
Br(3)#1-Bi(1)-Br(2)	178.01(3)	Br(5)-Bi(1)-Br(2)	89.28(3)
Br(6)-Bi(1)-Br(2)	89.42(3)	Br(3)-Bi(1)-Br(2)#1	178.01(3)
Br(3)#1-Bi(1)-Br(2)#1	84.22(3)	Br(5)-Bi(1)-Br(2)#1	89.28(3)
Br(6)-Bi(1)-Br(2)#1	89.42(3)	Br(2)-Bi(1)-Br(2)#1	97.78(4)
Br(7)-Bi(2)-Br(7)#2	177.18(6)	Br(7)-Bi(2)-Br(1)	87.83(3)
Br(7)#2-Bi(2)-Br(1)	90.18(3)	Br(1)-Bi(2)-Br(1)#2	89.98(5)
Br(7)-Bi(2)-Br(4)	89.87(3)	Br(7)#2-Bi(2)-Br(4)	92.21(3)
Br(1)-Bi(2)-Br(4)	176.51(3)	Br(1)#2-Bi(2)-Br(4)	92.66(3)
Br(4)-Bi(2)-Br(4)#2	84.81(4)	Br(7)-Bi(2)-Cs(2)#3	124.57(2)
Br(7)#2-Bi(2)-Cs(2)#3	55.64(2)	Br(1)-Bi(2)-Cs(2)#3	58.31(2)
Br(1)#2-Bi(2)-Cs(2)#3	127.82(2)	Br(4)-Bi(2)-Cs(2)#3	121.32(2)
Br(4)#2-Bi(2)-Cs(2)#3	52.301(19)	Br(7)#2-Bi(2)-Cs(2)#4	124.57(2)
Br(1)-Bi(2)-Cs(2)#4	127.82(2)	Cs(2)#3-Bi(2)-Cs(2)#4	172.876(17)
Br(1)#5-Cs(3)-Br(3)#4	139.59(3)	Br(1)#5-Cs(3)-Br(6)#6	134.31(3)
Br(3)#4-Cs(3)-Br(6)#6	71.90(2)	Br(1)#5-Cs(3)-Br(5)	97.66(3)
Br(3)#4-Cs(3)-Br(5)	120.91(3)	Br(6)#6-Cs(3)-Br(5)	76.27(2)
Br(1)#5-Cs(3)-Br(7)#7	75.40(3)	Br(3)#4-Cs(3)-Br(7)#7	68.88(3)
Br(6)#6-Cs(3)-Br(7)#7	139.06(3)	Br(5)-Cs(3)-Br(7)#7	135.33(3)
Br(1)#5-Cs(3)-Br(4)	77.20(3)	Br(3)#4-Cs(3)-Br(4)	69.78(2)
Br(6)#6-Cs(3)-Br(4)	93.95(2)	Br(5)-Cs(3)-Br(4)	160.80(3)
Br(7)#7-Cs(3)-Br(4)	61.86(2)	Br(1)#5-Cs(3)-Br(2)	89.80(3)
Br(3)#4-Cs(3)-Br(2)	95.41(3)	Br(6)#6-Cs(3)-Br(2)	125.24(2)
Br(5)-Cs(3)-Br(2)	65.41(2)	Br(7)#7-Cs(3)-Br(2)	70.43(2)
Br(4)-Cs(3)-Br(2)	132.26(2)	Br(1)#5-Cs(3)-Br(2)#6	70.40(2)
Br(3)#4-Cs(3)-Br(2)#6	131.49(3)	Br(6)#6-Cs(3)-Br(2)#6	65.06(2)
Br(5)-Cs(3)-Br(2)#6	69.46(2)	Br(7)#7-Cs(3)-Br(2)#6	140.61(3)
Br(4)-Cs(3)-Br(2)#6	91.49(3)	Br(2)-Cs(3)-Br(2)#6	127.246(16)

Br(1)#5-Cs(3)-Cs(2)#4	116.88(2)	Br(3)#4-Cs(3)-Cs(2)#4	51.834(17)
Br(6)#6-Cs(3)-Cs(2)#4	48.245(17)	Br(5)-Cs(3)-Cs(2)#4	124.39(2)
Br(7)#7-Cs(3)-Cs(2)#4	96.59(2)	Br(4)-Cs(3)-Cs(2)#4	47.135(16)
Br(2)-Cs(3)-Cs(2)#4	147.04(2)	Br(2)#6-Cs(3)-Cs(2)#4	82.247(19)
Br(1)#5-Cs(3)-Cs(2)	51.81(2)	Br(3)#4-Cs(3)-Cs(2)	168.55(2)
Br(6)#6-Cs(3)-Cs(2)	100.12(2)	Br(5)-Cs(3)-Cs(2)	48.030(16)
Br(7)#7-Cs(3)-Cs(2)	120.33(2)	Br(4)-Cs(3)-Cs(2)	119.82(2)
Br(2)-Cs(3)-Cs(2)	82.421(18)	Br(2)#6-Cs(3)-Cs(2)	46.561(17)
Cs(2)#4-Cs(3)-Cs(2)	128.764(18)	Br(1)#5-Cs(3)-Cs(2)#8	115.06(2)
Br(3)#4-Cs(3)-Cs(2)#8	50.589(17)	Br(6)#6-Cs(3)-Cs(2)#8	110.54(2)
Br(5)-Cs(3)-Cs(2)#8	100.47(2)	Br(7)#7-Cs(3)-Cs(2)#8	49.021(18)
Br(4)-Cs(3)-Cs(2)#8	98.42(2)	Br(2)-Cs(3)-Cs(2)#8	46.383(17)
Br(2)#6-Cs(3)-Cs(2)#8	169.52(2)	Cs(2)#4-Cs(3)-Cs(2)#8	101.992(12)
Cs(2)-Cs(3)-Cs(2)#8	128.753(15)	Br(1)#5-Cs(3)-Cs(1)#9	54.49(2)
Br(3)#4-Cs(3)-Cs(1)#9	111.25(2)	Br(6)#6-Cs(3)-Cs(1)#9	86.661(19)
Br(5)-Cs(3)-Cs(1)#9	115.10(2)	Br(7)#7-Cs(3)-Cs(1)#9	96.77(2)
Br(4)-Cs(3)-Cs(1)#9	46.948(19)	Br(2)-Cs(3)-Cs(1)#9	144.28(2)
Br(2)#6-Cs(3)-Cs(1)#9	46.972(19)	Br(4)#10-Cs(2)-Br(2)#6	130.86(3)
Br(4)#10-Cs(2)-Br(6)#11	98.75(2)	Br(2)#6-Cs(2)-Br(6)#11	128.84(3)
Br(4)#10-Cs(2)-Br(5)	131.80(3)	Br(2)#6-Cs(2)-Br(5)	72.94(2)
Br(6)#11-Cs(2)-Br(5)	83.38(2)	Br(4)#10-Cs(2)-Br(7)#10	67.16(2)
Br(2)#6-Cs(2)-Br(7)#10	72.51(3)	Br(6)#11-Cs(2)-Br(7)#10	129.35(3)
Br(5)-Cs(2)-Br(7)#10	143.10(3)	Br(4)#10-Cs(2)-Br(3)#11	92.38(3)
Br(2)#6-Cs(2)-Br(3)#11	95.99(3)	Br(6)#11-Cs(2)-Br(3)#11	66.32(2)
Br(5)-Cs(2)-Br(3)#11	130.47(3)	Br(7)#10-Cs(2)-Br(3)#11	66.08(2)
Br(4)#10-Cs(2)-Br(3)	69.92(2)	Br(2)#6-Cs(2)-Br(3)	132.25(3)
Br(6)#11-Cs(2)-Br(3)	69.66(3)	Br(5)-Cs(2)-Br(3)	65.87(2)
Br(7)#10-Cs(2)-Br(3)	135.06(3)	Br(3)#11-Cs(2)-Br(3)	128.952(17)
Br(4)#10-Cs(2)-Br(1)#5	67.81(2)	Br(2)#6-Cs(2)-Br(1)#5	70.08(2)
Br(6)#11-Cs(2)-Br(1)#5	157.06(3)	Br(5)-Cs(2)-Br(1)#5	92.02(2)
Br(7)#10-Cs(2)-Br(1)#5	64.18(2)	Br(3)#11-Cs(2)-Br(1)#5	130.25(2)
Br(3)-Cs(2)-Br(1)#5	87.91(3)	Br(4)#10-Cs(2)-Bi(2)#10	39.705(15)
Br(2)#6-Cs(2)-Bi(2)#10	91.17(2)	Br(6)#11-Cs(2)-Bi(2)#10	136.53(2)
Br(5)-Cs(2)-Bi(2)#10	130.393(19)	Br(7)#10-Cs(2)-Bi(2)#10	38.893(14)
Br(3)#11-Cs(2)-Bi(2)#10	97.059(19)	Br(3)-Cs(2)-Bi(2)#10	97.40(2)
Br(1)#5-Cs(2)-Bi(2)#10	39.062(14)	Br(4)#10-Cs(2)-Cs(3)#10	51.523(16)
Br(2)#6-Cs(2)-Cs(3)#10	177.59(2)	Br(6)#11-Cs(2)-Cs(3)#10	48.779(16)
Br(5)-Cs(2)-Cs(3)#10	105.75(2)	Br(7)#10-Cs(2)-Cs(3)#10	109.21(2)
Br(3)#11-Cs(2)-Cs(3)#10	83.313(19)	Br(3)-Cs(2)-Cs(3)#10	47.739(17)
Br(1)#5-Cs(2)-Cs(3)#10	112.13(2)	Bi(2)#10-Cs(2)-Cs(3)#10	91.205(13)
Br(4)#10-Cs(2)-Cs(3)	108.27(2)	Br(2)#6-Cs(2)-Cs(3)	51.916(18)
Br(6)#11-Cs(2)-Cs(3)	130.99(2)	Br(5)-Cs(2)-Cs(3)	48.140(17)
Br(7)#10-Cs(2)-Cs(3)	99.02(2)	Br(3)#11-Cs(2)-Cs(3)	147.90(2)
Br(3)-Cs(2)-Cs(3)	82.11(2)	Br(1)#5-Cs(2)-Cs(3)	45.860(15)
Br(4)#10-Cs(2)-Cs(3)#6	111.53(2)	Br(2)#6-Cs(2)-Cs(3)#6	50.687(18)
Br(6)#11-Cs(2)-Cs(3)#6	105.37(2)	Br(5)-Cs(2)-Cs(3)#6	114.19(2)
Br(7)#10-Cs(2)-Cs(3)#6	47.979(16)	Br(3)#11-Cs(2)-Cs(3)#6	46.881(17)
Br(3)-Cs(2)-Cs(3)#6	175.04(2)	Br(1)#5-Cs(2)-Cs(3)#6	97.03(2)
Br(1)-Cs(1)-Br(4)#15	124.20(3)	Br(1)-Cs(1)-Br(7)	63.09(2)
Br(4)#15-Cs(1)-Br(7)	61.13(2)	Br(1)-Cs(1)-Br(4)#9	171.21(4)
Br(4)#15-Cs(1)-Br(4)#9	60.93(2)	Br(7)-Cs(1)-Br(4)#9	121.71(3)

Br(1)-Cs(1)-Br(2)#3	85.43(2)	Br(4)#15-Cs(1)-Br(2)#3	150.04(3)
Br(7)-Cs(1)-Br(2)#3	147.92(3)	Br(4)#9-Cs(1)-Br(2)#3	90.32(2)
Br(1)-Cs(1)-Br(3)#3	86.44(3)	Br(4)#15-Cs(1)-Br(3)#3	121.74(3)
Br(7)-Cs(1)-Br(3)#3	121.50(3)	Br(4)#9-Cs(1)-Br(3)#3	84.79(2)
Br(2)#3-Cs(1)-Br(3)#3	58.05(2)	Br(1)-Cs(1)-Br(1)#16	89.81(3)
Br(4)#15-Cs(1)-Br(1)#16	71.08(2)	Br(7)-Cs(1)-Br(1)#16	67.83(3)
Br(4)#9-Cs(1)-Br(1)#16	98.84(3)	Br(2)#3-Cs(1)-Br(1)#16	108.43(3)
Br(3)#3-Cs(1)-Br(1)#16	166.20(3)	Br(1)-Cs(1)-Br(7)#9	114.83(3)
Br(4)#15-Cs(1)-Br(7)#9	62.02(2)	Br(7)-Cs(1)-Br(7)#9	87.81(3)
Br(4)#9-Cs(1)-Br(7)#9	59.91(2)	Br(2)#3-Cs(1)-Br(7)#9	112.59(3)
Br(3)#3-Cs(1)-Br(7)#9	60.10(2)	Br(1)#16-Cs(1)-Br(7)#9	133.08(3)

Symmetry transformations used to generate equivalent atoms: #1 $x, y, -z+1/2$; #2 $x, -y-1/2, -z$; #3 $x-1, -y-1/2, -z$; #4 $x-1, y, z$; #5 $x+1, -y-1/2, -z$; #6 $-x+1, y-1/2, z$; #7 $-x, y+1/2, z$; #8 $-x+1, y+1/2, z$; #9 $-x, -y-1, -z$; #10 $x+1, y, z$; #11 $-x+2, y-1/2, z$; #12 $-x+2, y+1/2, -z+1/2$; #13 $-x+2, y+1/2, z$; #14 $-x+1, y+1/2, -z+1/2$; #15 $-x, y-1/2, z$; #16 $-x-1, -y-1, -z$; #17 $x, -y-3/2, -z$; #18 $-x+1, -y-1, -z$.

Table S4. Anisotropic displacement parameters ($\text{\AA}^2 \times 10^3$) for Cs_3BiBr_6 . The anisotropic displacement factor exponent takes the form: $-2 \pi^2 [h^2 a^{*2} U_{11} + \dots + 2 h k a^* b^* U_{12}]$.

atom	U11	U22	U33	U23	U13	U12
Bi(1)	19(1)	22(1)	25(1)	0	0	2(1)
Bi(2)	25(1)	20(1)	19(1)	0(1)	0	0
Cs(3)	28(1)	46(1)	32(1)	6(1)	2(1)	2(1)
Cs(2)	32(1)	47(1)	30(1)	-3(1)	1(1)	0(1)
Br(5)	33(1)	28(1)	33(1)	0	0	-4(1)
Br(6)	32(1)	26(1)	32(1)	0	0	-2(1)
Br(7)	114(1)	25(1)	32(1)	9(1)	-6(1)	-2(1)
Br(4)	45(1)	65(1)	31(1)	-9(1)	-1(1)	-27(1)
Br(3)	50(1)	40(1)	55(1)	-6(1)	29(1)	5(1)
Br(2)	50(1)	41(1)	47(1)	4(1)	-24(1)	8(1)
Br(1)	48(1)	60(1)	46(1)	-2(1)	-21(1)	-17(1)
Cs(1)	103(1)	58(1)	47(1)	-9(1)	-19(1)	29(1)

Table S5. Crystallographic and electronic parameters for the known perovskites.

	Space group	a	b	c
Cs_3BiCl_6	C2/c	27.017	8.252	13.121
Rb_3BiBr_6	Pnma	13.311	26.63	8.603
Cs_2SnCl_6	Fm-3m	10.347	10.347	10.347
Cs_2SnBr_6	Fm-3m	10.771	10.771	10.771
Cs_2SnI_6	Fm-3m	11.631	11.631	11.631
$\text{Cs}_2\text{AgInCl}_6$	Fm-3m	10.469	10.469	10.469
Cs_3BiBr_6	Pbcm	8.689	13.628	27.694

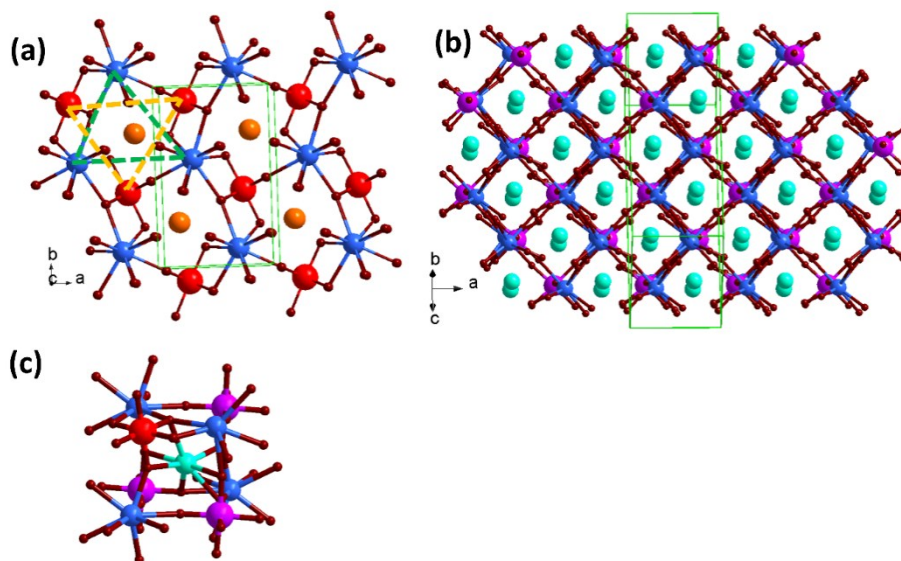


Fig. S1 View of the structures constructed by (a) Bi1, Cs3; and (b) Bi1, Bi2, Cs3 on the mirror plane, respectively. (c) A basic unit constructed from the Bi1, Bi2, Cs3. Color code: Bi1, red; Bi2, purple; Cs1, green; Cs2, orange; Cs3, blue; Br, Brown.

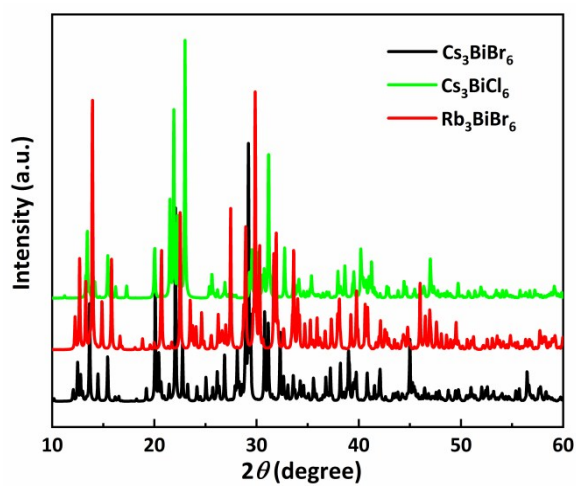


Fig. S2 Comparison of XRD pattern for Cs_3BiBr_6 , Rb_3BiBr_6 , Cs_3BiCl_6 .

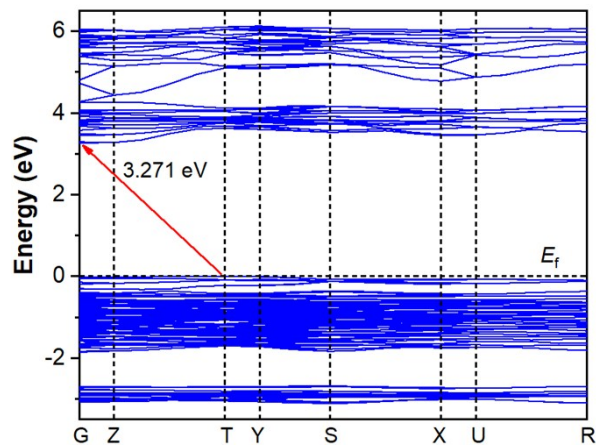


Fig. S3 The bandgap calculated from the DFT.

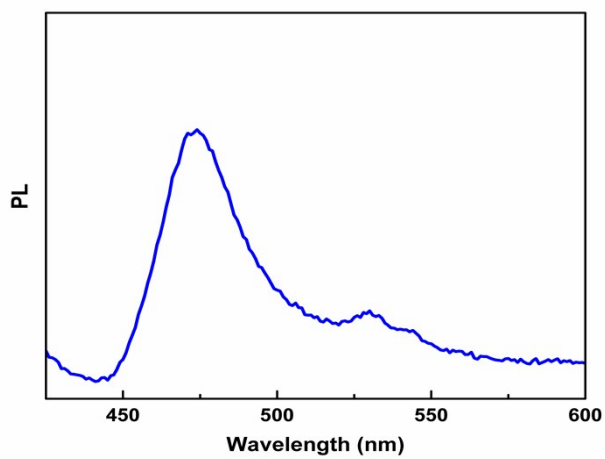


Fig. S4 The PL spectra for the Cs₃BiBr₆.

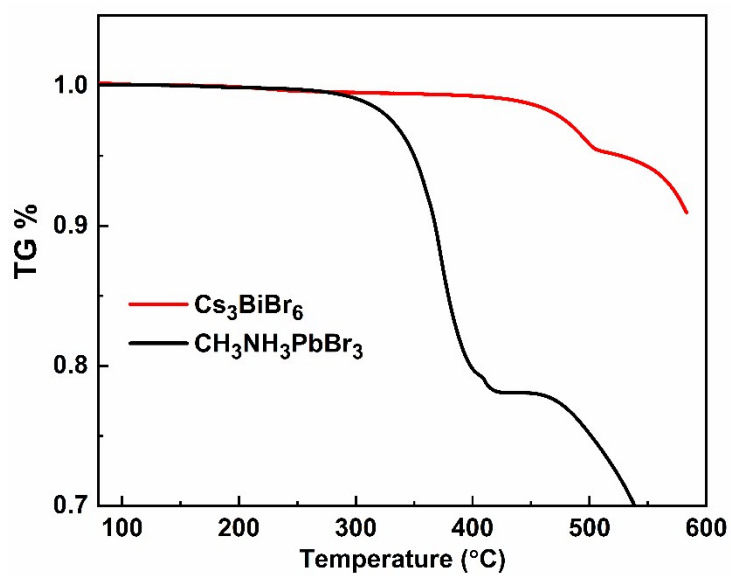


Fig. S5 TGA curves of Cs₃BiBr₆ and CH₃NH₃PbBr₃.

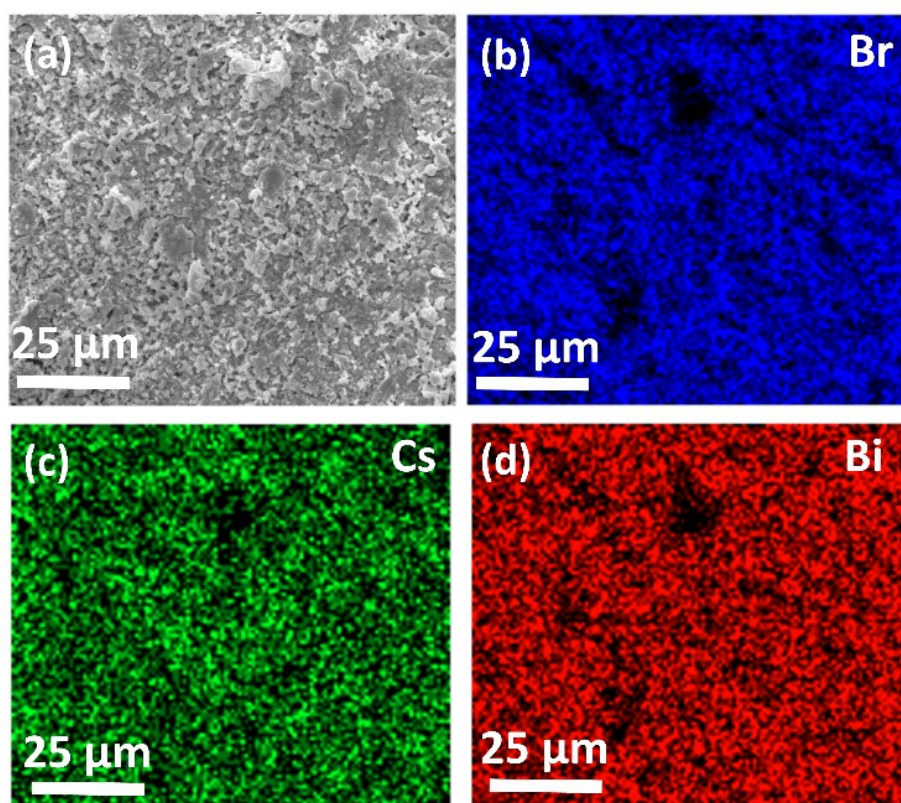


Fig. S6 (a) Electron micrograph of the microstructure for the photodetector. (b)-(d) Energy dispersive X-ray (EDX) mapping of the element distribution: (b) Br, (c) Cs, (d) Bi.

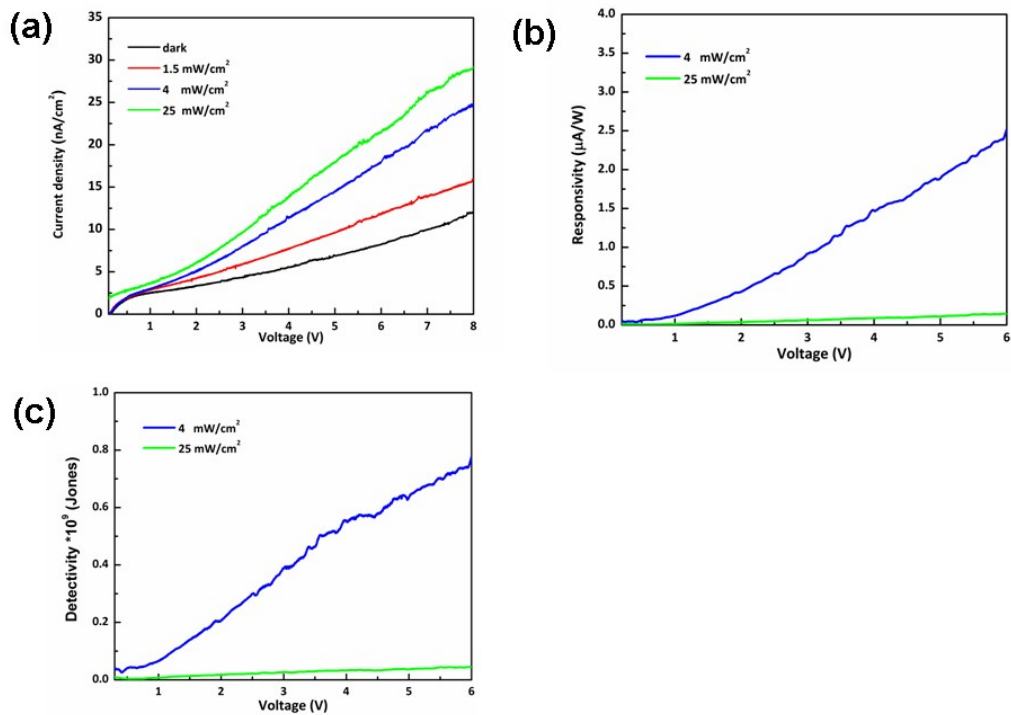


Fig. S7 (a) I-V characteristics under different power density. (b) Photocurrent responses under various light densities at bias voltage of 0- 6 V. (c) Comparison of the detectivity at two different light densities.

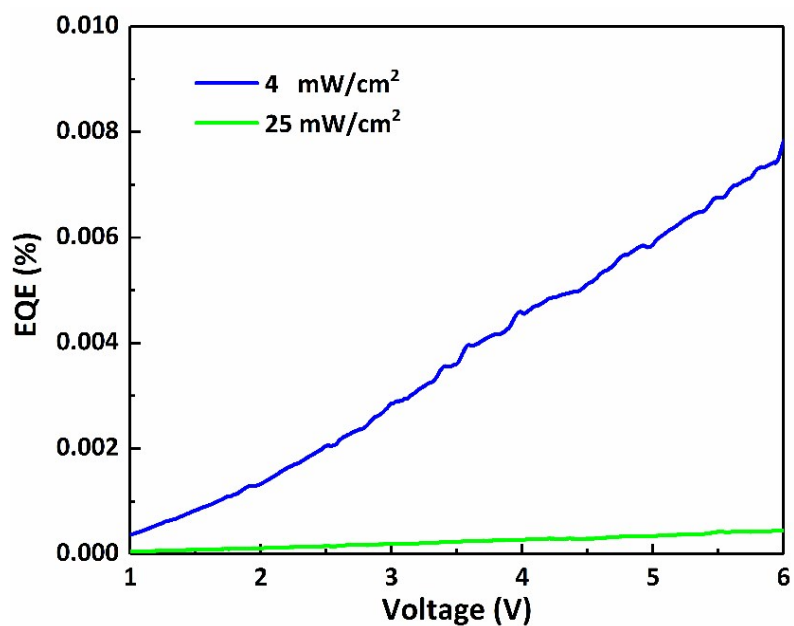


Fig. S8 EQE versus voltage under light illumination of 4 mW/cm² and 25 mW/cm².

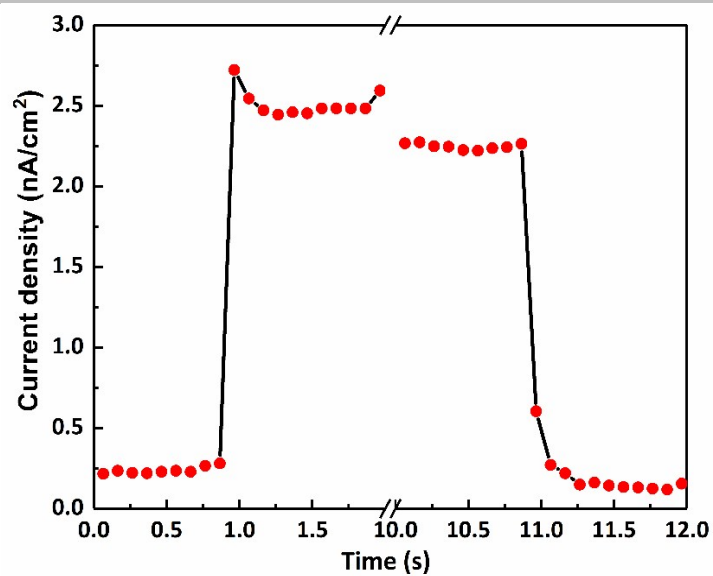


Fig. S9 The high-resolution I-t curve of Cs₃BiBr₆ devices towards 400 nm illumination with a powder intensity of 25 mW/cm².

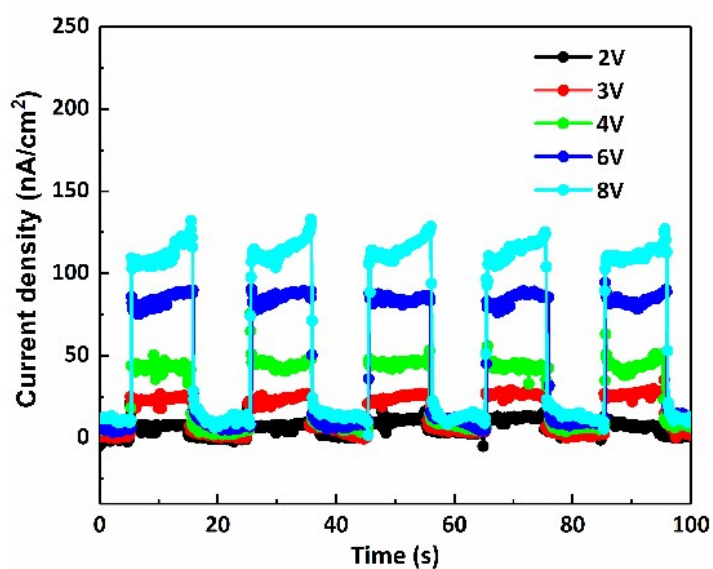


Fig. S10 Photoresponse of Cs₃BiBr₆ under white light illumination with power density of 350 mW/cm².

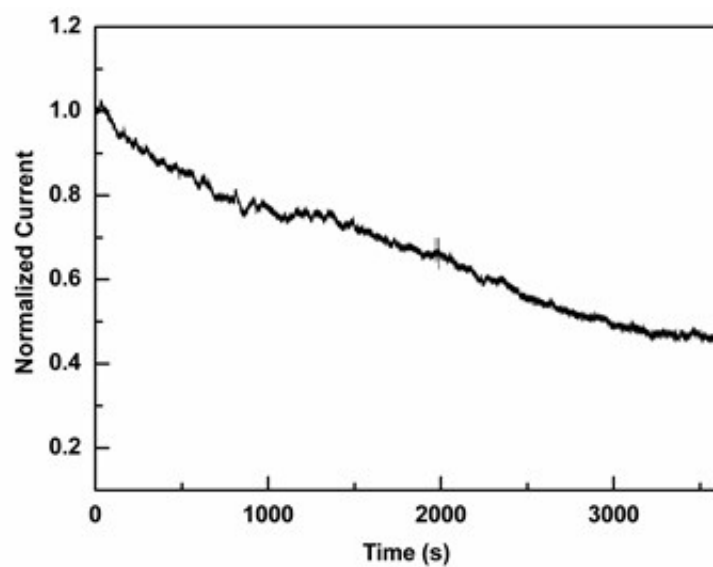


Fig. S11 The stability for the photodetector under light illumination.